Topological Phenomena in Time-Multiplexed Resonator Networks

Thesis by
Christian R. Leefmans

In Partial Fulfillment of the Requirements for the
Degree of
Doctor of Philosophy

CALIFORNIA INSTITUTE OF TECHNOLOGY
Pasadena, California

2024
Defended November 10, 2023

© 2024

Christian R. Leefmans
ORCID: 0000-0002-7708-3727

All rights reserved

ACKNOWLEDGEMENTS

First, I would like to thank my family, whose unwavering support throughout my graduate studies made this research possible. I am especially indebted to my parents and to my brother, Ian Leefmans, who have always been there to offer comfort in difficult moments and to celebrate moments of success.

Second, I would like to thank my friends, from Caltech, Cornell, and beyond, who have supported me throughout my PhD. I would especially like to thank Gabe Salmon, who was a great friend and roommate during my PhD. I am also especially grateful for my girlfriend, Elizabeth Zhou, whose kindness and encouragement helped make this thesis possible.

Third, I would like to thank Alireza Marandi both for the opportunity to work in his group and for his mentorship and support throughout my PhD.

Next, I would like to thank the members of the Marandi group who assisted me throughout my PhD. I am grateful to James Willams, whose FPGA programming made the experiments in this thesis possible. I am grateful to Midya Parto, with whom I collaborated on numerous projects and who provided valuable insight, feedback, and support. I am grateful to Gordon Li, whose insightful questions improved the quality of the topological temporally mode-locked laser experiments. I am grateful to Robby Gray, who helped make the soliton autocorrelation measurements in this thesis possible. I am also grateful to all the members of the Marandi group, past and present, who provided their support throughout the years.

I would also like to thank the many people with whom I have had the honor to work during my graduate studies. I am grateful to Avik Dutt, who taught me a great deal about running photonics experiments and whose contributions to the project "Topological Dissipation in a Time-Multiplexed Resonator Network" were invaluable. I am grateful to Franco Nori, whose support and feedback helped to improve the manuscripts that I wrote during my PhD. I am grateful to Nicolas Englebert, who taught me a great deal about cavity solitons and the design of active cavity resonators. I am also grateful to Shanhui Fan, Luqi Yuan, Nathan Goldman, Simon-Pierre Gorza, and François Leo, who provided helpful feedback and insight during my graduate studies.

ABSTRACT

In 2008, the prediction that gyromagnetic photonic crystals could host analogs of the quantum Hall effect sparked a revolution in photonics, as it became apparent that the synergy between photonics and topological physics provides distinct opportunities for fundamental research and technological innovation. Since then, topological photonics has produced experimental realizations of numerous theories from topological condensed matter physics, while the inherent robustness of topological edge states has enabled novel devices like topological lasers and topological quantum sources. Despite this success, practical challenges limit the breadth of topological phenomena accessible to the existing experimental platforms for topological photonics. Therefore, to accelerate the pace of scientific discovery and to inspire the next generation of topological technologies, it is desirable to develop a platform that overcomes the limitations of traditional topological photonic architectures. In this thesis, I propose time-multiplexed resonator networks as a next-generation platform for topological photonics, and I present three experimental projects that demonstrate the diverse capabilities of this platform.

In the first project, I use a time-multiplexed resonator network to demonstrate topological dissipation, in which nontrivial topology is encoded in the dissipation spectrum of a resonator array. I show measurements of dissipative topological phenomena in one- and two-dimensions and discuss how topological dissipation can be used to design resonator arrays with topologically robust quality factors. In the second project, I adapt a time-multiplexed resonator network to realize a topological mode-locked laser, and I show that this laser can realize non-Hermitian topological phenomena that had not previously been demonstrated in topological photonics. Finally, I experimentally study the dynamics of cavity solitons in a topological resonator array. This project demonstrates a general technique for realizing cavity solitons in large arrays of coupled resonators, which has become a relevant challenge in the soliton community over the past several years.

PUBLISHED CONTENT AND CONTRIBUTIONS

Leefmans, Christian, Nicolas Englebert, et al. (2023). "Cavity Solitons on a Lattice". In: *arXiv:2311.04873*. URL: `https://arxiv.org/abs/2311.04873`.
C.L., N.E., and A.M. conceived the idea. N.E. and C.L. performed the simulations. C.L., N.E., and J.W. designed and constructed the experiments. C.L. collected the data. C.L. and N.E. analyzed the data.

Parto, Midya, Christian Leefmans, James Williams, and Alireza Marandi (May 2023). "Enhanced sensitivity via non-Hermitian topology". In: *arXiv:2305.03282*. URL: `https://arxiv.org/abs/2305.03282`.
M.P. and C.L. designed and constructed the experiments.

Parto, Midya, Christian Leefmans, James Williams, Franco Nori, et al. (Mar. 2023). "Non-Abelian effects in dissipative photonic topological lattices". en. In: *Nature Communications* 14.1. DOI: `https://doi.org/10.1038/s41467-023-37065-z`.
M.P., C.L., and A.M. conceived the idea and devised the experiments and the underlying theory. M.P., C.L., and J.W. constructed the experimental setup and performed the experiments. M.P. and C.L. collected the data.

Leefmans, Christian, Avik Dutt, et al. (Apr. 2022). "Topological dissipation in a time-multiplexed photonic resonator network". en. In: *Nature Physics* 18.4. DOI: `https://doi.org/10.1038/s41567-021-01492-w`.
C.L., A.D. and A.M. devised the experiments and the underlying theory. C.L., A.D. and J.W. constructed and performed the experiments. C.L. collected the data and analyzed the data for the SSH band structure and edge state. A.D. analyzed the bulk occupation of the Harper Hofstadter edge state.

Leefmans, Christian, Midya Parto, et al. (Sept. 2022). "Topological Temporally Mode-Locked Laser". In: *arXiv:2209.00762*. URL: `https://arxiv.org/abs/2209.00762`.
C.L. and A.M. conceived the idea. C.L., A.D., and J.W. constructed the experimental setup. C.L. developed the theory, performed the simulations and experiments, and analyzed the data.

Roy, Arkadev et al. (Mar. 2022). "Topological optical parametric oscillation". en. In: *Nanophotonics* 11.8. DOI: `https://doi.org/10.1515/nanoph-2021-0765`.
C.L. provided feedback on the manuscript.

TABLE OF CONTENTS

LIST OF ILLUSTRATIONS

Chapter 1

INTRODUCTION

1.1 Overview

A classic example from the field of topology concerns the number of holes in an object. For instance, consider a bagel and a mug. Both objects typically have one hole, and if we had a malleable replica of a bagel, we could imagine continuously reshaping it into a mug without closing or ripping its hole. In this sense, the bagel and mug are "topologically equivalent," and they can be characterized by a topological invariant called the genus number g, which essentially counts the number of holes in an object (Hasan and Kane, 2010). For the bagel and mug, $g = 1$, and all objects with $g = 1$ can be continuously transformed into one another without changing g (closing the hole). In contrast, the cookie and pizza typically have no holes and are characterized by a genus number $g = 0$. We would have to tear a hole in them to fashion them into the shape of a mug.

While the example above seems far removed from physics, it turns out that related topological ideas can be used to characterize the band structures in condensed matter systems (Hasan and Kane, 2010). The idea of assigning topological invariants to band structures originated shortly after the discovery of the quantum Hall effect in 1980 (Klitzing, Dorda, and Pepper, 1980), when it was observed that the quantized Hall resistance could be understood by assigning a nontrivial topological invariant, the Chern number C, to each band in the system (Thouless et al., 1982). This discovery led to an explosion of research in topological condensed matter physics and has led to the discovery of myriad topological phenomena, including the fractional quantum Hall effect, topological superconductors, and topological insulators, to name only a few (Bernevig and Zhang, 2006; König et al., 2007; Fu, Kane, and Mele, 2007; Hsieh et al., 2009).

Nearly 30 years after the discovery of the integer quantum Hall effect, topological physics was introduced into photonics when it was observed that gyromagnetic photonic crystals should exhibit analogs of the quantum Hall effect (Raghu and Haldane, 2008; Haldane and Raghu, 2008). It quickly became apparent that photonics presents distinct opportunities to study topological phenomena (Ozawa, Price, et al., 2019). For instance, photonic systems can be constructed and addressed with site-level specificity, which allows one to controllably study edge effects and the effects of disorder (Zheng Wang et al., 2009; Ziteng Wang et al., 2023). Moreover, photonic systems can be designed to achieve lattices that have not been observed theoretically in condensed matter, which enables one to test theoretical predications that have not been confirmed in material systems. This capability has led to the realization of dynamic topological phenomena, such as Thouless pumping (Kraus and Zilberberg, 2016), and the realization of theoretical models like the Haldane model in photonic systems (Haldane, 1988; Liu, Jung, et al., 2021). As we shall see, the ability to controllably introduce nonlinearity, gain, and loss in photonic systems also substantially broadens the range of phenomena accessible to topological photonics (Smirnova et al., 2020; Bergholtz, Budich, and Kunst, 2021; Parto et al., 2021).

Beyond exciting opportunities to study fundamental topological physics, a major catalyst for the rise of topological photonics was the promise of topological photonic technologies (Ozawa, Price, et al., 2019). Topological lattices are associated with topological edge states, which lie at the boundary of a topological lattice and can be both agnostic to the shape of the boundary and robust against disorder in the underlying lattice. On one hand, the notion of topological robustness can be used to design photonic devices that are robust against fabrication errors. On the other hand, the properties of topological edge states can be leveraged to enhance device capabilities. For example, in recent years, topological edge states have been used to construct topological lasers with enhanced slope efficiencies (Bandres et al., 2018), arbitrary cavity geometries (Bahari et al., 2017; Zeng et al., 2020), or enhanced spatial coherence (Dikopoltsev et al., 2021) and to improve phase matching in photon pair generation (Mittal, Goldschmidt, and Mohammad Hafezi, 2018).

Given the potential of topological photonics for both fundamental research and technological advancement, it is important to consider what photonic platforms are well suited to realizing topological lattices. Perhaps the most natural platforms to consider are spatial platforms, which include various types of photonic crystals (Tang et al., 2022), coupled waveguide arrays (Blanco-Redondo et al., 2018; Mukherjee and Rechtsman, 2020; Maczewsky, Heinrich, et al., 2020; Jürgensen et al., 2023), and coupled resonator arrays (M. Hafezi et al., 2013; Mittal, Orre, et al., 2019; Zhao et al., 2019; Mittal, Moille, et al., 2021). In these spatial platforms, nontrivial topology is introduced by engineering a photonic structure in real space to achieve the desired topological properties in the system's band structure. Spatial topological photonics platforms have achieved substantial success since the inception of topological photonics and, in addition to the initial demonstration of topological photonics, have enabled photonic realizations of phenomena like anomalous Floquet topological insulators (Maczewsky, Zeuner, et al., 2017), Weyl points (Lu et al., 2015), and the quantum valley Hall effect (Noh et al., 2018). Moreover, spatial platforms have been investigated extensively as platforms for topological photonic technologies Bandres et al., 2018. However, despite this success, there are numerous challenges associated with studying topological photonics in spatial systems.

Major challenges associated with studying topological photonics with spatial structures are tied to the difficulty of fabricating certain lattices in real space. For example, three challenges of spatial topological photonics are implementing higher-dimensional topological lattices, implementing long range coupling, and achieving tunable boundary conditions. While experiments have utilized three-dimensional photonic crystals to study phenomena such as photonic topological insulators (Y. Yang et al., 2019), in some cases it is desirable to access physics in even higher dimensions. For example, directly implementing the four-dimensional quantum Hall effect (Zilberberg et al., 2018; Lohse et al., 2018) would require constructing a four-dimensional spatial structure. Meanwhile, the challenges associated with realizing long range coupling and tunable boundary conditions are related to the difficulty of physically connecting spatially separated elements. While next-nearest-neighbor couplings have been demonstrated with ring resonator arrays (Mittal, Orre, et al., 2019; Liu, Jung, et al., 2021), the space requirements of the individual resonators present a substantial challenge for achieving arbitrary site-to-site coupling. Similarly, it is unclear how to practically achieve periodic boundary conditions in greater than one-dimension with spatial topological photonic platforms.

To overcome the challenges faced by spatial topological photonic platforms, topological photonics adopted the concept of synthetic dimensions (Ozawa and Price, 2019). Synthetic dimensions are internal degrees of freedom in a system that can be treated as additional, albeit artificial, spatial dimensions. While experiments have utilized orbital angular momentum (Cardano et al., 2017) or spatial modes as synthetic dimensions (Lustig, Weimann, et al., 2019; Lustig, Maczewsky, et al., 2022), the frequency synthetic dimension (Yuan, Dutt, and Fan, 2021) and the temporal synthetic dimension (Regensburger, Bersch, Hinrichs, et al., 2011) have gained substantial traction both in and beyond topological photonics.

The frequency synthetic dimension maps the frequency modes of a resonator to the

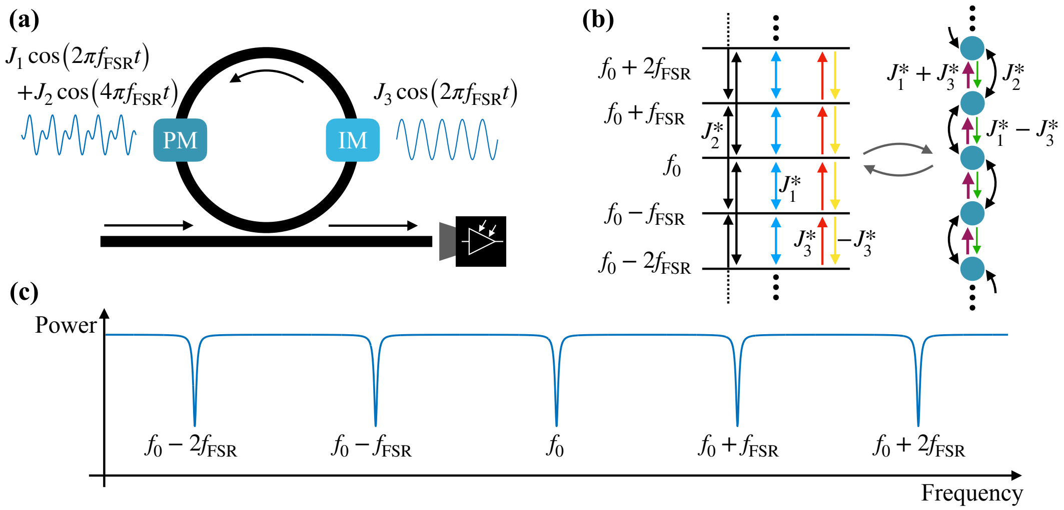

Figure 1.1: Frequency Synthetic Dimension in a Ring Resonator

Frequency Synthetic Dimension in a Ring Resonator (a) Phase and intensity modulation of a ring resonator can create coupling between the different frequency modes of the resonator. **(b)** Illustration of how the coupled frequency modes of the ring resonator in (a) can be mapped to a synthetic lattice with both long range coupling and non-Hermitian coupling. **(c)** Schematic illustration of equally-spaced frequency modes in a ring resonator without dispersion.

sites of a synthetic lattice (Yuan, Shi, and Fan, 2016; Yuan, Dutt, and Fan, 2021). Introducing phase or amplitude modulation into the resonator couples these sites to one another, leading to the formation of a synthetic lattice. The example of a frequency synthetic dimension shown in Fig. 1.1 highlights two of the major advantages of frequency synthetic dimensions. First, in contrast to real-space lattices, it is straightforward to produce long-range couplings in a synthetic frequency lattice by modulating the modulators in Fig. 1.1(a) at a multiple of the cavity free spectral range. Second, by including the intensity modulator in Fig. 1.1(a), it is possible to realize non-Hermitian couplings between the sites of a synthetic frequency lattice (K. Wang, Dutt, K. Y. Yang, et al., 2021; K. Wang, Dutt, Wojcik, et al., 2021). While is possible to realize these non-Hermitian couplings in spatial systems (Liu, Wei, et al., 2022), the convenience of implementing non-Hermitian couplings in synthetic frequency lattices has contributed to their role in groundbreaking experiments in non-Hermitian topological photonics (K. Wang, Dutt, K. Y. Yang, et al., 2021; K. Wang, Dutt, Wojcik, et al., 2021). An additional advantage of frequency synthetic lattices is their size. One recent experiment demonstrated a frequency synthetic lattice in the soliton regime that hosted more that 240, 000 lattice sites (Englebert et al., 2023), which is substantially larger than any real-space photonic lattice realized

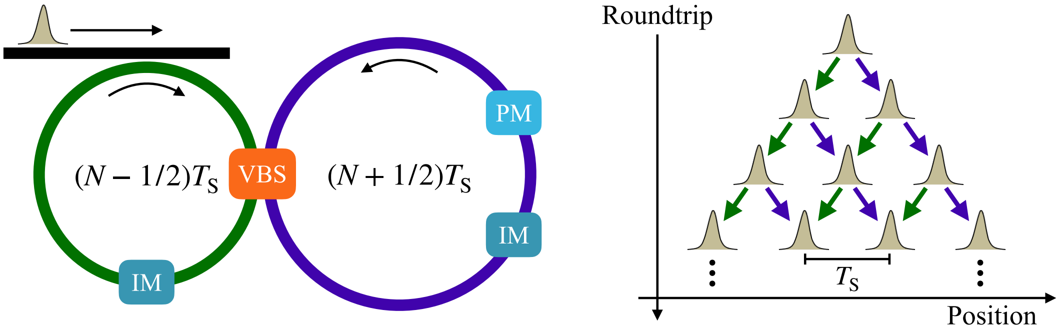

Figure 1.2: Two-Loop Architecture for Temporal Synthetic Dimensions

Two-Loop Architecture for Temporal Synthetic Dimensions (a) The two loop architecture consists of two fiber loops of staggered lengths coupled at a variable beam splitter. Each loop contains modulators to enable control over the phase and intensity of the site-to-site coupling in the temporal synthetic lattice. **(b)** At the beginning of an experiment, a single pulse is injected into the two-loop setup. Here we show how this single pulse evolves from roundtrip to roundtrip in the temporal mesh lattice. This figure is adapted from Regensburger, Bersch, Miri, et al., 2012; Weidemann, Kremer, Longhi, et al., 2022.

to date.

While frequency synthetic dimensions provide advantages in terms of long-range couplings, non-Hermitian couplings, and lattice sizes, they also encounter several challenges. First, it is also difficult to control the boundary conditions of frequency synthetic dimensional lattices. The use of an auxiliary ring resonators to produce a boundary was only recently demonstrated (Dutt, Yuan, et al., 2022), and periodic boundary conditions have not been realized. Second, while it is straightforward to implement nonreciprocal and non-Hermitian couplings in frequency lattices, it is difficult to realize inhomogeneous couplings and lattice potentials in frequency synthetic dimensions (Yuan, Shi, and Fan, 2016; Z. Yang et al., 2020; Dutt, Minkov, et al., 2020; Li et al., 2023). The difficulties of controlling the boundary conditions and of introducing inhomogeneity in synthetic frequency lattices may create challenges in terms of studying topological robustness in disordered topological lattices with frequency synthetic dimensions.

Like frequency synthetic dimensions, temporal synthetic dimensions provide a viable alternative to spatial topological photonics experiments. The time-multiplexed resonator network discussed in this thesis utilizes temporal synthetic dimensions, but first we will discuss a different, commonly used platform for temporal synthetic dimensions, which is shown in Fig. 1.2(a). This platform, which we will call the "two-loop architecture," has gained popularity in topological photonics (Wimmer et al., 2015; Vatnik et al., 2017; Bisianov et al., 2019; Weidemann, Kremer, Longhi, et al., 2021), and, therefore, it is worthwhile introducing this platform so that we may contrast it with our time-multiplexed resonator networks in Sec. 1.2.

The two-loop architecture consists of two fiber loops with staggered lengths that are conservatively coupled with a variable beam splitter (Regensburger, Bersch, Hinrichs, et al., 2011). If the separation between two pulses in the mesh lattice is T_{s}, then the roundtrip delay through the larger loop is $(n + 1/2)T_{\mathrm{s}}$, while the delay through the shorter loop is $(n-1/2)T_{\mathrm{s}}$, for some integer n. As we show in Fig. 1.2(b), the staggered loop lengths create nearest-neighbor coupling between the sites of a mesh lattice. When a single site is excited, the excitation undergoes a random walk, analogous to what occurs when a single waveguide is excited in a one-dimensional waveguide array.

The two-loop architecture has successfully enabled numerous groundbreaking photonics experiments, including the realizations of parity-time (PT) symmetric lattices (Regensburger, Bersch, Miri, et al., 2012), topological funneling (Weidemann, Kremer, Helbig, et al., 2020), and a triple topological phase transition (Weidemann, Kremer, Longhi, et al., 2022). However, despite these successes, the two-loop architecture appears to still encounter several challenges. While the two-loop architecture enables the realization of non-reciprocal and non-Hermitian couplings Weidemann, Kremer, Helbig, et al., 2020; Weidemann, Kremer, Longhi, et al., 2021, it has mostly been used to study one-dimensional photonic mesh lattices with nearest-neighbor couplings. Moreover, while a two-dimensional extension of the two-loop architecture has been realized (Chalabi et al., 2019), this design has not been extended to higher dimensions. Finally, while domain walls have been realized in the two-loop architecture (Weidemann, Kremer, Helbig, et al., 2020), periodic boundary conditions have not been demonstrated in the two-loop architecture. The realization of periodic boundary conditions in these systems could be useful for studying disorder in bulk non-Hermitian topological lattices Hatano and Nelson, 1996; Gong et al., 2018.

The time-multiplexed resonator networks studied in this thesis have the potential to overcome some of the limitations encountered by frequency synthetic dimensions and the two-loop architecture for temporal synthetic dimensions. As we will explain in the next section, time-multiplexed resonator networks are scalable to large lattice sizes and to multiple synthetic dimensions, are adaptable to different lattice types,

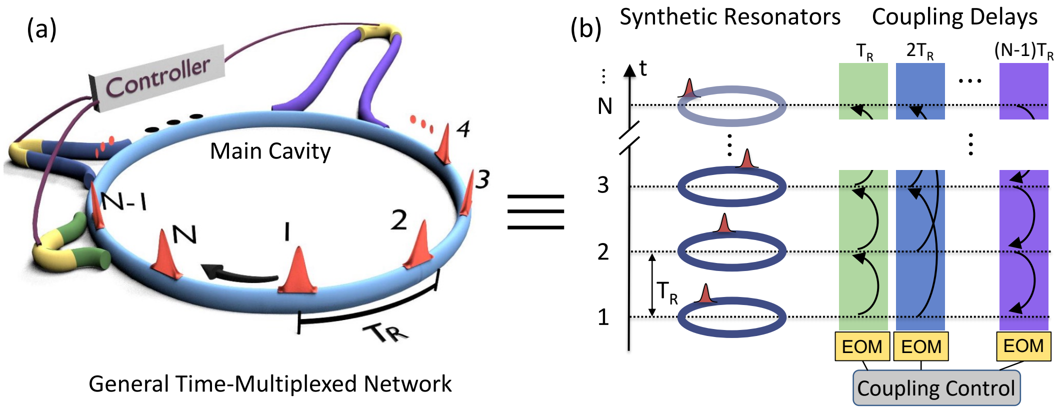

Figure 1.3: Generic Time-Multiplexed Resonator Network

Generic Time-Multiplexed Resonator Network (a) Schematic depiction of a generic time-multiplexed resonator with N delay lines. With N delay lines, this network is capable of producing all-to-all couplings. **(b)** Illustration showing the mapping between the time-multiplexed resonator network and N synthetic resonators with all-to-all couplings.

and are capable of inhomogeneous, non-reciprocal, and dynamic couplings.

1.2 Time-Multiplexed Resonator Networks

We present a generic figure of a time-multiplexed resonator network in Fig. 1.3(a). This network consists of a primary resonant loop (the “main cavity”) along with a series of N delay lines. We populate this cavity with N resonant pulses separated by a repetition period T_{R}, and we carefully choose the lengths of the N delay lines to introduce all-to-all connections between the pulses in the network. Moreover, by including intensity and phase modulators in the delay lines, it is possible to arbitrarily control the strengths and phases of the couplings between any two lattice sites. The dynamics of the pulses in our time-multiplexed network are analogous to those of an array of spatially coupled resonators. However, as is evident from Fig. 1.3, a major advantage of using time-multiplexed networks is that we can realize dense connectivity between the resonators in our synthetic resonator array without the fabrication challenges associated with spatial arrays.

One major difference between our time-multiplexed resonator networks and the spatially coupled resonator arrays frequently used for topological photonics experiments is that our time-multiplexed resonator networks utilize dissipative couplings rather than conservative couplings. We illustrate the differences between dissipative and conservative couplings in Fig. 1.4.

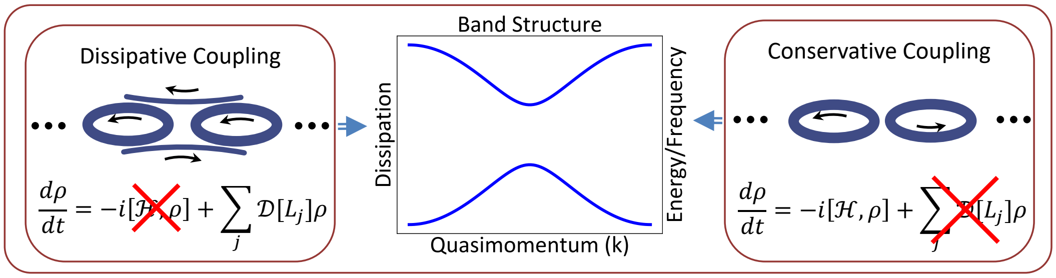

Figure 1.4: Conservative and Dissipative Coupling

Conservative and Dissipative Coupling Dissipative coupling, which is depicted on the left, gives rise to bands of dissipation. On the other hand, conservative coupling, which is depicted on the right, produces bands of energy or frequency.

Conservative coupling, which is also sometimes called Hamiltonian coupling, occurs when two elements, such as two atoms or two ring resonators, are directly coupled through their overlapping modes. A schematic representation of a conservative coupling is shown in Fig. 1.4. With conservative coupling, information is exchanged directly between the two ring resonators and energy is conserved. The conservation of energy restricts the set of phase relationships possible in conservative couplings, as the scattering matrix that describes the coupling process must be unitary. It is well established that conservative couplings give rise to energy or frequency splitting in systems of coupled atoms or coupled resonators.

In stark contrast, dissipative coupling occurs when two elements are coupled through an intermediate reservoir. An example of this is shown in Fig. 1.4, where two ring resonators are coupled through bus waveguides that each play the role of a unidirectional reservoir[1]. Each resonator couples light into the bus waveguides. In general, a portion of this light continues through the open port and is irrevocably lost from the system, but the remainder of the light couples back into the other resonator. Because light is lost into the open port, energy is not conserved in the process. As a result, the scattering matrix that defines the effective coupling between the two resonators no longer needs to be unitary. Indeed, because we can tune the length of each bus waveguide, we now have full control over the coupling phases. It turns out that the coupling phases determine what sort of splitting we see in a dissipatively coupled system. When the coupling phases are 0 or π, a dissipatively coupled system exhibits splitting purely in the dissipation spectrum of

---

[1] In our time-multiplexed resonator network, the optical delay lines act analogously to the bus waveguides in Fig. 1.4 by acting as unidirectional, intermediate reservoirs between the pulses in the network.

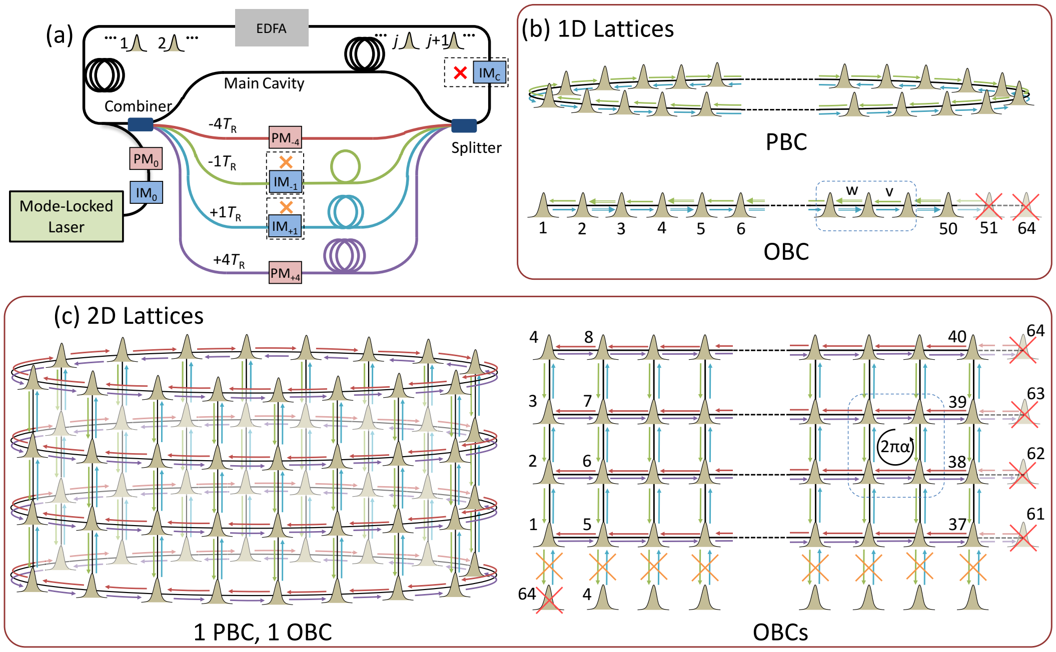

Figure 1.5: Time-Multiplexed Resonator Network With Four Delay Lines

Time-Multiplexed Resonator Network With Four Delay Lines (a) An example of a time-multiplexed resonator network with four delay lines. **(b)** This time-multiplexed resonator network may be mapped to a one-dimensional chain with nearest-neighbor coupling and fourth nearest-neighbor couplings. **(c)** The same network may also be mapped to a two-dimensional lattice. We can use the intensity modulators in the network to implement the lattice with either periodic boundary conditions or open boundary conditions along one direction.

their modes. However, this is not the only possibility with dissipative couplings: when the coupling phases are $\pi/2$, the system exhibits energy or frequency splitting, just like in conservatively coupled systems. For other values of the coupling phases, splitting can appear simultaneously in the frequency spectra and in the dissipation spectra of dissipatively coupled systems.

So far, we have generally discussed how time-multiplexed networks can enable all-to-all dissipative couplings between the pulses in the network. To engineer nontrivial topology into such a network, we design our dissipative couplings to map the pulses in our network to the sites of a synthetic topological lattice. An example of this is shown in Fig. 1.5, where we show the mapping between a time-multiplexed network with four delay lines and a two-dimensional, Harper-Hofstadter lattice. We first note that this four-delay line network can be represented by a one-dimensional lattice with nearest-neighbor and fourth nearest-neighbor coupling. However, simply by redefining the mapping between the pulses and the target lattice, we can consider these same fourth nearest-neighbor couplings in the one-dimensional lattice as nearest-neighbor couplings along a second synthetic dimension. The phase modulators in the $\pm 4T_{\mathrm{R}}$ delay lines enable us to engineer a synthetic magnetic flux into each plaquette of the two-dimensional synthetic lattice. Moreover, the intensity modulators in the main cavity and in the delay lines enable us to implement this synthetic lattice with either open boundary conditions along both directions or with a periodic boundary condition along one direction.

The mapping between the time-multiplexed network in Fig. 1.5(a) and the Harper-Hofstadter lattices in Fig. 1.5(c) demonstrates several important benefits of time-multiplexed networks. As we saw, it is straightforward to introduce additional synthetic dimensions in time-multiplexed resonator networks by properly defining the mapping between the delay line couplings and the target lattice. Therefore, by adding more delay lines, it is straightforward to realize higher-dimensional lattices with this approach. Alternatively, the mapping to the one-dimensional lattice in Fig. 1.5(b) shows that it is also straightforward to implement long-range couplings with additional delay lines. In addition, this example also illustrates how the flexibility of the time-multiplexed resonator network architecture enables tunable boundary conditions. Finally, the phase modulators in the figure introduce inhomogeneous and nonreciprocal coupling phases to achieve the synthetic magnetic fluxes in Fig. 1.5(c).

In addition to the benefits demonstrated by our example, there are several other advantages of time-multiplexed systems. First, the time-multiplexed architecture is scalable to large lattice sizes because we can add additional sites to a synthetic lattice simply by increasing the length of the system's main cavity. Secondly, it is straightforward to produce non-Hermitian couplings between the synthetic lattice sites because each delay line controls only one direction of each coupling. Finally, as we shall see later in this thesis, it is straightforward to add nonlinearity to our synthetic lattices. This is because, by adding a single nonlinear element to our main cavity, we ensure that every site in the synthetic lattice sees this nonlinear element as it circulates in the cavity.

From the discussion above, we see that time-multiplexed resonator networks overcome several of the limitations faced by both frequency synthetic dimensional architectures and by the two-loop architecture for synthetic dimensions. As we discussed, it is straightforward for frequency synthetic dimensional architectures to realize long-range and non-Hermitian couplings, but it is challenging to achieve inhomogeneous coupling and to implement controllable boundary conditions. Similarly, with the two-loop architecture it is straightforward to implement inhomogeneous coupling, but extensions of this architecture to long-range couplings or to multidimensional lattices remain rare, and it has not been shown how to implement periodic boundary conditions with this approach. In contrast, time-multiplexed resonator networks exhibit a straightforward way to implement multidimensional lattices while also enabling controllable boundary conditions and long-range, non-Hermitian, and inhomogeneous couplings. Therefore, we see that time-multiplexed networks manage to combine many of the advantages of working with frequency synthetic dimensions or the two-loop architecture while also overcoming a number of the challenges associated with these other platforms.

1.3 Outlook

The rest of this thesis will discuss the application of time-multiplexed resonator networks to the study of topological photonics. This thesis is organized as follows.

In Chapter 2 and Chapter 3, we study how dissipative couplings influence the dynamics of linear, topological lattices. Here, we introduce the concept of topological dissipation, which arises when nontrivial topological invariants appear in the dissipation spectrum of a dissipatively coupled topological lattice. We apply our time-multiplexed resonator network to measure the dissipation spectra of a topological lattice, and we demonstrate the existence of topological edge states in dissipatively coupled SSH and Harper-Hofstadter topological lattices. These demonstrations lay the foundation for the remaining chapters of the thesis, in which we study topological dissipation in nonlinear topological systems.

In Chapter 4 and Chapter 5, we discuss the topological temporally mode-locked laser. By bringing our time-multiplexed resonator network above threshold, this work combines the notion of topological dissipation with the idea of temporal mode-locking, in which intracavity couplings lock the relative amplitudes and phases of the pulses in a harmonically mode-locked laser. Using this idea, we study topological temporal mode-locking in point-gap topological lattices, and we demonstrate several aspects of point-gap topological physics that had not been shown before in photonics. For example, we demonstrate that the Hatano-Nelson model with periodic boundary conditions is robust against disorder-induced localization. To the best of our knowledge, this work was the first to study a photonic topological lattice in a mode-locked laser.

In Chapter 6 and Chapter 7, we study the dynamics of cavity solitons in a dissipatively coupled SSH lattice. We discover an operating regime in which cavity solitons form preferentially at the boundaries of an SSH lattice in the topological phase but not at the boundaries of an SSH lattice in the trivial phase. In addition to demonstrating new physics, this study demonstrates a novel technique for studying cavity solitons in large-scale arrays of coupled resonators. Given recent interest in studying cavity soliton dynamics in arrays of coupled resonators, we believe that our approach with time-multiplexed resonators could find numerous applications in the soliton community.

Chapter 2

TOPOLOGICAL DISSIPATION IN A TIME-MULTIPLEXED RESONATOR NETWORK

2.1 Abstract

Topological phases feature robust edge states that are protected against the effects of defects and disorder. These phases have largely been studied in conservatively coupled systems, in which nontrivial topological invariants arise in the energy or frequency bands of a system. Here we show that, in dissipatively coupled systems, nontrivial topological invariants can emerge purely in a system's dissipation. Using a highly scalable and easily reconfigurable time-multiplexed photonic resonator network, we experimentally demonstrate one- and two-dimensional lattices that host robust topological edge states with isolated dissipation rates and measure a dissipation spectrum that possesses a nontrivial topological invariant. Furthermore, we demonstrate topological protection of the network's quality factor. The topologically nontrivial dissipation of our system exposes new opportunities to engineer dissipation in both classical and quantum systems. Moreover, our experimental platform's straightforward scaling to higher dimensions and its ability to implement inhomogenous, nonreciprocal, and long-range couplings may enable future work in the study of synthetic dimensions.

2.2 Introduction

Most topological phases in condensed matter (Hasan and Kane, 2010), ultracold atoms (Cooper, Dalibard, and Spielman, 2019), and photonics (Ozawa, Price, et al., 2019) rely on conservative couplings to achieve nontrivial topological invariants. Conservative couplings arise when the elements of a system, such as the atoms of a quantum system or the ring resonators of a photonic system [see Fig. 2.1(a)], exchange information directly through their overlapping modes. The conservation of energy imposes a particular set of possible phase relationships on conservative couplings due to the unitary nature of the scattering matrix. In topological lattice models, conservative couplings engender energy or frequency spectra whose bands are characterized by quantized, nonzero topological invariants. The presence of nontrivial topological invariants in turn gives rise to topologically protected edge states at the boundaries of the lattice (Jackiw and Rebbi, 1976; Hatsugai, 1993), whose existence is robust against the presence of defects and disorder. The edge states of conservatively coupled systems are touted for their unusual and exceptional transport dynamics, which may be unidirectional and free from back-scattering.

Dissipative couplings indirectly couple the elements of a system through an intermediate reservoir (Metelmann and Clerk, 2015; Mukherjee, Mogilevtsev, et al., 2017), such as a bath of atomic modes or the modes of a bus waveguide (Ding et al., 2019) [see Fig. 2.1(a)]. Dissipative couplings may be thought of as two separate couplings: information from one element of the system first couples into the reservoir and then couples from the reservoir into a second element of the system. In general, some information is irrevocably lost to the reservoir in this process, and dissipative couplings do not conserve energy. However, dissipative couplings enable additional freedom to engineer the coupling phases, as the system's scattering matrix is no longer unitary[1]. As shown in Fig. 2.1(a), the right choice of coupling phases can introduce splittings purely in the dissipation modes of a system. Other coupling phases may introduce splittings in the frequency modes of a system or in a combination of the frequency and dissipation modes [see Sec. 3.3]. Such dissipation engineering plays an important role in superconducting circuits, ultracold atoms, and photonics, where it is used for reservoir engineering (Barreiro et al., 2011), for laser mode-locking (Haus, 2000; Wright et al., 2020), and for quantum and photonic computing (Verstraete, Wolf, and Ignacio Cirac, 2009; Marandi et al., 2014; Inagaki et al., 2016). Several recent studies have proposed combining dissipative and conservative couplings to enable time-reversal symmetry breaking couplings (Fang, Luo, et al., 2017) and to induce nontrivial topological invariants (Wanjura, Brunelli, and Nunnenkamp, 2020; Gneiting et al., 2022; Dasbiswas, Mandadapu, and Vaikuntanathan, 2018; Li et al., 2019; Wang, Dutt, et al., 2021). These proposals suggest that dissipative coupling, like nonlinearity (Mukherjee and Rechtsman, 2020; Maczewsky et al., 2020; Xia et al., 2021) and local gain and loss (Zhao, Miao, et al., 2018; Zhao, Qiao, et al., 2019; Weidemann et al., 2020), may enable new topological phases and topology-inspired technologies for quantum and classical applications. However, the topological phases that arise in lattices with purely dissipative couplings remain largely unexplored (Bardyn et al., 2013; Yoshida and Hatsugai, 2021).

Here, we experimentally realize topological phases with purely dissipative cou-

---

[1] It is essential to distinguish dissipative couplings from the on-site gain and loss produced by, say, laser gain and absorption. The latter phenomena, combined with conservative couplings, have been extensively studied in both theory and experiment in non-Hermitian topological photonics. In this work, we study nontrivial topology that appears solely due to dissipative couplings. Such a phenomenon has not been experimentally studied in topological photonics.)

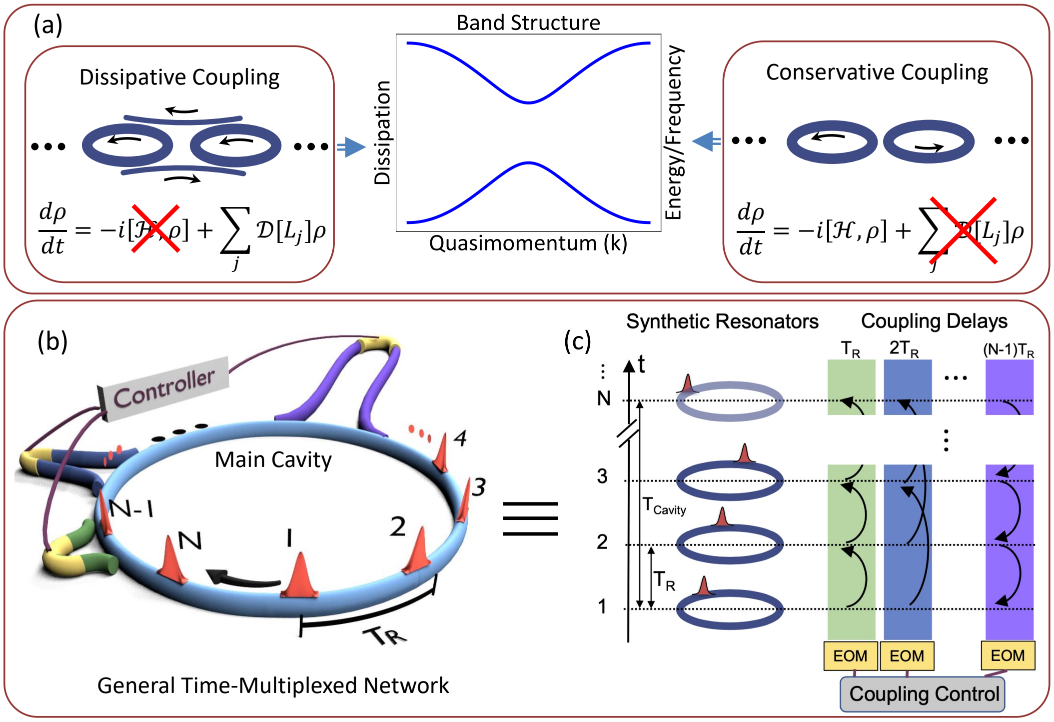

Figure 2.1: Topological dissipation and time-multiplexed resonator networks

Topological dissipation and time-multiplexed resonator networks. (a) Dissipatively coupled resonators (left panel) can map the energy spectrum of a tight-binding model to the dissipation spectrum of the resonators. The dynamics of dissipatively coupled resonators can be described by the dissipators, $\mathcal{D}[L_j]$, of a Lindblad master equation [see Eq. 2.1]. Note that with purely dissipative coupling, there are no Hamiltonian dynamics ($\mathcal{H} = 0$) [See Sec. 3.5 for a detailed derivation]. On the other hand, conservatively coupled resonators (right panel) map the energy bands of a tight-binding model to the frequency spectrum of the resonators. In the absence of loss, the dynamics of a conservatively coupled system exhibit only Hamiltonian dynamics: $\rho = -i[\mathcal{H},\rho]$. **(b)** Schematic of a resonant cavity loop (light blue) that supports N pulses separated by a repetition period, T_R, and possesses delay lines of various lengths. The delay lines contain electro-optic modulators (EOMs, yellow), driven by a controller. **(c)** Equivalent synthetic resonator representation of (b). Each synthetic resonator consists of a single, recirculating pulse. The time-multiplexed network is built by coupling the pulses with delay lines, which are indicated by the shaded boxes.

plings. In contrast to previous work, our dissipatively coupled topological lattices exhibit topologically nontrivial bands of dissipation rates and feature robust topological edge states with dissipation rates between those of the bulk bands.

Our experimental platform consists of a time-multiplexed resonator network [Fig. 2.1(b,c)] that uses the notion of synthetic dimensions (Ozawa and Price, 2019; Yuan et al.,

2018) to generate dissipatively coupled lattices that are capable of hosting nontrivial topological invariants. A general implementation of this network [see Fig. 2.1(b)] contains N resonant optical pulses separated by a repetition period T_{R}. Each pulse represents a single, synthetic lattice site, represented by a synthetic resonator in Fig. 2.1(c). As the pulses traverse the primary fiber loop (the "Main Cavity" in Fig. 2.1(b)), a portion of each pulse enters the network's $(N-1)$ delay lines. These delay lines act analogously to the bus waveguides shown in Fig. 2.1(a) by mediating unidirectional couplings between the network's time-multiplexed resonators. The lengths of the $(N-1)$ delay lines are chosen so that each pulse couples to the other $(N-1)$ pulses in the network, and the electro-optic modulators (EOMs) in the delay lines determine the strengths and phases of the couplings (Marandi et al., 2014). By mapping the couplings of the network to a particular lattice model, our network represents the connections of the model under study.

While previous studies have realized time-multiplexed random walks in synthetic photonic lattices (Wimmer et al., 2017; Chen et al., 2018; Chalabi et al., 2019; Weidemann et al., 2020), these traveling-wave architectures relied on conservatively coupled fiber loops and functioned similarly to real-space waveguide arrays. Moreover, it has not been shown how to extend these architectures beyond nearest-neighbor coupling or to higher than two-dimensions. In contrast, the flexible site-to-site couplings of our resonator-based design are akin to those of the original optical Ising machine (Marandi et al., 2014), and, by simply adding more delay lines, it is straightforward to realize long-range couplings, different lattice types, and additional synthetic dimensions with our network architecture. In addition, our network may be reconfigured to realize different lattice models or different parameter regimes by reprogramming the modulator driving signals that control the strengths and phases of the couplings. In this work, we demonstrate our network's ability to readily implement multiple synthetic dimensions, tunable boundary conditions, dynamic and inhomogeneous couplings, and time-reversal symmetry breaking gauge potentials. Simultaneously achieving these behaviors presents a substantial challenge to existing platforms for synthetic dimensions (Yuan et al., 2018; Ozawa and Price, 2019; Lustig et al., 2019; Dutt et al., 2020). Furthermore, the dissipation introduced by our system's dissipative couplings stands in sharp contrast to the on-site gain and loss used to realize non-Hermitian topology (Zeuner et al., 2015; Weimann et al., 2017) or nonreciprocal couplings in previous, conservatively coupled experiments (Weidemann et al., 2020). It is our dissipative couplings that give rise to topologically nontrivial bands of dissipation rates in our system and that distinguishes our work

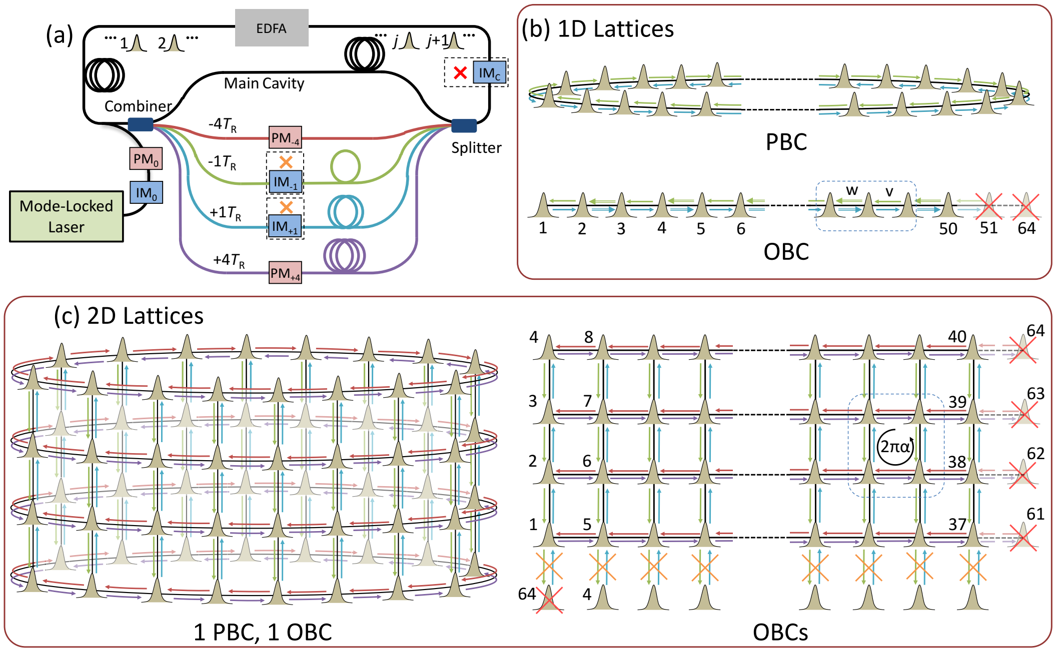

Figure 2.2: Realizing 1D and 2D synthetic lattices with switchable boundary conditions in a time-mutliplexed resonator network

Realizing 1D and 2D synthetic lattices with switchable boundary conditions in a time-mutliplexed resonator network. **(a)** We construct a four-delay line, time-multiplexed network capable of implementing two synthetic dimensions. **(b)** With the $\pm 4T_\mathrm{R}$ delay lines blocked, we use the intensity modulators (IM) in the $\pm T_\mathrm{R}$ delay lines, IM$_{\pm 1}$, to implement a 1D chain with the staggered couplings (w and v) of the SSH model. The intercavity IM, IM$_\mathrm{C}$, enables both periodic boundary conditions (PBCs) and open boundary conditions (OBCs). **(c)** With all four delay lines, the network can implement a 2D square lattice. The PMs in the $\pm 4T_R$ delay lines, PM$_{\pm 4}$, produce the time-reversal symmetry breaking couplings of the Harper-Hofsatdter model, while IM$_{\pm 1}$ enforces OBCs along the “vertical” direction. IM$_\mathrm{C}$ enables PBCs or OBCs along the “horizontal” direction.

from previous work in topological photonics.

To study the dissipatively coupled equivalents of the Su-Schrieffer-Heeger (SSH) (Su, Schrieffer, and Heeger, 1979) and Harper-Hofstadter (HH) (Hofstadter, 1976; Harper, 1955) models, we construct the four-delay-line network shown in Fig. 2.2(a), which hosts $N = 64$ synthetic lattice sites and can implement 1D chains and 2D square lattices with either open boundary conditions (OBCs) or a single periodic boundary condition (PBC) [Figs. 2.2(b,c)]. The details of this setup are described in Sec. 3.1. We model the dynamics of this network by the general Lindblad master equation

$$\frac{d}{dt}\rho = \mathcal{L}\rho = -i[\mathcal{H}, \rho] + \sum_j \mathcal{D}[L_j]\rho. \tag{2.1}$$

Here $\mathcal{H}$ denotes the Hermitian Hamiltonian dynamics due to conservative couplings between sites labeled by j [see the right panel of Fig. 2.1(a)]. Because our network possesses purely dissipative couplings [see the left panel of Fig. 2.1(a)], we consider the case in which $\mathcal{H} = 0$. Instead, the dissipators $\mathcal{D}[L_j]\rho = L_j \rho L_j^\dagger - \{L_j^\dagger L_j, \rho\}/2$, with nonlocal jump operators $L_j = \sqrt{\Gamma}\,(a_j + e^{-i\theta} a_{j+1})$, completely describe the purely dissipative coupling between our synthetic lattice sites (Wanjura, Brunelli, and Nunnenkamp, 2020). In Sec. 3.5, we derive the jump operators for our network's delay line architecture [Fig. 2.1(b)] and show how to implement dissipatively coupled SSH and HH lattices. We also show how to engineer the phases of the delay lines to emulate purely conservative and hybrid conservative-dissipative dynamics with our network's dissipative couplings. Although our current experimental results can be explained by the classical, mean-field behavior of Eq. 2.1, the full quantum dynamics of this equation may be applicable to future implementations with lower intrinsic losses and greater nonlinearities. In this sense our work represents a step towards the experimental realization of photonic topological open quantum systems, where there is an interesting interplay between dark states, quantum jumps, and topology (Diehl et al., 2011; Bardyn et al., 2013; Gneiting et al., 2022).

2.3 Results

Starting from Eq. (2.1), we can express the evolution of the mean-field pulse amplitudes, $\langle a_j \rangle$, as

$$\frac{d\langle \mathbf{a} \rangle}{dt} = (K - \gamma)\langle \mathbf{a} \rangle + \mathbf{P}, \tag{2.2}$$

where t represents the slow-time (roundtrip-to-roundtrip) evolution of the network, γ represents the intrinsic losses of the resonators, $\mathbf{P}$ models a coherent drive, and K is the network's coupling matrix. Importantly, our time-multiplexed resonator network can implement arbitrary amplitudes and phases for the coupling matrix elements K_{mn} without any symmetry constraints. This is substantially beyond the capabilities of previous synthetic-dimensional architectures, including other time-multiplexed systems (Chalabi et al., 2019; Weidemann et al., 2020; Wimmer et al., 2017; Chen et al., 2018) and architectures that utilize alternative synthetic dimensions (Lustig et al., 2019; Dutt et al., 2020; Wang, Dutt, et al., 2021; Bell et al., 2017). By engineering K to implement the couplings of the SSH or the HH model, our dissipatively coupled network acquires a dissipation spectrum identical to the topologically nontrivial band structure of the model under study. Moreover, the mean-field eigenstates of Eq. 2.2 also become the eigenstates of the model implemented by K. As the topological invariants of the SSH and of the HH models depend solely on the models' eigenstates, the topological invariants of our dissipatively coupled network are therefore identical to those of the familiar, conservatively coupled systems, but the topological invariants are now associated with topologically nontrivial dissipation bands [see Sec. 3.4]. As a result, in the presence of OBCs our network is guaranteed to possess the same topological edge states as its conservatively coupled counterparts, and the edge states inherit the same robustness against disorder in the system [see Sec. 3.4].

Introducing a properly engineered coherent drive into our network [$\mathbf{P}$ in Eq. 2.2] allows us to probe specific states in our dissipative topological lattice. We generate the desired $\mathbf{P}$ by using the modulators IM_0 and PM_0 in Fig. 2.2(a) to excite a specific state of the network, and we track the state's evolution to glean information about the underlying synthetic lattice. For instance, to probe the network's topological edge state, we program $\mathbf{P}$ to excite the edge state. If the edge state is an eigenstate of the network, then the edge state excitation will remain localized as it resonates within the network. On the other hand, if the edge state is not an eigenstate, then the edge state excitation will undergo diffusive dynamics dictated by Eq. 2.2. Similarly, when we institute the network's single PBC, we can choose $\mathbf{P}$ to excite a lattice's complete set of Bloch eigenstates. Measuring the steady states of these eigenstates allows us to reconstruct the 1D band structure of the model under study [see Sec. 3.2].

To demonstrate purely dissipative topological phenomena, we first program our network to implement the couplings of the SSH model (Su, Schrieffer, and Heeger, 1979; Asbóth, Oroszlány, and Pályi, 2016). The SSH model describes a 1D dimerized chain with intra-dimer coupling w and inter-dimer coupling v [see Fig. 2.3] (Malkova et al., 2009), and the model's band structure is characterized by a topological winding number, $\mathcal{W}$. When $w < v$, $\mathcal{W} = 0$, and the system is in a topologically trivial phase. However, when $w > v$, $\mathcal{W} = 1$, and the system is in a topological phase that hosts mid-gap, topologically protected edge states.

We probe the SSH model's topological edge state by implementing a 50-site SSH lattice with OBCs and by inducing a topological phase transition between the SSH model's trivial and topological phases [Fig. 2.3(a)]. In addition to allowing us to probe the SSH model's trivial and topological phases in a single experiment, this measurement highlights our network's ability to implement dynamic couplings. For 50 roundtrips, we excite the network with the SSH edge state corresponding to the

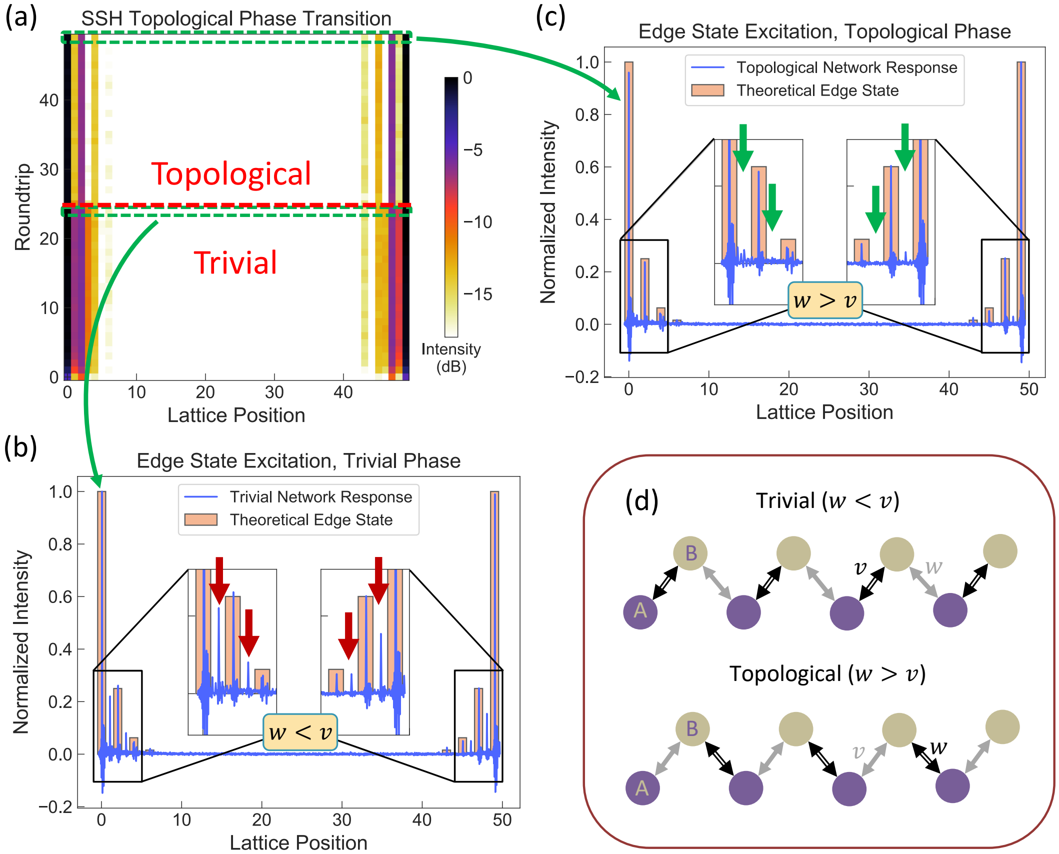

Figure 2.3: Observations of the SSH edge state and a topological phase transition

Observations of the SSH edge state and a topological phase transition. (a) For 50 roundtrips, we excite the SSH edge state corresponding to a coupling ratio of $w/v = 2$ in our time-multiplexed network while we tune the delay line couplings to induce a topological phase transition between the trivial and topological phases of the SSH model. **(b)** For the first 25 roundtrips, we set the network coupling ratio to the trivial phase ($w/v = 1/2$), and we observe that the edge state diffuses away from the edge as it resonates in the network (indicated by the thick red arrows). **(c)** After 25 roundtrips, we switch the coupling ratio to the topological phase ($w/v = 2$). The strong localization of the edge state in the topological phase (indicated by the thick green arrows) suggests that the edge state is an eigenstate of the network and corroborates our observation of a dynamic topological phase transition. **(d)** Depictions of the SSH lattice corresponding to the trivial and topological phases.

coupling ratio $w/v = 2$. For the first 25 roundtrips, we prepare our SSH lattice in the trivial phase by setting the coupling ratio of the network to $w/v = 1/2$; for the remaining 25 roundtrips, we switch the synthetic lattice into the topological phase by changing the coupling ratio to $w/v = 2$. As shown in Fig. 2.3(b), when the lattice's couplings are in the trivial phase, the edge state excitation diffuses into the initially unoccupied states of the lattice. In contrast, when the couplings are in the topological phase, the edge state excitation remains strongly localized in the theoretically predicted edge state. This localization confirms the existence of a purely dissipative topological edge state in our time-multiplexed resonator network.

We next investigate the robustness of the dissipative SSH edge state in the presence of disorder in the couplings of the network. In Fig. 2.4, we show the measured resonant steady states in a network without coupling disorder [Fig. 2.4(a,c)] and in a network with additional coupling disorder drawn from $\mathrm{Unif}(-0.1w, -0.1w)$ [Fig. 2.4b,d]. As discussed in Sec. 3.4, in the presence of such chiral-symmetry-preserving disorder, we expect the dissipation rate of the disordered edge state to be identical to that of the edge state in the unperturbed system. *This corresponds to topological robustness of the quality factor of the dissipative topological edge mode.* We verify this robustness by measuring the total intensities (I; sum of the peak powers) in measurements of the edge state with and without disorder. Under the right experimental conditions, this comparison is equivalent to comparing the dissipation rates [see Methods]. In the unperturbed system we find $I_{\mathrm{unpert}} = 0.377 \pm 0.001$ V, while in the disordered system we find $I_{\mathrm{dis}} = 0.378 \pm 0.001$ V. The agreement between these two measurements provides strong evidence that the dissipation rate (and consequently the quality factor) of the SSH edge state is protected against the presence of chiral-symmetry preserving disorder in the network.

Next, we experimentally reconstruct the dissipation bands of our SSH lattice in the topological phase ($w/v = \sqrt{2}$) and at the phase transition point ($w/v = 1$). For both coupling ratios, we implement a 64-site SSH lattice with PBCs. In each case, we sequentially excite the network with each of its 64 Bloch eigenstates, and we measure the steady-state amplitude of each state. Then, using the fit procedure described in Sec. 3.2, we extract the dissipation spectra from the measured steady state amplitudes [Figs. 2.5(b,c)]. To evaluate the quality of our band structure measurements, we compare the coupling ratios, w/v, extracted from our fit procedure with the expected coupling ratios. This comparison provides a suitable metric for the quality of our measurements because, up to a constant, the SSH coupling ratio completely

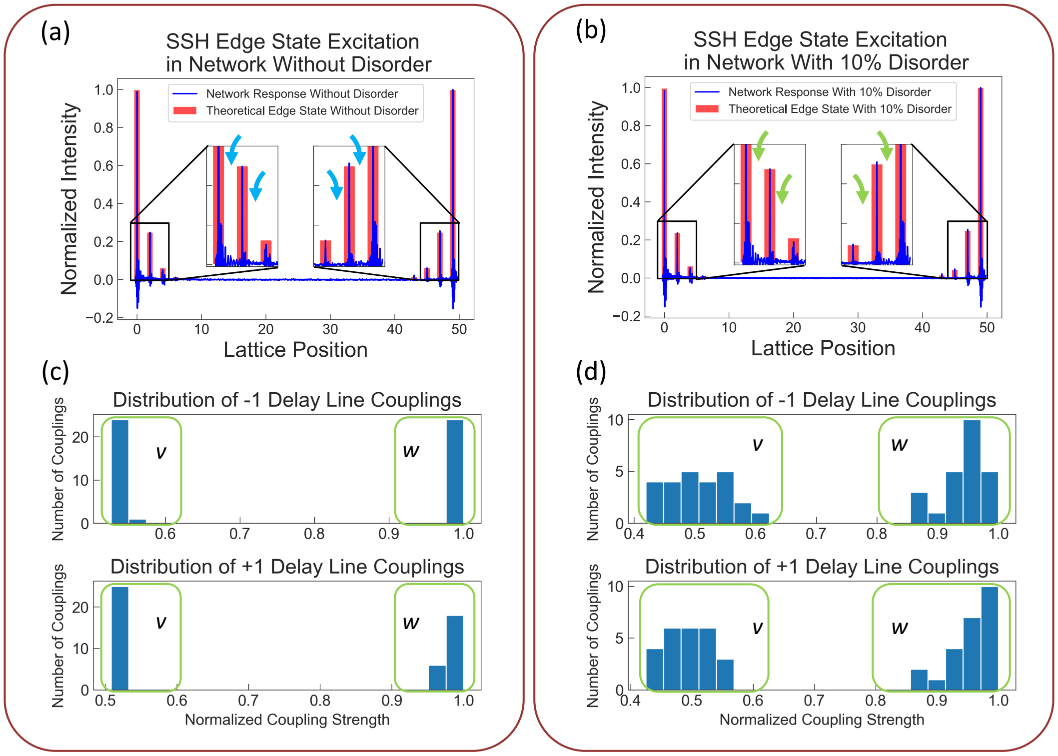

Figure 2.4: Robustness of the Dissipative SSH Edge State and Its Quality Factor

Robustness of the Dissipative SSH Edge State and Its Quality Factor. **(a)** Measured SSH edge state in a lattice without intentional disorder. **(b)** Measured SSH edge state in the presence of disorder. In the presence of chiral-symmetry preserving disorder, the SSH edge state persists, despite the slight change in the eigenstate. Furthermore, we expect the dissipation rate of the edge state to be unchanged, which is a hallmark of topological protection in our dissipatively coupled SSH lattice. We verify the robustness of the dissipation rate and the quality factor of the edge state by measuring the total intensities of the unperturbed and disordered steady-states of the network, which, under our experimental conditions, allows a comparison equivalent to comparing the dissipation rates. **(c)** Distribution of the measured coupling strengths in the unperturbed lattice. Here the variation in the couplings is due to experimental imperfections. (w is the inter-dimer coupling; v is the intra-dimer coupling) **(d)** Distribution of the measured coupling strengths in the disordered lattice. We add disorder to each coupling that is drawn from the uniform distribution $\text{Unif}(-0.1w, 0.1w)$. Comparing **(c)** and **(d)** suggests that the additional disorder is substantially stronger than the disorder introduced by experimental imperfections.

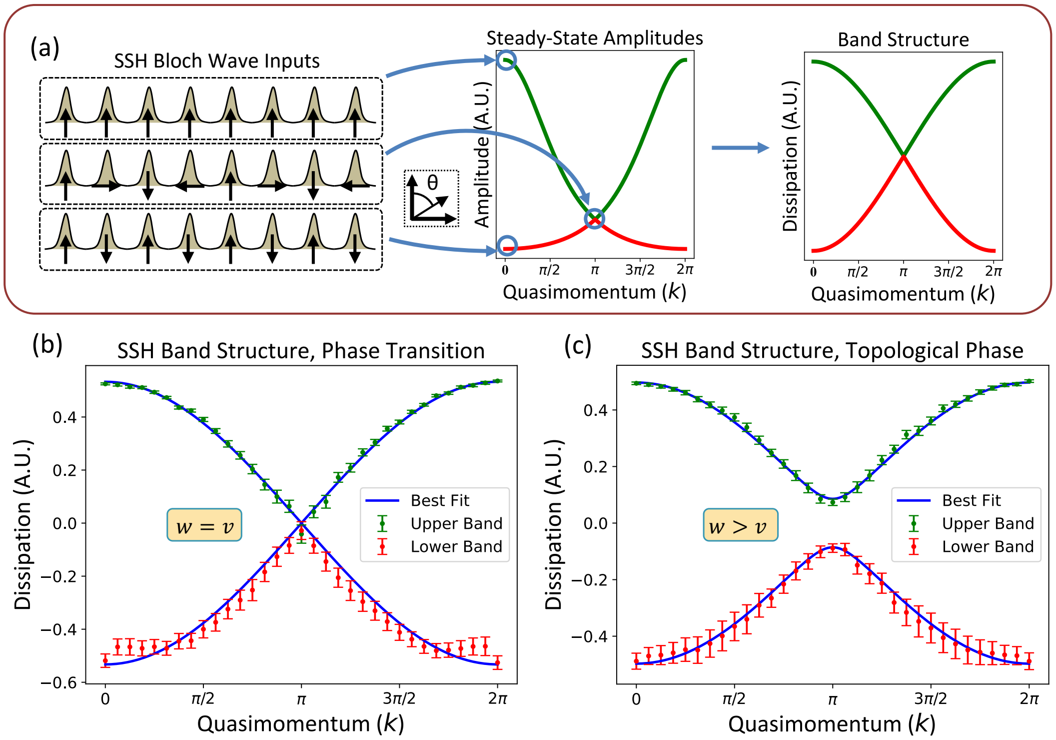

Figure 2.5: Measurements of the SSH band structure

Measurements of the SSH band structure. (a) To measure the SSH band structure at a given coupling ratio, w/v, we excite the complete set of Bloch wave eigenstates in the network and measure the steady-state amplitude of each state. Using Eq. (2.2), we transform these amplitudes into the SSH band structure. **(b)**,**(c)** Measurements of the SSH band structure at the phase transition point and in the topological phase. Using the best fit curves, we extract the coupling ratios for each measurement. We measure $w/v \approx 1.0$ (expected $w/v = 1$) and $w/v \approx 1.4$ (expected $w/v = \sqrt{2} \approx 1.414$) for the measurements in **(b)** and **(c)**, respectively. Note that the error bars represent the standard errors of 5 measurements at each quasimomentum.

determines the band structure (Asbóth, Oroszlány, and Pályi, 2016). For the band structure at the phase transition point (expected $w/v = 1$), we measure $w/v \approx 1.0$, while for the band structure in the topological phase (expected $w/v = \sqrt{2} \approx 1.414$), we find $w/v \approx 1.4$. The excellent agreement between the measured bands and the theoretical predictions confirms that our network possesses a topologically nontrivial dissipation spectrum.

Finally, to showcase the scalability and flexibility of our time-multiplexed network architecture, we reconfigure our synthetic lattice to probe the topological edge state of the HH model. The HH model describes a 2D square lattice subjected to a perpendicular magnetic field (Ozawa, Price, et al., 2019; Hofstadter, 1976; Harper, 1955), whose strength is characterized by a dimensionless magnetic field parameter, α. For rational α, the bands of the HH model acquire a nonzero topological invariant known as the Chern number, C, which gives rise to topologically protected edge states (Hatsugai, 1993). In our network we use the modulators $\mathrm{PM}_{\pm 4}$ in Fig. 2.2(a) to achieve an effective magnetic field with $\alpha = 1/3$ in a 4×10 synthetic HH lattice with OBCs [see Fig. 2.6(a)]. Because the dissipative couplings of our network are time-modulated and unidirectional, the synthetic magnetic field generated by the delay lines breaks time-reversal symmetry—meaning that our network possess truly nonzero Chern numbers [see Sec. 3.6]. This is in stark contrast with earlier optical implementations of the HH model, which either do not break time-reversal symmetry (Hafezi et al., 2013) or only break z-reversal symmetry (Rechtsman et al., 2013).

As shown in Fig. 2.6(d), when we excite a topologically protected edge state of the HH model in the presence of the synthetic magnetic field, the edge state remains well localized. Interestingly, this edge state is strongly localized at the edges of the 4×10 lattice, despite only two bulk sites separating the edges along the narrow direction. On the other hand, when we excite the edge state in the absence of the synthetic magnetic field ($\alpha = 0$), the lattice represents a trivial insulator, and the edge state diffuses into the "bulk" of the synthetic lattice [see Fig. 2.6(e)]. As the initial edge state excitation is prominent in both the topological and trivial network responses in Figs. 2.6(d,e), in Fig. 2.6(f) we plot only the occupation in the bulk sites to clearly show that the edge state remains localized in the topological phase but not in the trivial phase. We quantify this contrast between the trivial and topological phases by defining a bulk occupation fraction $f_{\mathrm{bulk}} = \sum_{n_x,n_y \in \mathrm{bulk}} |\psi_{n_x,n_y}|^4$, subject to the normalization $\sum_{n_x,n_y} |\psi_{n_x,n_y}|^2 = 1$. We calculate $f_{\mathrm{bulk}}^{\mathrm{topo}} = 5.6 \times 10^{-4}$ and $f_{\mathrm{bulk}}^{\mathrm{trivial}} = 2.2 \times 10^{-3}$ for the topological and trivial phases respectively. As our 4×10 lattice has 16 bulk sites and 24 edge sites, $f_{\mathrm{bulk}}^{\mathrm{trivial}} / f_{\mathrm{bulk}}^{\mathrm{topo}} \approx 4$ indicates a substantially stronger penetration into the bulk for the lattice in the trivial phase. Based on this observation, we conclude that our time-multiplexed synthetic HH lattice hosts a multidimensional topological edge state.

From the nontrivial topology of the dissipatively coupled HH model's dissipation bands, we expect that the topological edge states of dissipative HH lattices should be robust against the effects of defects and disorder. We demonstrate this robustness by simulating the evolution of a 4×10 dissipatively coupled HH lattice with and without a defect added to one corner of the lattice. The results of these simulations are shown in Figs. 2.6(b,c). In both cases, we find that when we excite the dissipative HH lattice with one of its topological edge states, the edge state remains localized in the initial excitation. In the dissipative HH lattice with a corner defect [Fig. 2.6(c)], this is a clear manifestation of topological protection. The details of these simulations are discussed in Sec. 3.8.

2.4 Outlook

Our dissipatively coupled implementations of the 1D SSH model and the 2D HH model experimentally demonstrate the existence of topological phenomena in the presence of purely dissipative couplings. We leverage our time-multiplexed network's dissipative dynamics for edge state and band structure measurements, and we utilize the time-reversal symmetry breaking nature of our dissipative couplings to introduce nonzero Chern numbers. Our time-multiplexed resonator architecture also offers a promising platform for future work in synthetic dimensions. Our design can be extended to lattices in higher than two dimensions (S.-C. Zhang and Hu, 2001; Petrides, Price, and Zilberberg, 2018; Lohse et al., 2018; Zilberberg et al., 2018; Wang, Bell, et al., 2020) and to lattices with long-range couplings (Bell et al., 2017), can achieve dense connectivity between lattice sites, and can realize dynamic and inhomogeneous synthetic gauge fields (Fang and Fan, 2013)—a combination that is not easy to achieve with other experimental platforms. We anticipate that dissipative couplings will enable new topological devices with applications to quantum computing and photonics. Immediate extension of our current experiments include exploring non-Hermitian (Helbig et al., 2020; Parto et al., 2021) and nonlinear (Smirnova et al., 2020) topological behaviors in dissipatively coupled time-multiplexed networks.

2.5 Methods

Network Architecture

The time-multiplexed optical network studied in this work hosts $N = 64$ time-multiplexed resonators and possesses four delay lines, labeled the $\pm T_\mathrm{R}$ and the $\pm 4T_\mathrm{R}$ delay lines [Fig. 2.2(a)]. Each delay line differs in length from the corresponding section in the main cavity by an integer multiple of the pulse repetition period T_R. The "$-$" ("+") indicates that the delay line is shorter (longer) than the corresponding main loop section, and the accompanying number denotes the range of the coupling (e.g., the $\pm 4T_\mathrm{R}$ delay lines implement fourth-nearest neighbor coupling). As the

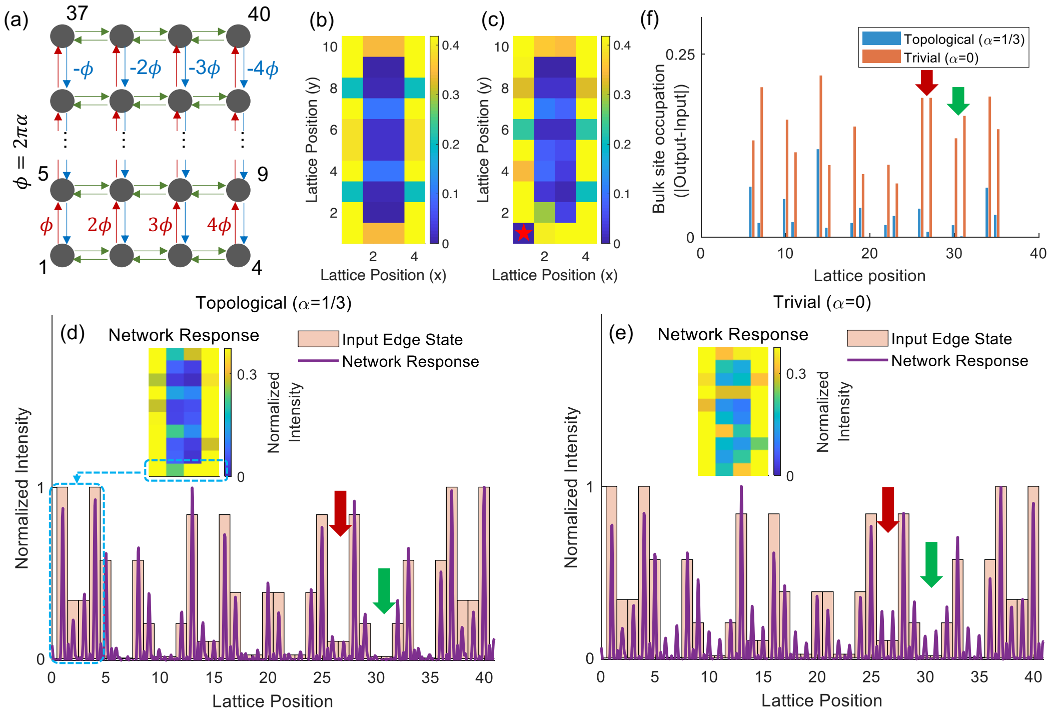

Figure 2.6: Measurement of the Harper-Hofstadter edge state and its localization

Measurement of the Harper-Hofstadter edge state and its localization. **(a)** Schematic of the Harper-Hofstadter (HH) model with a magnetic flux of $\phi = 2\pi\alpha$ per plaquette. The horizontal couplings do not have any phase, while the vertical couplings implement the Peierl's phases $\phi, 2\phi, \cdots$ (red) and $-\phi, -2\phi, \cdots$ (blue). **(b)** Simulated steady-state of a theoretical HH edge state in a 4×10 dissipatively coupled lattice. The same edge state is studied in our experiments. **(c)** Simulated steady-state of a HH edge state in a 4×10 dissipatively coupled lattice with a corner defect. The new edge state wraps around the defect, demonstrating the robustness of the topological edge state in a dissipatively coupled lattice. **(d, e)** Time traces of the measured steady-state pulse amplitudes in the network. As indicated by the dashed blue arrow in (d), each set of four pulses maps to one row in the inset color map, with earlier pulses in the time traces corresponding to lower rows in the color maps. **(d)** When the delay line phase modulators implement the coupling phases of the HH model with $\alpha = 1/3$, the edge state is an eigenstate of the network, and it resonates in the system. **(e)** When we turn off these coupling phases to achieve $\alpha = 0$, the edge state no longer resonates in the network. In particular, notice that light leaks into the "bulk" in the time trace of this measurement. **(f)** The difference between the bulk site occupation for the topological case (blue) and the trivial case (orange). The thick red and green arrows in (d)-(f) indicate the bulk sites with the highest contrast between the topological and trivial cases. Note that the presence of edge occupation that is visually apparent in (e) arises from the input excitation being predominantly localized on the edge (shaded rectangles), and hence the bulk occupation contrast in (f) provides a better comparison between the trivial and topological phases. Furthermore, note that the colormaps in (b-e) are saturated to emphasize the contrast between the edges and the bulk.

separate $\pm NT_{\mathrm{R}}$ delay lines provide independent control over each direction of the N^{th}-nearest neighbor couplings, it is straightforward to implement nonreciprocal couplings between sites.

The Su-Schrieffer-Heeger (SSH) model only requires nearest-neighbor coupling, so to study the SSH model, we block the $\pm 4T_{\mathrm{R}}$ delay lines. We then map the pulses in the main cavity to the one-dimensional chain pictured in Fig. 2.2(c), where the colors of the couplings correspond to the colors of the delay lines that implement them. The intensity modulators inserted in the $\pm T_R$ delay lines provide pulse-to-pulse control over the coupling strengths of each delay line and enable us to implement the staggered couplings of the SSH model. Moreover, while the topology of the main cavity lends itself to periodic boundary conditions (PBCs), the intensity modulator (IM) within the main cavity (IM_C in Fig. 2.2(a)) provides control over the boundaries of the synthetic 1D lattice. We can switch the boundary conditions to open boundary conditions (OBCs) simply by using IM_{C} to suppress time-slots in the main cavity [Fig. 2.2(c)].

To realize the HH model in the network of Fig. 2.2(a), we use the $\pm 4T_{\mathrm{R}}$ delay lines to define nearest-neighbor couplings along the second dimension of a synthetic square lattice (Yuan et al., 2018). By using the IMs in the $\pm T_R$ delay lines to suppress the "spiraling" boundary condition along this second synthetic dimension, we arrive at the lattices presented in Fig. 2.2(c), where, once again, IM_{C} enables us to implement either a strip with a single PBC or a square lattice with OBCs. To achieve the time-reversal symmetry breaking coupling phases of the HH model, we place phase modulators (PMs) in the $\pm 4T_{\mathrm{R}}$ delay lines. We utilize our independent control over each delay line to introduce a synthetic magnetic flux in each plaquette of the synthetic lattice [Fig. 2.2(c)].

For the measurements presented in the main text, we probe the properties of the network by exciting states in the network and recording the network's steady-state response. To excite the desired edge states and Bloch wave eigenstates, we use an IM (IM_0) and a PM (PM_0) at the input to the main cavity [Fig. 2.2(a)]. These modulators encode the intensities and phases of the desired state onto a stream of pulses from a mode-locked laser. Upon entering the cavity, these pulses excite the sites of the synthetic lattice (i.e. the time bins of the network) with particular amplitudes and phases. By exciting each site repeatedly over multiple roundtrips of the network, we bring the cavity to a resonant steady-state condition.

Measurement Procedures

SSH Band Structure Measurements

To measure the SSH band structure, we generate the modulator driving signals to implement the desired coupling ratio within the network (using $\text{IM}_{\pm 1}$), and the Bloch wave excitations at the input to the cavity (using PM_0). By not using the intercavity IM, IM_C, the network inherently implements a PBC, so that we implement a 64 pulse (32 dimer) SSH lattice.

To execute the experiment, we excite each Bloch eigenstate in the network and record the network's steady-state response to each Bloch state. We repeat this measurement 5 times for each Bloch wave and compile the data from the different measurements to generate a plot of the mean steady-state amplitudes versus wavevector. We then solve Eq. (2.2) to relate the steady state amplitudes of the Bloch waves, $|c(k)|^2$, to the dissipation eigenvalues of the SSH model. We find

$$|c(k)|^2 = \frac{A}{(\gamma - \lambda_{\text{SSH}})^2} + d, \tag{2.3}$$

where γ is the network loss, $\lambda_{\text{SSH}} = \pm\sqrt{w^2 + v^2 + 2wv\cos(k)}$, and A and d account for the detector scaling and bias, respectively.

We fit the measured amplitudes with a rescaled version of Eq. (2.3) using Markov chain Monte Carlo simulations (Aster, Borchers, and Thurber, 2019). We use the fit parameters to transform the measured amplitudes into the SSH band structures shown in Figs. 2.5(a),(b).

Edge State Measurements

Our edge state measurements follow a procedure similar to that of our band structure measurements. To observe the HH model's edge state, we first generate the modulator driving signals to implement the synthetic gauge field of the HH model (using $\text{PM}_{\pm 4}$) and to produce the HH edge state at the input to the network (using IM_0 and PM_0). As suggested in Fig. 2.2(c), we use the delay line IMs, $\text{IM}_{\pm 1}$, to create OBCs along the one direction of the lattice, while IM_C produces OBCs along the other direction. The result is that we implement a finite, 4 × 10 HH lattice with an effective synthetic magnetic field strength corresponding to $\alpha = 1/3$.

To probe the topologically nontrivial state of our lattice, we excite the HH edge state in the network and record the system's steady-state. In the presence of the synthetic gauge field, the edge state is an eigenstate of the network, so the excited edge state resonates unperturbed within the network. This result is shown in Fig. 2.6(c).

To confirm that the lattice hosts a 2D topological edge state, we next turn off the synthetic gauge field by turning off the driving signals on $\mathrm{PM}_{\pm 4}$. The network then implements a trivial 4×10 square lattice. We excite the same topological edge state in the trivial lattice and observe that the network's steady state response deviates from the edge state excitation [Fig. 2.6(d)]. This confirms that, in the presence of the synthetic gauge field, the topological edge state is an eigenstate of the network.

For the SSH model, we first observe the topological edge state in the context of a dynamical topological phase transition between the trivial and topological phases [Fig. 2.3(c)]. We begin by generating the modulator driving signals to implement the SSH model's couplings and to excite the SSH edge state. In addition, we now use IM_{C} to implement a 50 pulse SSH lattice with OBCs. We excite the SSH edge state in the network for 50 roundtrips. For the first 25 roundtrips, we program the couplings so that the network is in the trivial phase of the SSH model. In this case, we observe that the steady-state response of the network deviates from the excited edge state. For the final 25 roundtrips, we switch the coupling strengths so that the network is in the SSH model's topological phase. Now we observe that the network response remains strongly localized in the edge state. This indicates that the topological edge state is an eigenstate of the network when the network is in the topological phase.

We investigate the robustness of the SSH edge state using a similar procedure. We first program the network's couplings to implement the SSH model with no disorder and then program the couplings to implement the SSH model with additional disorder distributed according to $\mathrm{Unif}(-0.1w, 0.1w)$. In each case, we perform the edge state measurement 40 times and average the results. In both cases, we excite the network with the predicted SSH edge state for 15 roundtrips and record the steady state of the network on the fifteenth roundtrip.

Because we excite the network with eigenstates in the disordered and unperturbed cases, Eq. 2.2 again reduces to scalar equation, and its solution can be written in the form

$$c_{\mathrm{edge}}^2 = \frac{A}{\left(\gamma - \lambda_{\mathrm{edge}}\right)^2} + d, \tag{2.4}$$

which is very similar to Eq. 2.3 but now specialized to the case of the SSH edge state. During our calibration, we take care to ensure that the probed edge states have the same normalization in both the disordered and the unperturbed lattices, so that the pump parameter [A in Eq. 2.3] is the same for both the disordered and unperturbed cases. Then comparing the total intensities in the resonant steady-states becomes equivalent to comparing the dissipation rates of the two states. We use this comparison to conclude that the dissipation rate of the dissipatively coupled SSH edge state is robust against the chiral-symmetry preserving disorder introduced into the system.

Note that all of the time traces plotted in Figs. 2.3, 2.4, and 2.6 are normalized by rescaling the time trace by the maximum value in the averaged trace. The data plotted in the colormap in Fig 2.3(a) is not normalized, and the reference level used to plot this data in units of decibels is the maximum intensity in the entire data set.

Chapter 3

SUPPLEMENTARY INFORMATION FOR “TOPOLOGICAL DISSIPATION IN A TIME-MULTIPLEXED RESONATOR NETOWRK

3.1 Detailed Explanation of the Experimental Procedure

In this section, we provide a detailed explanation of our experimental procedure. We first provide a high-level description of the network shown in Fig. 3.1. Then, to provide an exhaustive picture of how to construct and operate our experiment, we follow a pulses’ trajectories through the network, discussing the effect of each element in Fig. 3.1 as we go along. After this, we briefly discuss the protocols used to calibrate the various modulators in the network, and, finally, we provide an in-depth discussion of our measurement procedures.

Overview of the Experimental Setup

Our basic network design consists of a long fiber loop, which we call the “main cavity.” We divide the main cavity into time bins that are separated by the repetition rate of an input 1550 nm mode-locked laser. The repetition rate is 250 MHz, so that the pulse separation is T_R=4 ns. In our experiment, we set the length of the main cavity so that it supports 64 time-multiplexed optical resonators.

To introduce topological behaviors into our network, we couple the pulses in the main cavity through four optical delay lines. The delay lines couple each pulse of the network to other pulses a fixed number of time bins away. To construct these delay lines, we insert a 1×8 splitter and a 1×8 combiner into the main cavity, and we construct additional paths between the splitter and the combiner that differ in delay by integer multiples of the pulse separation time relative to the section of the main cavity that lies between the splitter and the combiner. The delay lines shorter than the corresponding section of the main cavity (labeled with a “−” in Fig. 3.1) couple to “earlier” time bins, while the the delay lines longer than the corresponding section of the main cavity (labeled with a “+” in Fig. 3.1 couple to “later” time bins. For our experiments, we construct $\pm T_{\mathrm{R}}$ and $\pm 4T_{\mathrm{R}}$ delay lines.

The delay lines establish the lattice type and the coupling lengths present on the lattice, but to study topological tight-binding models we must also control the strength and phase of each coupling. Accordingly, we insert intensity modulators (IMs) and phase modulators (PMs) into the delay lines. These modulators set the intensities and phases of the network's couplings so that they correspond to the couplings of the topological model under study. For the models studied in this work, the Su-Schrieffer-Heeger (SSH) model and the Harper-Hofstadter (HH) model, it is only necessary to have either a phase modulator or an intensity modulator in each delay line. However, one could insert an IM and a PM into each delay line to enable greater control over the phase and intensity of each coupling.

Details of the Experimental Setup

Figure 3.1 details the optical, electronic, detection, and stabilization elements of our experiment. Many of these elements are interdependent, so, to explain Fig. 3.1, we will start from the 1550 nm mode-locked laser and follow each path to its terminus, discussing the components we encounter as we go.

The 1550 mode-locked laser produces a steady stream of pulses with a 250 MHz repetition rate. These pulses first encounter a 50:50 splitter, which divides each pulse evenly between two paths. Along the first of these paths, which is the leftmost path in Fig. 3.1, the pulses pass directly to a 1.2 GHz photodetector. We pass the output of this detector through a 300 MHz low pass filter, which isolates the 250 MHz component of the optical pulse train. We use this 250 MHz signal as a reference clock for the FPGA used to generate the experiment's modulator driving signals. Clocking the FPGA with a sinusoid derived directly from the optical signal reduces any drift between the FPGA's electronics and the optical pulses.

The full details of the FPGA's firmware are available upon reasonable request. For the purposes of this discussion, all that matters is that we load modulator driving waveforms from a PC onto the various channels of the FPGA, and we use the computer to trigger each experiment. Upon a trigger event, the FPGA outputs the waveform stored on each output channel. This waveform passes through an amplification stage and is then transmitted to a certain modulator (see blue dashed arrows in Fig. 3.1), where it modulates the pulses either before or in the network. The amplitudes of the modulator driving waveforms are determined by a calibration procedure that will be discussed in Section 3.1.

Let us now return to the 1550 femtosecond laser in the top left corner of Fig. 3.1 and follow the path containing IM_0. Directly after this intensity modulator is a Mach-Zehnder interferometer (MZI) with PM_0 and a "switch" in one arm. This MZI is

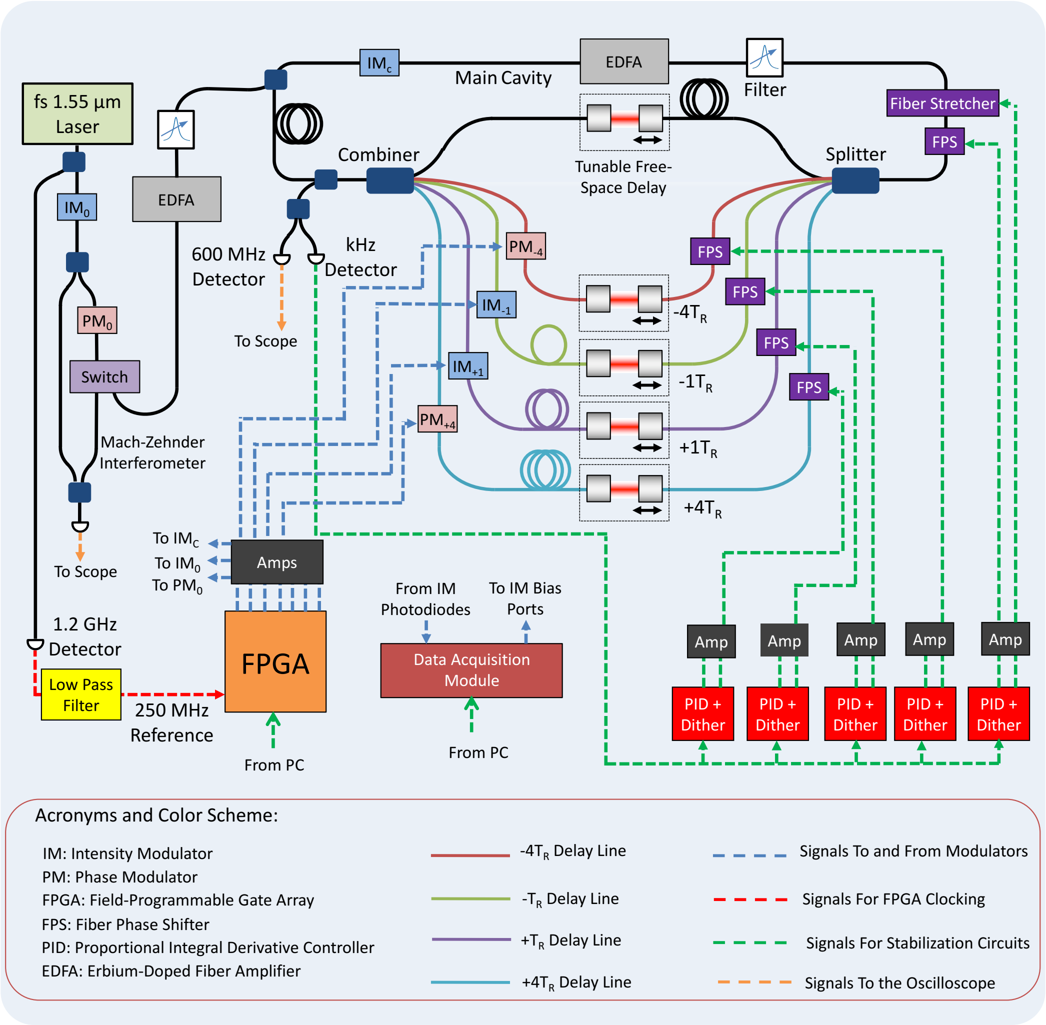

Figure 3.1: Detailed schematic of the experimental setup

Detailed schematic of the experimental setup.

used to calibrate PM_0. In practice, we implement the switch manually unplugging the fiber pigtail of PM_0 from the input to the main cavity and connecting it to the MZI. This MZI is used to calibrate the phase vs. voltage response of PM_0.

Continuing along the input to the main cavity, we next encounter an EDFA. This EDFA, which sits before the main cavity increases the power in the main cavity without adding additional gain to the main cavity. Before adding this EDFA we found that the signal at the network's output was quite faint but that the network would go above threshold when we increased the gain with the intracavity EDFA. Adding the EDFA before the main cavity enabled us to increase our signal to noise ratio while remaining sufficiently below threshold. The filter directly after the EDFA removes amplified spontaneous emission (ASE) generated by the EDFA.

We now arrive at the input to the main cavity, located at the top of Fig. 3.1. Pulses enter the main cavity via a 90:10 splitter, which is configured so that 10% of the light from the laser is passed into the main cavity. After this 90:10 splitter, the pulses pass through the intracavity intensity modulator, $\mathrm{IM_C}$, and the second EDFA, which compensates for losses in the main cavity and the delay lines. As with the first filter, the filter after the intracavity EDFA suppresses ASE noise. After the filter, the pulses pass through a fiber stretcher and a fiber phase shifter (FPS), which are used to stabilize the main cavity, before being split between the delay lines.

As mentioned above, the delay lines contain PMs or IMs that control the couplings between the pulses. The delay lines also contain FPSs for stabilization, and they, along with the section of the main cavity that lies between the splitter and the combiner, contain tunable free-space delays. These tunable delays and phase shifters provide coarse and fine control over the length of each optical path, respectively. This ensures that (1) that the main cavity is on resonance and that (2) the delay lines interfere with the pulses in the main cavity when they meet at the combiner. After the delay lines and the main cavity recombine, the pulses are passed to another 90:10 splitter, which passes 10% of the cavity power to the experiment's detectors. The remaining light returns to the first 90:10 splitter at the input, where 90% of the light recirculates through the main cavity.

At the output of the main cavity, we split our signal between two detectors using a 50:50 splitter. One detector is a "fast," DC-coupled, 600 MHz detector, which we use to measure the amplitudes of individual pulses. The second detector is a slow, kHz detector that is used to stabilize the various paths of the network. We note that the SSH edge state data in the main text was collected using an EDFA pre-amp and a DC-coupled 5 GHz biased detector in place of the 600 MHz detector.

To stabilize the main cavity and the four delay lines, we use a top-of-fringe dither locking scheme for each path (Black, 2001). The lock-in modules in Fig. 3.1, which are Red Pitaya STEMLabs, send dither signals to the FPSs in each path. In order to minimize cross-talk between the locks, we choose the frequency of each dither signal so that no one signal is a harmonic of any other. The FPSs in each path dither the lengths of the paths at their respective dither frequencies, which slightly modulates the interferences within network. This modulation is picked up by the setup's slow detector, and the lock-in modules in Fig. 3.1 demodulate the detector signal to generate error signals that quantify each paths position relative to the constructive interference (top-of-fringe) condition. The error signals are then fed to the lock-in modules' built-in proportional-integral-derivative (PID) controllers, which produce feedback signals to stabilize their respective paths. In the case of the delay lines, we add the feedback signal to the dither signal, so that we dither the delay lines and perform feedback on the same FPSs. In the case of the main cavity, we dither an FPS (which permits a higher dithering frequency), but we apply the feedback signal to a fiber stretcher. The fiber stretcher has a greater range than the FPS and is more convenient for locking the main cavity, which is the longest path in the system.

The final element of Figure 3.1 is a National Instruments data acquisition tool (NI-DAQ), which sets the bias of the network's IMs. Using a custom graphical user interface (GUI), we can either manually set the bias voltage of each IM or automatically set its bias to enable maximum or minimum throughput. If we choose to allow maximum or minimum throughput, then the program monitors the output of IMs' built-in photodiodes and adjusts the bias accordingly. For the purposes of our experiments, we always bias $\mathrm{IM_C}$ and $\mathrm{IM}_{\pm 1}$ to maximize their throughput, and we bias $\mathrm{IM_0}$ to minimize its throughput. We picture the modulator driving signals as "opening" $\mathrm{IM_0}$ to let light into the cavity, while they selectively close the IMs in the network either partially or completely during the experiments.

Modulator Calibration

To observe meaningful results in our network, we must calibrate the responses of each modulator over a sufficient range of driving voltages. To mitigate the effects of long-term drifts in the setup's electronics, we perform our calibration procedure before each round of measurements.

To calibrate the IMs, we reconfigure the paths in Figure 3.1 so that, one-by-one, there is a direct path from the laser, through each IM, to the 600 MHz detector. Then, using $\mathrm{IM_0}$, we send 100 consecutive pulses through this path, while applying a 100 step voltage ramp to these 100 pulses. This ramp varies from some negative voltage value to its equal and opposite positive voltage value in equally spaced steps. We measure the amplitudes of these 100 pulses and apply a polynomial fit to generate an amplitude vs. voltage plot. For each IM, we use its amplitude versus voltage curve to select the proper driving voltages for a given experiment. Note that, to calibration $\mathrm{IM_0}$, we apply the same voltage ramp to $\mathrm{IM_0}$ and measure the resulting amplitude versus voltage plot.

To calibrate the phase modulators, we need a local oscillator to interfere each phase modulated pulse with. Furthermore, we must calibrate each phase modulator in-place to ensure that the timing information of the optical and electronic pulses is the same during the calibration as it is during the experiments. This is why we build the MZI around the input PM, PM_0. For the delay line modulators, we selectively block the free space portions of the delay lines to interfere either the $+4T_R$ delay line or the $-4T_R$ delay line with the main cavity. The main cavity therefore acts as reference path for these delay lines.

Once we have constructed an interferometer for each phase modulator, we calibrate it in much the same way that we calibrate the intensity modulators. We sweep the phase modulator driving voltage with the same 100 pulse sequence, and we use the measured amplitudes to generate an amplitude versus voltage curve. Then, using the maximum and minimum points of this curve as reference points, we convert the amplitude versus voltage curve into a phase versus voltage curve. We use this phase versus voltage curve to assign driving voltages to a given phase modulator in our experiments.

The Locking and Experiment Modes

To ensure that our optical network is stable during an experiment, we must run the dither locking scheme described in Section 3.1 prior to the experiment and then transition from this “locking mode” to an “experiment mode” to perform our experiment. We switch between these modes using the FPGA in Fig. 3.1, which outputs different modulator driving waveforms in the locking and experiment modes. In this section, we briefly detail the process of switching between the locking and experiment modes and discuss how the optical response of our network appears on our detector in the two modes. This section serves as a prelude to the next section, in which the optical response in the locking mode plays a key role in accepting or discarding experiment runs.

As briefly mentioned in Section 3.1, we bias IM_0 to minimize its throughput. This allows us to selectively open IM_0 to send pulses into the main cavity during the experiment mode. However, during the locking mode, we would like to steadily inject pulses into all of the network’s paths so that we can generate usable error signals from the output of the slow detector. Therefore, in the locking mode, we program the FPGA to send a steady pulse train to IM_0 to allow all pulses to pass through the modulator. When the network is properly locked, we observe these

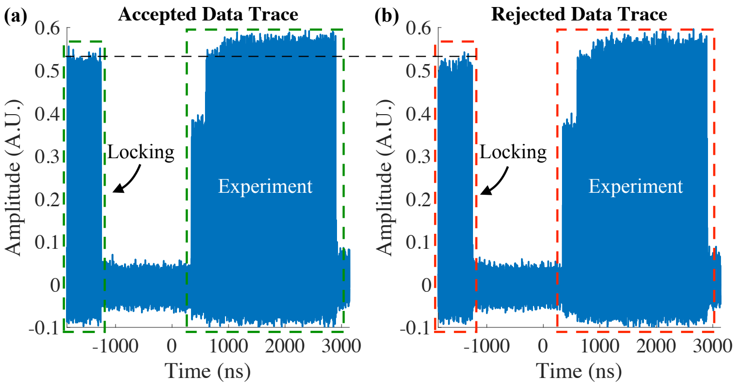

Figure 3.2: Locking and Experiment Modes

Locking and Experiment Modes Example oscilloscope traces showing the locking and experiment modes and illustrating the measurement selection procedure. The amplitude during the locking cycle is slightly greater in (a) than in (b). The trace in (a) passes our measurement acceptance procedure, while the trace in (b) fails. Note that the individual pulses of the locking and experiment modes are not visible at the timescales in these plots.

pulses as a constant stream of roughly equal amplitude pulses on the fast detector and as a DC signal on the slow detector.

As we must change this input pulse pattern to run our experiments, we do not lock the paths of our network during the experiment mode. However, in practice this is not an issue, as the paths of our network drift on a millisecond timescale, while each experiment takes only a few microseconds. A greater concern is to ensure that residual pulses from the locking mode have completely dissipated before we inject pulses for an experiment. To avoid any overlap between the locking and experiment modes, the FPGA shuts off its output for a programmable period of time between exiting the locking mode and beginning the experiment mode. This closes IM_0 and gives the light in the network from the locking mode time to dissipate. The FPGA implements a similar delay after the experiment before it resumes the locking mode.

For a typical experiment run, we observe the tail end of the locking mode on our fast detector, followed by our experiment mode. The tail end of the locking mode typically appears as a constant stream of pulses that exponentially decays once the FPGA shuts off its input. The experiment cycle appears as an exponentially growing set of pulses that settle into a steady-state at some amplitude. Examples of such oscilloscope traces are shown in Fig. 3.2.

Setting a Threshold to Accept or Discard Band Structure Measurements

Our ability to record meaningful band structure data relies on our ability to determine when the optical network is stable. If any of the paths of the experiment “fall off lock” at the moment of our experiment, the relative phases of the pulses or the coupling phases of the delay lines will change and will introduce error into our measurement. To mitigate this error, we adopt a procedure to automatically cull data traces that fail to meet a certain “locking threshold,” which we define as the metric by which we evaluate the stability of our experiment at any given time. In this section we introduce our locking threshold and discuss how we use it discriminate between “successful” and “unsuccessful” experiments.

In Section 3.1, we explained how the oscilloscope traces in Fig. 3.2 originated from the locking and experiment modes. Because all paths in the network are locked to constructive interference, the amplitudes of the pulses during the locking modes provide a sense of how stable the system is during the experiment mode. In particular, the fact that the amplitude of the pulses during the locking mode are lower in Fig. 3.2(b) than in Fig. 3.2(a) tells us that the system fell off lock before the experiment in Fig. 3.2(b). To efficiently collect data, we systematically reject data traces that exhibit “low” pulse amplitudes during the locking cycle.

To determine which traces should be discarded, we first establish a baseline amplitude for the pulses during the locking cycle. This is done by running an arbitrary experiment on the order of 50 times. For each experiment, we discard the data from the experiment mode and average the amplitudes of the pulses in the locking cycle. We take the maximum average pulse amplitude across these trials to be our baseline locking amplitude.

We next set a “threshold value” for discarding measurements. After collecting a data trace during an experiment, we only accept a data trace if the percent difference between the trace’s average locking-mode amplitude and the baseline amplitude is less than the threshold value. For our SSH band structure measurements in the main text, we used a threshold of 2%. For our measurement in the topological phase, we achieved a measurement acceptance rate of 90%, while for our measurement at the phase transition point, we achieved a measurement acceptance rate of 86%.

For HH edge state measurements, we did not take advantage of this measurement selection scheme. However, given the high measurement acceptance rates of our band structure measurements, we do not believe the selection procedure would meaningfully change HH edge state results.

For the SSH phase transition and the SSH topological protection measurements, we used a threshold of 5%.

Experimental Procedure

We next discuss the procedures used to perform the band structure and edge state measurements. We will explain our measurement procedures in the contexts of the models studied in this paper, but the same procedures can be extended to other models that can be mapped to our network.

Band Structure Measurements

A diagram of our band structure measurement procedure is shown in Figure 3.3. The delay line couplings discussed above ensure that the eigenstates of our optical network are identical to those of the condensed matter tight-binding model under study. For reasons we shall explain in Section 3.3. We probe the eigenstates of the network by exciting them directly with the pulse stream input into the network.

We begin our band structure measurements by numerically calculating the Bloch wave eigenstates. We then generate the corresponding modulator driving signals to implement the desired couplings and to generate the Bloch wave eigenstates using the modulators at the input to the cavity. Because the SSH model with periodic boundary conditions (PBCs) exhibits discrete spatial translation symmetry, the amplitudes of the Bloch wave eigenstates are uniform, and we only need PM_0, the PM before the network, to produce each Bloch wave. Meanwhile, the two delay line IMs, $\mathrm{IM}_{\pm 1}$ implement the staggered couplings of the SSH model, while we disconnect the $\pm 4T_R$ delay lines to eliminate their couplings. Finally, we note that the intracavity IM, IM_C is unused for these band structure experiments. IM_C allows us to control the boundary conditions or our synthetic lattice, and when it is unused, it enables PBCs in the network.

To execute the experiment, we excite a particular Bloch wave eigenstate of the network and record its steady-state amplitude. As we will discuss in Section 3.2, we can relate this steady-state amplitude to the photonic dissipation rate in the network. This dissipation rate maps directly to the energy of the SSH Hamiltonian.

We repeat this procedure for all 64 Bloch wave eigenstates of the system (there are 2 bands and 32 eigenstates per band). With the complete set of measured steady-state amplitudes, we generate a plot of steady-state amplitudes versus wavevector. Then,

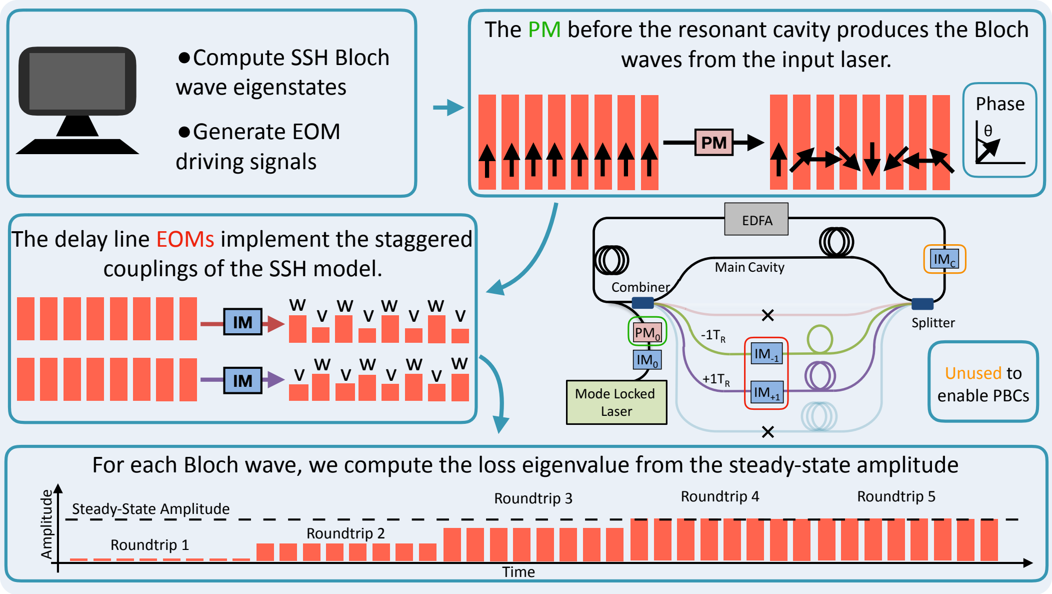

Figure 3.3: Procedure used to measure the SSH band structure

Procedure used to measure the SSH band structure.

using the statistical procedure outlined in Section 3.2, we transform the measured amplitudes into the SSH band structure.

Edge State Measurements

Our edge state measurements follow a procedure similar to that of the band structure measurements, but there are a few differences. Here we will explain the edge state measurements in the context of the Harper-Hofstadter (HH) measurement. The SSH phase transition measurement discussed in the main text uses a nearly identical procedure, but the couplings are switched halfway through the experiment.

A diagram of the HH edge state measurement procedure is shown in Fig. 3.4. We begin this procedure by numerically calculating one of the HH edge states, and we generate the necessary modulator driving signals. The amplitudes of the edge state are not uniform, so we need to use both IM_0 and PM_0 to encode the HH edge state from the 1550 nm laser's output pulse stream.

When we work in the Landau gauge, we only need to apply hopping phases along one direction of our two-dimensional lattice to implement the HH model. We introduce these hopping phases with the PMs in the delay lines. Furthermore, as the hopping intensities are uniform in the HH model, we only need the delay line IMs to turn off certain couplings so that we can enforce finite boundary conditions

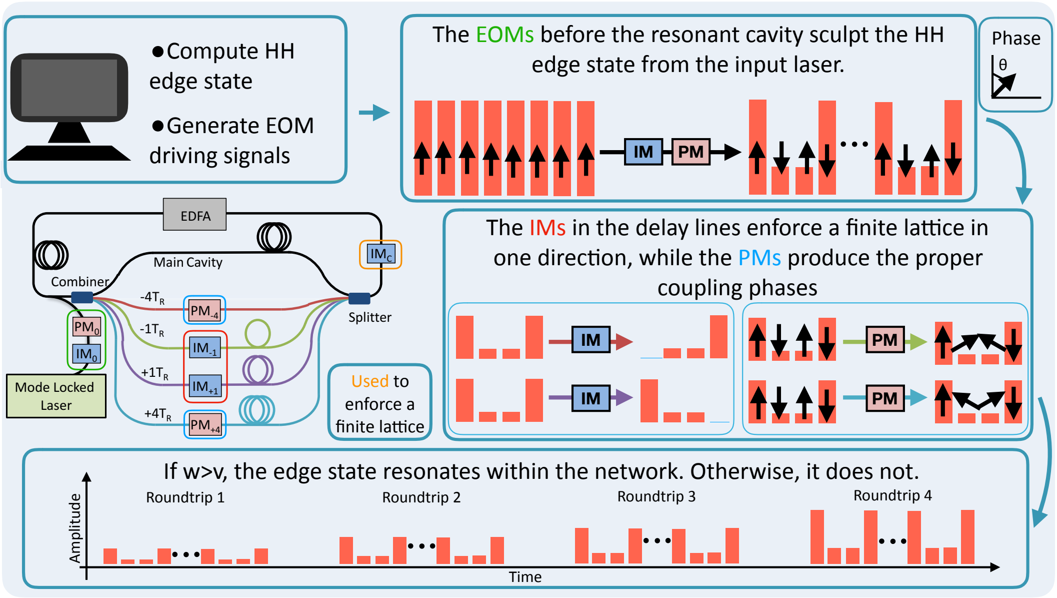

Figure 3.4: Procedure used to measure the HH edge state

Procedure used to measure the HH edge state.

along one direction of the synthetic lattice. While the delay line IMs implement finite boundary conditions along one direction, the intracavity IM, IM$_{\mathrm{C}}$ implements finite boundary conditions along the other by suppressing pulses in the main cavity. The effect of the IMs in the network is to ensure that we study a finite, 4×10 lattice in our experiments.

As with our band structure measurements, we excite the network directly with the HH edge states. When the delay line PMs are on and implement the correct phases, the edge state is an eigenstate of the system. Therefore, we expect the edge state to resonate within the network. However, when we turn off the delay line PMs, the edge state is no longer an eigenstate of the system, and the light should no longer remain localized in the edge state as it resonates within the network.

3.2 Band Structure Analysis

As described in Section 3.1, we measure the steady-state amplitudes of the optical network's Bloch wave eigenstates, and we fit the measured amplitude versus wavevector plot to transform the amplitudes into the SSH band structure. To extract a band structure from this type of measurement, we must consider the error associated with measuring the steady-state amplitudes of the individual eigenstates, the procedure used to fit the measured amplitudes, and the uncertainty bounds placed on our fit parameters. Each of these points present their own challenges, and we will address each of these challenges in turn.

A Single Amplitude Measurement

As we mentioned above, the Bloch wave eigenstates of the SSH model have uniform amplitudes because the 1D chain with PBCs exhibits discrete translation symmetry. Given this, we would expect that when we excite an eigenstate into the network, the resulting steady-state should also have a uniform amplitude. However, in our experiments we observe some deviation from this behavior for nonzero quasimomentum, k. In Fig. 3.5, we show two traces from the top band of our SSH band structure measurement at the phase transition point ($w = v$). Figs. 3.5(a) and (b) show the observed steady-state amplitudes of the SSH network at $k = 0$ and π respectively. While the steady-state amplitude is constant across the entire pulse train for $k = 0$, the steady-state amplitude of the Bloch wave at $k = \pi$ exhibits periodic oscillations. Note that the period of the oscillations are correlated with the phase rotation rate applied on PM_0, which indicates that the source of this discrepancy could be the phase errors on the input phase modulator PM_0. For example, the network response at $k = \pi$ exhibits oscillations with a period of approximately four pulses. This is the periodicity we would expect for a Bloch wave at $k = \pi$ on a two-site lattice like the SSH model.

To estimate the origin of this discrepancy, we simulate a simple 1D one-band model, $H_{1D} = J \sum_x a^\dagger_{x+1} a_x + \mathrm{H.C.}$ and look at the $k = \pi/4$ eigenstate excitation. In our experiment, a phase of $\phi = 0$ corresponds to PM_0 being almost completely off (in practice, what is considered $\phi = 0$ might be slightly shifted by the calibration). Therefore, we assume that the PM_0 implements $\phi = 0$ accurately but that it undershoots the remaining phases in the Bloch wave. For example, when $\phi > 0$, we imagine that the phase modulator actually implements $\phi - \alpha$, for some small $\alpha > 0$. With these phases, we simulate the measurement procedure described in Section 3.1. With $J = 0.1$, the intrinsic loss $\gamma = 0.4$, and $\alpha = \pi/10$, the resulting steady-state amplitude [Fig. 3.6] exhibits an oscillatory pattern similar to that observed in Fig. 3.5. These oscillations can be reduced by decreasing the coupling strength, J, or by reducing the phase undershoot. While the exact form of the phase error might be different, the qualitative agreement between Figs. 3.5 and 3.6 provides compelling evidence that the observed amplitude oscillations arise due to phase errors from PM_0.

To mitigate the effect of these pulse-to-pulse amplitude oscillations on the band

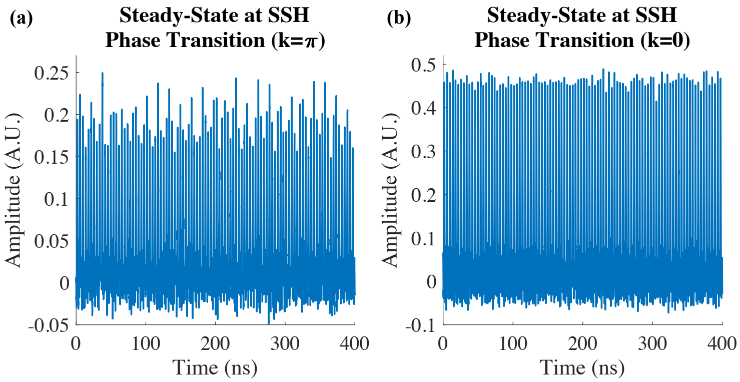

Figure 3.5: Observed steady-state traces with SSH Bloch wave excitations

Observed steady-state traces with SSH Bloch wave excitations Observed traces showing the steady-state time traces of the network output in response to excitations with SSH Bloch wave eigenstates (a) at $k = \pi$ and (b) at $k = 0$.

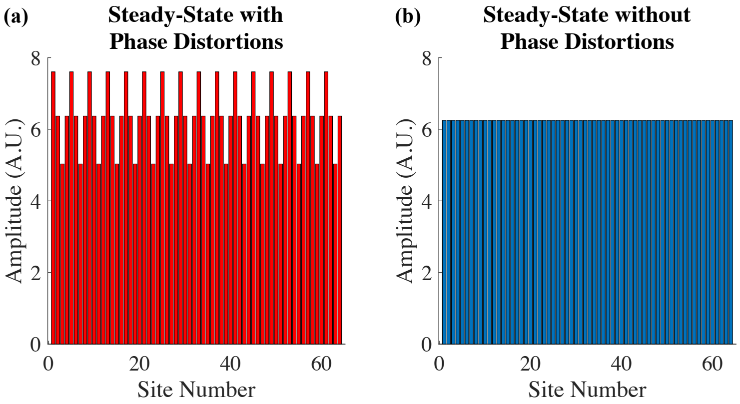

Figure 3.6: Effect of phase error on network response

Effect of phase error on network response Simulated effect of input phase error on the network's steady-state response. This simulated conditions are discussed in the text.

structure measurements, we average over the pulse amplitudes of the steady-state network response. This procedure is justified by our simulations: despite the presence of amplitude oscillations, the average steady-state amplitude in Fig. 3.5(b) is only 1.5% from the expected steady-state amplitude. Our network reaches a steady-state after only 3 or 4 roundtrips, and a full experiment lasts 10 roundtrips. With this long of a steady-state, we select a large portion of these final 6 roundtrips to average over.

To generate more statistics for our band structure reconstructions, we acquire 5 data traces at each point on a band structure, using the procedure discussed in Section 3.1

to verify the stability of the network at measurement time. Using the same averaging window for each trace, we compute the averages of the pulse amplitudes and the standard errors of these averages. We use these averages and standard errors to reconstruct the band structure.

Reconstructing a Band Structure

Having devised a procedure to assign amplitudes to the measured steady states, we can now reconstruct the SSH band structure. To do this, we need a model to map the measured amplitudes to the eigenvalues of the SSH model, which correspond to the dissipation rates of the network's Bloch wave eigenstates. Recall that the dynamical equation of our network is

$$\frac{d\mathbf{a}}{dt} = (K - \gamma)\,\mathbf{a} + \mathbf{P}, \tag{3.1}$$

where the matrix K represents the couplings of the SSH model, γ represents the intrinsic optical losses, and $\mathbf{P}$ is a constant drive.

Note that if the dynamical matrix K is Hermitian, then it may also be thought of as an anti-Hermitian Hamiltonian. For example, if we temporarily neglect γ and $\mathbf{P}$, then we can rewrite Eq. 3.1 as $\partial_t \mathbf{a} = i(-iK)\mathbf{a}$. If K is Hermitian, then this equation is just the Schrödinger equation with the anti-Hermitian Hamiltonian $H = -iK$.

If the constant drive $\mathbf{P}$ is an eigenstate of the system, then we can diagonalize Eq. (3.1). As the network is initialized to zero amplitude, only one entry in the state vector is nonzero after diagonalization, and we can replace Eq. (3.1) by a single, scalar differential equation:

$$\frac{dc}{dt} = (\lambda - \gamma)\,c + \beta. \tag{3.2}$$

Here λ is the eigenvalue of K that corresponds to the eigenstate labeled by c. Solving for c, we find:

$$c = \frac{\beta}{\gamma - \lambda}\left(1 - e^{-(\lambda-\gamma)t}\right). \tag{3.3}$$

In our experiment, we measure $\left(|c|^2 + d\right)$ when $t \to \infty$, where d is the bias of our photodetector. Furthermore, to construct a fit model, we note that the β drive parameter can be absorbed into the denominator of Eq. (3.3). The resulting model is

$$|c|^2 = \frac{1}{(\Gamma - \Lambda)^2} + d. \tag{3.4}$$

For the SSH model, $\lambda = \pm\sqrt{w^2 + v^2 + 2wv\cos(k)}$, so we can express the specific model for our band structure measurements as

$$|c_{\pm}(k;\mathbf{x})|^2 = \frac{1}{\left(\Gamma \mp \sqrt{W^2 + V^2 + 2WV\cos(k)}\right)^2} + d, \tag{3.5}$$

where $W = w/\beta$ and $V = v/\beta$. In addition to being a function of k, we let $c_{\pm}$ be a function of the model parameters, $\mathbf{x} = (\Gamma, W, V, d)$. To reconstruct the SSH band structure, we use the Metropolis-Hastings algorithm to construct a posterior distribution for the fit parameters in Eq. (3.5). An advantage of using Markov chain Monte Carlo (MCMC) simulations to fit our data is that the simulations provide both estimates for the fit parameters and Bayesian confidence intervals for our estimates. Detailed descriptions of the Metropolis-Hastings sampler can be found elsewhere (Aster, Borchers, and Thurber, 2019); here we will simply summarize the steps used in our implementation of the algorithm. Our discussion of the Metropolis-Hastings sampler is adapted from that in (Aster, Borchers, and Thurber, 2019).

We begin by defining a quantity called the acceptance ratio, A, defined as

$$A(\mathbf{x},\mathbf{y}) = \min\left(1,\ \frac{p(\mathbf{y})\mathcal{L}(\mathbf{d}|\mathbf{y})q(\mathbf{x},\mathbf{y})}{p(\mathbf{x})\mathcal{L}(\mathbf{d}|\mathbf{x})q(\mathbf{y},\mathbf{x})}\right). \tag{3.6}$$

Here $\mathbf{x}$ is a vector of the current model's parameters and $\mathbf{y}$ is a vector of a proposed model's parameters, $\mathcal{L}(\mathbf{d}|\mathbf{x})$ is the likelihood function for the data $\mathbf{d}$ given the model with parameters $\mathbf{x}$, and $p(\mathbf{x})$ is the prior distribution on the model parameters. The vector $\mathbf{y}$ is drawn from the proposal distribution, $q(\mathbf{x},\mathbf{y})$, which we take to be

$$q(\mathbf{x},\mathbf{y}) \propto \exp\left[-\frac{1}{2}\sum_i \left(\frac{|x_i - y_i|^2}{\eta_i^2}\right)\right] \tag{3.7}$$

for each fit parameter. The standard deviations, η_i, are parameters of the algorithm, and we shall return to these values momentarily. Because the proposal distribution, Eq. (3.7), is even with respect to $x_i - y_i$, the proposal distributions cancel in the numerator and denominator of Eq. (3.6).

To make use of the acceptance ratio in the Metropolis-Hastings algorithm, we must define the likelihood functions and the prior distribution. We assume that each measured amplitude is distributed according to a normal distribution to its sample mean, d_i and standard error, σ_i. Then the likelihood function can be written as

$$\mathcal{L}(\mathbf{d}|\mathbf{x}) \propto \exp\left[-\frac{1}{2}\sum_i\sum_{\alpha=\pm}\left(\frac{|d_i - c_\alpha(k_i;\mathbf{x})|^2}{\sigma_i^2}\right)\right] \tag{3.8}$$

where $c_\pm(k_i;\mathbf{x})$ is the fit model defined by Eq. (3.5) evaluated at the quasimomentum $k = k_i$ that corresponds to the measured amplitude, d_i.

There is considerably more latitude in our selection of the prior distribution. Given the best-fit values of the parameters and the physical restrictions on the possible parameter values (e.g. the coupling parameters w and v should be positive), we selected the following prior distribution for the band structure measurement at the phase transition point:

$$p_{w=v}(\mathbf{x}) \propto \begin{cases} 0, & V < 0 \\ 0, & W < 0 \\ 0, & \Gamma \leq \sqrt{W^2 + V^2 + 2WV} \\ 1, & \text{Otherwise} \end{cases} \tag{3.9}$$

Note that we need not specify the constants of proportionality in Eq. (3.8) or Eq. (3.9). As with the proposal distribution, these constants will cancel in Eq. (3.6). For the band structure measurement in the topological phase, we add the additional constraint that $w > v$:

$$p_{w=v}(\mathbf{x}) \propto \begin{cases} 0, & V < 0 \\ 0, & W < 0 \\ 0, & W > V \\ 0, & \Gamma \leq \sqrt{W^2 + V^2 + 2WV} \\ 1, & \text{Otherwise} \end{cases} \tag{3.10}$$

This validity of this constraint is easily verified by measuring the coupling strengths of our network. Once again, we do not need to specify the constant of proportionality.

With the acceptance ratio and the distributions defined above, we run the Metropolis-Hastings algorithm, which consists of four basic steps (Aster, Borchers, and Thurber, 2019). First, we propose a set of model parameters, $\mathbf{y}$ from the proposal distribution $q(\mathbf{y},\mathbf{x})$, where $\mathbf{x}$ is the set of current model parameters. Second, we calculate the quantity $\log A(\mathbf{x},\mathbf{y})$. Next, we generate a value t from the distribution $\mathrm{Unif}(0,1)$. Finally, if $\log t \geq \log A(\mathbf{x},\mathbf{y})$, then we set $\mathbf{y}$ as the current model parameters. Otherwise, retain $\mathbf{x}$ as the current model parameters.

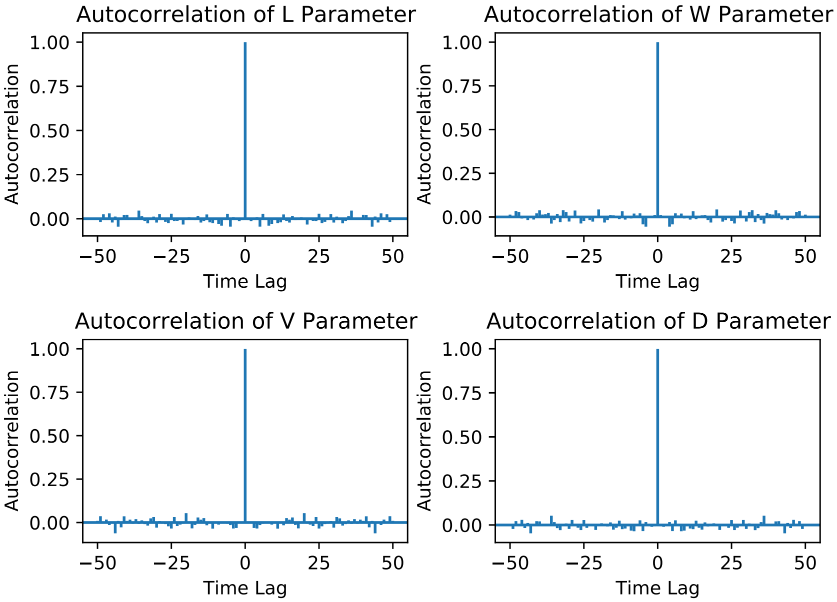

Figure 3.7: Autocorrelation plots at phase transition point

Autocorrelation plots at phase transition point. Autocorrelation plots for the Metropolis-Hastings algorithm run on the band measurement at the phase transition point.

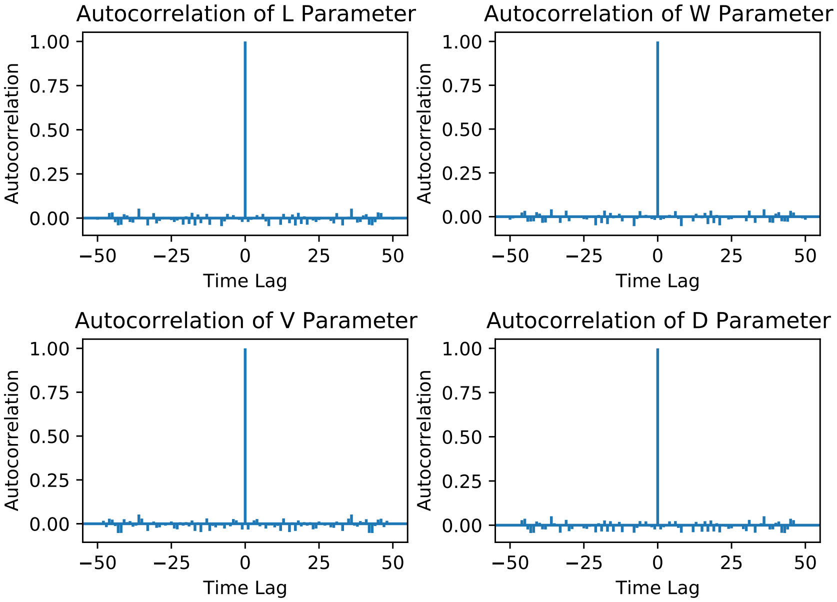

Figure 3.8: Autocorrelation plots in the topological phase

Autocorrelation plots in the topological phase. Autocorrelation plots for the Metropolis-Hastings algorithm run on the band measurement in the topological phase.

The “acceptance rate” (as opposed to the acceptance ratio) is defined as the rate at which we update the current model parameters in Step (4). This rate is set by the standard deviation of the proposal distribution in Eq. (3.7). We select $\eta_i = 0.0015$ for both band structure measurements to achieve an acceptance rate of 39.7% for the measurement in the topological phase and an acceptance rate of 31.3% for the measurement at the phase transition. Both acceptance rates lie within the recommended 20%-50% range (Aster, Borchers, and Thurber, 2019).

To generate sufficient statistics to construct confidence intervals, we run the Metropolis-Hastings algorithm for 80,100,000 iterations. For each band structure measurement, we initialize the algorithm with the best fit model of our nonlinear regression algorithm and use a warm-up period of 100,000 iterations to ensure that our samples are independent of the initialization. After this warm-up period, we collect samples only every 40,000 iterations to decorrelate the samples. The autocorrelation plots in Figs. 3.7 and 3.8 verify that the samples for each parameter are uncorrelated. With the chosen sampling rate, warm-up period, and total number of iterations, we collect a 2,000 samples, which we use to compute the means and 95% confidence intervals of the model parameters.

To quantitatively assess the quality of our band structure measurments, we are most interested in the ratio of the coupling parameters w and v, as this ratio indicates where our network lies relative to the topological phase transition. To estimate the mean coupling ratio $w/v = W/V$, we use the output of our MCMC simulations to construct a distribution for the ratio W/V. Then, we compute the mean and 95% confidence interval for this ratio. For the band structure measurement at the phase transition point, we find $W/V = 1.0\ (0.76, 1.25)$, and for the band structure measurement in the topological phase we find $W/V = 1.42\ (1.34, 1.49)$. The quantities in parentheses are the 95% confidence intervals for the extracted parameters. These numbers agree well with the expected values of 1.0 and $\sqrt{2} \approx 1.414$, which were the intended coupling ratios of the network during these measurements.

3.3 Conservatively and Dissipatively Coupled Resonator Arrays

In the main text, we analyzed our network with a Lindblad-like master equation. This approach illuminates connections between the dissipation engineering in our work and dissipation engineering in open quantum systems. Here we present a coupled mode theory of both conservatively and dissipatively coupled resonators to compare our dissipative time-multiplexed resonators with the conservatively coupled resonators previously studied in topological photonics. Afterwards, we discuss the possibility of using dissipative coupling to emulate conservative coupling within a certain bandwidth.

Coupled Amplitude Theory

Near resonance, systems of coupled resonators are well described by coupled-amplitude theory (Ozawa, Price, et al., 2019). For a conservatively coupled resonator array, we can describe the dynamics within the coupled-amplitude approximation by

$$\frac{d\mathbf{a}_c}{dt} = (iH - \gamma)\,\mathbf{a}_c + \mathbf{P}(t). \tag{3.11}$$

Here H is the coupling matrix, γ describes the optical losses of each resonator, and $\mathbf{P}(t)$ represents a time-varying drive. When $\gamma, \mathbf{P}(t) \rightarrow 0$, Equation (3.11) closely resembles the Schrödinger equation. In this limit, assuming that H is Hermitian, the solutions of Eq. (3.11) can be written as linear combinations of plane waves. On the other hand, for a dissipatively coupled resonator array, the dynamical equation within the coupled-amplitude approximation is

$$\frac{d\mathbf{a}_d}{dt} = (K - \gamma)\,\mathbf{a}_d + \mathbf{P}(t). \tag{3.12}$$

Equation (3.12)'s eigenfuctions are real exponentials when K is Hermitian. Here we explain how topological behaviors can arise in the dissipation of such a dissipatively coupled system.

For comparison, we first solve Eq. (3.11) to show that, by exciting a conservatively coupled system with a particular frequency ω, one predominantly excites eigenstates in the vicinity of that frequency ω. We transform Eq. (3.11) into a rotating frame by defining $\mathbf{a}_c = \tilde{\mathbf{a}}_c e^{i\omega t}$ and $\mathbf{P} = \tilde{\mathbf{P}} e^{i\omega t}$. We obtain

$$\frac{d\tilde{\mathbf{a}}_c}{dt} = [i(H - \omega) - \gamma]\,\tilde{\mathbf{a}}_c + \tilde{\mathbf{P}}(t). \tag{3.13}$$

Next, we diagonalize H by defining $H = S\Lambda S^{-1}$, with $\Lambda = \mathrm{diag}\{\ldots, \lambda_i, \ldots\}$. Defining $\mathbf{c} = S^{-1}\tilde{\mathbf{a}}_c$ and $\mathbf{P}_c(t) = S^{-1}\tilde{\mathbf{P}}(t)$, we find

$$\frac{d\mathbf{c}}{dt} = [i(\Lambda - \omega) - \gamma]\,\mathbf{c} + \mathbf{P}_c(t). \tag{3.14}$$

Using the initial condition $c(t = 0) = 0$, we solve Eq. 3.14 with an integrating factor and obtain

$$\mathbf{c}(t) = e^{[i(\Lambda-\omega)-\gamma]t} \int_0^t e^{-[i(\Lambda-\omega)-\gamma]t'} \mathbf{P}_c(t')\,dt'. \tag{3.15}$$

To evaluate the integral, we assume that $\mathbf{P}_c(t')$ varies on a slow time scale with respect to the loss rate γ. Then we can make the approximation $\mathbf{P}_c(t') = \mathbf{P}_c(0)$, and we can pull this term out of the integral. The remaining integral yields

$$\mathbf{c}(t) \approx \left(\frac{1 - e^{[i(\Lambda - \omega) - \gamma]}}{\gamma - i\,(\Lambda - \omega)} \right) \mathbf{P}_c(0). \tag{3.16}$$

Note that the prefactor multiplying $\mathbf{P}_c(0)$ is a diagonal matrix with entries

$$\frac{1 - e^{[i(\Lambda_{ii} - \omega) - \gamma]}}{\gamma - i\,(\Lambda_{ii} - \omega)} = \frac{1 - e^{[i(\lambda_i - \omega) - \gamma]}}{\gamma - i\,(\lambda_i - \omega)}, \tag{3.17}$$

where λ_i is the eigenvalue corresponding to the eigenstate, $c_i(t)$.

We are interested in squared projection of the system's state into one of the eigenstates, $c_i(t)$, which we can write as $|c_i(t)|^2$. At late times, this projection is given by

$$|c_i(t \to \infty)|^2 \approx \frac{1}{(\lambda_i - \omega)^2 + \gamma^2} |P_{ci}(0)|^2. \tag{3.18}$$

The frequency dependent factor is a Lorentzian of width 2γ. Therefore, in the conservatively coupled case, the projection $|c_i(t \to \infty)|^2$ depends on two things: the overlap of the drive, $\mathbf{P}_c$ with the ith eigenstate and the proximity of the driving frequency ω to the eigenvalue, λ_i. This calculation captures the essential content of conservatively coupled resonator arrays: Conservative coupling induces a frequency splitting in the eigenmodes of the system. When one drives the system at a certain frequency, one primarily excites the eigenstates within γ of the driving frequency.

For a dissipatively coupled system, we can solve Eq. (3.12) in a similar manner. We immediately diagonalize K by defining $K = S\Lambda S^{-1}$, $\mathbf{P}_d = S^{-1}\mathbf{P}(t)$ and $\mathbf{d} = S^{-1}\mathbf{a}_d$. With the initial condition $\mathbf{d}(t = 0) = \mathbf{0}$, the solution reads

$$\mathbf{d}(t) = e^{[\Lambda - \gamma]t} \int_0^t e^{-[\Lambda - \gamma]t'} \mathbf{P}_d(t')\, dt'. \tag{3.19}$$

We are interested in how we can excite a single eigenstate of the system, $d_i(t)$. When K corresponds to a topologically nontrivial Hamiltonian, this will tell us how to excite the edge state.

To bound the maximum "occupation" of a particular eigenstate, $d_i(t)$, given an arbitrary drive, $\mathbf{P}_d(t)$, we replace each element of $\mathbf{P}_d(t)$ by its maximum on the interval $[0, t]$. We can then perform the integral in Eq. (3.19) exactly to obtain the bound

$$|d_i(t)|^2 \leq \left(\frac{e^{[\lambda_i - \gamma]t} - 1}{\lambda_i - \gamma}\right)^2 \max\left\{|P_{di}(0 \leq t' \leq t)|^2\right\}. \tag{3.20}$$

In our experiments we use a constant drive, for which Equation (3.20) holds with equality. Furthermore, for Eq. (3.20) to hold in our experiments, our network must remain in the linear regime (i.e., below the lasing threshold), where $\lambda_l < \gamma, \ \forall \ \lambda_l$. We conclude that the projection $|d_l(t)|^2$ also depends on two things: the overlap of the drive $\mathbf{P}_d$ with the lth eigenstate and the eigenvalue, λ_l, which determines the loss rate of the lth eigenstate.

In the conservatively coupled case, the frequency of the drive, ω, "picked out" the eigenstates with eigenvalues near ω. However, in the dissipatively coupled case, the magnitude of $P_{dl}(t)$ (the projection of the driving term into the lth eigenstate) bounds the projection into $d_l(t)$. Now the influence of λ_l in Eq. (3.20) is to suppress the eigenstates with smaller eigenvalues, λ_l, more greatly than the eigenstates with larger λ_l. Let us now study the effect of this suppression, still limiting ourselves to the linear regime in which $\lambda_l < \gamma, \ \forall \ \lambda_l$. Assuming that the bound in Eq. (3.20) is tight, we can approximately express the ratio between the projections into the ith and jth eigenstates as $t \to \infty$ as

$$\left|\frac{d_i(t \to \infty)}{d_j(t \to \infty)}\right|^2 \approx \left(\frac{\lambda_j - \gamma}{\lambda_i - \gamma}\right)^2 \left(\frac{\max\left\{|P_{di}(0 < t' < t)|^2\right\}}{\max\left\{\left|P_{dj}(0 < t' < t)\right|^2\right\}}\right)^2. \tag{3.21}$$

If $|d_i(t \to \infty)|^2 = |d_{\text{top}}(t \to \infty)|^2$ corresponds to a topological edge state, then there exist states $|d_j(t \to \infty)|^2$ such that $\lambda_j > \lambda_i = \lambda_{\text{top}}$ because topological edge states occur in the gap between two bulk bands. Thus, to maximize the ratio $\left|d_{\text{top}}(t \to \infty)/d_j(t \to \infty)\right|^2$, we should minimize the second factor on the right-hand side of Eq. (3.21), that is, one must be careful not to excite other states with lower dissipation. Additionally, since the overall dissipation γ should be large enough to prevent the lowest-loss state from lasing (i.e., $\gamma \geq \max_j \lambda_j$), and the coupling constants J are inherently linked to the dissipation rates (see Section 3.5), it is not straightforward to achieve a large contrast $\left[\left(\lambda_{\text{top}} - \gamma\right) / \left(\lambda_j - \gamma\right)\right]^2$ for bulk states ($\lambda_j < \lambda_{\text{top}}$) below the band gap.

Emulating Conservative Coupling in Dissipatively Coupled Resonator Arrays

In this subsection, we analyze pairs of conservatively and dissipatively coupled resonators to show that, within a finite bandwidth, dissipative couplings can emulate the behaviors of conservative couplings. Our results suggest that, in future experiments, we might be able to study certain behaviors of conservatively coupled systems in our dissipatively coupled time-multiplexed resonator networks.

Coupled amplitude analysis

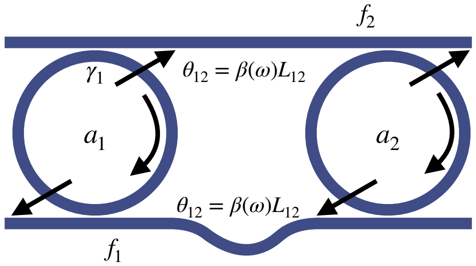

Figure 3.9: Two identical rings coupled by two connecting waveguides.

Consider the pair of identical ring resonators shown in Fig. 3.9, which are connected by two waveguide buses. The rings couple to the waveguides with a coupling strength γ_1, and the bus lengths, L_{12} and L_{21}, produce coupling phases $\theta_{12,21}(\omega) = \beta(\omega)L_{12,21}$ between the resonators. The equations for the mode fields inside the rings are

$$\frac{\mathrm{d}}{\mathrm{d}t}a_1 = -2\gamma_1 a_1 + i\sqrt{2\gamma_1}\, f_1 \tag{3.22}$$

$$\frac{\mathrm{d}}{\mathrm{d}t}a_2 = -2\gamma_1 a_2 + i\sqrt{2\gamma_1}\, f_2, \tag{3.23}$$

where the two factors of γ_1 arise from the outcoupling of the resonators into the two buses, and the fields f_1 and f_2 describe the coupling between the resonators:

$$f_1 = i\sqrt{2\gamma_1}\, a_2 e^{i\theta_{21}}; \quad f_2 = i\sqrt{2\gamma_1}\, a_1 e^{i\theta_{12}}. \tag{3.24}$$

Note that we ignored the intrinsic losses of the waveguides in Eqs. (3.22)

Substituting the expressions for f_1 and f_2 in Eqs. (3.22), we obtain

$$\begin{pmatrix} \dot{a}_1 \\ \dot{a}_2 \end{pmatrix} = \begin{pmatrix} -2\gamma_1 & -2\gamma_1 e^{i\theta_{21}} \\ -2\gamma_1 e^{i\theta_{12}} & -2\gamma_1 \end{pmatrix} \begin{pmatrix} a_1 \\ a_2 \end{pmatrix}. \tag{3.25}$$

We can add gain g to each ring to partially compensate the diagonal loss terms. In this case the diagonal loss becomes $\gamma_0 = \gamma_1 - g$, and the coupling matrix takes the form

$$\begin{pmatrix} -\gamma_0 & -2\gamma_1 \exp\left[i\theta_{21}\right] \\ -2\gamma_1 \exp\left[i\theta_{12}\right] & -\gamma_0 \end{pmatrix}. \tag{3.26}$$

Let us call the eigenvalues of this matrix $i\omega_{1,2}$, such that the system evolves with the time dependence $e^{i\omega_{1,2}t}$. We find

$$\omega_{1,2} = -i\gamma_0 \pm i\sqrt{2\gamma_1}\, \exp\left[i(\theta_{12} + \theta_{21})/2\right]. \tag{3.27}$$

Note that the phases $\theta_{12,21}$ are themselves ω-dependent, so this equation must be solved in a self-consistent manner in the strong coupling regime. For $\theta_{12} + \theta_{21} = \pi$, the eigenvalues are real except for the overall loss $-i\gamma_0$. This corresponds to a split resonance, as would be expected for conservative coupling. Thus, when we set the locks such that the + delay is constructive $\theta_{12} = 0$ and the − delay is destructive $\theta_{21} = \pi$, we obtain conservative coupling. For $\theta_{12} + \theta_{21} = 0$, we get purely imaginary eigenvalues, as would be expected for dissipative coupling. This corresponds to setting the + and − delays both to constructive interference or both to destructive interference.

Scattering matrix method

In this section, we apply scattering matrices to systems of two identical, coupled resonators to illustrate how a dissipatively coupled system can emulate a conservatively coupled one. In general, we find that the frequency response of two dissipatively resonators can correspond exactly to that of two, lossy conservatively coupled resonators at a single frequency. Furthermore, within a certain bandwidth about this frequency, the frequency response of the dissipatively coupled resonators continues to closely resemble that of the conservatively coupled system, even though the correspondence is not exact. Specifically, we demonstrate that by properly engineering the coupling phases of the dissipatively coupled resonators, we can induce a frequency mode splitting analogous to the Autler-Townes effect in conservatively coupled resonators.

The layouts of two conservatively coupled resonators and two dissipatively coupled ring resonators are shown Fig. 3.10. The conservatively coupled resonators in Fig. 3.10(a) are evanescently coupled, while the dissipatively coupled resonators are

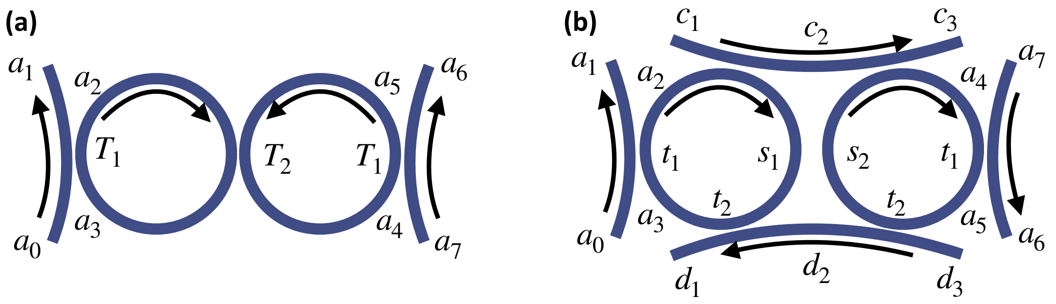

Conservative Coupling **Dissipative Coupling**

Figure 3.10: Conservatively and dissipatively coupled resonators

Conservatively and dissipatively coupled resonators Rings coupled directly (conservative) vs. indirectly coupled via bus waveguides (dissipative).

coupled via a bus waveguide. While the coupling phase between the conservatively coupled resonators is fixed at $\pi/2$, it is possible to modify the coupling phases between the dissipatively coupled resonators by adjusting the lengths of the buses. We are interested in selecting these lengths so that the the frequency response of Fig. 3.10(b) emulates that of Fig. 3.10(a). For simplicity, here we consider the case in which the two buses have equal lengths.

We begin by analyzing the pair of identical, conservatively coupled resonators. To undertake this analysis, we label the field at different points in Fig. 3.10(a) by a_i, with $i = 0 \ldots 7$. Each label corresponds to the field either directly before or directly after the nearby coupling region.

The power splitting ratio of the couplers are $T_1^2 : (1 - T_1^2)$ and $T_2^2 : (1 - T_2^2)$. We are interested in the frequency response of the field a_6 in response to an drive on the field a_0. By tracking the phases acquired through each section of the system, we find the following relation between the various fields of the system:

$$\begin{bmatrix} a_2 \\ a_3 \\ a_4 \\ a_5 \end{bmatrix} = \begin{bmatrix} 0 & \sqrt{1 - T_1^2} & 0 & 0 \\ e^{i\theta_c}\sqrt{1 - T_2^2} & 0 & 0 & iT_2 e^{i\theta_c} \\ iT_2 e^{i\theta_c} & 0 & 0 & e^{i\theta_c}\sqrt{1 - T_2^2} \\ 0 & 0 & \sqrt{1 - T_1^2} & 0 \end{bmatrix} \begin{bmatrix} a_2 \\ a_3 \\ a_4 \\ a_5 \end{bmatrix} + \begin{bmatrix} iT_1 a_0 \\ 0 \\ 0 \\ 0 \end{bmatrix}. \quad (3.28)$$

Here $\theta_c = n\omega L/c - \gamma_c L$, where L is the length of the resonators, n is the index of refraction, ω is the optical frequency, and γ_c is the loss per unit length. The output field is given by $a_6 = iT_1 a_4$.

To select the coupling phases for the dissipatively coupled system so that it emulates the conservatively coupled system, we perform a similar scattering matrix analysis for the resonators in Fig. 3.10(b). To maintain a consistent notation between the result of this analysis and the result of analyzing conservatively coupled system, we label the additional fields in Fig. 3.10(b) by q_i, r_i, and s_i. The transfer coefficients in Fig. 3.10(b) are t_1 and t_2. As in the conservatively coupled system, we can derive a relation between the fields of the system. We find

$$\begin{bmatrix} a_2 \\ a_3 \\ a_4 \\ a_5 \end{bmatrix} = \begin{bmatrix} 0 & \sqrt{1-t_1^2} & 0 & 0 \\ e^{i\theta_d}(1-t_2^2) & 0 & 0 & -t_2^2 e^{i(\phi+\theta_d/2)} \\ -t_2^2 e^{i(\phi+\theta_d/2)} & 0 & 0 & e^{i\theta_d}(1-t_2^2) \\ 0 & 0 & \sqrt{1-t_1^2} & 0 \end{bmatrix} \begin{bmatrix} a_2 \\ a_3 \\ a_4 \\ a_5 \end{bmatrix} + \begin{bmatrix} it_1 a_0 \\ 0 \\ 0 \\ 0 \end{bmatrix}. \tag{3.29}$$

Here $\theta_d = n\omega L/c + i\gamma_d L$, where γ_d is the loss per unit length of the dissipatively coupled resonators. Note that we take the lengths of the conservatively and dissipatively coupled resonators to be equal, while we allow their intrinsic losses to differ. Furthermore, $\phi = n\omega\ell/c - \gamma_d\ell$, where ℓ is the length of the buses. This equation shows that we can adjust the phase acquired through the buses by adjusting the lengths of the buses.

Armed with Eqs. (3.28) and (3.29), we want to solve for the parameters of the dissipatively coupled system that enable it to emulate the conservatively coupled system. To equate Eq. (3.28) and Eq. (3.29), there are three equations that we must satisfy

$$\sqrt{1-T_1^2} = \sqrt{1-t_1^2} \tag{3.30a}$$

$$e^{i\theta_c}\sqrt{1-T_2^2} = e^{i\theta_d}\left(1-t_2^2\right) \tag{3.30b}$$

$$iT_2 e^{i\theta_c} = -t_2^2 e^{i(\phi+\theta_d/2)} \tag{3.30c}$$

From Eq. (3.30a) it is evident that $T_1 = t_1$. Meanwhile, the complex exponentials in of Eq. (3.30b) cancel because the lengths of the resonators are the same. The real exponentials of Eq. (3.30b) satisfy

$$\exp\left[-\gamma_c L\sqrt{1-T_2^2}\right] = \exp\left[-\gamma_d L\left(1-t_2^2\right)\right]. \tag{3.31}$$

To analyze Eq. (3.30c), we equate the magnitudes and phases separately. Equating the phases gives

$$e^{i\left(\frac{n\omega L}{2c}\right)} = e^{i\left(\frac{n\omega \ell}{c}+\frac{\pi}{2}\right)}, \tag{3.32}$$

which holds when

$$\begin{aligned} \ell &= L + \frac{2\pi c N}{n\omega} - \frac{\pi c}{2n\omega} \\ &= L + N\lambda/n - \lambda/4n, \end{aligned} \tag{3.33}$$

for $N \in \mathbb{Z}$. In the second line we have rewritten the condition on ℓ in terms of the wavelength. Written in terms of the wavelength, it is evident that the dissipatively coupled system only emulates the conservatively coupled system when the length of the bus exactly compensates for the additional $\pi/2$ phase accumulated when light couples into and out of the buses. Note that, in a more general analysis, in which we allow the lengths of the buses to be different, this condition becomes that the sum of the phases accumulated through the two buses must sum to π, which is exactly the result obtained with the coupled amplitude equations earlier.

Equation (3.33) tell us why we can only equate Eq. (3.28) and Eq. (3.29) at a single frequency: The lengths of the buses are fixed, so Eq. (3.33) only holds with equality at one frequency. However, for some bandwidth $\Delta\omega \ll \omega$, these equations will still hold approximately. Within this bandwidth, the dissipatively coupled system can emulate a conservatively coupled one.

Equating the magnitudes in Eq. (3.30c), we find that

$$T_2 e^{-\gamma_C (L/2)} = t_2^2 \exp\left[-\gamma_D \left(\ell + L\right)\right]. \tag{3.34}$$

Using Eqs. (3.31), (3.33), and (3.34), we can solve for γ_d and t_2. We find

$$T_2 = \sqrt{\frac{x^2}{1+x^2}} \tag{3.35a}$$

$$\gamma_C = \gamma_D - \frac{1}{L}\ln\left(\frac{1-t_2^2}{\sqrt{1-T_2^2}}\right), \tag{3.35b}$$

where

$$x = \frac{t_2^2}{1-t_2^2}\exp\left[-\gamma_D \ell\right]. \tag{3.36}$$

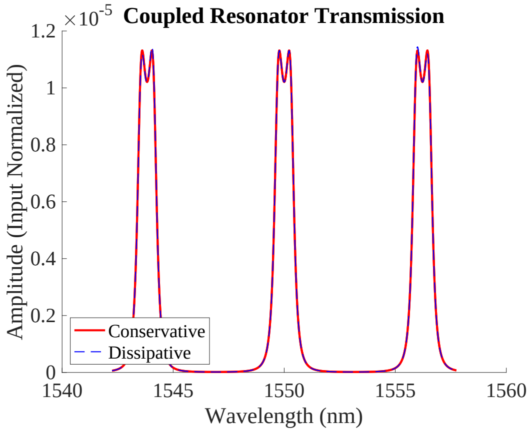

Figure 3.11: Emulating conservative coupling

Emulating conservative coupling. Emulating conservative coupling with dissipatively coupled resonators.

Equations. (3.35a) and (3.35b) can be inverted numerically to solve for t_2 and γ_D.

Eqs. (3.35a) and Eq. (3.36) provide an intuitive picture of how the conservatively coupled and dissipatively coupled systems are related. Using Eq. (3.35a) and Eq. (3.36) we can show that $\left(1 - t_2^2\right) / \sqrt{1 - T_2^2} < 1$ for $0 < t_2, T_2$. This allows us to conclude, from Eq. (3.35a), that $\gamma_c > \gamma_d$. In other words, the dissipatively coupled system always corresponds to a more lossy conservatively coupled system. This additional loss is to be expected, as the open ports in Fig. 3.10(b) behave like an additional source of loss in the dissipative system.

We have now shown in what sense a dissipatively coupled network can emulate a conservatively coupled one. By selecting the coupling phases of the dissipatively coupled network's bus waveguides properly, the frequency response of the dissipatively coupled system can approximate that of a conservatively coupled system over some bandwidth, with an exact correspondence holding at a particular frequency. As an example of this correspondence, we use the equations derived in this section to plot the frequency responses of a pair of dissipatively coupled resonators and the frequency responses of their conservatively coupled counterpart. These plots are shown in Fig. 3.11. We see that the conservatively coupled and dissipatively coupled systems exhibit an Autler-Townes splitting. In addition, the responses of the dissipatively and conservatively coupled system are in excellent agreement overall several different resonances.

To end this section, we briefly contrast the conditions for the Autler-Townes splitting discussed above and those required to realize the optical analog of electromagnet-

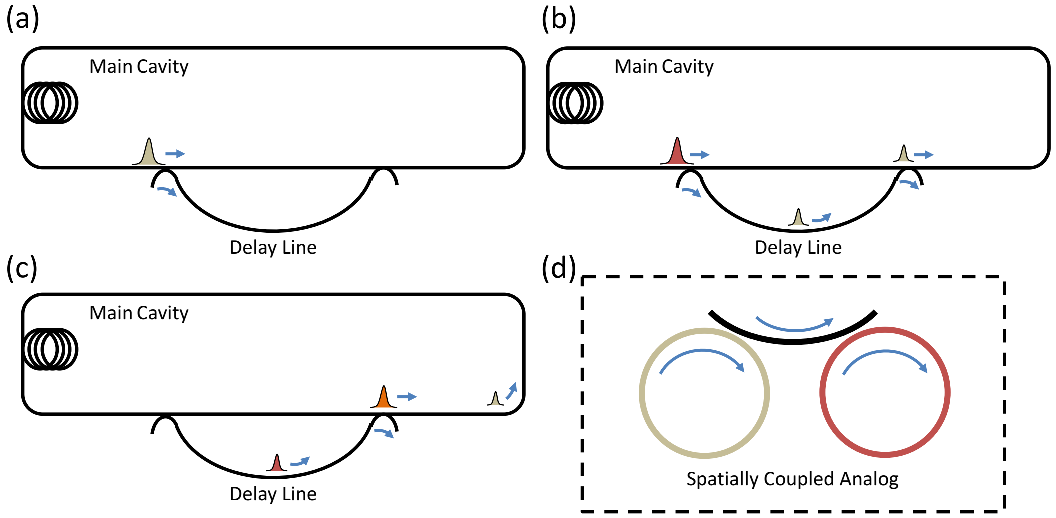

Figure 3.12: Delay line dissipative couplings

Delay line dissipative couplings. Illustration of a dissipative delay line coupling and its spatial analog in ring resonators.

ically induced transparency (EIT) in pairs of dissipatively coupled resonators (Xu et al., 2006; Mancinelli et al., 2011; Smith et al., 2004). In the analysis above, we considered two identical resonators, and we induced a mode splitting by tuning the coupling phases between the resonators. In contrast, to achieve EIT-like behavior with two dissipatively coupled resonators, one must operate in a regime in which the coupling rate between the resonators is much larger than the detuning of the two resontors and in which the detuning of the two resonators is much larger than the intrinsic losses of the resonators Maleki et al., 2004. This is very distant from the regime in which we performed the our analysis. Note that a separate set of conditions exist to realize EIT-like behavior with two conservatively coupled resonators Peng et al., 2014.

Why Delay Lines Produce Dissipative Couplings

The dissipative nature of our delay line couplings in our photonic resonator network is essential to the experimental results presented in this work. Let us briefly discuss why these delay line couplings are dissipative.

As discussed above, two ring resonators coupled by bus waveguides are dissipatively coupled, and the bus waveguides act as an intermediate reservoir that connects the two resonators. As illustrated in Fig. 3.12, the optical delay lines of a time-multiplexed network act analogously to bus waveguides for time-multiplexed resonators. Like all dissipative couplings, the delay line couplings of our network may be decomposed into two couplings: first a portion of one pulse is coupled into the modes of the optical delay line, and later a portion of this light is coupled back into another pulse in the network. In this way, the modes of the delay lines act as reservoirs that connect the pulses of our time-multiplexed system.

Figure 3.12 shows the correspondence between a delay line coupling between two photonic pulses and the bus waveguide coupling between two ring resonators. Figure 3.12(a-c) show the process by which the beige pulse couples to a later red pulse. In Fig. 3.12(a), the beige pulse is split between the delay line and the main cavity. The beige pulse continues along both paths, while in the meantime the red pulse reaches the splitter [Fig. 3.12(b)]. In Fig. 3.12(c), part of the beige pulse in the delay line couples to the red pulse in the main cavity, while the rest of the beige pulse in the delay line is lost through the open port. This coupling process is the time-multiplexed version of the coupled resonators shown in Fig. 3.12(d), in which the beige and red ring resonators are dissipatively coupled by a waveguide bus.

3.4 Robustness of the Dissipative Topological Edge State

In the main text we claim that our network exhibits “topological dissipation,” by which we mean that topologically protected edge states occur in the band gap of the network’s dissipation spectrum. These topological edge states are distinct from those that have been studied previously in topological photonics, which rely on optical analogs of the Schrödinger equation and which occur in the band gaps of a system’s frequency spectrum. Given the novelty of the edge states studied in this paper, it is valid to wonder whether our topological edges states experience the same sort of topological protection. In this section, we show that the usual bulk-boundary correspondence applies to the dissipative topological models studied in this text.

We begin by reformulating the dynamical matrix that describes our dissipatively coupled system as an anti-Hermitian Hamiltonian. In particular, with no driving term and in the lossless limit, we can express the dynamics of our network as

$$\frac{d\mathbf{a}}{dt} = H\mathbf{a}, \tag{3.37}$$

where H describes the coupling between sites. In practice, we choose H so that it corresponds to a Hermitian, tight-binding Hamiltonian.

We can rewrite Eq. (3.37) in analogy with the Schrödinger equation as follows:

$$i\frac{d\mathbf{a}}{dt} = A\mathbf{a}, \tag{3.38}$$

where $A = iH$ is a non-Hermitian Hamiltonian. We want to show that the spectra of A and H possess the same topological invariants.

Let us first consider the case in which H is the Hamiltonian of a static, noninteracting, 2D tight-binding model, so that the topology of H is described completely by the Chern number Ozawa, Price, et al., 2019. Recall that the Chern number of band i is given by

$$C_i = \frac{1}{2\pi}\int_{BZ} d^2k\ \Omega_i\left(\mathbf{k}\right), \tag{3.39}$$

where $\Omega_i\left(\mathbf{k}\right)$ is the Berry curvature,

$$\Omega_i\left(\mathbf{k}\right) = i\nabla_{\mathbf{k}} \times \left\langle c_i\left(\mathbf{k}\right)\right| \nabla_{\mathbf{k}} \left|c_i\left(\mathbf{k}\right)\right\rangle. \tag{3.40}$$

Here $\left|c_i\left(\mathbf{k}\right)\right\rangle$ are the eigenstates of the reciprocal space representation of the Hamiltonian in the ith band. We will denote the reciprocal space representation of H as H_k. It follows that the reciprocal-space representation of A is $A_k = iH_k$.

Together, Eq. (3.39) and Eq. (3.40) tell us that the Chern numbers C_i depend only on the eigenvectors on H_k. Therefore, to evaluate the topological properties of our system, we should consider the eigenvalues and eigenvectors of A_k. From the relation $A_k = iH_k$ we immediately see that $\operatorname{spec}\left(A_k\right) = i\operatorname{spec}\left(H_k\right)$ and that the eigenvector of A_k corresponding to any eigenvalue $i\lambda_i\left(\mathbf{k}\right)$ is identical to the eigenvector of H_k corresponding to the eigenvalue $\lambda_i\left(\mathbf{k}\right)$. This property enables us to conclude that, if H_k has N bands, then A_k has N bands that are identical up to a factor of i. Furthermore, because H_k and A_k have the same eigenvectors, it is evident that the bands of H_k have the same Chern numbers as A_k. Therefore, we conclude that the edge states of A_k are guaranteed by the same bulk-boundary correspondence that guarantees the edge states of H_k. In other words, our dissipative network also exhibits topologically protected edge states.

We can make a similar argument regarding the SSH model. In particular, the topological invariant of the SSH model is the winding number (Asbóth, Oroszlány, and Pályi, 2016), which can be calculated as

$$\mathcal{W} = \frac{1}{2\pi} \int \left(\frac{\mathbf{h}(k)}{|\mathbf{h}(k)|} \times \frac{d}{dk} \frac{\mathbf{h}(k)}{|\mathbf{h}(k)|} \right) \cdot \hat{\mathbf{z}}\, dk, \tag{3.41}$$

where $\mathbf{h}(k)$ is defined in terms of the SSH Hamiltonian as $H_{\mathrm{SSH}} = \mathbf{h}(k) \cdot \sigma$. Once again, this topological invariant depends only on the eigenstates of the Hamiltonian. Similar arguments to those used above establish the validity of the bulk-boundary correspondence in this instance.

The arguments above frame the bulk-boundary correspondence in terms of a Schrödinger-like equation to draw a connection with the more common, Hamiltonian manifestations of topological photonics, but this procedure is contrived. The topological properties of the linear, time-independent system considered here are defined entirely by the time-independent eigenstates of that system. As long as these eigenstates are the eigenstates of a topologically nontrivial Hamiltonian, one can define a topological invariant with Eq. (3.39) or Eq. (3.41). The details of the time-evolution determine how the states of a system evolve, but they leave the topology intact.

To further elucidate the notion of dissipative topological protection, we examine the fluctuations in the optical power stored in the topological edge state $|\psi_0\rangle$ arising in the SSH lattice implemented in our arrangement in the presence of random coupling disorders. In this scenario, one can write

$$\frac{d}{dt} |\psi_0\rangle = H_{SSH} |\psi_0\rangle + \Delta H |\psi_0\rangle = -\lambda_0 |\psi_0\rangle + \Delta H |\psi_0\rangle, \tag{3.42}$$

where H_{SSH} is the unperturbed SSH Hamiltonian while $|\psi_0\rangle$ represents the edge-state wavefunction with its corresponding eigenvalue $-\lambda_0$. In addition, ΔH signifies a random coupling perturbation given by the matrix representation (here without loss of generality we consider a half-infinite left-edge eigenstate)

$$\Delta H = \begin{bmatrix} 0 & \delta\kappa_1 & 0 & 0 & \dots \\ \delta\kappa_1 & 0 & \delta\kappa_2 & 0 & \dots \\ 0 & \delta\kappa_2 & 0 & \delta\kappa_3 & \dots \\ 0 & 0 & \delta\kappa_3 & 0 & \dots \\ \dots & \dots & \dots & \dots & \dots \end{bmatrix}. \tag{3.43}$$

Under such conditions, the time evolution of the edge-mode optical power stored within the cavity is given by

$$\frac{d}{dt}\langle\psi_0|\psi_0\rangle = -2\lambda_0\langle\psi_0|\psi_0\rangle + \langle\psi_0|\Delta H|\psi_0\rangle + \left\langle\psi_0|\Delta H^\dagger|\psi_0\right\rangle. \tag{3.44}$$

We now claim that for any off-diagonal matrix ΔH (corresponding to perturbations in the coupling coefficients of the 1D lattice) $\langle\psi_0|\Delta H|\psi_0\rangle = 0$. This can be shown by expanding ΔH in terms of its columns $\Delta H = \begin{bmatrix}\mathbf{C_1} & \mathbf{C_2} & \dots & \mathbf{C_n} & \dots\end{bmatrix}$ and by making the observation that $\langle\psi_0|\mathbf{C_n}\rangle = (-1)^{(n/2-1)}e^{-(n/2-1)p}\times\delta\kappa_{n-1} + (-1)^{(n/2)}e^{-(n/2)p}\times\delta\kappa_n$, when n is even while it vanishes for the odd values of n. This observation is based on the alternate site occupation of the topological edge state in the SSH model, i.e. the amplitude identically vanishes in sublattice B (odd sites) if the edge state starts on sublattice A (even sites). Here, p is the extinction ratio associated with the exponentially decaying edge state. Subsequently,

$$\langle\psi_0|\Delta H|\psi_0\rangle = \begin{bmatrix}0 & \delta\kappa_1 - e^{-p}\times\delta\kappa_2 & 0 & -e^{-p}\times\delta\kappa_3 + e^{-2p}\times\delta\kappa_4 & 0 & \dots\end{bmatrix}\times\begin{bmatrix}1\\0\\-e^{-p}\\0\\e^{-2p}\\\dots\end{bmatrix} = 0. \tag{3.45}$$

Similarly, one can show that $\left\langle\psi_0|\Delta H^\dagger|\psi_0\right\rangle = 0$. Hence,

$$\frac{d}{dt}\langle\psi_0|\psi_0\rangle = -2\lambda_0\langle\psi_0|\psi_0\rangle. \tag{3.46}$$

This clearly indicates that the optical power associated with the topological edge state of the SSH lattice is robust against any coupling disorders.

3.5 Formalism of time-multiplexed dissipatively coupled networks of resonators

In this section, we establish a Lindblad-like master equation for the dynamics of time-bin modes in our resonator with optical delay line couplings. For simplicity, we will describe explicitly the case of two $\pm T_R$ delay lines, which represent a model with nearest-neighbor coupling in 1D [Fig. 3.13].

The finite difference equations for the j-th time-bin mode a_j, after one roundtrip T_{rt} through the main ring, can be written as

$$a_j(t+T_{\mathrm{rt}}) = (1-t_1^2)\,(1-t_2^2)\,a_j(t) + (it_1)^2e^{i\phi_1}\,a_{j+1}(t) + (it_2)^2e^{i\phi_2}\,a_{j-1}(t) \tag{3.47}$$

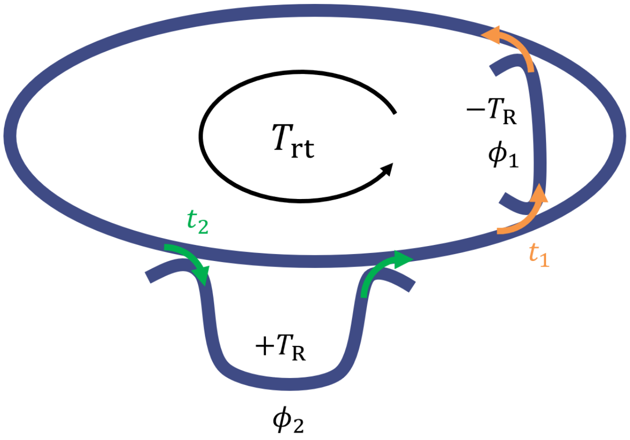

Figure 3.13: Schematic for master equation analysis

Schematic for master equation analysis. Schematic of $\pm T_{\mathrm{R}}$ delay lines for creating a 1D tight-binding lattice with nearest neighbor coupling in the time-multiplexed resonator. T_{rt} is the roundtrip time. t_1 and t_2 are the amplitude splitting ratios of the delay line couplers, which accumulate phases of ϕ_1 and ϕ_2 respectively.

Assuming the change in the field in each roundtrip is small, which is the case when the splitting ratios of the delay line couplers $t_1^2, t_2^2 \ll 1$, we obtain

$$T_{\mathrm{rt}}\, \dot{a}_j = (-t_1^2 - t_2^2)\, a_j(t) - t_1^2 e^{i\phi_1} a_{j+1}(t) - t_2^2 e^{i\phi_2} a_{j-1}(t) + O(t_1^2 t_2^2). \tag{3.48}$$

From this equation, we can read off the effective inter-site coupling terms $K_{j,j+1} = -it_1^2 e^{i\phi_1}/T_{rt}$, $K_{j+1,j} = -it_2^2 e^{i\phi_2}/T_{rt}$. Following the treatment of Ref. (Wanjura, Brunelli, and Nunnenkamp, 2020), we can write the (Hermitian/conservative) Hamiltonian coupling as $\mathcal{H} = \sum_j (Ja_j^\dagger a_{j+1} + J^* a_j a_{j+1}^\dagger)$, with

$$J = (K_{j,j+1} + K_{j+1,j}^*)/2. \tag{3.49}$$

Note that here J is in general complex, since we have not made any assumptions about t_1, t_2, ϕ_1, and ϕ_2.

The anti-Hermitian part or the dissipative coupling can be written as

$$\Gamma e^{-i\theta} = (K_{j,j+1} - K_{j+1,j}^*). \tag{3.50}$$

The Lindblad-like master equation for the system density matrix in the Schödinger picture for such a time-multiplexed resonator network is then

$$d\rho/dt = -i[\mathcal{H}, \rho] + \sum_j \mathcal{D}[L_j]\rho, \tag{3.51}$$

where the dissipator, $\mathcal{D}[L_j]\rho = L_j\rho L_j^\dagger - \{L_j^\dagger L_j, \rho\}/2$, and the jump operator, $L_j = \sqrt{\Gamma}\,(a_j + e^{-i\theta}a_{j+1})$, has a dissipative coupling rate Γ between neighboring sites.

To gain more insight about the role of t_1 and t_2 and the phases ϕ_1 and ϕ_2, let us assume that $t_1^2/T_{\mathrm{rt}} = t_2^2/T_{\mathrm{rt}} = \Gamma_0$. Then,

$$J = \Gamma_0\, e^{i(\phi_1+\phi_2)/2} \sin\left(\frac{\phi_1 - \phi_2}{2}\right) \tag{3.52}$$

$$\Gamma e^{-i\theta} = -i2\Gamma_0\, e^{i(\phi_1+\phi_2)/2} \cos\left(\frac{\phi_1 - \phi_2}{2}\right). \tag{3.53}$$

Thus, $\Gamma = 2\Gamma_0 \cos((\phi_1 - \phi_2)/2)$, $\theta = (\pi - \phi_1 - \phi_2)/2$ and $J = |J| \exp(i(\pi/2 - \theta))$ with $|J| = \Gamma_0 \sin((\phi_1 - \phi_2)/2)$. Let us look at a few special cases:

1. $\phi_1 = 0, \phi_2 = \pi$:
   $\Rightarrow |J| = \Gamma_0,\ \Gamma = 0$. *Purely Hermitian Hamiltonian* dynamics.
2. $\phi_1 = 0, \phi_2 = 0$:
   $\Rightarrow |J| = 0,\ \Gamma = 2\Gamma_0, \theta = \pi/2$. *Purely dissipative Lindbladian* dynamics.
3. $\phi_1 = \pi/2, \phi_2 = \pi/2$:
   $\Rightarrow |J| = 0,\ \Gamma = 2\Gamma_0,\ \theta = 0$. *Purely dissipative Lindbladian* dynamics.
4. $\phi_1 = 0, \phi_2 = \pi/2$:
   $\Rightarrow |J| = 1/\sqrt{2},\ \Gamma = \sqrt{2}\Gamma_0,\ \theta = \pi/4$. *Mixed dynamics, with characteristics of both Hermitian Hamiltonian evolution and dissipative Lindbladian evolution.*

3.6 Time-Reversal Symmetry Breaking in a Time-Multiplexed Resonator Network

In this section we clarify the remark from the main text that our network implements time-reversal symmetry breaking couplings.

Often, when one says that a system breaks time-reversal symmetry, what is mean is that it breaks time-reversal symmetry in a restricted sense Asadchy et al., 2020. One defines the system as a subsystem of the larger world and only considers the time-reversal of the system. A classic example of this is the motion of a charge in a constant magnetic field. It is commonly accepted that time-reversal symmetry is broken in such a system: if we reverse time, the direction of the magnetic field does not change. However, imagine that the magnetic field is generated by an electromagnet. If we include an electromagnet as a part of our system, then the magnetic field does change directions because the current in the electromagnet switches directions when we reverse time. Therefore, such a system only breaks time-reversal symmetry if we treat the source of the magnetic field as outside of our system.

Similarly, in our photonic network, we mean that our system breaks time-reversal symmetry in a restricted sense. As is standard practice in nonreciprocal photonic systems (Asadchy et al., 2020), we restrict our system to only consist of the photonic portion of the network. When we do this, some portions of our experiment, such as the modulator driving signals, are considered to be outside of our system, and they do not change when we reverse time in the system.

With this established, let us consider two ways in which our system breaks time-reversal symmetry.

One way to think about the time-reversal symmetry breaking in our dissipatively coupled system is as follows: Imagine light traveling clockwise in the dissipatively coupled resonators shown in Fig. 3.10(b). As light couples from the left resonator to the right resonator, some light is lost from the system through the open port because not all of the light in the bus waveguide is coupled into the right resonator. This loss is purely a feature of the dissipative coupling: Even if the resonators and the bus waveguides were lossless, this additional coupling loss would still be present. The presence of this coupling loss means that energy is not conserved in a pair of dissipatively coupled resonators, and, equivalently, time-reversal symmetry is broken.

However, it is important to note that this is a “trivial” time-reversal symmetry breaking. While dissipation inherently breaks time-reversal symmetry because it breaks energy conservation, this type of time-reversal symmetry breaking cannot endow our system with a nonzero Chern number. Therefore, our dissipatively coupled system requires another, “nontrivial” way of breaking time-reversal symmetry.

The second sense in which our system breaks time-reversal symmetry is in terms of the couplings. Consider the schematic representations of delay line couplings in a time-multiplexed network shown in Fig. 3.14. We consider three pulses traveling through delay lines of length $\pm T_{\mathrm{R}}$, as well as through the corresponding section of the main loop. In both delay lines we place phase modulators that control the coupling phases between the various pulses.

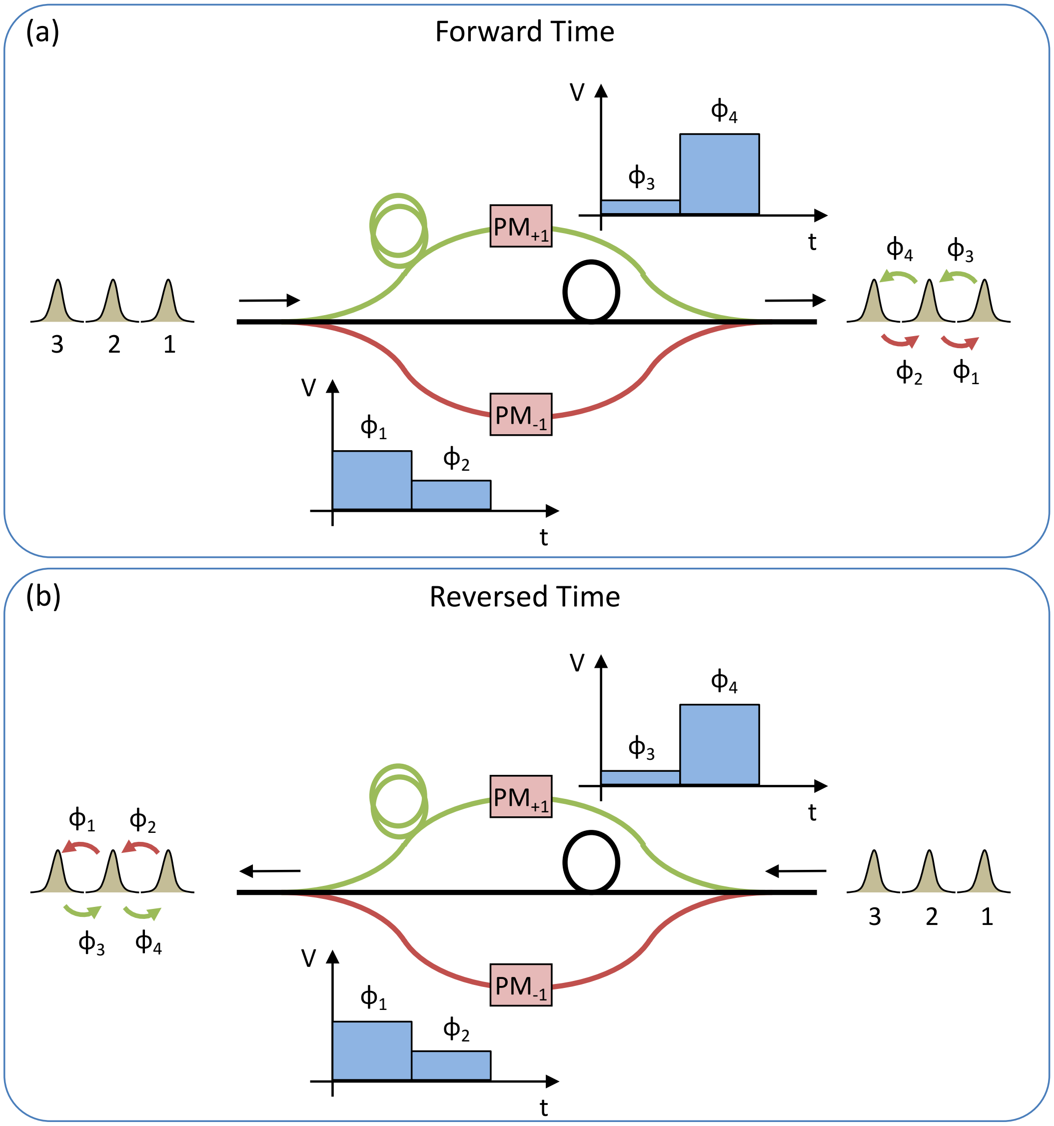

Figure 3.14: Time-reversal symmetry breaking in time-multiplexed networks

Time-reversal symmetry breaking in time-multiplexed networks.
(a) Forward-time passage through the delay lines of a time-multiplexed network.
(b) Time-reversed passage through the delay lines of a time-multiplexed network.

Let us first consider what happens when we run time forwards, as is illustrated in Fig. 3.14(a). The modulator in the $-T_\mathrm{R}$ delay line is programmed to couple Pulse 2 to Pulse 1 with a coupling phase of ϕ_1 and to couple Pulse 3 to Pulse 2 with a coupling phase of ϕ_2. The modulator in the $+T_\mathrm{R}$ delay line is programmed to couple Pulse 1 to Pulse 2 with a coupling phase of ϕ_3 and to couple Pulse 2 to Pulse 3 with a coupling phase of ϕ_4.

Next let us consider what happens when we reverse time in the network. While the pulses now propagate in the opposite direction through the delay lines, it is essential to note that two key things do not change. First, because the modulator driving signals are considered external to the system, we do not change the phase pattern imparted by the phase modulators in the delay lines. Second, we do not relabel our pulses. This is because each pulse is mapped to a specific lattice site in our synthetic lattice. When we reverse time, the order in which the synthetic lattice sites propagate through the delay lines changes, but the lattice sites retain their same positions in the synthetic lattice.

With this in mind, we can draw the phases acquired when the pulses propagate through the delay lines in a time-reversed fashion. This process is shown in Fig. 3.14(b). Now we see that Pulse 2 couples to Pulse 1 through the $+T_\mathrm{R}$ delay line with a phase of ϕ_4, while Pulse 3 couples to Pulse 2 through the $+T_\mathrm{R}$ delay line with a phase of ϕ_3. Through the $-T_\mathrm{R}$ delay line, Pulse 1 couples to Pulse 2 with a phase of ϕ_2 and Pulse 2 couples to Pulse 3 with a phase of ϕ_1. Note that these coupling phases are not the time-reversed phases of those encountered in the forward-time analysis.

This time-reversal symmetry breaking process is fundamentally different than the situation encountered in two passive, dissipatively coupled ring resonators, such as those shown in Fig. 3.10(b). The dynamics of two such resonators does not break time-reversal symmetry, for if the CW mode acquires a phase β as it couples from the left resonator to the right resonator, then the CCW mode also acquires the phase β as it couples from the second resonator to the first resonator. Therefore, in terms of the phases acquired by the CW and CCW modes, the CCW mode experiences the time-reversed dynamics of the CW mode. The system does still break time-reversal symmetry because of the dissipation in the couplings, but as discussed above, this is a "trivial" time-reversal symmetry breaking.

What distinguishes our time-multiplexed system from the case of two spatially coupled resonators is that the modulators in our network are time-modulated. Because the modulators are driven by external signals, when we time-reverse the system, the system exhibits non-reciprocal behavior. However, if we remove this external drive, then the system becomes time-reversal symmetric. This can be seen directly from the system considered in Fig. 3.14: if one turns off the modulators so that the delay lines exhibit constant phases, then the system respects time-reversal symmetry. Note that this idea of using external modulation to break time-reversal symmetry is one way to construct a photonic isolator (Doerr, Dupuis, and L. Zhang, 2011).

3.7 Ring-Down Measurement of the SSH Edge State

In the main text, we presented so-called steady-state measurements of the SSH and HH edge states. To perform these measurements, we repeatedly excited an edge state of the model under study and observed the steady-state behavior of the network. The degree of localization in the edge state once the system reached steady state allowed us to distinguish between the topologically trivial and nontrivial phases of the network. An alternative way to probe topological edge states in our network is to perform "ring-down" measurements, in which we excite a topological edge state in our network and then observe the dynamics of the state as it decays in the network. As in the steady-state experiments, we expect that the topological edge state will remain localized in the excited edge state if the network is in the topological phase and that it will not if the network is in the trivial phase. In this section, we present ring-down measurements of the SSH edge state.

To perform the ring-down measurements in our network, we first prepare the couplings to be in either the topological or trivial phases with $w/v = 2$. We then excite the network with one of the theoretically expected edge states from the topological phase. We excite the network for 5 roundtrips to build up power in the network, and then we observe the decay of the excitation over another 15 roundtrips. The results of our measurement are shown in Fig. 3.15.

In Fig. 3.15(a), we plot the ring-down of the network in the topological phase as well as the final roundtrip on which we excite the network, which we label the 0th roundtrip. In Fig. 3.15(c), we plot the state of the network on the 10th roundtrip. We observe that the state of the network remains well localized in the excited topological edge state, which confirms that our network is in a topological phase. The small discrepancies between the theoretical edge state and the observed state are likely due to both inaccuracies in our network's couplings and nonlinear gain dynamics, which we will discuss shortly.

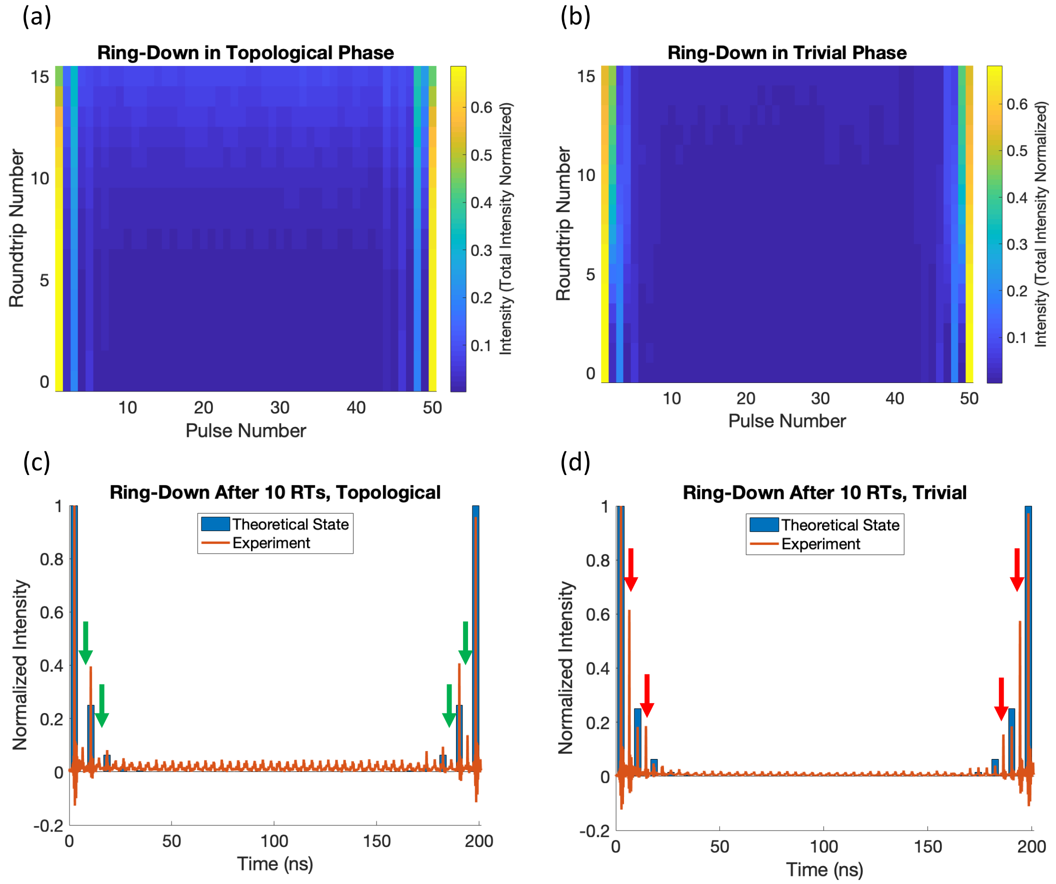

Figure 3.15: Ring-down measurements of the SSH edge state

Ring-down measurements of the SSH edge state. (a) Ring-down measurement in the topological phase. Each cell of the plot represents the peak power of the pulse at that location and roundtrip. To show how the power spreads between the pulses of the network, the vector comprised of the plotted peak powers is normalized on each roundtrip. (b) Ring-down measurements in the trivial phase. (c) Time trace of the network state on the 10th roundtrip in the topological phase. The state of the network closely resembles the theoretical topological edge state, which indicates that the network is in the topological phase. (d) Time trace of the network state on the 10th roundtrip in the trivial phase. As expected, the state no longer resembles the theoretical topological edge state of the SSH model.

Similarly, in Fig. 3.15(b), we plot the ring-down of the network in the trivial phase. Now, by the 10th roundtrip, the state of the network deviates substantially from the excited topological edge state. In particular, rather than seeing light predominantly in alternate sites of our synthetic lattice, we see that the sites adjacent to the edges exhibit the second-highest occupation in the lattice. This provides strong evidence that the network is now in the trivial phase.

When we observe the network for more roundtrips in either the trivial or the topological phases, we find that gain fluctuations in the network degrade the visibility of the edge state excitation. In order to observe $\gtrsim 5$ roundtrips in our network, it is necessary for us to operate our network very close to threshold. This introduces some nonlinear gain dynamics in the system, which amplifies spurious pulses in the system after ~ 8 roundtrips. This effect is already noticeable in Fig. 3.15(c). Because the extinction ratio of the modulators at the input to the main cavity is imperfect, some light leaks into the cavity. When we operate very close to threshold, the EDFA in the main cavity can amplify these spurious pulses, causing the very slight bulk occupation visible in the figure. Moreover, the emergence of these spurious pulses in the bulk coincides with the incipient degradation of the excited edge state, which indicates that the discrepancies between the observed state in Fig. 3.15(c) and the theoretical edge state could be, in part, due to nonlinear gain dynamics. On successive roundtrips, the growth of these spurious pulses overwhelms the edge state excitation, and the topological edge state is no longer visible. However, before these nonlinear gain dynamics dominate the system, the system decays exponentially and remains localized in the initially excited edge state, as we would expect in the linear case. This suggests that the linear dynamics govern the initial dynamics of the system.

The degree to which the state of the network deviates from the edge state excitation in the trivial case is limited primarily by the gain and loss in the network. As mentioned above, near threshold, nonlinear gain dynamics prevents us from observing the dynamics of the excitation for more roundtrips than what is shown in Fig. 3.15. Farther below threshold, loss limits the number of roundtrips we can observe because the system quickly drops below the noise floor of our detector. The difficulty of observing more roundtrips limits the degree to which we observe the edge state spreading into the bulk. In Fig. 3.16, we simulate our ring-down experiments over 100 roundtrips. In these simulations we observe substantially more penetration into the bulk in the trivial phase.

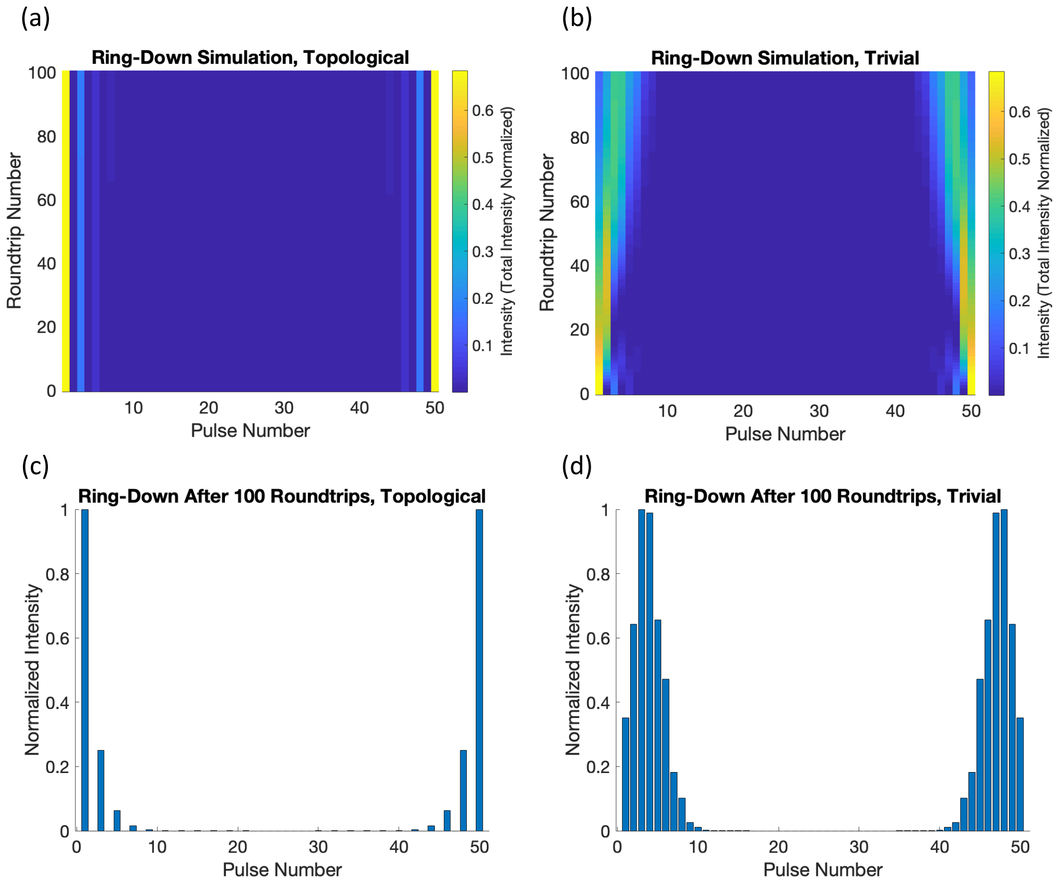

Figure 3.16: Simulation of the SSH ring-down experiment

Simulation of the SSH ring-down experiment. (a) Simulation of the ring-down experiment over 100 roundtrips in the topological phase. (b) Comparable simulation in the trivial phase. (c) State of the topological network on the 100th roundtrip. (d) State of the trivial network on the 100th roundtrip. Note that the normalizations in this figure are the same as those in Fig. 3.15.

Note that the simulations in Fig. 3.16 are performed by simulating the discrete time version of Eq. 3.12,

$$\mathbf{a}_{n+1} = (K - \gamma)\, \mathbf{a}_n, \tag{3.54}$$

where K implements of the couplings of the model under study (here the SSH model) and $\mathbf{a}_0$ is chosen to be a topological edge state of the model. Each iteration of the difference equation in Eq. 3.54 models the roundtrip dynamics of our time-multiplexed network. For the simulations in Fig. 3.16 we must specify three parameters, which are the SSH coupling strengths w and v and the roundtrip loss γ. For the simulations in Fig. 3.16 we use $w = 0.1$, $v = 0.05$, and $\gamma = 0.25$.

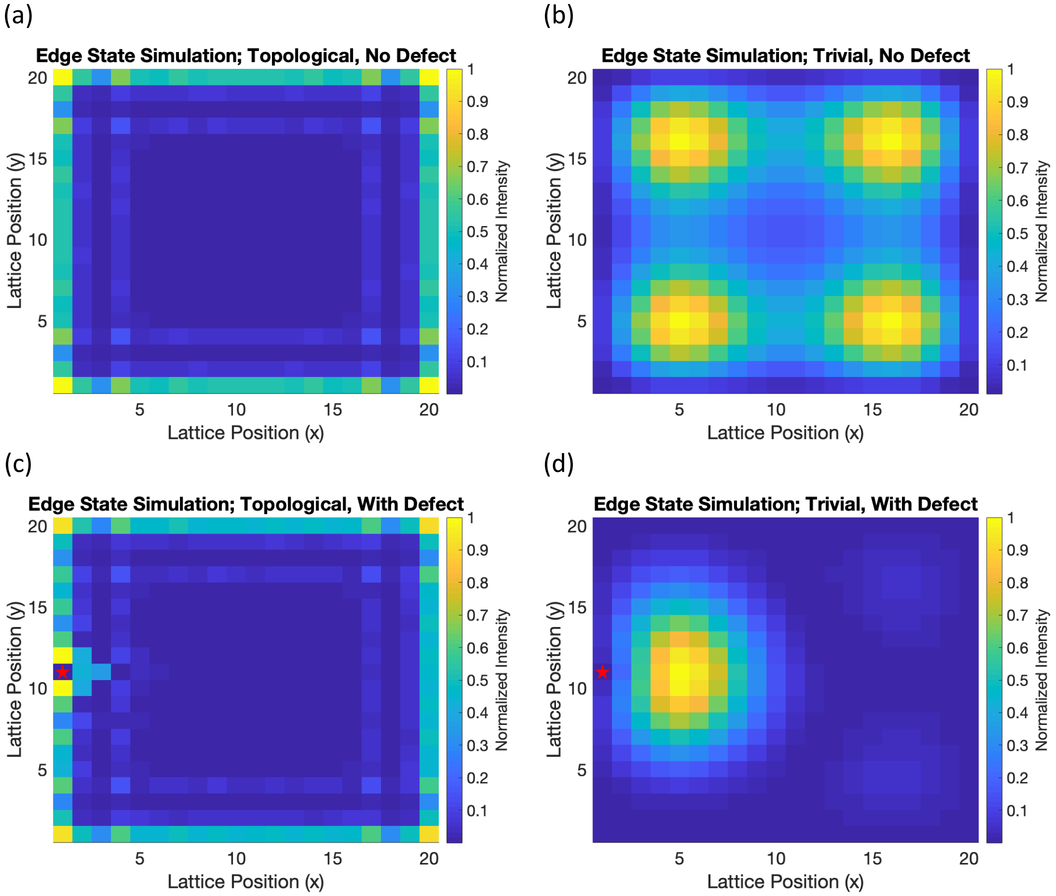

Figure 3.17: Simulations of a HH ring-down experiment

Simulations of a HH ring-down experiment. Each simulation shows the evolution of an edge-state excitation after 100 roundtrips in a dissipatively coupled HH synthetic lattice. (a) Simulation in a topological lattice with no defect. (b) Simulation in a trivial lattice with no defect. (c) Simulation in a topological lattice with a defect. (d) Simulation in a trivial lattice with a defect. Note that the location of the defect is indicated in (c,d) by a small red star on the left edge.

3.8 Simulations of Topological Robustness in a HH Lattice with Purely Dissipative Couplings

In Fig. 2.6, we presented simulations of topological edge states in a 4×10 HH lattice with and without a defect introduced on the corner of the lattice. Here we discuss how topological robustness manifests in dissipatively coupled HH lattices and discuss the details of the simulations presented in the main text. We also provide additional simulations that show the topological robustness of the HH edge state in a 20×20 dissipatively coupled HH lattice.

In a system with purely dissipative couplings, we cannot observe topological protection in the same manner as in conservatively coupled systems (Hafezi et al., 2013). In conservatively coupled HH lattices, one may observe robustness by removing a site on the edge of the lattice to introduce a defect. One may then excite the system with a frequency in the system's bandgap and observe that the excitation propagates around the defect without backscattering. However, as discussed in Sec. 3.3, in systems with purely dissipative couplings, there is no topological transport, and therefore we would not expect to see propagation around an edge defect in our system.

With that said, in the presence of a defect, the topology of our dissipatively coupled system still guarantees the existence of topological edge states in the presence of a defect or in the presence of any disorder that does not close the dissipative topological bandgap. This is a direct consequence of the bulk-boundary correspondence (Hatsugai, 1993): the difference in topological invariants between the lattice and the surrounding vacuum guarantees the existence of localized states at the boundary, regardless of the boundary's shape. The dynamics of these states, whether conservative or dissipative, does not influence the *existence* of the edge states.

Because the HH edge states are guaranteed to exist in the presence of defects or disorder, we can imagine probing the HH edge states that emerge in these disordered lattices using the same experimental procedures discussed in this text. Here and in the main text, we show simulations of ring-down experiments similar to those discussed in Sec. 3.7. In our simulations we excite our network with the HH edge state that exists either in the presence of a defect or in the absence of a defect. With a synthetic magnetic field either on or off, we let the edge state excitation evolve for 100 roundtrips and record the final state of the network.

The results of ring down simulations for a 20×20 HH lattice are shown in Fig. 3.17.

The final state in each plot is normalized by dividing the final state by the maximum intensity. Note that the simulations in the main text are normalized in the same manner. In Fig. 3.17(a), we show the final state for the HH lattice with a synthetic magnetic field of $\alpha = 1/3$. As expected, the final state observed in this figure is indistinguishable from the edge state excitation. When we turn off the synthetic magnetic field ($\alpha = 0$), the edge state excitation no longer remains localized at the edge. After 100 roundtrips, the initial excitation "diffuses" entirely into the bulk of the lattice, which correctly indicates that the system is in a trivial phase.

In Fig. 3.17(c), we introduce a defect in the left edge of the dissipatively coupled lattice. In the figure, the location of the defect is marked by a small red star on the left edge. As guaranteed by the bulk-boundary correspondence, topological edge states appear at the boundary of the new lattice. When we excite one of these edge states in the presence of a synthetic magnetic field ($\alpha = 1/3$), the system remains in the excited edge state, and the final state in Fig. 3.17(c) is indistinguishable from the excitation. Finally, when we turn off the synthetic magnetic field in the presence of the defect, we again observe that the edge state excitation no longer remains localized at the edge of the lattice, as the system is now in a trivial phase.

Note that for the simulations performed in Fig. 3.17 and in Fig. 6 of the main text, we again simulate Eq. 3.54, but now we choose K to implement the HH model. For these simulations we must specify the coupling strength of the HH model J, the strength of the effective magnetic field α, and the roundtrip loss in the network γ. For the simulations here and in the main text we choose $J = 0.2$ and $\gamma = J$. We switch α between $1/3$ and 0 depending on whether the lattice is topological or trivial.

References

Asadchy, Viktar S. et al. (Oct. 2020). "Tutorial on Electromagnetic Nonreciprocity and its Origins". In: *Proceedings of the IEEE* 108.10. Conference Name: Proceedings of the IEEE, pp. 1684–1727. ISSN: 1558-2256. DOI: `10.1109/JPROC.2020.3012381`.

Asbóth, János K., László Oroszlány, and András Pályi (2016). *A Short Course on Topological Insulators*. Vol. 919. Lecture Notes in Physics. Cham: Springer International Publishing. ISBN: 978-3-319-25607-8. DOI: `10.1007/978-3-319-25607-8`. URL: `http://link.springer.com/10.1007/978-3-319-25607-8` (visited on 02/03/2023).

Aster, Richard C., Brian Borchers, and Clifford H. Thurber (Jan. 2019). “Chapter Twelve - Epilogue”. en. In: *Parameter Estimation and Inverse Problems (Third Edition)*. Ed. by Richard C. Aster, Brian Borchers, and Clifford H. Thurber. Elsevier, pp. 307–308. ISBN: 978-0-12-804651-7. DOI: `10.1016/B978-0-12-804651-7.00017-1`. URL: `https://www.sciencedirect.com/science/article/pii/B9780128046517000171` (visited on 03/15/2023).

Bardyn, C.-E. et al. (Aug. 2013). “Topology by dissipation”. en. In: *New J. Phys.* 15.8. Publisher: IOP Publishing, p. 085001. ISSN: 1367-2630. DOI: `10.1088/1367-2630/15/8/085001`. URL: `https://dx.doi.org/10.1088/1367-2630/15/8/085001` (visited on 07/23/2023).

Barreiro, Julio T. et al. (Feb. 2011). “An open-system quantum simulator with trapped ions”. en. In: *Nature* 470.7335. Number: 7335 Publisher: Nature Publishing Group, pp. 486–491. ISSN: 1476-4687. DOI: `10.1038/nature09801`. URL: `https://www.nature.com/articles/nature09801` (visited on 07/23/2023).

Bell, Bryn A. et al. (Nov. 2017). “Spectral photonic lattices with complex long-range coupling”. EN. In: *Optica, OPTICA* 4.11. Publisher: Optica Publishing Group, pp. 1433–1436. ISSN: 2334-2536. DOI: `10.1364/OPTICA.4.001433`. URL: `https://opg.optica.org/optica/abstract.cfm?uri=optica-4-11-1433` (visited on 07/23/2023).

Black, Eric D. (Jan. 2001). “An introduction to Pound–Drever–Hall laser frequency stabilization”. In: *Am. J. Phys.* 69.1. Publisher: American Association of Physics Teachers, pp. 79–87. ISSN: 0002-9505. DOI: `10.1119/1.1286663`. URL: `https://aapt.scitation.org/doi/10.1119/1.1286663` (visited on 04/08/2022).

Chalabi, Hamidreza et al. (Oct. 2019). “Synthetic Gauge Field for Two-Dimensional Time-Multiplexed Quantum Random Walks”. en. In: *Phys. Rev. Lett.* 123.15, p. 150503. ISSN: 0031-9007, 1079-7114. DOI: `10.1103/PhysRevLett.123.150503`. URL: `https://link.aps.org/doi/10.1103/PhysRevLett.123.150503` (visited on 01/05/2023).

Chen, Chao et al. (Sept. 2018). “Observation of Topologically Protected Edge States in a Photonic Two-Dimensional Quantum Walk”. In: *Phys. Rev. Lett.* 121.10. Publisher: American Physical Society, p. 100502. DOI: `10.1103/PhysRevLett.121.100502`. URL: `https://link.aps.org/doi/10.1103/PhysRevLett.121.100502` (visited on 07/23/2023).

Cooper, N. R., J. Dalibard, and I. B. Spielman (Mar. 2019). “Topological bands for ultracold atoms”. In: *Rev. Mod. Phys.* 91.1. Publisher: American Physical Society, p. 015005. DOI: `10.1103/RevModPhys.91.015005`. URL: `https://link.aps.org/doi/10.1103/RevModPhys.91.015005` (visited on 01/31/2022).

Dasbiswas, Kinjal, Kranthi K. Mandadapu, and Suriyanarayanan Vaikuntanathan (Sept. 2018). “Topological localization in out-of-equilibrium dissipative systems”. In: *Proceedings of the National Academy of Sciences* 115.39. Publisher: Proceedings of the National Academy of Sciences, E9031–E9040. DOI: `10.1073/pnas.1721096115`. URL: `https://www.pnas.org/doi/10.1073/pnas.1721096115` (visited on 07/23/2023).

Diehl, Sebastian et al. (Dec. 2011). “Topology by dissipation in atomic quantum wires”. en. In: *Nature Phys* 7.12. Number: 12 Publisher: Nature Publishing Group, pp. 971–977. ISSN: 1745-2481. DOI: `10.1038/nphys2106`. URL: `https://www.nature.com/articles/nphys2106` (visited on 07/23/2023).

Ding, Jiajie et al. (Nov. 2019). “Dispersive versus Dissipative Coupling for Frequency Synchronization in Lasers”. In: *Phys. Rev. Applied* 12.5. Publisher: American Physical Society, p. 054039. DOI: `10.1103/PhysRevApplied.12.054039`. URL: `https://link.aps.org/doi/10.1103/PhysRevApplied.12.054039` (visited on 01/05/2022).

Doerr, Christopher R., Nicolas Dupuis, and Liming Zhang (Nov. 2011). “Optical isolator using two tandem phase modulators”. EN. In: *Opt. Lett., OL* 36.21. Publisher: Optica Publishing Group, pp. 4293–4295. ISSN: 1539-4794. DOI: `10.1364/OL.36.004293`. URL: `https://opg.optica.org/ol/abstract.cfm?uri=ol-36-21-4293` (visited on 08/09/2023).

Dutt, Avik et al. (Jan. 2020). “A single photonic cavity with two independent physical synthetic dimensions”. In: *Science* 367.6473. Publisher: American Association for the Advancement of Science, pp. 59–64. DOI: `10.1126/science.aaz3071`. URL: `https://www.science.org/doi/10.1126/science.aaz3071` (visited on 07/02/2023).

Fang, Kejie and Shanhui Fan (Nov. 2013). “Controlling the Flow of Light Using the Inhomogeneous Effective Gauge Field that Emerges from Dynamic Modulation”. en. In: *Phys. Rev. Lett.* 111.20, p. 203901. ISSN: 0031-9007, 1079-7114. DOI: `10.1103/PhysRevLett.111.203901`. URL: `https://link.aps.org/doi/10.1103/PhysRevLett.111.203901` (visited on 07/23/2023).

Fang, Kejie, Jie Luo, et al. (May 2017). “Generalized non-reciprocity in an optomechanical circuit via synthetic magnetism and reservoir engineering”. en. In: *Nature Phys* 13.5. Number: 5 Publisher: Nature Publishing Group, pp. 465–471. ISSN: 1745-2481. DOI: `10.1038/nphys4009`. URL: `https://www.nature.com/articles/nphys4009` (visited on 07/23/2023).

Gneiting, Clemens et al. (Apr. 2022). “Unraveling the topology of dissipative quantum systems”. In: *Phys. Rev. Res.* 4.2. Publisher: American Physical Society, p. 023036. DOI: `10.1103/PhysRevResearch.4.023036`. URL: `https://link.aps.org/doi/10.1103/PhysRevResearch.4.023036` (visited on 07/23/2023).

Hafezi, M. et al. (Dec. 2013). “Imaging topological edge states in silicon photonics”. en. In: *Nature Photon* 7.12. Number: 12 Publisher: Nature Publishing Group, pp. 1001–1005. ISSN: 1749-4893. DOI: `10.1038/nphoton.2013.274`. URL: `https://www.nature.com/articles/nphoton.2013.274` (visited on 09/09/2022).

Harper, P. G. (Oct. 1955). “The General Motion of Conduction Electrons in a Uniform Magnetic Field, with Application to the Diamagnetism of Metals”. en. In: *Proc. Phys. Soc. A* 68.10, p. 879. ISSN: 0370-1298. DOI: `10.1088/0370-1298/68/10/305`. URL: `https://dx.doi.org/10.1088/0370-1298/68/10/305` (visited on 07/23/2023).

Hasan, M. Z. and C. L. Kane (Nov. 2010). “Colloquium: Topological insulators”. In: *Rev. Mod. Phys.* 82.4. Publisher: American Physical Society, pp. 3045–3067. DOI: `10.1103/RevModPhys.82.3045`. URL: `https://link.aps.org/doi/10.1103/RevModPhys.82.3045` (visited on 01/05/2022).

Hatsugai, Yasuhiro (Nov. 1993). “Chern number and edge states in the integer quantum Hall effect”. In: *Phys. Rev. Lett.* 71.22. Publisher: American Physical Society, pp. 3697–3700. DOI: `10.1103/PhysRevLett.71.3697`. URL: `https://link.aps.org/doi/10.1103/PhysRevLett.71.3697` (visited on 01/05/2022).

Haus, H.A. (Nov. 2000). “Mode-locking of lasers”. In: *IEEE J. Sel. Top. Quantum Electron.* 6.6. Conference Name: IEEE Journal of Selected Topics in Quantum Electronics, pp. 1173–1185. ISSN: 1558-4542. DOI: `10.1109/2944.902165`.

Helbig, T. et al. (July 2020). “Generalized bulk–boundary correspondence in non-Hermitian topolectrical circuits”. en. In: *Nat. Phys.* 16.7. Bandiera_abtest: a Cg_type: Nature Research Journals Number: 7 Primary_atype: Research Publisher: Nature Publishing Group Subject_term: Electronic and spintronic devices;Topological matter Subject_term_id: electronic-and-spintronic-devices;topological-matter, pp. 747–750. ISSN: 1745-2481. DOI: `10.1038/s41567-020-0922-9`. URL: `https://www.nature.com/articles/s41567-020-0922-9` (visited on 01/05/2022).

Hofstadter, Douglas R. (Sept. 1976). “Energy levels and wave functions of Bloch electrons in rational and irrational magnetic fields”. In: *Phys. Rev. B* 14.6. Publisher: American Physical Society, pp. 2239–2249. DOI: `10.1103/PhysRevB.14.2239`. URL: `https://link.aps.org/doi/10.1103/PhysRevB.14.2239` (visited on 03/24/2023).

Inagaki, Takahiro et al. (Nov. 2016). “A coherent Ising machine for 2000-node optimization problems”. In: *Science* 354.6312. Publisher: American Association for the Advancement of Science, pp. 603–606. DOI: `10.1126/science.aah4243`. URL: `https://www.science.org/doi/10.1126/science.aah4243` (visited on 07/23/2023).

Jackiw, R. and C. Rebbi (June 1976). “Solitons with fermion number 1/2”. In: *Phys. Rev. D* 13.12. Publisher: American Physical Society, pp. 3398–3409. DOI: `10.1103/PhysRevD.13.3398`. URL: `https://link.aps.org/doi/10.1103/PhysRevD.13.3398` (visited on 07/23/2023).

Li, Mengyao et al. (July 2019). “Topological phases and nonreciprocal edge states in non-Hermitian Floquet insulators”. In: *Phys. Rev. B* 100.4. Publisher: American Physical Society, p. 045423. DOI: `10.1103/PhysRevB.100.045423`. URL: `https://link.aps.org/doi/10.1103/PhysRevB.100.045423` (visited on 07/23/2023).

Lohse, Michael et al. (Jan. 2018). “Exploring 4D quantum Hall physics with a 2D topological charge pump”. en. In: *Nature* 553.7686. Number: 7686 Publisher: Nature Publishing Group, pp. 55–58. ISSN: 1476-4687. DOI: `10.1038/nature25000`. URL: `https://www.nature.com/articles/nature25000` (visited on 07/23/2023).

Lustig, Eran et al. (Mar. 2019). “Photonic topological insulator in synthetic dimensions”. en. In: *Nature* 567.7748. Number: 7748 Publisher: Nature Publishing Group, pp. 356–360. ISSN: 1476-4687. DOI: `10.1038/s41586-019-0943-7`. URL: `https://www.nature.com/articles/s41586-019-0943-7` (visited on 07/23/2023).

Maczewsky, Lukas J. et al. (Nov. 2020). “Nonlinearity-induced photonic topological insulator”. EN. In: *Science*. Publisher: American Association for the Advancement of Science. DOI: `10.1126/science.abd2033`. URL: `https://www.science.org/doi/abs/10.1126/science.abd2033` (visited on 01/05/2022).

Maleki, L. et al. (Mar. 2004). “Tunable delay line with interacting whispering-gallery-mode resonators”. en. In: *Opt. Lett.* 29.6, p. 626. ISSN: 0146-9592, 1539-4794. DOI: `10.1364/OL.29.000626`. URL: `https://opg.optica.org/abstract.cfm?URI=ol-29-6-626` (visited on 07/17/2022).

Malkova, Natalia et al. (June 2009). “Observation of optical Shockley-like surface states in photonic superlattices”. EN. In: *Opt. Lett., OL* 34.11. Publisher: Optica Publishing Group, pp. 1633–1635. ISSN: 1539-4794. DOI: `10.1364/OL.34.001633`. URL: `https://opg.optica.org/ol/abstract.cfm?uri=ol-34-11-1633` (visited on 07/23/2023).

Mancinelli, M. et al. (June 2011). “Coupled-resonator-induced-transparency concept for wavelength routing applications”. EN. In: *Opt. Express, OE* 19.13. Publisher: Optica Publishing Group, pp. 12227–12240. ISSN: 1094-4087. DOI: `10.1364/OE.19.012227`. URL: `https://opg.optica.org/oe/abstract.cfm?uri=oe-19-13-12227` (visited on 08/09/2023).

Marandi, Alireza et al. (Dec. 2014). “Network of time-multiplexed optical parametric oscillators as a coherent Ising machine”. en. In: *Nat. Photon.* 8.12. Bandiera_abtest: a Cg_type: Nature Research Journals Number: 12 Primary_atype: Research Publisher: Nature Publishing Group Subject_term: Nonlinear optics;Quantum optics;Ultrafast photonics Subject_term_id: nonlinear-optics;quantum-optics;ultrafast-photonics, pp. 937–942. ISSN: 1749-4893. DOI: `10.1038/nphoton.2014.249`. URL: `https://www.nature.com/articles/nphoton.2014.249` (visited on 01/05/2022).

Metelmann, A. and A. A. Clerk (June 2015). "Nonreciprocal Photon Transmission and Amplification via Reservoir Engineering". In: *Phys. Rev. X* 5.2. Publisher: American Physical Society, p. 021025. DOI: `10.1103/PhysRevX.5.021025`. URL: `https://link.aps.org/doi/10.1103/PhysRevX.5.021025` (visited on 07/23/2023).

Mukherjee, Sebabrata, Dmitri Mogilevtsev, et al. (Dec. 2017). "Dissipatively coupled waveguide networks for coherent diffusive photonics". en. In: *Nat Commun* 8.1. Bandiera_abtest: a Cc_license_type: cc_by Cg_type: Nature Research Journals Number: 1 Primary_atype: Research Publisher: Nature Publishing Group Subject_term: Integrated optics;Quantum simulation;Theoretical physics Subject_term_id: integrated-optics;quantum-simulation;theoretical-physics, p. 1909. ISSN: 2041-1723. DOI: `10.1038/s41467-017-02048-4`. URL: `https://www.nature.com/articles/s41467-017-02048-4` (visited on 01/05/2022).

Mukherjee, Sebabrata and Mikael C. Rechtsman (May 2020). "Observation of Floquet solitons in a topological bandgap". In: *Science* 368.6493. Publisher: American Association for the Advancement of Science, pp. 856–859. DOI: `10.1126/science.aba8725`. URL: `https://www.science.org/doi/10.1126/science.aba8725` (visited on 07/25/2023).

Ozawa, Tomoki and Hannah M. Price (May 2019). "Topological quantum matter in synthetic dimensions". en. In: *Nat Rev Phys* 1.5. Bandiera_abtest: a Cg_type: Nature Research Journals Number: 5 Primary_atype: Reviews Publisher: Nature Publishing Group Subject_term: Quantum optics;Topological matter;Ultracold gases Subject_term_id: quantum-optics;topological-matter;ultracold-gases, pp. 349–357. ISSN: 2522-5820. DOI: `10.1038/s42254-019-0045-3`. URL: `https://www.nature.com/articles/s42254-019-0045-3` (visited on 01/05/2022).

Ozawa, Tomoki, Hannah M. Price, et al. (Mar. 2019). "Topological photonics". In: *Rev. Mod. Phys.* 91.1. Publisher: American Physical Society, p. 015006. DOI: `10.1103/RevModPhys.91.015006`. URL: `https://link.aps.org/doi/10.1103/RevModPhys.91.015006` (visited on 12/30/2021).

Parto, Midya et al. (Jan. 2021). "Non-Hermitian and topological photonics: optics at an exceptional point". en. In: *Nanophotonics* 10.1. Publisher: De Gruyter, pp. 403–423. ISSN: 2192-8614. DOI: `10.1515/nanoph-2020-0434`. URL: `https://www.degruyter.com/document/doi/10.1515/nanoph-2020-0434/html` (visited on 01/05/2022).

Peng, Bo et al. (Oct. 2014). "What is and what is not electromagnetically induced transparency in whispering-gallery microcavities". en. In: *Nat Commun* 5.1. Number: 1 Publisher: Nature Publishing Group, p. 5082. ISSN: 2041-1723.

DOI: 10.1038/ncomms6082. URL: https://www.nature.com/articles/ncomms6082 (visited on 07/17/2022).

Petrides, Ioannis, Hannah M. Price, and Oded Zilberberg (Sept. 2018). “Six-dimensional quantum Hall effect and three-dimensional topological pumps”. In: *Phys. Rev. B* 98.12. Publisher: American Physical Society, p. 125431. DOI: 10.1103/PhysRevB.98.125431. URL: https://link.aps.org/doi/10.1103/PhysRevB.98.125431 (visited on 07/23/2023).

Rechtsman, Mikael C. et al. (Apr. 2013). “Photonic Floquet topological insulators”. en. In: *Nature* 496.7444. Bandiera_abtest: a Cg_type: Nature Research Journals Number: 7444 Primary_atype: Research Publisher: Nature Publishing Group Subject_term: Micro-optics;Topological matter Subject_term_id: micro-optics;topological-matter, pp. 196–200. ISSN: 1476-4687. DOI: 10.1038/nature12066. URL: https://www.nature.com/articles/nature12066 (visited on 01/05/2022).

Smirnova, Daria et al. (June 2020). “Nonlinear topological photonics”. In: *Appl. Phys. Rev.* 7.2. Publisher: American Institute of Physics, p. 021306. DOI: 10.1063/1.5142397. URL: https://aip.scitation.org/doi/10.1063/1.5142397 (visited on 01/05/2022).

Smith, David D. et al. (June 2004). “Coupled-resonator-induced transparency”. In: *Phys. Rev. A* 69.6. Publisher: American Physical Society, p. 063804. DOI: 10.1103/PhysRevA.69.063804. URL: https://link.aps.org/doi/10.1103/PhysRevA.69.063804 (visited on 08/09/2023).

Su, W. P., J. R. Schrieffer, and A. J. Heeger (June 1979). “Solitons in Polyacetylene”. In: *Phys. Rev. Lett.* 42.25. Publisher: American Physical Society, pp. 1698–1701. DOI: 10.1103/PhysRevLett.42.1698. URL: https://link.aps.org/doi/10.1103/PhysRevLett.42.1698 (visited on 01/06/2022).

Verstraete, Frank, Michael M. Wolf, and J. Ignacio Cirac (Sept. 2009). “Quantum computation and quantum-state engineering driven by dissipation”. en. In: *Nature Phys* 5.9. Number: 9 Publisher: Nature Publishing Group, pp. 633–636. ISSN: 1745-2481. DOI: 10.1038/nphys1342. URL: https://www.nature.com/articles/nphys1342 (visited on 07/23/2023).

Wang, Kai, Bryn A. Bell, et al. (July 2020). “Multidimensional synthetic chiral-tube lattices via nonlinear frequency conversion”. en. In: *Light Sci Appl* 9.1. Number: 1 Publisher: Nature Publishing Group, p. 132. ISSN: 2047-7538. DOI: 10.1038/s41377-020-0299-7. URL: https://www.nature.com/articles/s41377-020-0299-7 (visited on 07/23/2023).

Wang, Kai, Avik Dutt, et al. (Mar. 2021). “Generating arbitrary topological windings of a non-Hermitian band”. In: *Science* 371.6535. Publisher: American Association for the Advancement of Science, pp. 1240–1245. DOI: 10.1126/science.abf6568. URL: https://www.science.org/doi/10.1126/science.abf6568 (visited on 07/02/2023).

Wanjura, Clara C., Matteo Brunelli, and Andreas Nunnenkamp (June 2020). “Topological framework for directional amplification in driven-dissipative cavity arrays”. en. In: *Nat Commun* 11.1. Number: 1 Publisher: Nature Publishing Group, p. 3149. ISSN: 2041-1723. DOI: `10.1038/s41467-020-16863-9`. URL: `https://www.nature.com/articles/s41467-020-16863-9` (visited on 10/01/2022).

Weidemann, Sebastian et al. (Apr. 2020). “Topological funneling of light”. In: *Science* 368.6488. Publisher: American Association for the Advancement of Science, pp. 311–314. DOI: `10.1126/science.aaz8727`. URL: `https://www.science.org/doi/10.1126/science.aaz8727` (visited on 01/05/2023).

Weimann, S. et al. (Apr. 2017). “Topologically protected bound states in photonic parity–time-symmetric crystals”. en. In: *Nat. Mater.* 16.4, pp. 433–438. ISSN: 1476-1122, 1476-4660. DOI: `10.1038/nmat4811`. URL: `http://www.nature.com/articles/nmat4811` (visited on 06/01/2022).

Wimmer, Martin et al. (June 2017). “Experimental measurement of the Berry curvature from anomalous transport”. en. In: *Nature Phys* 13.6. Number: 6 Publisher: Nature Publishing Group, pp. 545–550. ISSN: 1745-2481. DOI: `10.1038/nphys4050`. URL: `https://www.nature.com/articles/nphys4050` (visited on 07/03/2023).

Wright, Logan G. et al. (May 2020). “Mechanisms of spatiotemporal mode-locking”. en. In: *Nat. Phys.* 16.5. Number: 5 Publisher: Nature Publishing Group, pp. 565–570. ISSN: 1745-2481. DOI: `10.1038/s41567-020-0784-1`. URL: `https://www.nature.com/articles/s41567-020-0784-1` (visited on 07/13/2022).

Xia, Shiqi et al. (Apr. 2021). “Nonlinear tuning of PT symmetry and non-Hermitian topological states”. en. In: *Science* 372.6537, pp. 72–76. ISSN: 0036-8075, 1095-9203. DOI: `10.1126/science.abf6873`. URL: `https://www.science.org/doi/10.1126/science.abf6873` (visited on 06/21/2023).

Xu, Qianfan et al. (Mar. 2006). “Experimental Realization of an On-Chip All-Optical Analogue to Electromagnetically Induced Transparency”. In: *Phys. Rev. Lett.* 96.12. Publisher: American Physical Society, p. 123901. DOI: `10.1103/PhysRevLett.96.123901`. URL: `https://link.aps.org/doi/10.1103/PhysRevLett.96.123901` (visited on 07/17/2022).

Yoshida, Tsuneya and Yasuhiro Hatsugai (Jan. 2021). “Bulk-edge correspondence of classical diffusion phenomena”. en. In: *Sci Rep* 11.1. Number: 1 Publisher: Nature Publishing Group, p. 888. ISSN: 2045-2322. DOI: `10.1038/s41598-020-80180-w`. URL: `https://www.nature.com/articles/s41598-020-80180-w` (visited on 07/23/2023).

Yuan, Luqi et al. (Nov. 2018). “Synthetic dimension in photonics”. EN. In: *Optica, OPTICA* 5.11. Publisher: Optical Society of America, pp. 1396–1405. ISSN: 2334-2536. DOI: `10.1364/OPTICA.5.001396`. URL: `https://www.`

`osapublishing.org/optica/abstract.cfm?uri=optica-5-11-1396` (visited on 01/06/2022).

Zeuner, Julia M. et al. (July 2015). “Observation of a Topological Transition in the Bulk of a Non-Hermitian System”. In: *Phys. Rev. Lett.* 115.4. Publisher: American Physical Society, p. 040402. DOI: `10.1103/PhysRevLett.115.040402`. URL: `https://link.aps.org/doi/10.1103/PhysRevLett.115.040402` (visited on 01/05/2022).

Zhang, Shou-Cheng and Jiangping Hu (Oct. 2001). “A Four-Dimensional Generalization of the Quantum Hall Effect”. In: *Science* 294.5543. Publisher: American Association for the Advancement of Science, pp. 823–828. DOI: `10.1126/science.294.5543.823`. URL: `https://www.science.org/doi/10.1126/science.294.5543.823` (visited on 07/23/2023).

Zhao, Han, Pei Miao, et al. (Mar. 2018). “Topological hybrid silicon microlasers”. en. In: *Nat Commun* 9.1. Number: 1 Publisher: Nature Publishing Group, p. 981. ISSN: 2041-1723. DOI: `10.1038/s41467-018-03434-2`. URL: `https://www.nature.com/articles/s41467-018-03434-2` (visited on 12/07/2022).

Zhao, Han, Xingdu Qiao, et al. (Sept. 2019). “Non-Hermitian topological light steering”. EN. In: *Science* 365.6458. Publisher: American Association for the Advancement of Science. DOI: `10.1126/science.aay1064`. URL: `https://www.science.org/doi/abs/10.1126/science.aay1064` (visited on 01/05/2022).

Zilberberg, Oded et al. (Jan. 2018). “Photonic topological boundary pumping as a probe of 4D quantum Hall physics”. en. In: *Nature* 553.7686. Number: 7686 Publisher: Nature Publishing Group, pp. 59–62. ISSN: 1476-4687. DOI: `10.1038/nature25011`. URL: `https://www.nature.com/articles/nature25011` (visited on 07/23/2023).

Chapter 4

TOPOLOGICAL TEMPORALLY MODE-LOCKED LASER

4.1 Abstract

Mode-locked lasers play a crucial role in modern science and technology. They are essential to the study of ultrafast and nonlinear optics, and they have important applications to metrology, telecommunications, and imaging. Recently, there has been substantial interest in studying topological phenomena in mode-locked lasers. From a fundamental perspective, this pursuit promises to reveal novel nonlinear topological physics, while, from a practical perspective, it may lead to the development of topologically protected short-pulse sources. Despite this promising outlook, the interplay between topological photonic lattices and laser mode-locking has not been studied experimentally. In this work, we theoretically propose and experimentally realize a topological temporally mode-locked laser. We proceed to demonstrate a nonlinearity driven non-Hermitian skin effect in our laser cavity and to observe the robustness of our laser against disorder-induced localization. Our experiments demonstrate fundamental point-gap topological physics that was previously inaccessible to photonics experiments, and they suggest potential applications of our mode-locked laser to sensing, optical computing, and robust topological frequency combs. The experimental architecture employed in this work also provides a template to study topology in other mode-locked photonic sources, including dissipative cavity solitons and synchronously pumped optical parametric oscillators.

4.2 Introduction

Over the past several years, nonlinear topological phenomena have gained prominence in the study of topological photonics (Smirnova et al., 2020). Experimental realizations, including nonlinear Thouless pumps (Jürgensen, Mukherjee, and Rechtsman, 2021) and topological lasers (Parto, Wittek, et al., 2018; Bandres et al., 2018; Contractor et al., 2022), have demonstrated that the combination of nonlinearity and topology engenders exotic topological dynamics and may enable the development of topologically robust photonic technologies. Motivated by this success, there have been substantial efforts to incorporate topology into highly nonlinear, mode-locked photonic sources (Longhi, 2019; Zhaoju Yang et al., 2020; Zykin, D. V. Skryabin, and Kartashov, 2021; Tusnin, A. M. Tikan, and T. J. Kippenberg, 2021; A. Tikan et al., 2022; Fan, Puzyrev, and Dmitry V. Skryabin, 2022), including mode-locked lasers and dissipative cavity solitons. Theoretical work in this direction suggests that topological mode-locking could give rise to both exciting nonlinear physics and new topological devices, such as fabrication tolerant mode-locked lasers (Zhaoju Yang et al., 2020) and topologically robust frequency combs (Mittal et al., 2021). However, despite this promising potential, to the best of our knowledge, topological photonic lattices have not been experimentally demonstrated in mode-locked lasers.

Theoretical proposals for topological mode-locking frequently focus on spectral mode-locking, where the amplitudes and phases of the spectral, or longitudinal, modes of a resonator are synchronized by a mode-locking mechanism (Haus, 2000; Tobias J. Kippenberg et al., 2018). Many of these proposals incorporate topological lattices either in the form of spatially coupled resonators (Tusnin, A. M. Tikan, and T. J. Kippenberg, 2021; A. Tikan et al., 2022; Mittal et al., 2021) or by using frequency synthetic dimensions (Longhi, 2019; Zhaoju Yang et al., 2020). However, proposals for topological mode-locking in spatially coupled resonator arrays require challenging fabrication processes, which may make them difficult to realize and to scale in size. Meanwhile, proposals for topological mode-locking in frequency synthetic dimensions encounter the challenges of realizing controllable boundary conditions Dutt et al., 2022 and inhomogeneous couplings Li et al., 2023, which could limit the topological physics accessible to these systems. Together, these difficulties motivate the search for an alternative approach to topological mode-locking.

In this work, we overcome the challenges of topological mode-locking in spatial and frequency lattices by theoretically proposing and experimentally demonstrating the topological temporally mode-locked laser. Unlike existing proposals, our topological mode-locked laser leverages the flexibility of temporal synthetic dimensions and relies on the principal of temporal mode-locking, where an additional mode-locking mechanism synchronizes the amplitudes and phases of the temporal modes [i.e., pulses] in a harmonically mode-locked laser. By engineering topological couplings between the temporal modes that make up our synthetic lattices, we endow our temporally mode-locked laser with nontrivial topology. Because temporal synthetic dimensions may be used to implement large lattice sizes, multidimensional lattices, inhomogeneous and long-range couplings, and tunable boundary conditions, our experimental approach provides a way to access a diversity of topological behaviors in our topological mode-locked system (Leefmans et al., 2022; Parto, Leefmans, et al., 2023).

Here, we leverage our topological temporally mode-locked laser to demonstrate topological mode-locked lasing in point-gap non-Hermitian topological lattices (Gong et al., 2018; Kawabata et al., 2019). We first identify a nonlinearity driven non-Hermitian skin effect (NHSE) (Yao and Z. Wang, 2018) that arises due to the nonlocal nonlinear dynamics of our mode-locked laser. Then, in a series of firsts for photonic systems, we tune the boundary conditions in our mode-locked laser to experimentally connect the existence of a point-gap topological winding number to the existence of the NHSE (Zhang, Zhesen Yang, and Fang, 2020), and we experimentally observe the robustness of the Hatano-Nelson model against disorder-induced localization (Hatano and Nelson, 1997; Hatano and Nelson, 1998). Our topological temporally mode-locked laser may enable the design of robust frequency combs, while our general, temporal mode-locking architecture may have applications to sensing and optical computing [see Sec 5.7 and Sec. 5.8].

4.3 Operating Principle and Experimental Setup

As we illustrate in Fig. 4.1(a), a topological temporally mode-locked laser consists of three basic elements, which are nonlocal gain saturation, a pulse formation mechanism [here, amplitude modulation], and intracavity temporal couplings. A conventional, harmonically mode-locked laser possesses the first two of these elements (Haus, 2000), which together give rise to N, evenly spaced temporal modes, or pulses, in a laser cavity. While the amplitudes of these pulses are uniform, their phases may drift relative to one another (Quinlan et al., 2009) [Fig. 4.1(b)]. The addition of intracavity couplings stabilizes the relative phases and amplitudes of the pulses, giving rise to what we refer to as temporal mode-locking [Fig. 4.1(c)]. While simple implementations of temporal mode-locking have been studied previously as a technique to suppress supermode noise in harmonically mode-locked lasers (Quinlan et al., 2009; Harvey and Mollenauer, 1993; Pottiez et al., 2002; Srinivasan et al., 2014), here we show that, by engineering our intracavity couplings to produce synthetic temporal topological lattices, temporal mode-locking may be used to realize complex, nonlinear topological phenomena [Fig. 4.1(c,d)].

At sufficiently low powers, where the Kerr nonlinearity may be neglected, the dynamics of our topological temporally mode-locked laser can qualitatively be described by a modified master equation for active mode-locking (Haus, 2000). This master equation may be approximated as a tight-binding model of the form,

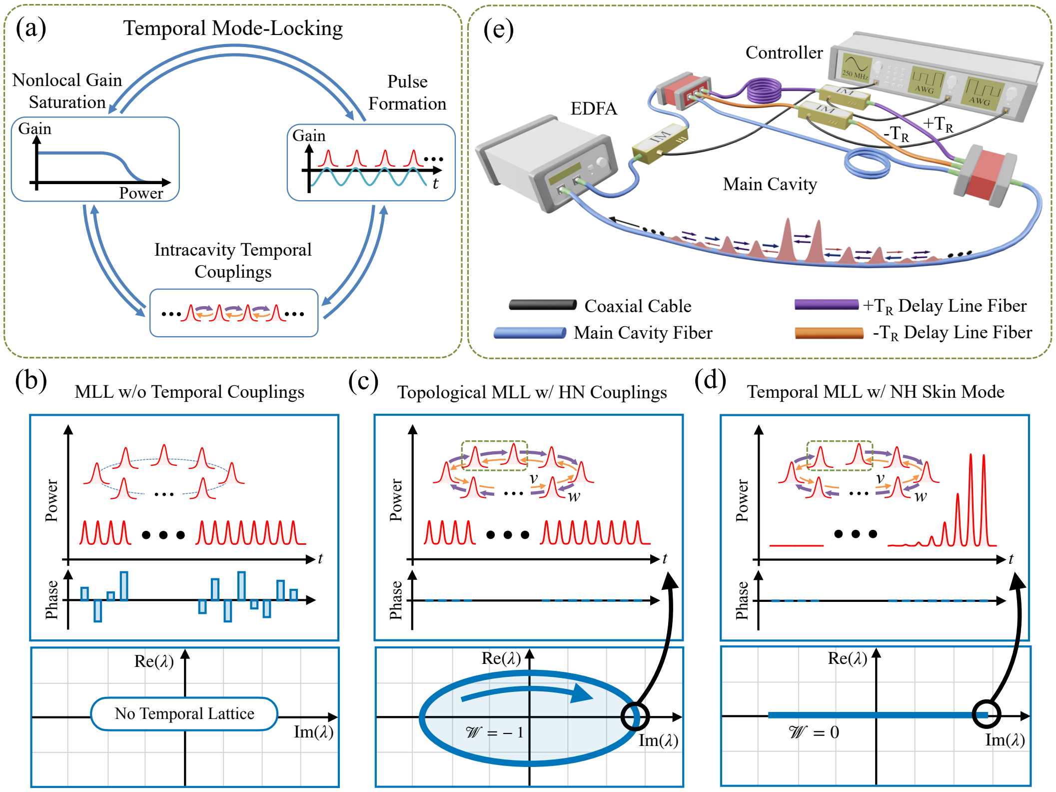

Figure 4.1: Topological Temporal Mode-Locking

Topological Temporal Mode-Locking. **(a)** The constituent elements of temporal mode-locking. **(b)** In a harmonically mode-locked laser without temporal mode-locking, the pulse-to-pulse phases may not be correlated. **(c)** Intracavity couplings can lock the pulse-to-pulse amplitudes and phases and produce synthetic temporal lattices with nontrivial topology. **(d)** Properly engineering the intracavity couplings can reveal non-Hermitian topological phenomena such as the nonlinearity driven NHSE studied in this work. Note that, due to the nature of dissipative couplings, $\mathrm{Im}(\lambda)$ appears on the abscissa while $\mathrm{Re}(\lambda)$ appears on the ordinateLeefmans et al., 2022 **(e)** Schematic of the proof-of-principal topological temporally mode-locked laser built for our experiments.

$$\frac{\partial a_n}{\partial T} = \left[K_n^{\mathrm{L}} a_{n-1} + K_n^{\mathrm{R}} a_{n+1}\right] + \left(g\left(T\right) - \Gamma\right) a_n \tag{4.1a}$$

$$\frac{\partial g}{\partial T} = -\gamma \left(g - g_0 + g\epsilon \sum_n \left|a_n\left(T\right)\right|^2\right). \tag{4.1b}$$

Here a_n is the amplitude of the nth pulse (or, the nth site of our synthetic lattice), $g(T)$ describes the nonlinear laser gain, g_0 is the small signal gain, Γ is the effective linear loss, $\gamma = T_{\mathrm{RT}}/\tau$ is the ratio of the roundtrip period to the gain relaxation time, ϵ is related to the saturation intensity, and $K_{\mathrm{n}}^{\mathrm{L}}$ and $K_{\mathrm{n}}^{\mathrm{R}}$ describe nearest-neighbor couplings between the pulses in the mode-locked laser.

From Eq. 4.1, we observe that the combined nonlinear dynamics of the intracavity couplings and the gain saturation nonlinearity produce temporal mode-locking. Crucially, we assume that the relaxation time of our gain medium is much slower than the roundtrip time of our laser cavity. As a result, the gain saturates only due to the average power in our topological temporally mode-locked laser. In this sense, the gain saturation constitutes a nonlocal nonlinearity that acts equally on all sites a_n in our temporal synthetic lattice. As we show in Sec. 5.4, the result of this nonlocal gain saturation is to drive the pulse amplitudes a_n towards the lowest-loss eigenstate defined by the couplings K_n^{L} and K_n^{R}.

While Eq. 4.1 qualitatively describes the dynamics of our topological temporally mode-locked laser at sufficiently low powers, where the Kerr nonlinearity may be neglected, at higher intracavity powers, the Kerr nonlinearity can introduce additional dynamics. We consider the effect of the Kerr nonlinearity in Sec. 5.5.

The fact that, at sufficiently low powers, the steady state of our topological temporally mode-locked laser tends towards the lowest-loss eigenstate defined by the intracavity couplings makes the topological temporally mode-locked laser well suited to study non-Hermitian point-gap topology. Unlike Hermitian topological lattices, point-gap topological lattices exhibit the NHSE, where all states, including the lowest-loss state, localize near a boundary in the system Yao and Z. Wang, 2018; Bergholtz, Budich, and Kunst, 2021. This enables our topological mode-locked laser to probe the existence of the NHSE in synthetic point-gap topological lattices.

To demonstrate the interplay between point-gap topology and topological temporal mode-locking, in Figs. 4.1(c,d) we schematically illustrate topological temporal mode-locking with a Hatano-Nelson lattice Hatano and Nelson, 1997; Hatano and

Nelson, 1998, which consists of a one-dimensional chain with asymmetric couplings and . In the presence of periodic boundary conditions, the Hatano-Nelson model exhibits a topologically nontrivial winding around a reference point in the complex energy plane Kawabata et al., 2019, which can be associated with a topological winding number . In this case, we expect the temporal structure in our laser to possess uniform amplitudes and phases because of the lattice's translational symmetry [Fig. 4.1(c)]. On the other hand, in the presence of open boundary conditions [Fig. 4.1(e)], the eigenvalues of the Hatano-Nelson model collapse onto a line, the lattice's topological winding number becomes trivial Gong et al., 2018, and the mode-locked temporal structure becomes strongly localized near the boundary. It is important to note that, although this NHSE occurs in the topologically trivial phase, it is a distinctly topological phenomenon, in the sense that it both guarantees and is guaranteed by the presence of a topological invariant in the bulk lattice Zhang, Zhesen Yang, and Fang, 2020.

To experimentally realize a topological temporally mode-locked laser, we construct the system presented in Fig. 4.1(e). This proof-of-principle temporally mode-locked laser consists of a fiber cavity ($T_{RT} = 256$ ns) and two optical delay lines, which are responsible for implementing nearest-neighbor dissipative couplings between the laser's temporal modes. A commercial erbium-doped fiber amplifier (EDFA) provides the system's nonlocal gain saturation ($T_{RT}/\tau \sim 10^{-5}$), while we sinusoidally modulate an intensity modulator in the main cavity to generate $N = 64$ mode-locked pulses with widths of ~ 100 ps and a repetition period of $T_R = 4$ ns. Additional intensity modulators in the optical delay lines control the coupling strengths between the pulses and enable us to dynamically tune both the lattice model under study as well as the boundary conditions of our synthetic lattice. Notably, because each delay line controls only one direction of the coupling between two pulses, it is straightforward to realize non-Hermitian topological lattice models in our system (Leefmans et al., 2022).

While we expect a temporally mode-locked laser to fix both the phases and amplitudes of the laser's pulses, our experimental capabilities only enable us to monitor the intensity distributions of the pulse patterns emitted by our laser. In this work, we will focus exclusively on models for which Eq. 4.1 predicts the pulse patterns produced by our laser to have uniform phases.

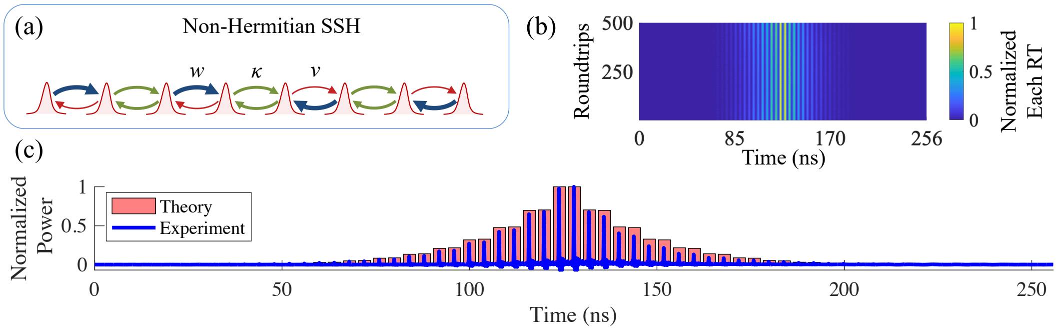

Figure 4.2: Nonlinearity Driven NHSE in a Topological Mode-Locked Laser

Nonlinearity Driven NHSE in a Topological Mode-Locked Laser. **(a)** Schematic representation of the NH-SSH domain wall implemented in our mode-locked laser's synthetic lattice. **(b)** Heat map of our mode-locked laser's output over 500 roundtrips. The pulses are broadened for visibility. **(c)** Mode-locked pulse pattern in our topological mode-locked laser. The data is averaged using the procedure described in Sec. 5.3. The theory is the steady state of Eq. 4.1.

4.4 Topological Mode-Locking at a Non-Hermitian Domain Wall

As a first demonstration of topological temporal mode-locking, we observe a nonlinearity driven NHSE in a non-Hermitian SSH (NH-SSH) lattice (Su, Schrieffer, and Heeger, 1979; Yin et al., 2018)[1]. We begin by tuning our EDFA gain to achieve a small signal gain of ~ 23.1 dB, which, in the presence of the NH-SSH domain wall, results in an output power of ~ 42 μW. At first, we operate our laser with homogeneous, nearest-neighbor couplings, so that our laser supports a train of 64 mode-locked pulses. We then switch the intracavity couplings in our mode-locked laser to implement the NH-SSH domain wall illustrated in Fig. 4.2(a). Shortly after, the pulse pattern in the laser forms a skin mode at the domain wall of the synthetic NH-SSH lattice [Fig. 4.2(a,b)]. While the exact pulse pattern fluctuates slightly due to instabilities in the laser, we find that the distribution of the pulse intensities exhibits excellent agreement with the lowest-loss eigenstate of the theoretical NH-SSH lattice, in accordance with Eq. 4.1.

While domain wall skin modes have been observed previously in linear, photonic lattices (Weidemann, Kremer, Helbig, et al., 2020; Xiao et al., 2020), the dynamics that drive skin mode formation in our topological mode-locked laser are unambiguously different. In linear photonics experiments, skin modes form due to random

---

[1] While the point-gap topological winding number of this lattice is trivial, the observed nonlinearity driven NHSE arises due to the nontrivial point-gap topology of the bulk NH-SSH lattice (Weidemann, Kremer, Helbig, et al., 2020).

walks on conservatively coupled lattices with asymmetric couplings. In stark contrast, skin modes in our laser form due to the combined nonlinear dynamics of our laser's nonlocal gain saturation and dissipative, intracavity couplings. Unlike in the linear regime, where an external excitation is required to see skin mode formation, the nonlinear dynamics of our system enable skin modes to form spontaneously within our system. Moreover, while the skin modes in linear systems inevitably decay due to intrinsic losses, the net gain in our system supports the skin modes as long as our laser is stable. Because of the radically different dynamics that govern the skin modes in our system, we refer to skin mode formation in our laser as a nonlinearity driven NHSE.

4.5 Tuning the Boundary Conditions of the Hatano-Nelson Model

We next investigate the sensitivity of the Hatano-Nelson model to its boundary conditions by dynamically tuning the boundary conditions of the temporal synthetic lattice in our topological mode-locked laser. As the occurrence of the NHSE both guarantees and is guaranteed by the existence of a nontrivial topological winding number Zhang, Zhesen Yang, and Fang, 2020, this experiment confirms the existence of a nontrivial topological winding number in our Hatano-Nelson lattice with periodic boundary conditions.

We first tune our EDFA to operate with a small signal gain of 22.2 dB, and we program our delay line couplings to implement the Hatano-Nelson model with $w/v = \sqrt{2}$ and periodic boundary conditions [Fig. 4.3(b)]. In this case, our laser emits a uniform pulse train, as we would expect from translation symmetry [Fig. 4.3(a)]. Next, we dynamically reduce the coupling at the boundary of the Hatano-Nelson lattice [Fig. 4.3(c)]. After a series of relaxation oscillations, the pulse pattern in the laser localizes near the new boundary [Fig. 4.3(d)]. While the finite extinction ratio of our delay line intensity modulators prevents us from achieving perfect open boundary conditions, the observed nascent skin mode presages the skin mode that emerges in the presence of perfect open boundary conditions. From this nascent skin mode, we conclude that the Hatano-Nelson lattice implemented with periodic boundary conditions in our topological temporally mode-locked laser possesses a nontrivial topological winding number.

The sensitivity of point-gap topological lattices to their boundary conditions is a key feature of systems like the Hatano-Nelson model. However, previous photonic architectures, whether in the spatial (Liu et al., 2022), frequency (K. Wang et al.,

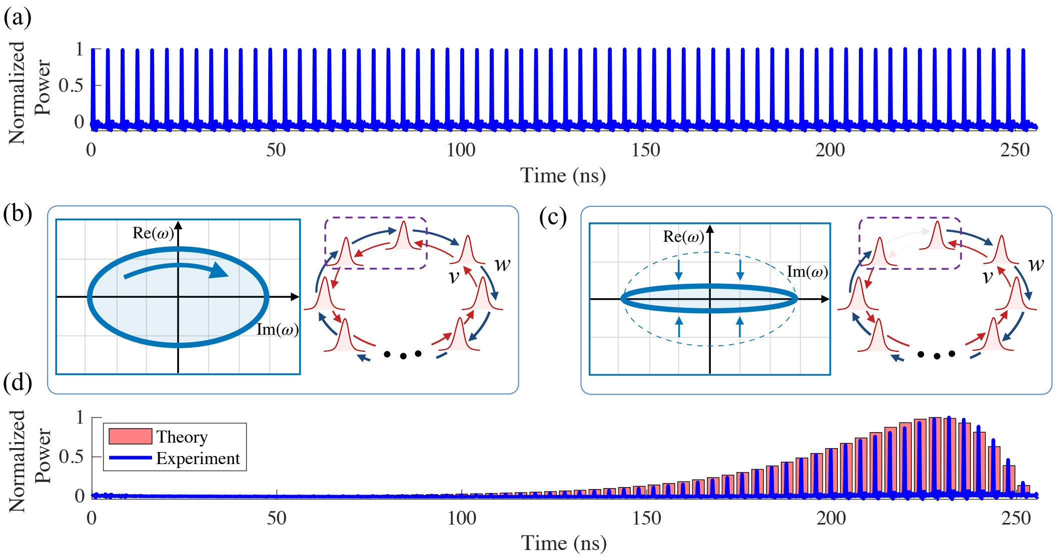

Figure 4.3: Topological Winding in a Topological Mode-Locked Laser

Topological Winding in a Topological Mode-Locked Laser. (a) Mode-locked pulse pattern in a Hatano-Nelson lattice with periodic boundary conditions. **(b)** This lattice possesses a nontrivial topological winding number. **(c)** Schematic of a Hatano-Nelson lattice with partially open boundary conditions. The change in the eigenvalues is exaggerated for illustrative purposes. **(d)** With the boundary present, we observe a nascent skin mode, which provides experimental evidence of the nontrivial topological winding number in the bulk Hatano-Nelson lattice. The plots in (a,d) are generated from the data in Fig. 4.6 using the averaging procedure discussed in Sec. 5.3.

2021), or temporal domains (Weidemann, Kremer, Helbig, et al., 2020; Xiao et al., 2020), have not demonstrated the control necessary to dynamically introduce a boundary in a periodic lattice. The fact that we can accomplish this in our topological temporally mode-locked laser highlights the fact that, in addition to producing a nonlinearity driven skin effect, our topological temporally mode-locked laser enables the study fundamental non-Hermitian topology that has not been realized on existing photonic platforms. Moreover, the observed sensitivity of our laser's pulse pattern to the boundary conditions of the Hatano-Nelson model suggests the possibility that our temporally mode-locked laser may be used for sensing. In Sec. 5.8, we explore this possibility.

4.6 Robustness of the Hatano-Nelson Model

Having established that the Hatano-Nelson lattice exhibits a nontrivial topological invariant in our mode-locked laser, we next verify that it exhibits robustness against disorder. Unlike trivial, Hermitian one-dimensional lattices, where any degree of disorder causes localization in the thermodynamic limit (Anderson, 1958; Longhi, 2021), the Hatano-Nelson model displays robustness against disorder-induced localization (Hatano and Nelson, 1998). It is believed that this robustness originates from the Hatano-Nelson model's nontrivial topology (Gong et al., 2018). In the present experiments, we observe the Hatano-Nelson model's robustness against disorder-induced localization and verify that it occurs in the presence of a nontrivial topological invariant.

We begin by programming the couplings of our laser to implement the Hatano-Nelson model with periodic boundary conditions and $w/v = \sqrt{2}$, and we add non-Hermitian coupling disorder distributed according to $\mathrm{Unif}(0, 0.2w)$ to each direction of each coupling. In the presence of this strong disorder, we observe that the resulting pulse pattern in our mode-locked laser is nonuniform but still distributed throughout the lattice. We then introduce a boundary into the Hatano-Nelson lattice. In the presence of the boundary, the pulse pattern in the laser forms a nascent skin mode, which establishes that the disordered Hatano-Nelson lattice with periodic boundary conditions still possesses a nontrivial winding number. Moreover, it is known that this sensitivity of the Hatano-Nelson model to the boundary conditions is an indication that the system with periodic boundary conditions is in a delocalized phase (Hatano and Nelson, 1997; Hatano and Nelson, 1998).

To contrast the behavior of the disordered Hatano-Nelson lattice with that of a trivial lattice, we repeat the experiment above with a trivial, Hermitian lattice. In this case, we find that, barring finite size effects [see Sec. 5.6], the pulse pattern observed in our mode-locked laser appears nearly identical in both the periodic lattice and in the lattice with a boundary. The lack of this system's sensitivity to the boundary conditions indicates that it has entered a localized phase.

Our robustness measurement is notable in several ways. First, the robustness of the Hatano-Nelson model's topological phase has not been demonstrated before in photonic systems, as previous photonic studies of point-gap topology have not implemented the Hatano-Nelson lattice with periodic boundary conditions. Second, our robustness measurement utilizes off-diagonal non-Hermitian disorder. Given recent theoretical interest in non-Hermitian disorder (Tzortzakakis, Makris, and Economou, 2020; Luo, Ohtsuki, and Shindou, 2021) and recent photonic demonstrations of diagonal non-Hermitian disorder (Weidemann, Kremer, Longhi, et al., 2021; Lin et al., 2022), our realization of off-diagonal non-Hermitian disorder provides an exciting direction for future study. Finally, the robustness of the Hatano-

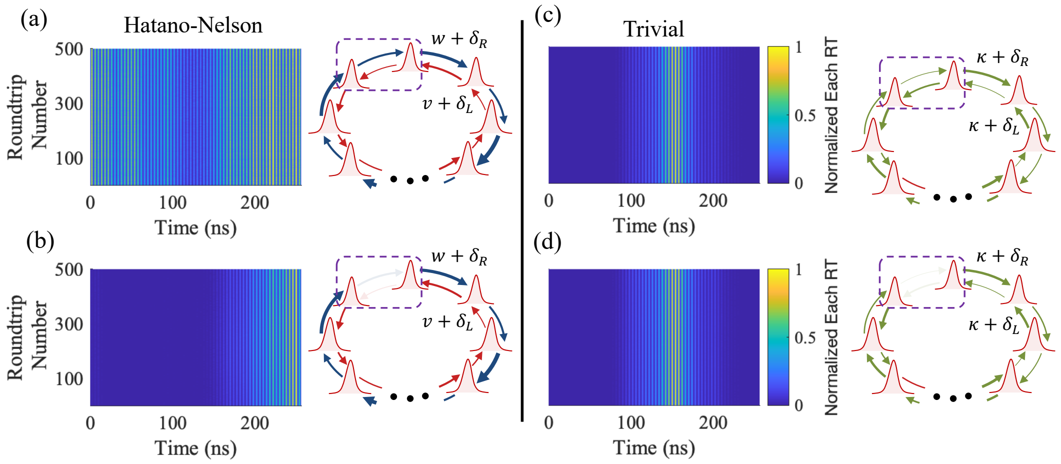

Figure 4.4: Robustness Against Disorder-Induced Localization

Robustness Against Disorder-Induced Localization. **(a)** Mode-locked pulse pattern of a disordered Hatano-Nelson lattice with periodic boundary conditions. **(b)** A nascent skin mode emerges upon introducing a boundary in the Hatano-Nelson lattice, which provides evidence of the system's robustness against disorder-induced localization. **(c)** Mode-locked pulse pattern in a disordered trivial lattice with periodic boundary conditions. **(d)** The pulse pattern is essentially unchanged in the corresponding lattice with a boundary. The pulses in (a-d) are broadened for improved visibility.

Nelson lattice in our laser may provide a path to realize robust topological frequency combs. We investigate this possibility in the Sec. 5.7.

4.7 Phase Synchronization

Up to this point, our measurements have focused on the intensity patterns that form in our topological temporally mode-locked laser. However, Eq. 4.1 predicts that the temporal couplings in our laser should determine the relative phases of the pulses in our laser in addition to their relative amplitudes. To verify this, we construct a topological temporally mode-locked laser that supports 69 pulses separated by $T_{\mathrm{R2}} = 8$ ns. The system possesses a single $+T_{\mathrm{R2}}$ delay line, which enables the topological temporally mode-locked laser to implement unidirectional Hatano-Nelson couplings with periodic boundary conditions. We send the output of this laser to the optical hybrid setup depicted in Fig. 4.5(a), which measures the relative phases between each pulse and its nearest neighbors in the mode-locked laser.

To begin our experiments, we first disconnect the $+T_{\mathrm{R2}}$ delay line and operate our system as a traditional harmonically mode-locked laser without temporal couplings.

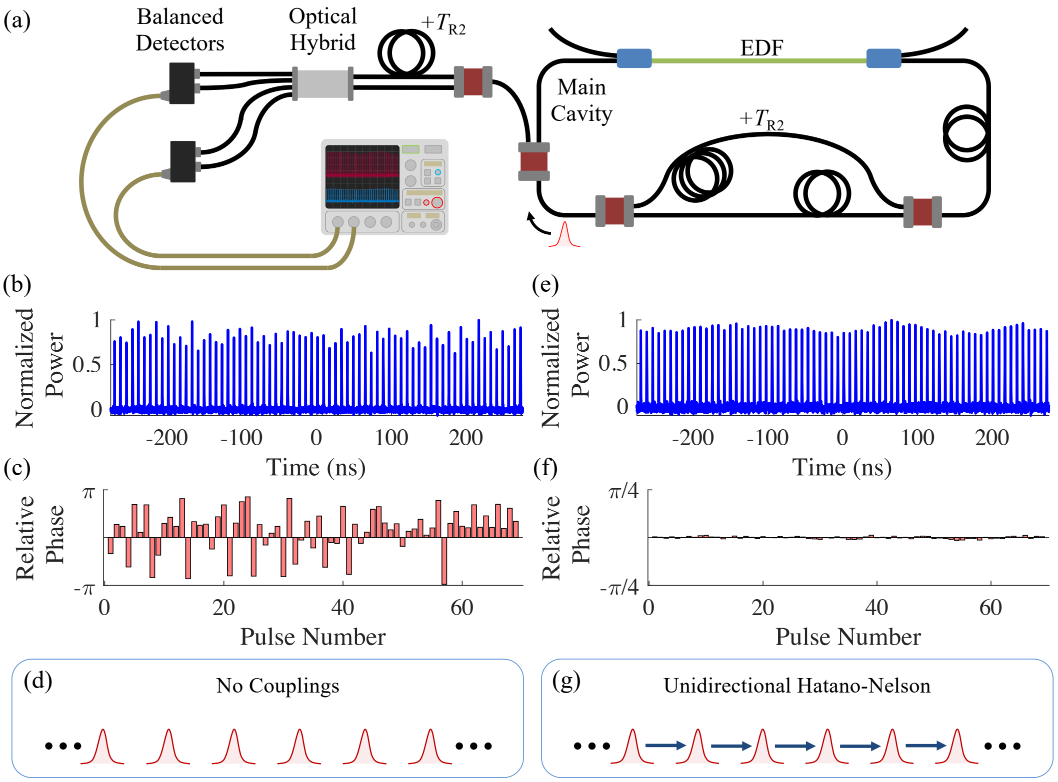

Figure 4.5: Robustness Against Disorder-Induced Localization

Robustness Against Disorder-Induced Localization. (a) Schematic of the optical hybrid setup used to measure the pulse-to-pulse phases. EDF: Erbium-doped fiber. **(b)** Pulse intensities measured on a single roundtrip of a traditional harmonically mode-locked laser. **(c)** Pulse-to-pulse phases corresponding to the pulses measured in (b). **(d)** Schematic representation of the pulses in a harmonically mode-locked laser without temporal couplings. **(e)** Pulse intensities measured on a single roundtrip of a topological temporally mode-locked laser with unidirectional Hatano-Nelson couplings. The pulse trains in (b) and (e) are measured using a photodetector not depicted in (a). **(f)** Pulse-to-pulse phases corresponding to the pulses measured in (e). Note that each bar in (c) and (f) represents the phase of a pulse in (b) or (e) relative to its subsequent nearest neighbor. The final bars in (c) and (f) represent the phases of the last pulses in (b) and (e) relative to the first pulses on the next roundtrip. **(g)** Schematic representation of a Hatano-Nelson lattice with unidirectional couplings.

In this case, we expect each pulse in our mode-locked laser to form independently, and we expect the pulse-to-pulse phases to be uncorrelated. Indeed, while the amplitudes of the measured pulses are relatively uniform [see Fig. 4.5(b)], the pulse-to-pulse phases appear to vary randomly [see Fig. 4.5(c)]. This situation changes dramatically once we reconnect the $+T_{\mathrm{R}2}$ delay line. In the presence of the topological temporal couplings, the measured pulse amplitudes remain relatively uniform, but now the pulse-to-pulse phases become synchronized, as we would expect from Eq. 4.1. This verifies that topological temporal mode-locking controls the pulse-to-pulse phases of a pulse train in addition to the pulse-to-pulse amplitudes.

4.8 Outlook

In summary, we have theoretically proposed and experimentally demonstrated the topological temporally mode-locked laser. Our demonstration overcomes the challenges faced by many of the existing theoretical proposals for topological mode-locking by utilizing temporal synthetic dimensions and the principal of temporal mode-locking. We use our topological mode-locked laser to study a novel, nonlinearity driven NHSE and to study the Hatano-Nelson model under different boundary conditions. We verify the existence of the Hatano-Nelson model's nontrivial topological invariant in our laser, and we observe this model's robustness against disorder induced localization.

Our observation that the pulse pattern in our laser is sensitive to the boundary conditions of the Hatano-Nelson model suggests that our laser may find use as a sensor, while our topological robustness measurement suggests that topological temporal mode-locking may provide a route to build topologically robust frequency combs. We explore these potential applications in Sec. 5.8 and Sec. 5.7. Moreover, the fact that we can measure pulse patterns that agree well with the predictions of Eq. 4.1 suggests that our temporally mode-locked laser may also provide a mechanism to physically compute eigenvectors.

Beyond these potential applications, the temporal mode-locking architecture demonstrated in this work provides promising directions for future work in nonlinear topological photonics. Due to the flexibility of our intracavity couplings, our temporal mode-locked laser may be adapted to study exciting phenomena such higher-dimensional NHSEs (Song et al., 2020), point-gap topological models with long-range couplings (K. Wang et al., 2021), and non-Hermitian topological Anderson insulators (Lin et al., 2022). Moreover, this same architecture may also be adapted to study topology in other mode-locked photonic sources, including synchronously pumped optical parametric oscillators (Roy, Parto, et al., 2022; Roy, Nehra, et al., 2022; Marandi et al., 2014) and dissipative Kerr cavities (Englebert et al., 2021). In future work, we will investigate topological phenomena in these other mode-locked photonic sources.

4.9 Methods

Experimental Setup and Calibration

As is shown in Fig. 1(e), the topological temporally mode-locked laser studied in this work consists of a main laser cavity and two optical delay lines, which are responsible for introducing nearest-neighbor intracavity couplings between the pulses in the laser. We construct each path from polarization-maintaining patch cables and discrete optical components, which are all terminated in FC/APC connectors to minimize back-reflections. The main cavity contains an erbium-doped fiber amplifier (EDFA) and an intensity modulator, which together produce pulses in the laser cavity. Each of the delay lines also possess intensity modulators, which provide reconfigurable pulse-to-pulse control over the intracavity couplings in our laser. The other elements in our temporally mode-locked laser are discussed in Sec. 5.1, where we present a more detailed schematic of our experimental setup.

We calibrate the intracavity couplings in our laser using a multi-step procedure. In the first step, we operate below threshold and inject pulses from an auxiliary mode-locked laser, which has the same repetition period as our temporally mode-locked laser, into our laser cavity. We first use these auxiliary pulses to set the length of the main cavity and to synchronize the lengths of the main cavity and the delay lines. Then, we disconnect the feedback in the main cavity path and, one at a time, analyze the throughput of the optical delays line on a fast photodetector. We send a burst of constant amplitude pulses through the delay lines and apply an RF voltage sweep to the intensity modulators. We use the observed photodetector signal to plot the throughput optical power as a function of the RF voltage, and, from this curve, we generate preliminary coupling waveforms for our experiments.

We next attempt to overlap the positions of the pulses generated in our laser cavity with those of the auxiliary pulses injected into the cavity. Still operating below threshold, we use a 10 MHz reference from our auxiliary mode-locked laser as a clock for the RF function generator that drives the main cavity's intensity modulator. We then set the frequency of the function generator's sinusoidal output to be the same as that of the auxiliary mode-locked laser. Finally, we use an RF phase shifter to adjust the phase of the amplitude modulation in the main cavity until we minimize the loss experienced by the auxiliary pulses as they resonate within the cavity. By doing this, our goal is that the pulses generated in our laser will localize in the positions occupied by the auxiliary pulses and therefore experience the same intensity modulator response functions in the delay lines.

The next step in our calibration procedure is to verify that our calibration remains valid once we bring our laser above threshold. To do this, we remove the auxiliary pulses and disconnect the delay lines so that they no longer couple back to the main cavity. We bring the laser above threshold, and we tune the length of the main cavity slightly until we observe a stable pulse train. We apply our preliminary coupling waveforms to the delay line intensity modulators, and, one at a time, we look at the throughput of the delay lines on a fast photodetector. If the throughput does not agree with the expected couplings, we tune the positions of the optical pulses with our RF phase shifter until the agreement with the desired couplings improves. If small discrepancies persist after this tuning, we manually update the coupling waveform to achieve the desired delay line throughput.

Experimental Procedure

To begin our experiments, we first block the free space delays in the two delay lines, and we bring just the main cavity above threshold. We then tune the length of the main cavity and the gain of the EDFA until we observe a train of uniformly spaced mode-locked pulses. We then unblock one delay line at a time, and we attempt to lock the delay lines to constructive interference with main cavity. After this, we utilize the fact that our laser's threshold is lower with the delay line couplings present to reduce the gain of the EDFA. By reducing the EDFA gain, we aim to reduce the effect of the Kerr nonlinearity on the observed mode-locked pules patterns.

At this point, our delay lines implement constant, nearest-neighbor couplings between the pulses. However, while the couplings are constant, they need not be Hermitian. When studying the Hatano-Nelson lattice under different boundary conditions, we find it convenient to tune the coupling strength in one delay line to be greater than that in the other, so that we implement the Hatano-Nelson model with periodic boundary conditions upon initializing our laser. We can then produce a boundary in this Hatano-Nelson lattice by reducing the coupling between two pulses with our delay line intensity modulators.

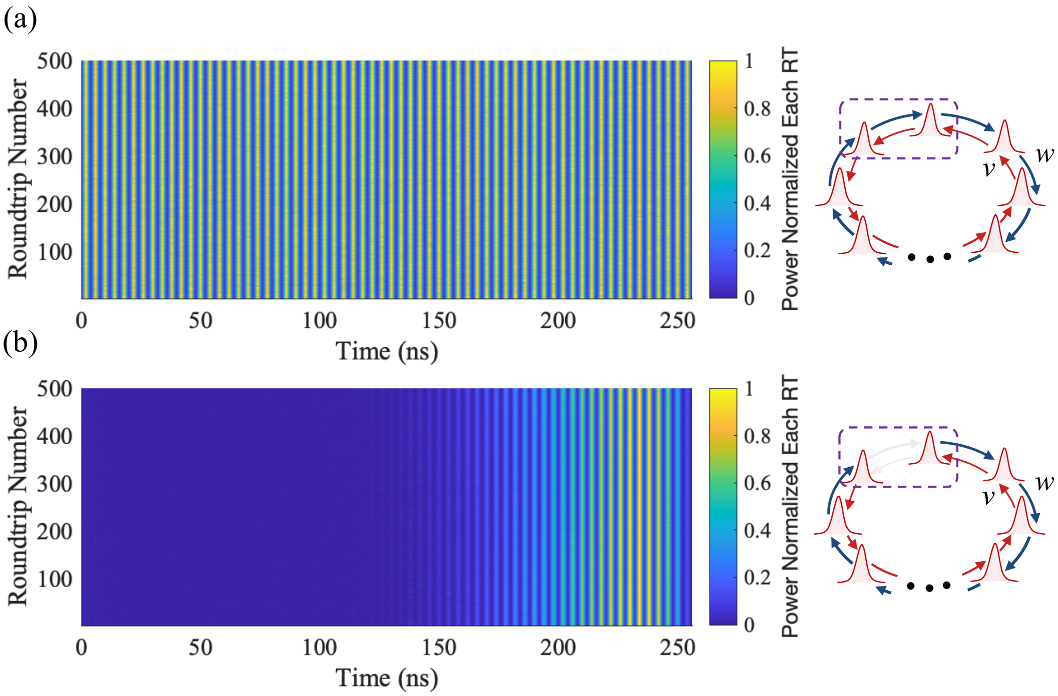

Figure 4.6: Extended Data for Fig. 4.3

Extended Data for Fig. 4.3. (a) Heat map of our mode-locked laser's output for 500 roundtrips. Here our laser's intracavity couplings implement the Hatano-Nelson model with periodic boundary conditions. **(b)** A similar heat map, but now where the laser's couplings implement a boundary in the Hatano-Nelson lattice. The plots in Fig. 4.3 are generated from this data using the averaging procedure described in Sec. 5.3. Note that the pulses in these heat maps are broadened for visibility.

After initializing our laser with constant, nearest-neighbor couplings, we abruptly modify the coupling waveforms applied to the delay line intensity modulators to implement the desired lattice model. We implement these couplings for several minutes at a time, and we detect the pulse pattern emitted by our laser with a fast photodetector. We observe this pulse pattern on a fast oscilloscope along with an auxiliary signal that allows us to establish the position of the pulse pattern in the laser's synthetic lattice. We describe this positioning procedure in Sec. 5.3.

4.10 Extended Data

Chapter 5

SUPPLEMENTARY INFORMATION FOR “TOPOLOGICAL TEMPORALLY MODE-LOCKED LASER”

5.1 Experimental Setup

We present a detailed schematic of our topological temporally mode-locked laser in Fig. 5.1. This figure shows the various components involved in calibrating, operating, and stabilizing the laser. In this section, we summarize these components and briefly mention their functions.

At the core of our topological temporally mode-locked laser is the “main cavity,” which is the fiber laser cavity colored blue in Fig. 5.1. In our system, the main cavity consists of individual patch cables connected with fiber mating sleeves. All fiber in the experiment is polarization maintaining, and the patch cables are terminated with FC/APC connectors to reduce back reflections. The other optical components in the main cavity are also terminated with FC/APC connectors.

The main cavity contains two 90:10 splitters. The first splitter acts as an input to the cavity, and, when we calibrate the length of the main cavity, we couple in the pulses of an auxiliary mode-locked laser with this splitter (see Methods). This splitter recirculates 90% of the light in the cavity and couples in 10% of the light from the input port.

The second 90:10 splitter is the output port. It couples out 10% of the light from the main cavity and recirculates the remaining 90%. The light coupled out of the cavity is sent to a 50:50 splitter, and one arm of this splitter goes to a fast 5 GHz detector. The other arm goes to a second 50:50 splitter, where the power is divided between a slow (kHz) detector and a power meter. The slow detector is used to stabilize the delay lines, and the power meter enables us to monitor the power in the laser.

After the first 90:10 splitter, there is an erbium-doped fiber amplifier (EDFA), which is the source of slow laser gain in the cavity. The EDFA is followed by a 200 GHz, Channel 34 dense wavelength division multiplexing (DWDM) filter, which removes amplified spontaneous emission (ASE) when we operate the cavity below threshold and inject auxiliary pulses to calibrate the system.

After the filter, the light in the main cavity is divided at a 50:50 splitter. Half of

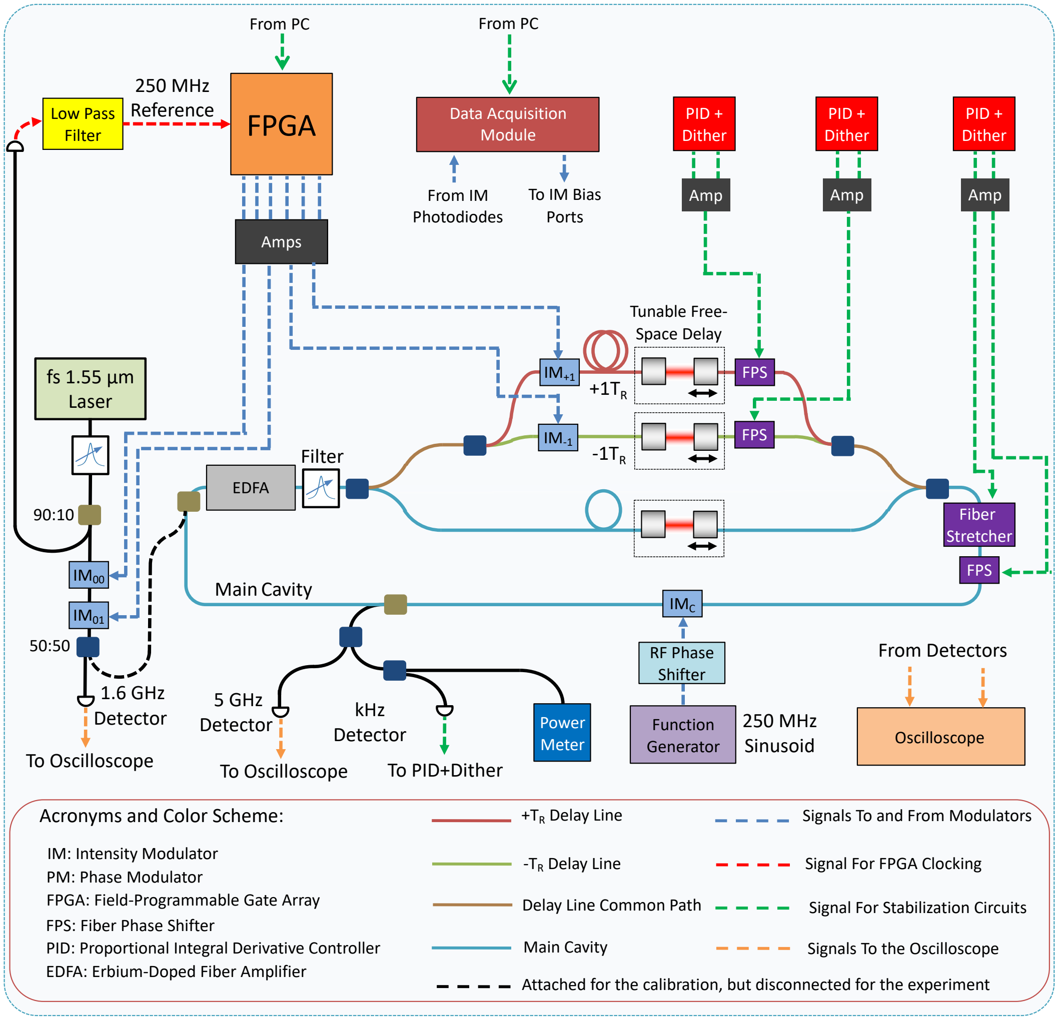

Figure 5.1: Detailed Schematic of the Topological Temporally Mode-Locked Laser

Detailed Schematic of the Topological Temporally Mode-Locked Laser.

the light continues in the main cavity (still colored blue), and the remaining light enters a common delay line path (colored brown). Another 50:50 splitter divides the light in the common delay line path between the $\pm T_R$ delay lines. Each delay line contains three elements: an intensity modulator, which enables us to modify the pulse-to-pulse couplings produced by the delay line; a free space delay, which enables us to coarsely tune the length of the delay line; and a fiber phase shifter, which is used to stabilize the delay line. The delay lines recombine into a common path at a 50:50 splitter before finally recombining with the main cavity at another 50:50 splitter.

The remaining elements in the main cavity are a fiber stretcher, a fiber phase shifter, and an intensity modulator. The fiber stretcher and the fiber phase shifter are used to stabilize the length of the main cavity during the calibration stage, but they are unused when we operate our topological temporally mode-locked laser above threshold. We drive the intensity modulator with a ~250 MHz sinusoid from an RF function generator. We use a 10 MHz reference from the auxiliary laser as a clock signal for the RF function generator.

The calibration portion of our system begins at the auxiliary mode-locked laser in Fig. 5.1. This mode-locked laser produces femtosecond pulses at a repetition rate of ~ 250 MHz. We first send these pulses through a Channel 34 DWDM filter to stretch the pulses to ~5 ps. Then, we divide the stretched pulses at a 90:10 splitter.

We send the output of 10% port directly to a 600 MHz detector. The RF output of this detector passes through a 300 MHz low pass filter to generate a ~ 250 MHz clock signal for the FPGA that drives our laser's delay line intensity modulators. In this way, we lock the electronic driving signals from the FPGA to the repetition rate of our auxiliary mode-locked laser.

We send the output of the 90% port through two consecutive intensity modulators, which control the pulse pattern that we transmit into the main cavity. We use two intensity modulators to achieve a greater extinction ratio Weidemann, Kremer, Helbig, et al., 2020; Leefmans et al., 2022.

After these intensity modulators, there is another 50:50 splitter in Fig. 5.1. This splitter is not actually present during the calibration, but it is used during our experiments. When this splitter is present, it sends 50% of the light from the auxiliary mode-locked laser to a 1.6 GHz detector, and we compare this signal to the output of our laser to determine the positions of the pulses in our synthetic lattice. We discuss the details of this positioning procedure in Sec. 5.3.

During calibration, when this 50:50 splitter is absent, the pulses from the auxiliary mode-locked laser are sent directly to the main cavity. We emphasize that this light is only injected into the main cavity during the calibration. During our experiments, we remove this external source.

To conclude this section, we summarize the electronics used to stabilize our delay lines, which are stabilized using a Pound-Drever-Hall (PDH) locking scheme Black, 2001. The output of the slow detector in Fig. 5.1 is sent to several Red Pitaya STEMlabs (shown as the PID+Dither elements in Fig. 5.1). These devices feature built-in PDH locking capabilities, and they generate the dither and feedback signals for both delay lines. We amplify and add these signals with commercial piezo-

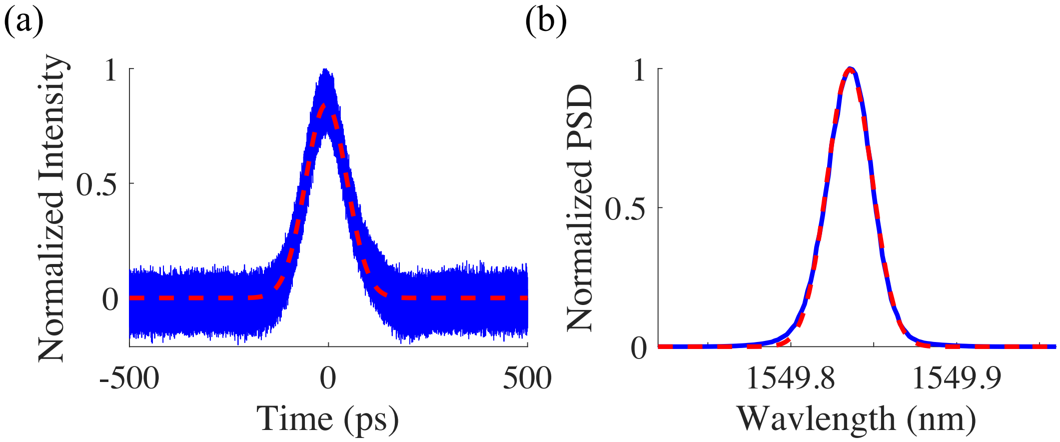

Figure 5.2: Reconstruction of the Laser Pulses

Reconstruction of the Laser Pulses. (a) Temporal reconstruction of the laser pulses in a temporally mode-locked laser with Hermitian nearest-neighbor coupling. **(b)** Power spectral density corresponding to the pulses measured in (a).

drivers and custom PCBs, and we apply these signals to the fiber phase shifters in the delay lines. A similar procedure is used to lock the main cavity during the calibration procedure. However, there we do not sum the dither and feedback signals. Instead, we apply the dither signal to a faster fiber phase shifter, and we apply the feedback signal to the fiber stretcher, which can produce a larger phase shift.

5.2 Pulse Characterization

We characterize the pulses in our temporally mode-locked laser by reconstructing the pulses with a fast photodetector and by measuring the spectrum with a spectrum analyzer. For these measurements, we program the couplings of our temporally mode-locked laser to implement Hermitian nearest-neighbor couplings.

To reconstruct the pulses in the time domain, we replace the 5 GHz detector in Fig. 5.1 with a 30 GHz detector. This detector has a nominal impulse response of 15 ps at 1560 nm. Using this detector, we record the output of our laser on a 20 GHz oscilloscope with a 80 GSa/s sampling rate. We use the samples from the recorded trace to reconstruct the pulse envelope, and this reconstruction is shown in Fig. 5.2(a). As shown by the red dashed curve, our pulse reconstruction is well fit by a Gaussian ($r^2 = 0.9675$), which reveals the width of the pulse reconstruction to be ~ 100 ps.

We show the power spectral density of the pulse train produced by our temporally

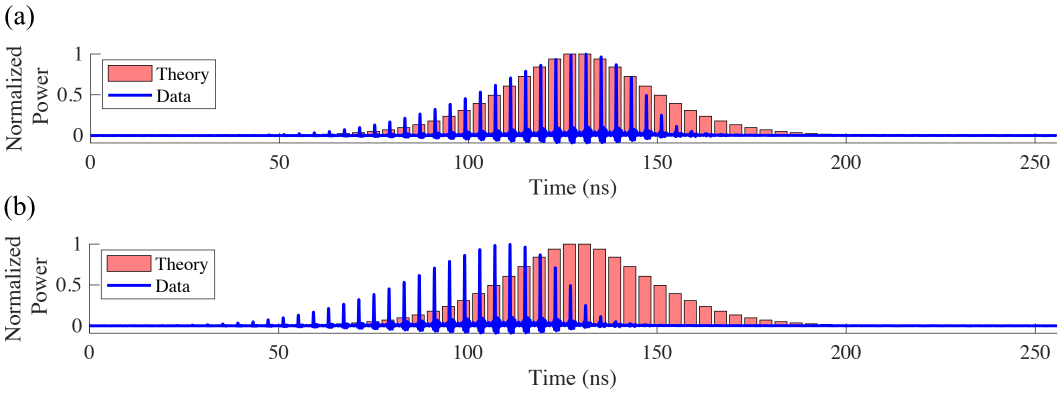

Figure 5.3: Catching an Erroneously Positioned Trace

Catching an Erroneously Positioned Trace. **(a)** The observed trace is theoretically predicted to occur at a Hatano-Nelson domain wall, and, based on its shape, one might mistakenly conclude that it is indeed localized there. **(b)** The positioning protocol reveals that the trace is localized to one side of the domain wall. The disagreement between the observed trace and the theory likely arises due to an error in the applied couplings.

mode-locked laser in Fig. 5.2(b). The power spectral density is also well fit by a Gaussian ($r^2 = 0.9967$).

5.3 Data Analysis

Positioning the Experimental Traces

An important part of analyzing the mode-locked pulse patterns in the main text is verifying that they appear where we expect them to occur in our laser's temporal synthetic lattice. This step is important because certain factors, such drift in the delay line couplings, can cause the observed pulse patterns to appear in unexpected locations. This could lead us to misidentify certain pulse patterns if the shape of the pulse pattern resembles the correct shape, but its location is incorrect.

We present an example of this situation in Fig. 5.3, in which we show a pulse pattern that appeared in the presence of a Hatano-Nelson domain wall in our topological temporally mode-locked laser. Theoretically, we expect that a skin mode should localize at the domain wall and, based on shape alone [Fig. 5.3(a)], we might conclude that observed pulse pattern does just that. However, using the positioning protocol outlined in this section, we find that the observed pulse pattern localizes to the left of the domain wall [Fig. 5.3(b)], likely due to an error in the applied couplings.

Our positioning procedure relies on the auxiliary mode-locked laser introduced in

Sec. 5.1. During an experiment, we program one of the intensity modulators outside of the main cavity in to transmit one of every 64 pulses to the 1.6 GHz detector shown in Fig. 5.1. Because our topological temporally mode-locked laser supports 64 pulses and has the same repetition rate as the auxiliary mode-locked laser, the reference pulses detected on the 1.6 GHz detector provide a reference from which we can determine the positions of the pulses in the lattice [see Fig. 5.4].

To use these reference pulses, we determine the position of the reference pulses relative to the 32nd timeslot defined by the coupling waveform, which is the pulse directly to the left of the domain wall in Fig. 5.3. We do this by configuring the 50:50 splitter outside of the cavity in Fig. 5.1 to transmit light both through the main cavity and to the 1.6 GHz detector. We launch a pulse through the splitter in what was defined to be the 32nd timeslot in our calibration, and we observe both the signal directly from the 50:50 splitter and the signal that traveled through the cavity on our oscilloscope. We measure the difference between the arrival times of the pulses from each path and account for the delay through the 50:50 splitter[1] to estimate the delay between the reference pulses and the 32nd timeslot of the main cavity. With this procedure, we estimate the delay between the reference pulses and the 32nd timeslot to be ~ 104.7 ns.

In our experiments, we observe some discrepancies between this estimated delay and the delay we measure between the reference pulses and the mode-locked pulses generated in the 32nd timeslot of our synthetic lattice. We believe that these discrepancies arise because, during our calibration procedure, we tune the phase of the RF drive applied to the intensity modulator in the main cavity (see Sec. 4.9). Changing the phase of this drive changes the positions of the mode-locked pulses in the main cavity.

Due to these discrepancies, we use the following procedure to compare our measured traces with the theoretically predicted states: First, we use the estimated position of the 32nd timeslot to ballpark the position of the 32nd pulse in our synthetic lattice. Then, we use the shape of the observed pulse pattern to resolve any residual ambiguity about where the 32nd pulse occurs. Using this procedure, we measure the delay between the reference pulse and the 32nd pulse in the Hatano-Nelson nascent skin mode to be ~ 105.2 ns, and we measure the delay between the reference pulse and the 32nd pulse in the NH-SSH skin mode to be ~ 107.2 ns.

---

[1] As we mentioned in Sec. 5.1, this 50:50 splitter is not present during our calibration (when we define the 32nd time slot in the main cavity), but it is present during the experiment.

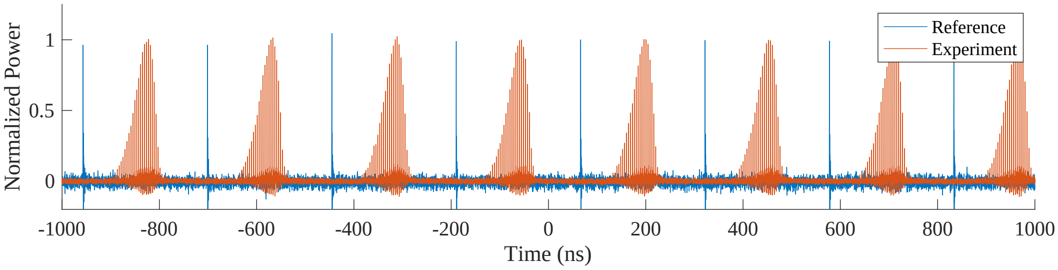

Figure 5.4: Reference Signal for Positioning Traces

Reference Signal for Positioning Traces. We determine the position of the mode measured in Fig. 5.3 using a reference pulse from our auxiliary mode-locked laser, which has the same repetition rate as our topological temporally mode-locked laser. On each roundtrip of our topological temporally mode-locked laser, we view one pulse from the auxiliary mode-locked laser on our oscilloscope, and this pulse acts as a reference to determine the positions of the pulses in our synthetic temporal lattice.

While the measured delay in the case of the NH-SSH skin mode differs from the estimated delay by $\sim$2.5 ns, we recall that the pulse repetition period in our mode-locked laser is $\sim$4 ns. Therefore, depending on where the RF driving signals overlap with the optical pulses in the delay line intensity modulators, there can be up to a roughly 4 ns window in which the 32nd pulse sees the correct couplings. Given the excellent agreement between the observed data and the theoretically predicted state, we have strong reason to believe that the pulse we identified as the 32nd pulse sees the correct couplings for the 32nd time window.

Plotting the Experimental Traces

Here, we summarize the procedures used to generate the averaged heat maps and data traces presented in the main text.

To produce the heat maps shown in Fig. 4.2, Fig. 4.4, and Fig. 4.6, we first divide our raw data trace into roundtrips using the known roundtrip time of the cavity and the positioning procedure discussed above. We remove any power fluctuations that might occur between roundtrips by normalizing the power in each roundtrip. Then, we compute the maxima of the pulses in each roundtrip, and we assign each maximum to be the amplitude of a Gaussian pulse whose width is chosen to be easily visible on the final heat map. We arrange the Gaussian pulses that correspond to the pulse maxima on a single roundtrip into a single row of the heat map, and we construct the full heat map by assembling the rows for all the roundtrips under study.

The averaged data traces in Fig. 4.2 and Fig. 4.3 illustrate the correspondence between the observed pulse patterns and the theoretically predicted states. To generate these plots, we divide the data trace under study into roundtrips, and we normalize the data from each roundtrip. Normalizing the traces in this manner removes any fluctuations in the power and enables us to more directly compare the pulse patterns observed on different roundtrips. Next, we average over the normalized roundtrip traces. Finally, we normalize the averaged trace so that we can compare our result with the theoretically predicted pulse pattern.

For the NH-SSH skin mode plotted in Fig. 4.2, the theoretical state is the lowest-loss right eigenstate corresponding to the domain wall described in the main text. On the other hand, the theoretical state for Fig. 4.3(d) is generated using a fitting procedure because it is difficult to accurately calibrate the boundary conditions of our Hatano-Nelson lattice. To perform this fitting procedure, we first assume that we correctly implement the desired coupling ratio $w/v = \sqrt{2}$ for the Hatano-Nelson model under consideration. We then compute the lowest-loss right eigenstate of the Hatano-Nelson lattice as we sweep the coupling between the first and final sites of the Hatano-Nelson lattice from open boundary conditions to periodic boundary conditions. At each point in the sweep, we compute the 2-norm of the difference between the theoretical lowest-loss state and the measured pulse amplitudes, and we consider the state that corresponds to the smallest 2-norm to be our best fit state. With this procedure, we find that the best fit occurs when the coupling between the first and final lattice sites is suppressed by a factor of ~ 11.6, which is reasonable given that our delay line intensity modulators have a nominal DC power extinction ratio of 22 dB.

5.4 Master Equation Description of Temporal Mode-Locking

Derivation of the Tight-Binding Model

In this section, we derive the tight-binding model presented in the main text. As our starting point, we propose a modified master equation for active mode-locking. This master equation has the form,

$$\frac{\partial \psi(T,t)}{\partial T} = \left(g - \ell + D_{\mathrm{g}} \frac{\partial^2}{\partial t^2} - \Delta_{\mathrm{IM}} \left(1 - \cos(\omega_{\mathrm{rep}} t)\right)\right) \psi(T,t) + \sum_{r}^{N} \kappa_r(t) \psi(T, t - rT_{\mathrm{RT}}/N) \tag{5.1a}$$

$$\frac{\partial g}{\partial T} = -\gamma \left(g - g_0 + \frac{g}{T_{\mathrm{RT}}} \int_{-T_{\mathrm{RT}}/2}^{T_{\mathrm{RT}}/2} |\psi(T,t)|^2 dt \right). \tag{5.1b}$$

Here $\psi(T,t)$ represents the field in the laser, g represents the laser gain, ℓ represents the roundtrip loss, D_{g} describes the gain bandwidth, Δ_{IM} describes the modulation depth, T_{RT} is the cavity roundtrip period, $\omega_{\mathrm{rep}} = 2\pi N/T_{\mathrm{RT}}$ is the angular frequency corresponding to the repetition rate of the laser, g_0 is the small signal gain, and $\gamma = T_{\mathrm{RT}}/T_{\mathrm{rel}}$ is the ratio of the roundtrip period to the gain relaxation time. The fast time t describes the time within a single roundtrip and the slow time T describes the evolution of the field from roundtrip to roundtrip. The functions $\kappa_r(t)$ describe the intracavity couplings between the different pulses in the laser. While, in our experiments, we only consider nearest-neighbor couplings, in our master equation we allow for all-to-all couplings between the pulses.

There are two primary differences between this modified master equation and the traditional master equation used to model actively mode-locked lasers Haus, 2000. First, while the traditional master equation is used to model a single mode-locked pulse, here our master equation models multiple pulses. Second, we introduce our intracavity coupling term into the master equation. This term is responsible for producing temporal mode-locking in the laser.

In practice, our experiment operates beyond several of the assumptions that go into deriving the master equation, such as the roundtrip gain and the roundtrip loss being small Haus, 2000. Nonetheless, we find that this modified master equation provides a convenient model to qualitatively analyze the behavior of our temporally mode-locked laser. Indeed, as we saw in the main text, the predictions of our modified master equation can agree quite well with what we observe in experiment. To verify that the predictions of the master equation hold beyond the assumptions that go into its derivation, we also perform lumped element simulations in Sec. 5.5.

To derive the tight-binding model presented in the main text from our modified master equation, we begin by assuming that the N pulses described by the equation are localized in their respective "gain wells," by which we mean that the pulses are localized near the minimum loss introduced by the cosine term in Eq. 5.1a. In this case, we can break Eq. 5.1a into N separate equations of the form,

$$\frac{\partial \psi_n(T,t)}{\partial T} = \left(g - \ell + D_\mathrm{g}\frac{\partial^2}{\partial t^2} - \frac{\Delta_\mathrm{IM}}{2}\left(\omega_\mathrm{rep}^2 t^2\right)\right)\psi_n(T,t) + \sum_{m=1}^{N}\kappa_{nm}\psi_m(T,t). \tag{5.2}$$

Here we implicitly redefine the fast time t to center each pulse at $t = 0$ in its own time window. The subscripts m and n label the fields of the different pulses.

The solutions to Eq 5.2 are Hermite-Gaussians, which allows us to expand $\psi_n(T,t)$ as

$$\psi_n(T,t) = \sum_k C_{nk}(T)H_k(\eta t)e^{-\eta^2 t^2/2}, \tag{5.3}$$

where $H_k(\eta t)$ is the kth-order Hermite polynomial, and the coefficients $C_{nk}(T)$ and η have yet to be determined.

Plugging Eq. 5.3 into Eq. 5.2, we find that $\eta^2 = \omega_\mathrm{rep}\sqrt{\Delta_\mathrm{IM}/2D_\mathrm{g}}$ and

$$\frac{\partial C_{nk}}{\partial T} = \left[(g-\ell) - \omega_\mathrm{rep}\sqrt{\frac{D_\mathrm{g}\Delta_\mathrm{IM}}{2}}(2k+1)\right]C_{nk} + \sum_m \kappa_{nm}C_{mk}. \tag{5.4}$$

In the steady state, $\partial C_{nk}(T)/\partial T = 0$, and we observe that only the $k = 0$ term is nonzero. The reason for this is that, if $\partial C_{n0}(T)/\partial T = 0$, the coefficients $C_{nk}(T)$ with $k > 0$ experience net loss. On the other hand, if $\partial C_{nk}(T)/\partial T = 0$ for $k > 0$, then $C_{n0}(T)$ experiences net gain and will experience net gain until $\partial C_{n0}(T)/\partial T = 0$. Therefore, to study the steady-state behavior of the pulses, we only need to consider the Gaussian solutions to Eq. 5.2. With this in mind, we will now drop the subscript k and let $C_{n0} \to C_n$.

We can also rewrite our expression for the gain (Eq. 5.1b) in terms of the amplitudes C_n. We rewrite Eq. 5.1b as

$$\frac{\partial g}{\partial T} = -\gamma\left(g - g_0 + \frac{g}{T_\mathrm{RT}}\int_{-\infty}^{\infty}\sum_n |\psi_n(T,t)|^2\,dt\right). \tag{5.5}$$

Here we have used the assumption that the pulses are strongly localized in their respective gain wells to take the limits on the integral to infinity. We plug in our Gaussian solution from above and find that

$$\frac{\partial g}{\partial T} = -\gamma \left(g - g_0 + \frac{g}{T_{\mathrm{RT}}} \int_{-\infty}^{\infty} \sum_n |C_n(T)|^2 \, e^{-\eta^2 t^2} dt \right). \tag{5.6}$$

Defining $\epsilon = \sqrt{\pi}/(\eta T_{\mathrm{RT}})$, we arrive at the expression

$$\frac{\partial g}{\partial T} = -\gamma \left(g - g_0 + g\epsilon \sum_n |C_n(T)|^2 \right). \tag{5.7}$$

Combining Eq. 5.7 with our equation of motion for $C_n(T)$, we arrive at the desired nonlinear tight-binding model, which can be reduced to that presented in the main text:

$$\frac{\partial \mathbf{C}}{\partial T} = \left[g - \ell - \omega_{\mathrm{rep}} \sqrt{\frac{D_{\mathrm{g}} \Delta_{\mathrm{IM}}}{2}} \right] \mathbf{C} + K\mathbf{C} \tag{5.8a}$$

$$\frac{\partial g}{\partial T} = -\gamma \left(g - g_0 + g\epsilon \sum_n |C_n(T)|^2 \right). \tag{5.8b}$$

Here $\mathbf{C}$ is a vector of the pulse amplitudes C_n, and K is a matrix with the entries $K_{nm} = \kappa_{nm}$.

Steady-State Behavior of the Tight-Binding Model

To understand the behavior of our modified master equation, we now derive the steady-state behavior of the tight-binding model in Eq. 5.8. We begin by assuming that the eigenvalues of K are nondegenerate. In this case, we diagonalize Eq. 5.8a in the right eigenbasis of K. In particular, we define a biorthogonal basis consisting of the right and left eigenvectors of K, and we define the matrices Ψ and Φ such that the columns of Ψ are the right eigenvectors of K and the rows of Φ are the left eigenvectors of K. Then, noting that $\Psi\Phi = \Phi\Psi = I$, where I is the identity, we write

$$\frac{\partial \mathbf{a}}{\partial T} = [\Lambda + g - \chi] \, \mathbf{a} \tag{5.9a}$$

$$\frac{\partial g}{\partial T} = -\gamma \left(g - g_0 + g\epsilon \sum_n \left| \sum_m \Psi_{nm} a_m \right|^2 \right), \tag{5.9b}$$

where $\chi = \ell + \omega_{\mathrm{rep}}\sqrt{D_{\mathrm{g}}\Delta_{\mathrm{IM}}/2}$, $\mathbf{a} = \Phi\mathbf{C}$, and $\Lambda = \Phi K \Psi$ is the diagonal matrix whose entries are the eigenvalues of K.

Next, we rewrite Eq. 5.9 in terms of real-valued equations for the amplitudes and phases of the fields a_j. Letting $a_j = A_j e^{i\xi_j}$ and $\Lambda_{jj} = \lambda_j e^{i\Gamma_j}$, we find that

$$\frac{\partial A_j}{\partial T} = \left[\lambda_j \cos(\Gamma_j) + g - \chi\right] A_j \tag{5.10a}$$

$$\frac{\partial g}{\partial T} = -\gamma\left(g - g_0 + g\epsilon \sum_n \left|\sum_m \Psi_{mn} a_m\right|^2\right) \tag{5.10b}$$

$$\frac{\partial \xi_j}{\partial T} = \lambda_j \sin(\Gamma_j)\,. \tag{5.10c}$$

To determine the steady-state behavior of the temporally mode-locked laser, we find the fixed points of Eq. 5.10. We find that the steady-state pulse pattern occurs when

$$\lambda_j \cos(\Gamma_j) - \chi + \frac{g_0}{1 + \epsilon \sum_n |\sum_m \Psi_{nm} a_m|^2} = 0. \tag{5.11}$$

In practice, this condition can always be satisfied because, in our laser, χ is at least as small as the largest magnitude of any of the eigenvalues λ_j. This occurs because the coupling losses associated with the system's dissipative couplings contribute to the magnitude of χ and enforce that $\chi > \lambda j \cos(\Gamma j)$ for all j. Therefore, we can achieve equality in Eq. 5.11 by suitably choosing the value of $\sum_n |\sum_m \Psi_{nm} a_m|^2$.

To determine the steady-state value of the quantity $\sum_n |\sum_m \Psi_{nm} a_m|^2$, we first observe that Eq. 5.11 can only be satisfied by a single nonzero A_j as long as $\lambda_m \cos(\Gamma_m) \neq \lambda_k \cos(\Gamma_k)$ for any A_m and A_k. Assuming that this is true, we observe from Eq. 5.10a that the only amplitude A_j that can correspond to a stable solution of the tight-binding model is the amplitude that corresponds to the lowest-loss right eigenstate of the coupling matrix K.

To see why this is true, observe that $\lambda_j \cos(\Gamma_j)$ is the real part of the eigenvalue corresponding to the amplitude A_j. In our dissipatively coupled system Leefmans et al., 2022, this corresponds to the dissipation associated with the couplings. In the steady state, the gain must satisfy $\lambda_j \cos(\Gamma_j) + g = \chi$ for some j. If j corresponds to the lowest-loss right eigenstate, then $\lambda_k \cos(\Gamma_k) < \lambda_j \cos(\Gamma_j)$ for all $k \neq j$, and therefore all fixed points but the one corresponding to the lowest-loss right eigenstate will experience net loss.

On the other hand, if j does not correspond to the lowest-loss right eigenstate, then $\lambda_{\text{low}} \cos(\Gamma_{\text{low}}) > \lambda_j \cos(\Gamma_j)$, and the lowest-loss right eigenstate will experience net gain. The lowest-loss right eigenstate will grow until it saturates the gain, at which point it will suppress the other, higher-loss eigenstates. This argument, combined with our master equation simulations below, provide compelling evidence that the lowest-loss right eigenstate defined by the coupling matrix K is a stable fixed point of this tight-binding model.

One caveat to the above conclusions is that they only hold for sufficiently large values of the small signal gain g_0. In other words, the gain must be large enough for the laser to go above threshold. This occurs when $\chi < \lambda_{\text{low}} \cos(\Gamma_{\text{low}}) + g_0$. On the other hand, when $\chi > \lambda_{\text{low}} \cos(\Gamma_{\text{low}}) + g_0$, then we expect $\mathbf{A} = 0$ to be a stable solution.

From our analysis in this section, we expect the pulse pattern in our temporally mode-locked laser to correspond to the lowest-loss eigenstate of the coupling matrix K. However, while we expect the relative amplitudes and phases of the pulses to be fixed in this state, Eq. 5.10c predicts that the pulse pattern can acquire a global phase over time. From Eq. 5.10c we see that this phase is governed by the imaginary part of the eigenvalue, $\lambda_j \sin(\Gamma_j)$.

Master Equation Simulations

To check the analytical results of the last section, we directly simulate the modified master equation in Eq. 5.1 for both the NH-SSH domain wall and the Hatano-Nelson nascent skin mode studied in Ch. 4. For these simulations we use the dimensionless parameters $g_0 = 4$, $\Delta_{\text{IM}} = 0.04$, $T_{\text{RT}} = 0.01$, $\omega_{\text{rep}} = 2\pi\,(64/T_{\text{RT}})$, $D_{\text{g}} \approx 2.5 \times 10^{-15}$, and $\gamma = 2.56 \times 10^{-5}$. The strengths of the coupling coefficients vary according to the model under study, and we set $\ell = \ell_{\text{base}} + \ell_{\text{coupling}}$, where $\ell_{\text{base}} = 0.04$ and ℓ_{coupling} equals the maximum sum of the coupling coefficients in any row of the coupling matrix that describes the model under study.

First, we simulate a boundary in a Hatano-Nelson lattice. We implement the Hatano-Nelson lattice shown in Fig. 5.5(a) with $w = 0.08$, $w/v = \sqrt{2}$, and the coupling between the first and final pulses in the lattice suppressed by a factor of 11.6. We initialize our simulation with Gaussian random noise ($\mu = 0$, $\sigma = 10^{-6}$) on both the real and imaginary parts of the field, and we inject noise distributed according

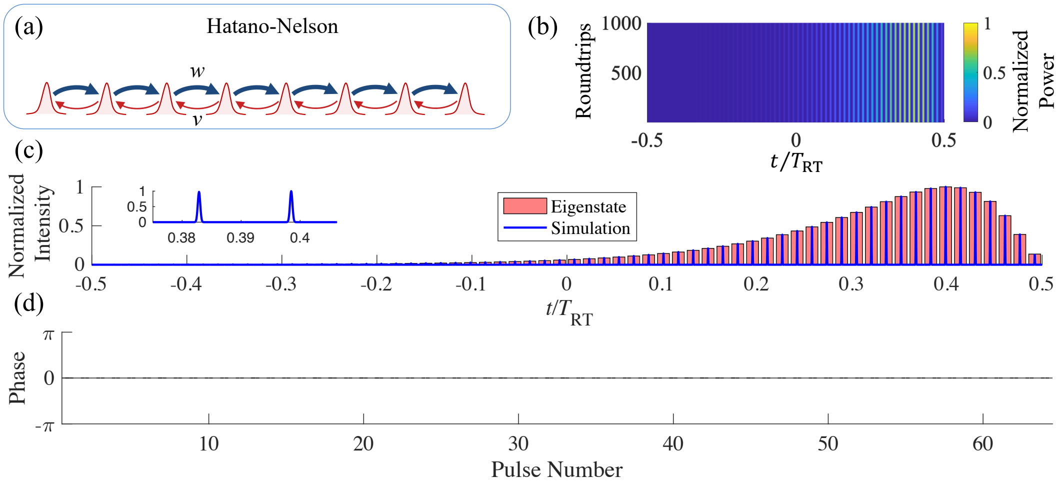

Figure 5.5: Master Equation Simulation of the Hatano-Nelson Nascent Skin Mode

Master Equation Simulation of the Hatano-Nelson Nascent Skin Mode. **(a)** Schematic of the Hatano-Nelson model. **(b)** Heat map of the final 1000 roundtrips in our simulation. The pulses in the heat map are broadened for visibility. **(c)** Comparison between the simulated nascent skin mode and the lowest-loss right eigenstate defined by the couplings. **(d)** The phases at the peaks of the pulses are uniform through the lattice.

to the same distribution into our simulation at the start of each roundtrip. We run our simulation for 10^5 roundtrips, the final 1000 of which are shown in Fig. 5.5(b). At this point, the simulation has reached steady state, and the pulse pattern in the simulation corresponds to the nascent skin mode predicted by the lowest-loss right eigenstate of the underlying lattice [Fig. 5.5(c)]. Note that, as expected, the pulse-to-pulse phases (as measured from the peaks of the pulses) are uniform [Fig. 5.5(d)].

We next repeat this simulation with a NH-SSH domain wall. This domain wall is shown in Fig. 5.6(a); we consider $w = 0.08$, $w/v = \sqrt{2}$, and $\kappa = (w+v)/2$. Here, we also find that the simulated steady state of the system corresponds to the lowest-loss right eigenstate of the model under consideration.

5.5 Lumped Element Simulations

As we mentioned in Sec. 5.4, our topological temporally mode-locked laser operates beyond some of the assumptions that enter the derivation of our master equation. For this reason, here we perform lumped element simulations to confirm that the predictions of our master equation are reasonable beyond the assumptions of the model. The lumped element simulations in this section are adapted from simulations found in the literature Le Nguyen Binh and Ngo, 2011.

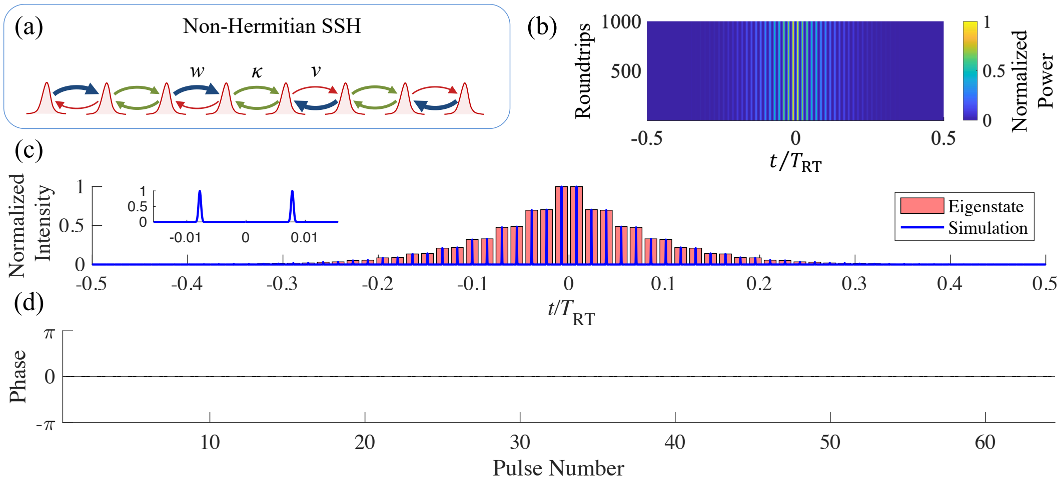

Figure 5.6: Master Equation Simulation of the NH-SSH Domain Wall

Master Equation Simulation of the NH-SSH Domain Wall. (a) Schematic of the NH-SSH domain wall. **(b)** Heat map of the final 1000 roundtrips in our simulation. The pulses in the heat map are broadened for visibility. **(c)** Comparison between the simulated domain wall skin mode and the lowest-loss right eigenstate defined by the couplings. **(d)** The phases at the peaks of the pulses are uniform through the lattice.

Elements of the Lumped Element Simulations

Our lumped element simulations divide our temporally mode-locked laser into five elements, which are passive optical fiber, erbium-doped fiber, a filter, an intensity modulator, and intracavity couplings. Below we outline how we implement each of these elements.

Passive Fiber

We model the passive fiber in our simulation with the nonlinear Schrödinger equation

$$\frac{\partial A}{\partial z} + \frac{i\beta_2}{2}\frac{\partial^2 A}{\partial T^2} + \frac{1}{2}\alpha A = i\gamma \left|A\right|^2 A. \tag{5.12}$$

Here A is the field in the fiber, β_2 is the group velocity dispersion (GVD), α is the loss coefficient, and γ is the nonlinear coefficient. In our simulations we consider dispersion shifted fiber with $\alpha = 0\ \mathrm{m}^{-1}$, $\beta_2 = -3.82 \times 10^{-9}\ \mathrm{ns}^2\mathrm{m}^{-1}$, and $\gamma = 1.53 \times 10^{-3}\ \mathrm{W}^{-1}\mathrm{m}^{-1}$. To speed up our simulation times, we consider only a short length of passive fiber ($L_{\mathrm{DSF}} = 2$ m) in our simulations. We simulate this fiber using the FFT to evaluate the derivative with respect to T and RK4 to propagate the field with respect to z.

Erbium-Doped Fiber

We model the EDFA in our simulation with a nonlinear Schrödinger equation that includes an additional gain term:

$$\frac{\partial A}{\partial z} + \frac{i}{2}\left(\beta_{2,\mathrm{EDFA}} + igT_2^2\right)\frac{\partial^2 A}{\partial T^2} - \frac{1}{2}\left(g - \alpha_{\mathrm{EDFA}} A\right) = i\gamma_{\mathrm{EDFA}} \left|A\right|^2 A. \tag{5.13a}$$

$$g = \frac{g_0 A}{1 + \frac{1}{P_{\mathrm{sat}}} \int_{T_{\mathrm{RT}}/2}^{T_{\mathrm{RT}}/2} \left|A\right|^2 dT} \tag{5.13b}$$

Here T_2 determines the gain bandwidth, g_0 is the small signal gain, and P_{sat} is the saturation power. Notice that our equation for the gain g explicitly assumes the slow gain saturation regime discussed in the main text. Assuming this simple form for the gain greatly simplifies our lumped element simulations.

For the erbium doped fiber, we use the following parameters: $\beta_{2,\mathrm{EDFA}} = -21.7 \times 10^{-9}$ ns^{2}m^{-1}, $\alpha_{\mathrm{EDFA}} = 0$ m^{-1}, $T_2 = 10^{-4}$ ns, and $P_{\mathrm{sat}} = 10^{-3}$ W. As we did for the dispersion shifted fiber, we consider only a short length of erbium doped fiber ($L_{\mathrm{EDF}} = 0.5$ m) in our simulations. Once again, we simulate the erbium doped fiber by using the FFT to evaluate the derivative with respect to T and RK4 to propagate the field with respect to z.

Filter

For the filter, we consider a Gaussian filter with the transfer function

$$H(f) = \alpha_{\mathrm{F}} \exp\left[-\frac{1}{2}\left(\frac{f}{B_0}\right)^2\right]. \tag{5.14}$$

Here α_{F} is the loss associated with the filter, and B_0 is the filter bandwidth. For our simulations we choose $\alpha_{\mathrm{F}} = 1$ and $B_0 = 400$ ns^{-1}.

Intensity Modulator

We model the intensity modulator in our simulations with the equation

$$T_{\mathrm{IM}}(t) = \alpha_{\mathrm{m}} \cos\left(\frac{\pi}{4}\left[\Delta_{\mathrm{m}} \cos(\omega_{\mathrm{m}} t) + \frac{2V_{\mathrm{B}}}{V_\pi}\right]\right). \tag{5.15}$$

Here α_m accounts for the loss in the intensity modulator, Δ_m is the modulation depth, V_B is the bias voltage applied to the modulator, V_π is the voltage needed to shift the modulator bias by π, and ω_m is the angular frequency associated with the repetition period T_RT/N, where N is the number of pulses in the laser cavity. For our simulations we choose $\alpha_\mathrm{m} = 1$, $\Delta_\mathrm{m} = 0.2$, and $V_\mathrm{B}/V_\pi = 0.5$.

Intracavity Couplings

For a laser with N pulses, we implement the intracavity couplings by decomposing the field in the laser into N segements of equal length, where each segment contains a single pulse. We treat these segments as the elements of a vector and operate on them with the coupling matrix K that describes the dissipative couplings of the model under study. At the same time, we also introduce coupling losses into each of these segments. We then combine the N segments and add them to the original laser field.

Lumped Element Simulations at Lower Power

We first perform our lumped element simulations in the "low power" regime, which we define to be the regime for which the Kerr nonlinearity does not appear to have a major effect on the simulation result. As we shall see, at higher powers, the Kerr nonlinearity appears capable of substantially changing the state of our temporally mode-locked laser relative to the predictions of our master equation. For the following simulations, we use a small signal gain of $g_0 = 2.0\ \mathrm{m}^{-1}$.

As our first simulation in the low power regime, we program the couplings in our simulation to implement a Hatano-Nelson lattice with $w/v = \sqrt{2}$ and with the couplings at the boundary suppressed by a factor of 11.6. Here, and for all the simulations in this section, we initialize the field in our simulations with noise distributed according to $\mathcal{N}(0, 10^{-9}) + i\mathcal{N}(0, 10^{-9})\ \mathrm{W}^{1/2}$, and, on each roundtrip of the simulation, we inject noise distributed according to the same distribution. We show the results of our simulation in Fig. 5.7. We observe that the results of our lumped element simulation are very similar to the results of the master equation simulation shown in Fig. 5.5. The one notable difference is that the pulse-to-pulse phases are no longer uniform in the lumped element simulation. This nonuniformity is a direct consequence of the presence of the Kerr nonlinearity in our lumped element simulation, and we have verified that, if we set $\gamma = \gamma_{EDFA} = 0\ \mathrm{W}^{-1}\mathrm{m}^{-1}$, this phase nonuniformity disappears.

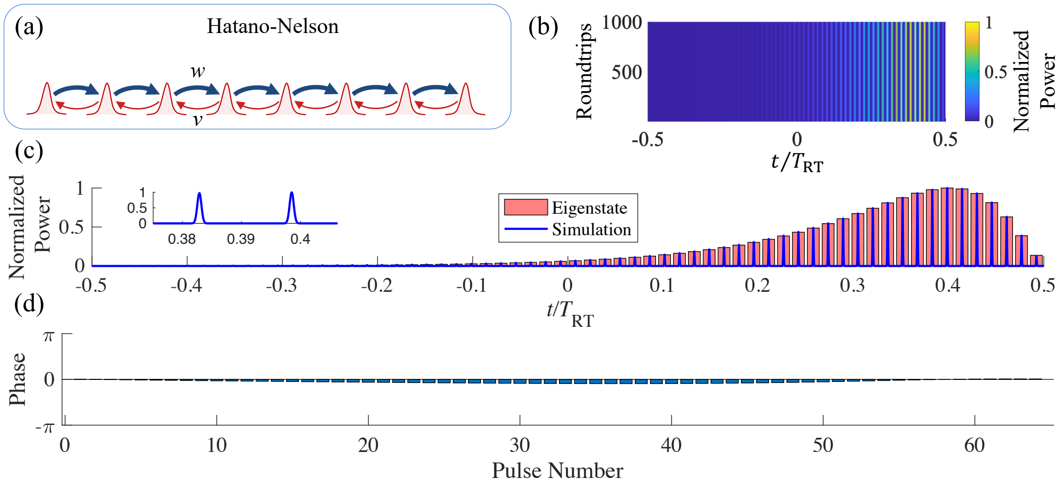

Figure 5.7: Low Power Lumped Element Simulation of the Hatano-Nelson Model

Low Power Lumped Element Simulation of the Hatano-Nelson Model. **(a)** Schematic of the Hatano-Nelson model. **(b)** Heat map of the final 1000 roundtrips in our simulation. The pulses in the heat map are broadened for visibility. **(c)** The amplitudes of the simulated pulse pattern are in excellent agreement with the predictions of the master equation. **(d)** A small degree of nonuniformity in the pulse-to-pulse phases arises because of the finite Kerr nonlinearity.

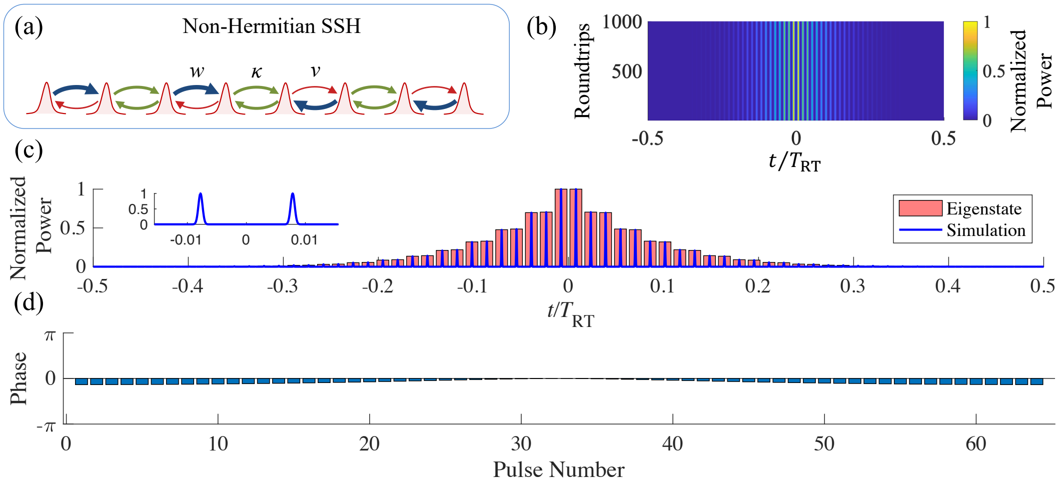

Figure 5.8: Low Power Lumped Element Simulation of the NH-SSH Domain Wall

Low Power Lumped Element Simulation of the NH-SSH Domain Wall. **(a)** Schematic of the NH-SSH domain wall. **(b)** Heat map of the final 1000 roundtrips in our simulation. The pulses in the heat map are broadened for visibility. **(c)** The amplitudes of the simulated pulse pattern are in excellent agreement with the predictions of the master equation. **(d)** A small degree of nonuniformity in the pulse-to-pulse phases arises because of the finite Kerr nonlinearity.

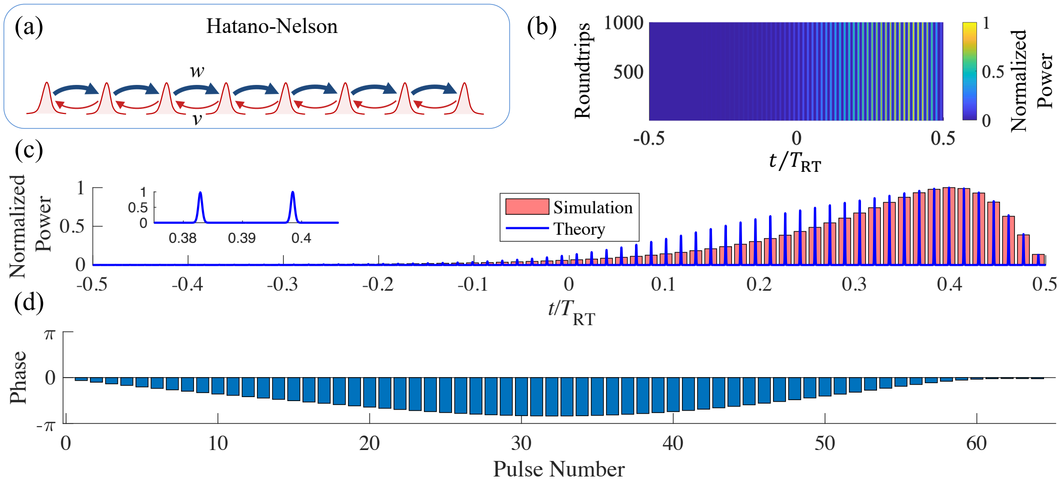

Figure 5.9: Higher Power Lumped Element Simulation of the Hatano-Nelson Model

Higher Power Lumped Element Simulation of the Hatano-Nelson Model. **(a)** Schematic of the Hatano-Nelson model. **(b)** Heat map of the final 1000 roundtrips in our simulation. The pulses in the heat map are broadened for visibility. **(c)** The steady state pulse pattern is substantially broadened relative to the prediction of the master equation. **(d)** The phases of the pulses exhibit a substantial nonlinear phase shift.

We next perform a lumped element simulation for a NH-SSH domain wall with $w/v = \sqrt{2}$ and $\kappa = (w+v)/2$. These results are shown in Fig. 5.8. Once again, we find that, except for small deviations in the pulse-to-pulse phases that result from the finite Kerr nonlinearity, our lumped element simulation exhibits excellent agreement with the predictions of our master equation.

Lumped Element Simulations at Higher Power

We next repeat the simulations from the previous section at higher powers, where the Kerr nonlinearity has a substantial impact on the dynamics of the laser. For these simulations, we use a small signal gain of $g_0 = 7.0\ \mathrm{m}^{-1}$.

We first repeat our simulation of the Hatano-Nelson lattice with $w/v = \sqrt{2}$ and the coupling reduced at the boundary by a factor of 11.6. The results of this simulation are shown in Fig. 5.9. Now we find that the simulated steady state pulse pattern is substantially broader than the prediction of our master equation [Fig. 5.5(c)]. It is evident from Fig. 5.9(d) that the Kerr nonlinearity gives rise to a substantial nonlinear phase shift at this higher power, and we believe that this nonlinear phase shift is responsible for broadening the observed pulse pattern.

Next, we repeat the simulation of the NH-SSH domain wall with $w/v = \sqrt{2}$ and

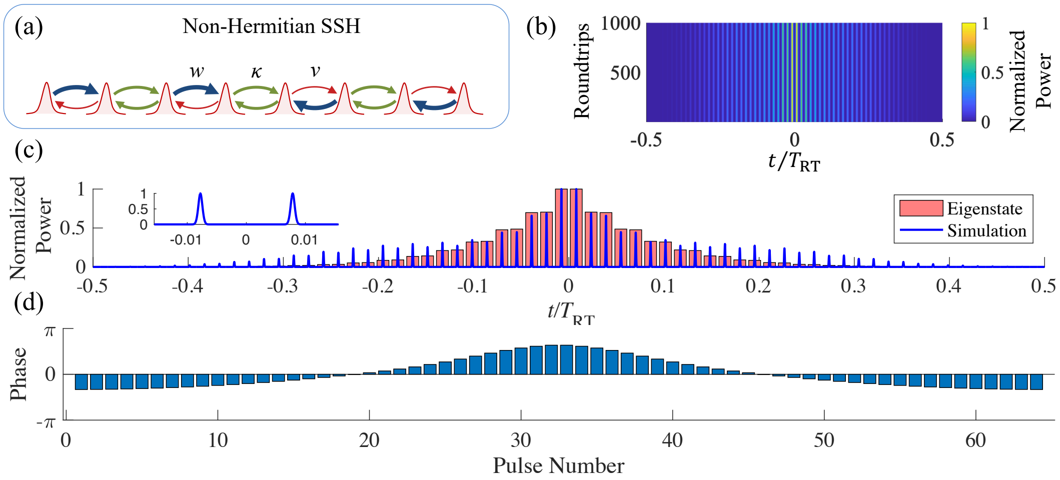

Figure 5.10: Higher Power Lumped Element Simulation of the NH-SSH Domain Wall

Higher Power Lumped Element Simulation of the NH-SSH Domain Wall. **(a)** Schematic of the NH-SSH domain wall. **(b)** Heat map of the final 1000 roundtrips in our simulation. The pulses in the heat map are broadened for visibility. **(c)** The pulse pattern in the steady state is substantially broadened relative to the predictions of our master equation. **(d)** The phases of the pulses on the final roundtrip of the simulation, which reveal the presence of a substantial nonlinear phase shift.

$\kappa = (w + v)/2$. The results of this simulation are shown in Fig. 5.10. Once again, we find that the pulse pattern in the laser is now substantially broader than what we would expect from the prediction of our master equation [Fig. 5.6(c)]. This broadening appears to be a result of the substantial nonlinear phase shift produced by the Kerr nonlinearity [Fig. 5.10(d)].

5.6 Robustness of the Hatano-Nelson Model

Here, we elaborate on the robustness measurements presented in the main text. We first present additional measurements for different realizations of disorder both in the topological, Hatano-Nelson lattice and in the trivial lattice. Then, we provide concrete localization metrics for the non-Hermitian lattices considered in this work, and we establish that the Hatano-Nelson model's sensitivity to the boundary conditions provides sufficient evidence of robustness against disorder-induced localization. Finally, we present simulations of larger lattices to account for finite size effects that can occur in our laser.

Additional Measurements

In Fig. 5.11 we present states measured at the output of our topological temporally mode-locked laser for a Hatano-Nelson lattice with four different realizations of non-Hermitian coupling disorder. As in the main text, we consider a Hatano-Nelson lattice with $w/v = 4$ and disorder nominally distributed according to $\mathrm{Unif}(0, 0.2w)$. In the presence of periodic boundary conditions [Fig. 5.11(a-d)], we observe that the measured state of the laser is distributed throughout the lattice for each realization of disorder. However, when we introduce boundaries at the edges of the Hatano-Nelson lattices [Fig. 5.11(e-h)], we observe that nascent skin modes form near the boundaries of each Hatano-Nelson lattice. As we discussed in the main text, these nascent skin modes precede the occurrence of the non-Hermitian skin effect (NHSE) in the case of perfect open boundary conditions Zhang, Zhesen Yang, and Fang, 2020. The NHSE guarantees the existence of a topological winding number in the lattice with periodic boundary conditions and provides experimental evidence for the claim that the robustness of the Hatano-Nelson model has a topological origin Gong et al., 2018.

In Fig. 5.12, we show additional measurements of the state in our temporally mode-locked laser for the case of a disordered trivial lattice ($w/v = 1$). With periodic boundary conditions [Fig. 5.12(a-d)], the state observed in our laser in general appears not to be spread throughout the lattice. Moreover, in the presence of a boundary [Fig. 5.12(e-h)], the observed state generally appears almost identical to the state with periodic boundary conditions. This lack of sensitivity to the boundary conditions suggests that the trivial lattice enters a localized phase.

The one exception to the general trend in Fig. 5.12 is the states measured in Fig. 5.12(d,h). Here, in the presence of periodic boundary conditions, the state appears to be spread across the lattice, while in the presence of the boundary, the state looks substantially different (although it does not form a nascent skin mode). It is believed that this exception is the result of finite size effects in our laser's synthetic temporal lattice. We examine the consequences of these finite size effects in the next subsection.

Alternative Metric of Localization and Finite Size Effects

Above, and in the main text, we noted the sensitivity of the observed state in the Hatano-Nelson lattice to the boundary conditions is a sign of robustness against disorder-induced localization Hatano and Nelson, 1997; Hatano and Nelson, 1998.

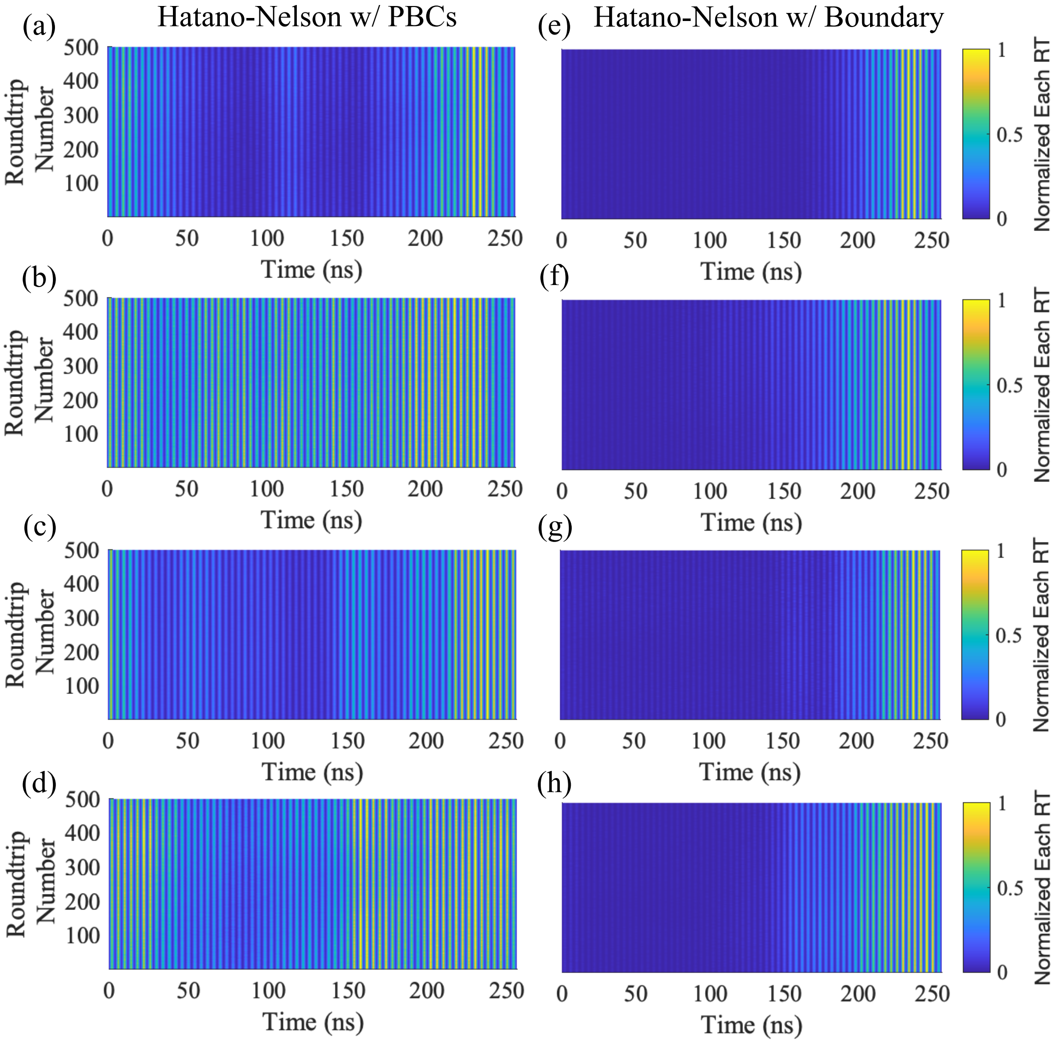

Figure 5.11: Additional Measurements of Disordered Hatano-Nelson Lattices

Additional Measurements of Disordered Hatano-Nelson Lattices. (a-d) Measured states in our topological temporally mode-locked laser for Hatano-Nelson couplings with periodic boundary conditions and different realization of disordered. **(e-h)** The states measured after introducing a boundary in the lattices. In all plots, the pulses are broadened for visibility.

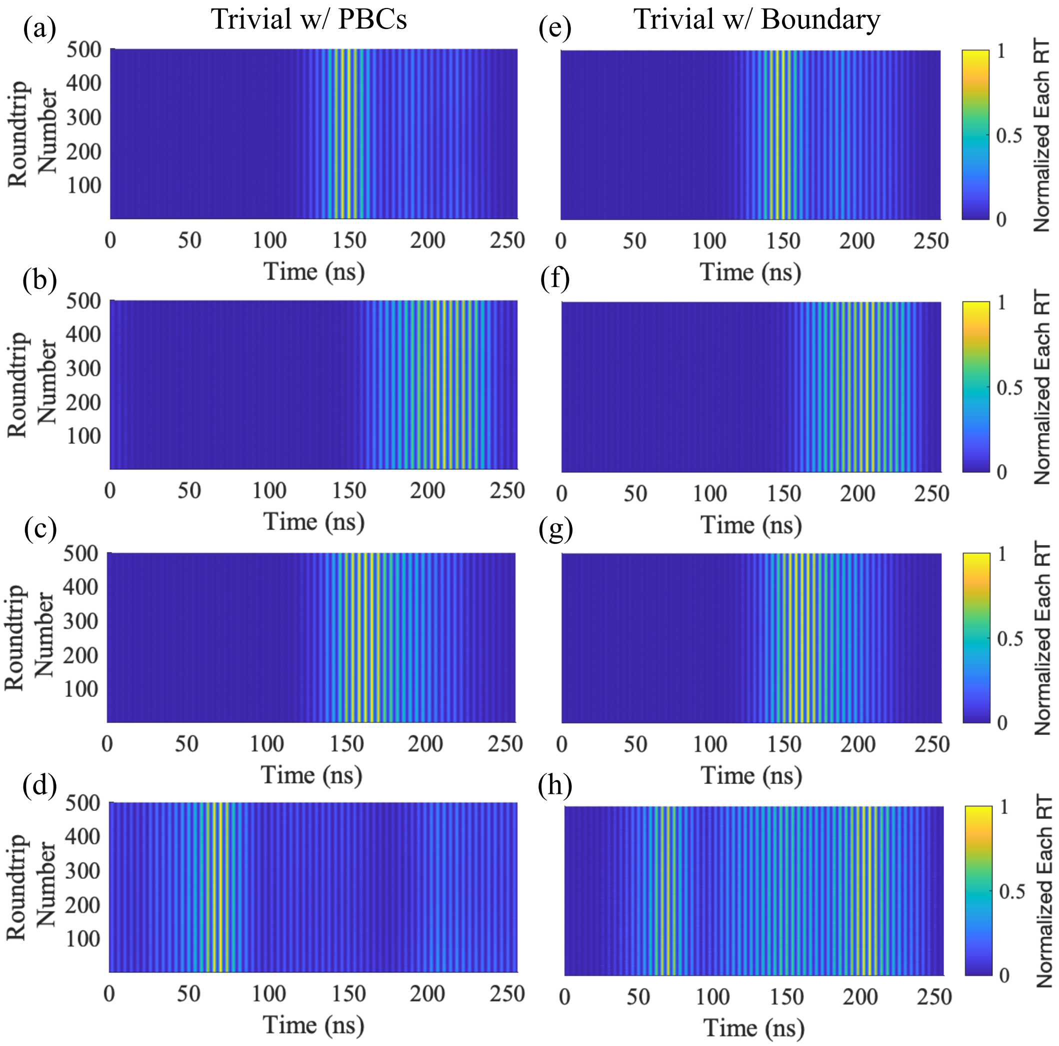

Figure 5.12: Additional Measurements of Disordered Trivial Lattices

Additional Measurements of Disordered Trivial Lattices. (a-d) Measured states in our temporally mode-locked laser for different realizations of non-Hermitian coupling disorder in a trivial lattice with periodic boundary conditions. **(e-h)** The states measured after introducing a boundary in the lattices. In each case, the pulses are broadened for visibility.

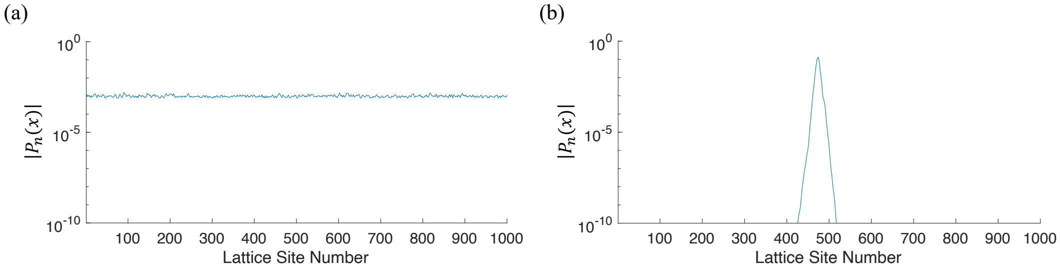

Figure 5.13: Plot of $|P_n(x)|$ for Delocalized and Localized Lattices

Plot of $|P_n(x)|$ for Delocalized and Localized Lattices. **(a)** Plot of the quantity $|P_n(x)|$ for a delocalized Hatano-Nelson lattice with periodic boundary conditions. **(b)** Plot of the quantity $|P_n(x)|$ for a localized trivial lattice with periodic boundary conditions.

Here, we provide another definition of localization, and we show that the Hatano-Nelson lattice studied in the main text appears to satisfy this definition, while the trivial lattice does not. We then show that this alternative definition of localization is consistent with the sensitivity to the boundary conditions used to claim robustness in our experiments.

We base our alternative metric of localization on the work of Hatano and Nelson Hatano and Nelson, 1998. We first recall that, in non-Hermitian quantum mechanics, the right and left eigenstates of a tight-binding Hamiltonian may be written in a biorthogonal basis. In our case, this means that the right eigenvectors $\left|\psi_m^{\mathrm{R}}\right\rangle$ and the left eigenvectors $\left\langle\psi_n^{\mathrm{L}}\right|$ satisfy the relationship

$$\left\langle\psi_n^{\mathrm{L}}\middle|\psi_m^{\mathrm{R}}\right\rangle = \delta_{mn}. \tag{5.16}$$

To define a localization metric in terms of $\left|\psi_m^{\mathrm{R}}\right\rangle$ and $\left\langle\psi_n^{\mathrm{L}}\right|$, we note that the density distribution in such a non-Hermitian quantum mechanical system is given by Hatano and Nelson, 1998

$$P_n(x) = \sum_i^N \left\langle\psi_n^{\mathrm{L}}\middle|x_i\right\rangle \left\langle x_i\middle|\psi_n^{\mathrm{R}}\right\rangle \left|x_i\right\rangle, \tag{5.17}$$

and therefore, from a physical perspective, $P_n(x)$ is the relevant quantity to consider when discussing the delocalized phase of the Hatano-Nelson model.

In Fig. 5.13, we plot the quantity $|P_n(x)|$ for the lowest-loss states of a Hatano-Nelson lattice ($w/v = 4$) and of a trivial lattice ($w/v = 1$). Both lattices contain 1000

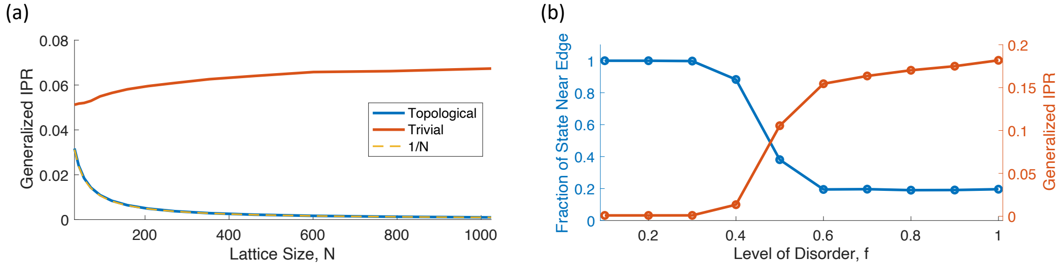

Figure 5.14: Finite Size Effects or Relationship Between Localization Metrics

Finite Size Effects or Relationship Between Localization Metrics. **(a)** Average generalized inverse participation ratios (IPRs) plotted as a function of lattice size for the lowest-loss state of Hatano-Nelson lattices and trivial lattices with coupling disorder. The average generalized IPR of the Hatano-Nelson lattices is fit well by $1/N$, where N is the lattice size. **(b)** The average generalized IPR plotted as a function of disorder, as well as the fraction of the state that lies in the rightmost 20% of a Hatano-Nelson lattice with coupling disorder drawn from $\mathrm{Unif}(0, fw)$.

sites and have additional non-Hermitian coupling disorder distributed according to $\mathrm{Unif}(0, 0.2w)$. Despite the disorder, we observe that $|P_n(x)|$ remains quite uniform across the Hatano-Nelson lattice [Fig. 5.13(a)], which indicates that the state of the Hatano-Nelson lattice is delocalized. In contrast, we see that $|P_n(x)|$ in the trivial lattice is strongly localized. This suggests that the lowest-loss state of the trivial lattice enters a localized phase in the presence of the coupling disorder.

The flatness of $|P_n(x)|$ in the delocalized phase motivates us to define a generalized inverse participation ratio (IPR) to measure the delocalization of our non-Hermitian lattices:

$$\mathcal{L} = \sum_{i}^{N} \left| \langle \psi_n^{\mathrm{L}} | x_i \rangle \langle x_i | \psi_n^{\mathrm{R}} \rangle \right|^2 . \tag{5.18}$$

Observe that $\mathcal{L}$ reduces to the conventional IPR in the case of a Hermitian lattice. If $|P_n(x)|$ remains roughly uniform throughout the lattice in the presence of disorder, then we expect that $\log_{N\to\infty} \mathcal{L} = 0$, where N is the size of the lattice.

In Fig. 5.14(a), we consider a Hatano-Nelson lattice with $w/v = 4$ and coupling disorder distributed according to $\mathrm{Unif}(0, 0.2w)$. We plot the average value of $\mathcal{L}$ over 1000 realizations of disorder for the lowest-loss state of the Hatano-Nelson lattice as a function of the lattice size, and we observe that $\mathcal{L}$ decreases as $1/N$. This behavior confirms that the lowest-loss state of the Hatano-Nelson lattice remains in a delocalized phase in the presence of this level of non-Hermitian coupling disorder.

A similar simulation for the corresponding trivial lattice ($w/v = 1$) shows that the average value of $\mathcal{L}$ increases as a function of N. This indicates that the trivial lattice enters a localized phase in the presence of disorder, and allows us to conclude that the measurements in Fig. 5.12(d,h) were the result of finite size effects.

Plotting $\mathcal{L}$ as a function of the lattice size enables us to conclude that the lowest-loss state of the Hatano-Nelson lattice remains in a delocalized phase for the level of disorder studied in our experiments. However, in practice, we do not have access to $\mathcal{L}$ because, in experiment, we measure the quantity $\sum_i^N \left|\langle x_i|\psi_n^R\rangle\right|^2 |x_i\rangle$. For this reason, we rely on the appearance of nascent skin modes to infer that the Hatano-Nelson lattice remains in a delocalized phase.

In Fig. 5.14(b), we provide evidence that $\mathcal{L}$ is correlated to the occurrence of the NHSE. Here, we plot the average fraction F_{20} of the lowest-loss state that lies in the rightmost 20% of a Hatano-Nelson lattice with $w/v = 4$, open boundary conditions, and coupling drawn from $\mathrm{Unif}(0, fw)$, where we define f as the level of disorder. We see that, for levels of disorder up to $f \approx 0.3$, F_{20} remains extremely close to unity, which suggests that the lowest-loss right eigenstate exhibits the NHSE in this regime. At higher levels of disorder F_{20} decreases rapidly to $\sim 1/5$, which is what we would expect if the lowest-loss state were randomly distributed in the lattice.

Along with F_{20}, in Fig. 5.14(b) we also plot the average generalized IPR $\mathcal{L}$ for the corresponding Hatano-Nelson lattices with periodic boundary conditions. We observe that $\mathcal{L}$ remains relatively flat up to levels of disorder of $f \approx 0.3$. For greater levels of disorder, $\mathcal{L}$ increases rapidly before beginning to level off at larger values of f. The increase in $\mathcal{L}$ indicates that the lowest-loss state of the Hatano-Nelson lattice is entering a localized phase.

The correlation between the drop in F_{20} and the rise in $\mathcal{L}$ leads us to conclude that the appearance of the NHSE is a reliable signature that the lowest-loss state of the Hatano-Nelson lattice with periodic boundary conditions is in a delocalized phase. From this, we conclude that the nascent skin modes observed in our topological temporally mode-locked laser provide sufficient evidence to conclude that the Hatano-Nelson lattice implemented in our laser is robust against disorder-induced localization.

5.7 Potential for Robust Frequency Combs

In the main text, we discussed how temporal mode-locking can stabilize both the relative amplitudes and phases of the pulse train in a harmonically mode-locked laser. Stabilizing the relative phases of the pulses is important from a technological perspective because it can make a harmonically mode-locked laser suitable for frequency domain applications Quinlan et al., 2009. In this section, we use lumped element simulations to explore how topological temporal mode-locking can stabilize the pulse-to-pulse phases of a harmonically mode-locked laser in a way that is robust against disorder.

First, to emphasize the role that temporal mode-locking plays in phase locking the pulses of a harmonically mode-locked laser, we simulate a traditional, harmonically mode-locked laser without intracavity couplings. For this simulation, we use the same parameters that were used in Sec. 5.5, and we use $g_0 = 7.0\ \mathrm{m}^{-1}$. Also, as in Sec. 5.5, we initialize the field in our simulation with noise distributed according to $\mathcal{N}\left(0, 10^{-9}\right) + i\mathcal{N}\left(0, 10^{-9}\right)\ \mathrm{W}^{1/2}$, and, on each roundtrip of the simulation, we inject noise distributed according to the same distribution. We let the simulation to reach steady state, and then we compute the Fourier transform of the final 1000 roundtrips in the steady state. We show our results in Fig. 5.15. As expected, we see that the amplitudes of the mode-locked pulses are uniform [Fig. 5.15(a)] but that the phases are random [Fig. 5.15(b)] due to the presence of noise in the simulation. As a result, the comb lines in the power spectral density have a random nature [Fig. 5.15(c)], which makes such a laser unsuitable for frequency domain applications.

Our simulation results change dramatically once we include temporal mode-locking. In Fig. 5.16(a-c) and Fig. 5.17(a-c), we simulate temporally mode-locked lasers that implement a Hatano-Nelson lattice with $w/v = 10$ and a trivial lattice, respectively. For each lattice, we consider 128 pulses and $g_0 = 2.0\ \mathrm{m}^{-1}$. In each case, we see that the pulse-to-pulse phases are now constant across the pulse trains. Together, these constant phases and amplitudes result in well defined, equally spaced comb lines. In sharp contrast to the laser without temporal mode-locking, the well-defined frequency combs suggest that these lasers could be suitable for frequency domain applications.

While both the topological Hatano-Nelson lattice and the trivial lattice can stabilize the pulse-to-pulses phases in the absence of disorder, we expect that the robustness of the topological Hatano-Nelson lattice will also make the frequency comb in Fig. 5.16(c) robust against disorder. In contrast, we expect that the trivial comb in Fig. 5.17(c) will be sensitive to disorder due to the lack of an Anderson transition in trivial one-dimensional lattices.

To verify this prediction, we simulate the Hatano-Nelson and trivial lattices with

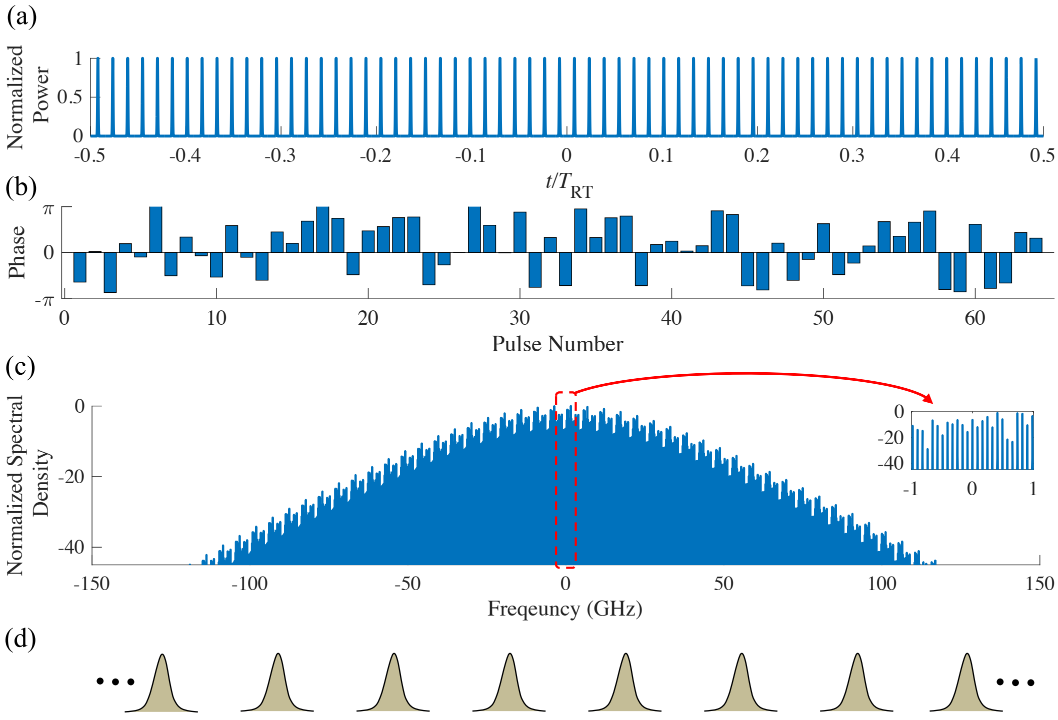

Figure 5.15: Harmonically Mode-Locked Laser without Temporal Mode-Locking

Harmonically Mode-Locked Laser without Temporal Mode-Locking. **(a)** The amplitudes in the harmonically mode-locked laser are uniform. **(b)** In the absence of temporal mode-locking, the phase of the pulses can drift randomly with respect to one another. **(c)** The randomness in the resulting frequency comb makes this laser unsuitable for frequency domain applications. **(d)** The pulses in a harmonically mode-locked laser without intracavity couplings.

additional non-Hermitian coupling disorder distributed according to $\mathrm{Unif}(0, 0.02w)$. Once again, we initialize the field in our simulation with noise distributed according to $\mathcal{N}\left(0, 10^{-9}\right) + i\mathcal{N}\left(0, 10^{-9}\right)$ $\mathrm{W}^{1/2}$, and we inject identically distributed noise on each roundtrip of the simulation. In the presence of the coupling disorder, we observe that the amplitudes and phases of the pulses in the topological Hatano-Nelson lattice remain largely uniform [Fig. 5.16(d,e)]. Zooming in on the central comb lines in the resulting frequency comb, we see that the nearest secondary comb line is still be suppressed by over 34 dB [Fig. 5.16(f)]. In contrast, the amplitudes and phases of the pulses in the trivial lattice are greatly altered by the disorder in the lattice [Fig. 5.17(d,e)]. As a result, when we zoom in on the central comb lines in the resulting frequency comb, we see that the nearest secondary comb line is suppressed by less than 7 dB [Fig. 5.17(f)]. Together, these results in Fig. 5.16 and Fig. 5.17 indicate that topological temporal mode-locking can offer a distinct advantage for

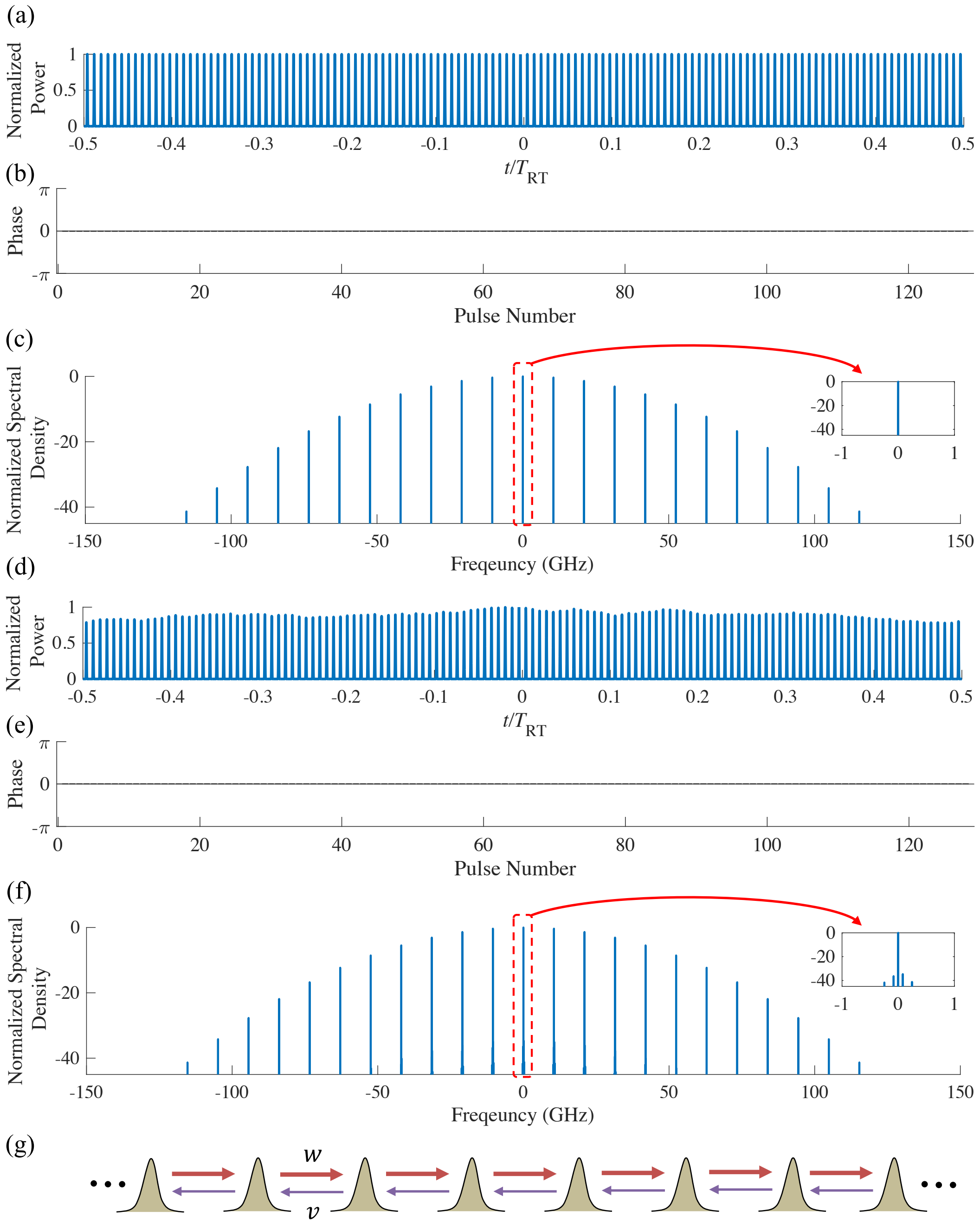

Figure 5.16: Temporal Mode-Locking with Hatano-Nelson Couplings

Temporal Mode-Locking with Hatano-Nelson Couplings. **(a-c)** Without disorder, the topological temporally mode-locked laser exhibits uniform pulse amplitudes, uniform pulse-to-pulse phases, and a well-defined frequency comb. **(d-f)** With the addition of coupling noise, the pulse train is only mildly perturbed, and secondary comb lines remain well suppressed. **(g)** Schematic of the Hatano-Nelson model without disorder.

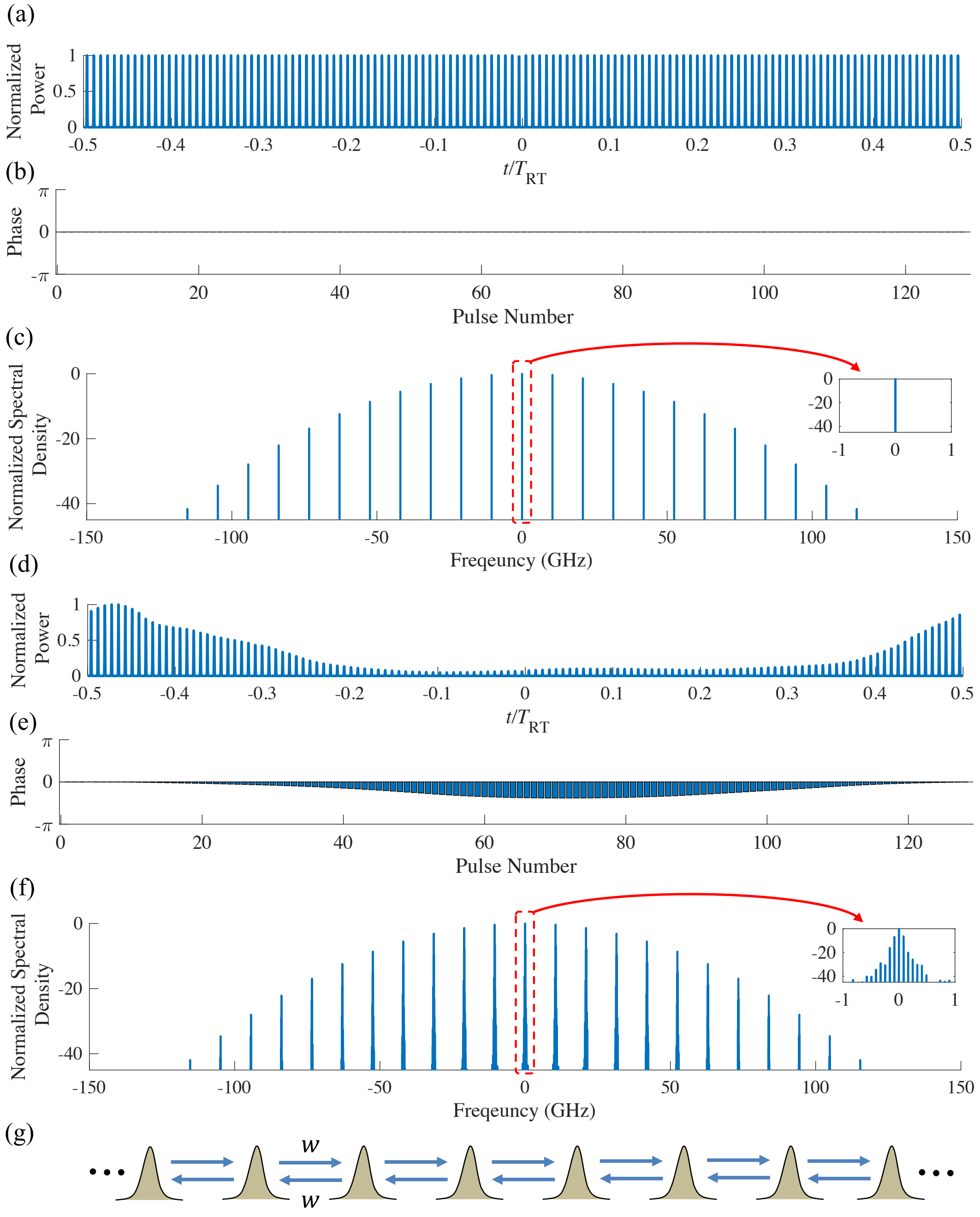

Figure 5.17: Temporal Mode-Locking with Trivial Couplings

Temporal Mode-Locking with Trivial Couplings. **(a-c)** Without disorder, the trivial temporally mode-locked laser exhibits uniform pulse amplitudes, uniform pulse-to-pulse phases, and a well-defined frequency comb. **(d-f)** With coupling disorder, the pulse train is strongly distorted, and the secondary comb lines become prominent. **(g)** Schematic of the trivial lattice without disorder.

building temporally mode-locked frequency combs over its trivial counterpart.

In addition to being robust against disorder in the coupling strengths, we also expect the Hatano-Nelson lattice implemented in our topological temporally mode-locked laser to be robust against disorder in the coupling phases. To illustrate this, we perform additional simulations with random non-Hermitian coupling phase disorder. Here we consider random phases distributed according to $2\pi\mathcal{N}(0, 1/32)$, so that we multiply each direction of each coupling by a term of the form $e^{i\zeta}$, where ζ is the random phase.

The static coupling phase disorder considered here effectively simulates low-frequency pulse-to-pulse phase noise. Therefore, these simulations demonstrate the robustness of our topological frequency comb against low-frequency phase noise.

We perform these simulations using the same parameters as in Sec. 5.5. We use $g_0 = 2\ \text{m}^{-1}$, and we simulate lattices with 64 pulses. As in our other simulations, we initialize the field with noise distributed according to $\mathcal{N}(0, 10^{-9}) + i\mathcal{N}(0, 10^{-9})\ \text{W}^{1/2}$, and we inject identically distributed noise on each roundtrip of the simulation.

In Fig. 5.18 we present a simulation of a topological Hatano-Nelson lattice with $w/v = 10$ and phase noise. In the absence of disorder, we expect to observe a uniform pulse train with uniform phases, as we observed in Fig. 5.16(a,b). In the Hatano-Nelson lattice, we observe that the steady-state amplitudes remain largely uniform in the presence of disorder. Meanwhile, the addition of the phase noise introduces some inhomogeneity in the pulse-to-pulse phases. Despite this inhomogeneity in the phases, we still observe well isolated comb lines in the disordered Hatano-Nelson lattice. Specifically, we find that the largest secondary comb line is suppressed by 13.6 dB relative to the primary comb line.

Our results for the Hatano-Nelson lattice stand in stark contrast to our simulations for a trivial lattice with phase noise. In Fig. 5.19 we present a simulation of a trivial lattice with phase noise. While we expect the pulse-to-pulse amplitudes and phases to be uniform in the absence of disorder, in the presence of phase noise we find that both the pulse-to-pulse amplitudes and phases become inhomogeneous in the trivial lattice. The additional phase noise greatly degrades the quality of the frequency comb produced in this case, and the largest secondary comb line is only suppressed by 1.2 dB relative to the primary comb line.

The degradation of the frequency comb in the disordered trivial lattice relative to that in the disordered Hatano-Nelson lattice strongly suggests that the frequency

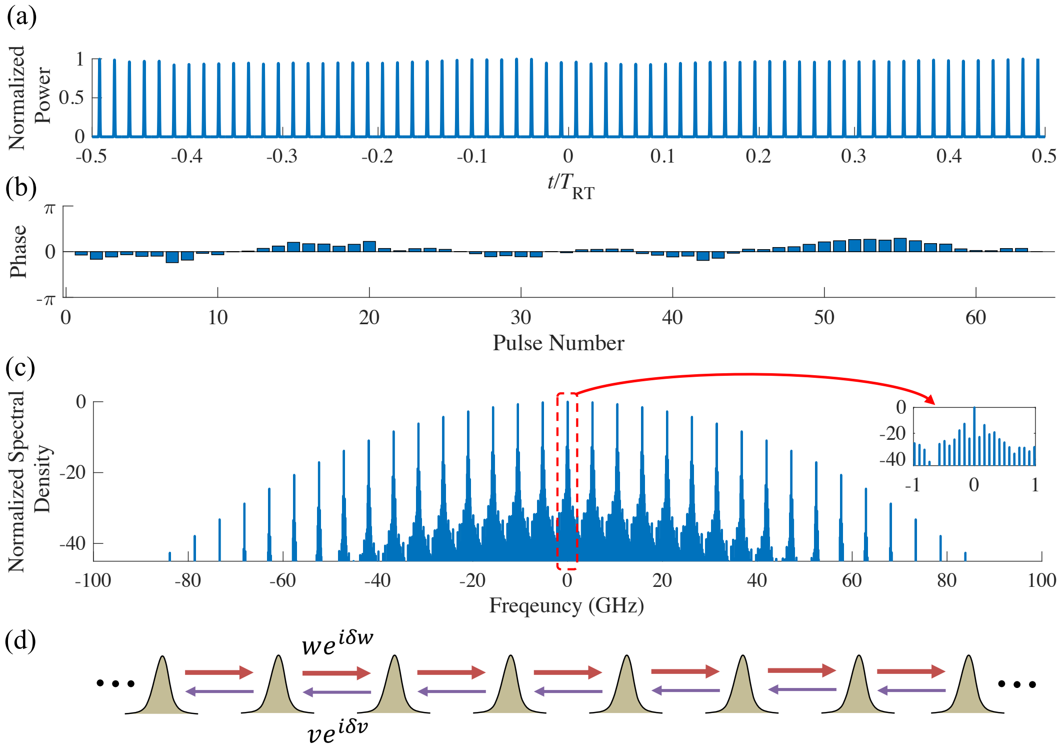

Figure 5.18: Temporal Mode-Locking with Hatano-Nelson Couplings and Phase Disorder

Temporal Mode-Locking with Hatano-Nelson Couplings and Phase Disorder. **(a)** In the presence of coupling phase disorder, the pulse amplitudes in the topological temporally mode-locked laser are only slightly distorted. **(b)** The addition of coupling phase disorder introduces some inhomogeneity in the pulse-to-pulse phases. **(c)** Despite the coupling phase disorder, the secondary comb lines are still suppressed by over 10 dB relative to the primary comb lines. **(d)** Schematic of a topological Hatano-Nelson lattice with non-Hermitian coupling phase disorder.

comb produced by the topological Hatano-Nelson lattice is also robust against the addition of phase noise in the couplings.

5.8 Potential for Sensing Applications

In the main text, we observed that the temporally mode-locked state of our laser can be sensitive to the couplings. We showed this by introducing a boundary into the Hatano-Nelson couplings in our laser and observing that the temporally mode-locked state changed from being uniform to forming a nascent skin mode near the boundary of the lattice. In this section, we propose a model that can potentially exploit the sensitivity of our laser's temporally mode-locked state for sensing.

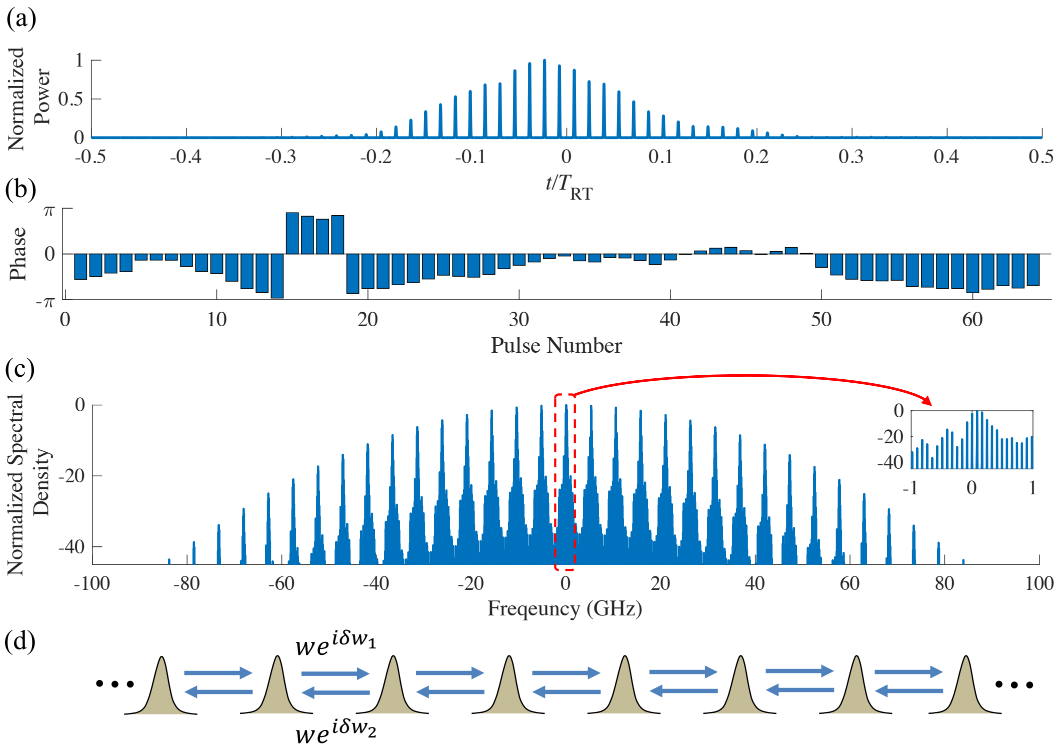

Figure 5.19: Temporal Mode-Locking with Trivial Couplings and Phase Disorder

Temporal Mode-Locking with Trivial Couplings and Phase Disorder. (a) In the presence of coupling phase disorder, the pulse amplitudes in the trivial temporally mode-locked laser are substantially distorted. **(b)** The addition of coupling phase disorder introduces substantial inhomogeneity in the pulse-to-pulse phases. **(c)** Due to the coupling phase disorder, the next largest secondary comb lines are only suppressed by less than 2 dB relative to the primary comb lines. **(d)** Schematic of a trivial lattice with non-Hermitian coupling phase disorder.

We show our proposed model in Fig. 5.20(a). Essentially, this model consists of N independent dimers. The coupling strengths in dimer are asymmetric and, for all the dimers but one, the coupling strengths are w in one direction and $v < w$ in the other. The one remaining dimer, which we call the sensing dimer, has a coupling strength w in one direction and a coupling strength κ in the other. As we illustrate in Fig. 5.20(b), these dimers exhibit the Jordan block form of an exceptional point when $v = \kappa = 0$. However, instead of directly utilizing these exceptional points for sensing, we propose a sensor that relies on changing the coupling strength κ in the sensing dimer relative to the coupling strength v in the remaining dimers.

While the dimers in Fig. 5.20(a) are not directly coupled to one another, in our temporally mode-locked laser they still interact through the laser's nonlocal gain saturation. Therefore, changes in the coupling strength κ in the sensing dimer can

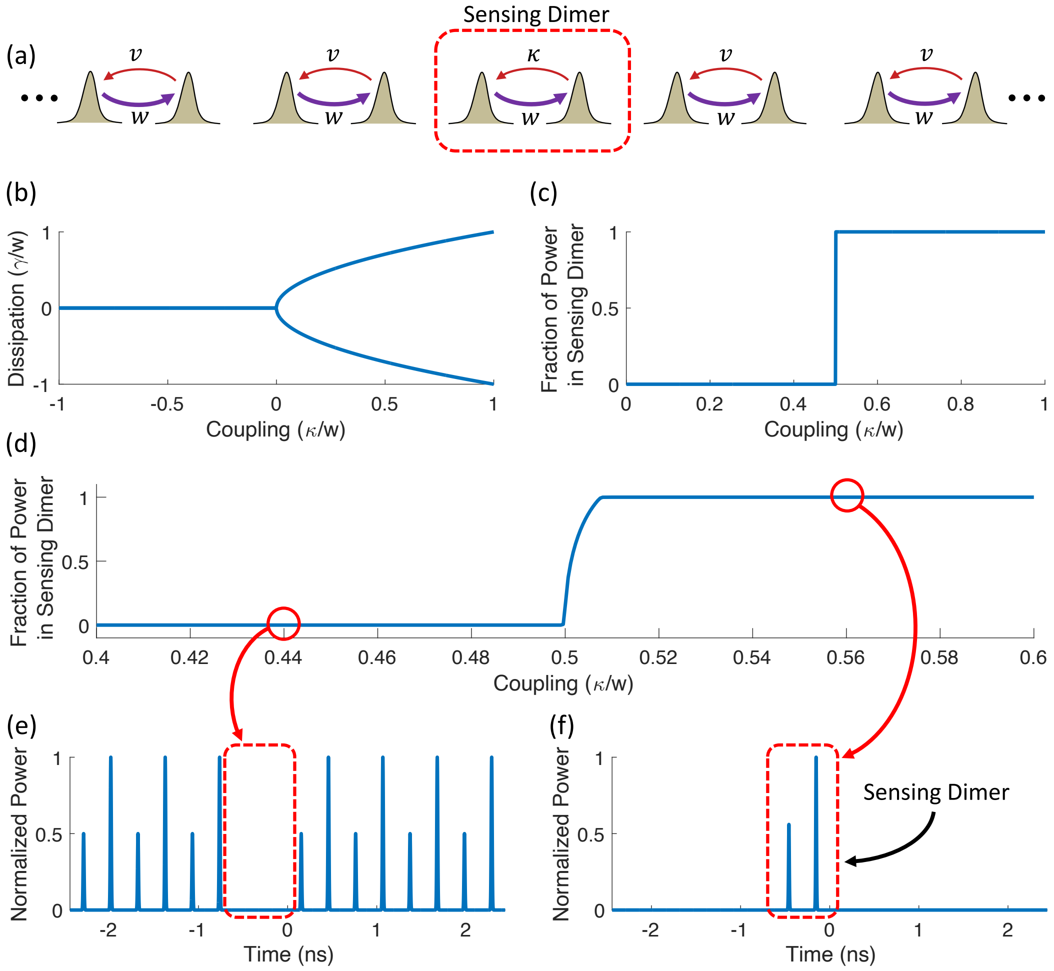

Figure 5.20: Proposed Model for Sensing with a Temporally Mode-Locked Laser

Proposed Model for Sensing with a Temporally Mode-Locked Laser. (a) Proposed model for sensing with a temporally mode-locked laser. **(b)** Eigenvalues of the sensing dimer, showing the presence of an exceptional point when $\kappa = 0$. **(c)** Expected fraction of the laser's power in the sensing dimer as a function of κ, determined from the eigenvalues of the linear lattice. **(d)** Simulated fraction of the laser's power in the sensing dimer as a function of κ with the Kerr nonlinearity included. In (c,d), $v/w = 0.5$. **(e)** Simulated state for $\kappa/w = 0.44$. **(f)** Simulated state for $\kappa/w = 0.56$.

influence the distribution of the laser's power between all the dimers in the system. When $\kappa < v$, the loss in the sensing dimer is greater than that in the other dimers, and we expect that lasing in the sensing dimer will be suppressed. In contrast, when $\kappa > v$, there is less loss in the sensing dimer than in the other dimers, and we expect that the sensing dimer will suppress lasing in the other dimers. We illustrate this in Fig. 5.20(c) by plotting the fraction of the lowest-loss eigenstate that is localized in the sensing dimer as a function of κ (here, $v/w = 0.5$). We see that there is a sharp transition from none of the state being in the sensing dimer to all the state being in the sensing dimer at $\kappa = v$.

Because Fig. 5.20(c) is calculated directly from the eigenstates, it does not include physics of our laser such as the Kerr nonlinearity. Therefore, we perform lumped element simulations of the model in Fig. 5.20(a) to better model the physics in our temporally mode-locked laser. For these simulations, we largely use the same parameters as in Sec. 5.5. However, to reduce the simulation time, we shorten the length of the dispersion shifted fiber to $L_{\text{DSF}} = 0.5$ m, and we only consider 16 pulses (8 dimers). Moreover, we use $g_0 = 4.0\ \text{m}^{-1}$, and we initialize our laser from a uniform background rather than simulating the effect of noise.

In Fig. 5.20(d), we present the results of our simulations. We observe that the Kerr nonlinearity "softens" the transition in the amount of power that localizes in the sensing dimer. Nonetheless, the amount of power localized in the sensing dimer still changes quite suddenly in the vicinity of $\kappa = v$. While additional considerations are necessary to determine whether this sudden change in the power localization can be used to construct a practical sensor, the rapid change observed in these simulations offers some evidence that such a sensor might be possible. Further exploring the possibility of sensing with temporally mode-locked lasers will be an interesting direction for future study.

5.9 Comparison with Earlier Work

In this section, we will compare our topological temporally mode-locked laser to earlier realizations of mode-locked lasers, topological lasers, and temporal synthetic dimensions. Our aim is to clarify how our topological temporally mode-locked laser differs from previous studies and to suggest possible advantages of using our topological temporally mode-locked laser for both practical applications and for studying non-Hermitian topological physics.

We begin by comparing our topological temporally mode-locked laser to "conven-

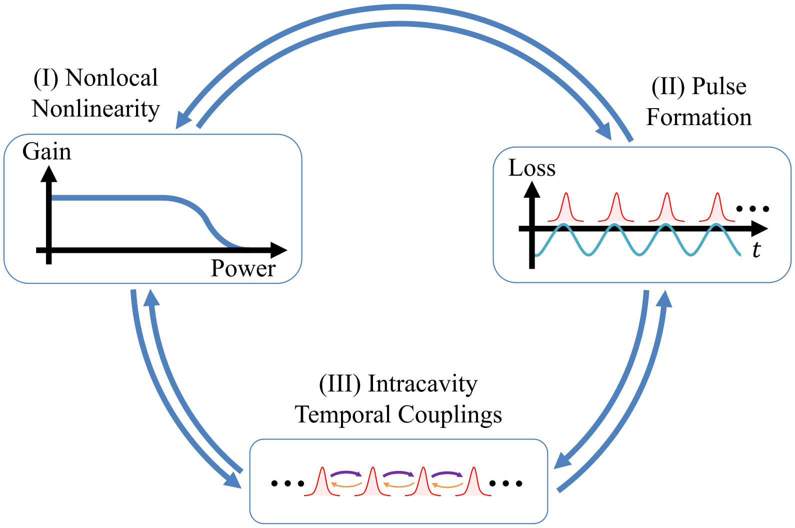

Figure 5.21: Components of a Temporally Mode-Locked Laser

Components of a Temporally Mode-Locked Laser. Temporally mode-locked lasers consist of three basic components: (I) a nonlocal nonlinearity, (II) a pulse formation mechanism, and (III) intracavity temporal couplings. A conventional harmonically mode-locked laser only consists of components (I) and (II).

tional" harmonically mode-locked lasers. Then, we compare our realization of temporal mode-locking to earlier realizations of temporal mode-locking. Third, we compare our topological temporally mode-locked laser with existing topological lasers. Finally, we discuss how our implementation of a temporal synthetic lattice differs from most other implementations of temporal synthetic lattices.

Comparison with Conventional Harmonically Mode-Locked Lasers

In the main text, we mentioned that a temporally mode-locked laser consists of three basic components, which are (I) a nonlocal nonlinearity, (II) a pulse formation mechanism, and (III) intracavity temporal couplings. We represent these three components schematically in Fig. 5.21.

In contrast to a temporally mode-locked laser, a conventional harmonically mode-locked laser only uses (I) a nonlocal nonlinearity and (II) a pulse formation mechanism. In a conventional harmonically mode-locked laser, the nonlocal nonlinearity might be slow gain saturation, while the pulse formation mechanism might be amplitude modulation at a harmonic of the cavity roundtrip frequency.

In the absence of any couplings, the phases of the pulses in the conventional harmonically mode-locked laser can evolve freely from one another, and this can preclude the use of these mode-locked lasers in frequency domain applications Quinlan et al., 2009.

In stark contrast, our temporally mode-locked laser combines (I) a nonlocal nonlinearity and (II) a pulse formation mechanism with (III) intracavity couplings to lock the relative amplitudes and phases of the pulses in our mode-locked laser. As we discussed in Sec. 5.7 and Sec. 5.8, our ability to lock the relative amplitudes and phases can provide both practical advantages over conventional harmonically mode-locked lasers and potentially enable novel applications that leverage the particular dynamics of temporal mode-locking.

Comparison with Other Temporally Mode-Locked Lasers

We use the term "temporal mode-locking" to describe the dynamics of our topological temporally mode-locked laser because we find that the dynamics of our laser are straightforwardly analyzed in terms of the laser's temporal modes. However, a simpler form of temporal mode-locking was previously investigated in mode-locked lasers as a method to suppress unwanted supermodes and to reduce supermode noise. Processes that force lasing in a single supermode are equivalent to temporal mode-locking because a single supermode describes a train of equally spaced, phase-locked pulses.

Two noteworthy architectures previously used intracavity couplings to study temporal mode-locking in harmonically mode-locked lasers. The first used a high-finesse, intracavity etalon to couple consecutive pulses in a mode-locked laser Quinlan et al., 2009; Harvey and Mollenauer, 1993. In the frequency domain, this intracavity etalon filters out all but one of the supermodes in the mode-locked laser. A similar idea was achieved on an integrated platform using an intracavity ring resonator Srinivasan et al., 2014. The second architecture used a composite cavity to suppress unwanted supermodes in a mode-locked laser. A preliminary study of the composite cavity approach found that, while this architecture could suppress many of the supermodes in a mode-locked laser, it did not reduce the average supermode noise O. Pottiez et al., 2002.

A major difference between our temporally mode-locked laser and previous mode-locked lasers with intracavity couplings is the level of complexity that we introduce into temporal mode-locking. Whereas previous efforts focused on isolating a single supermode of a mode-locked laser, we engineer the relative amplitudes and phases of the pulses in our mode-locked laser to realize nonuniform pulse patterns, such

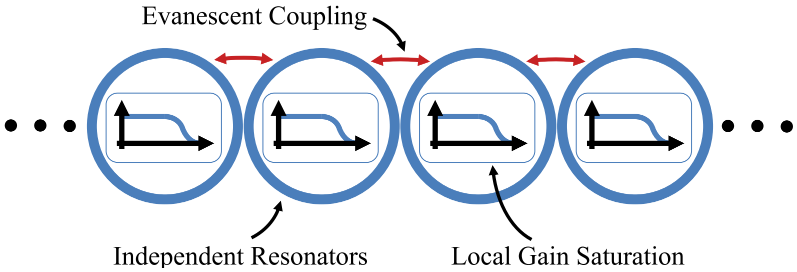

Figure 5.22: Continuous-Wave Topological Lasers

Continuous-Wave Topological Lasers. Many continuous-wave (CW) topological lasers consist of laser arrays composed of independent elements like the ring resonators shown here. Each ring resonator possesses its own gain medium, which saturates independently of the gain in the other resonators.

as the skin modes studied in the main text. Moreover, we show in simulation that topological temporal mode-locking can potentially give rise to robust topological frequency combs. To the best of our knowledge, these phenomena have not been previously explored.

Comparison with Continuous-Wave Topological Lasers

The use of a nonlocal nonlinearity in our topological mode-locked laser is a vital aspect of our work, and it stands in stark contrast to previous work on topological lasers.

Existing topological lasers St-Jean et al., 2017; Parto, Wittek, et al., 2018; Zhao et al., 2018; Bandres et al., 2018 have operated in the continuous-wave (CW) regime and have often relied on architectures like the one in Fig. 5.22. This architecture uses conservatively coupled spatial elements that each possess their own gain media. While these elements are represented by coupled ring resonators in Fig. 5.22, they could also be the components of a photonic crystal Bahari et al., 2017; Zeng et al., 2020; Dikopoltsev et al., 2021. Together, the entire laser array forms a lattice.

Because each element in a CW topological laser contains its own gain medium, the gain saturates independently in each element of the laser array. As a result, experiments with CW topological lasers frequently pump only the edges of a topological laser or some other subset of the laser array to observe lasing in a topological edge state Parto, Wittek, et al., 2018; Bandres et al., 2018; Zeng et al., 2020; Dikopoltsev et al., 2021.

In sharp contrast, in our mode-locked laser, all the sites (pulses) experience gain saturation due to the same gain medium, whose relaxation time is much slower

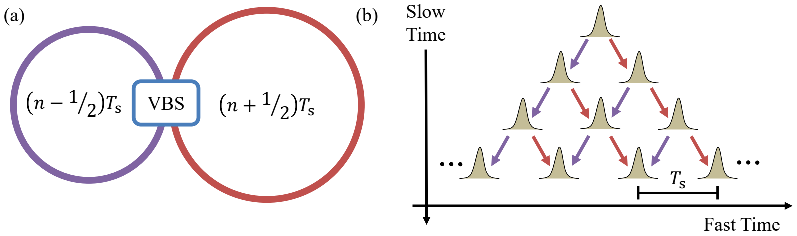

Figure 5.23: Two-Loop Architecture for Photonic Mesh Lattices

Two-Loop Architecture for Photonic Mesh Lattices. (a) The two-loop architecture consists of two fiber loops that are conservatively coupled with a variable beam splitter (VBS). **(b)** When a single pulse is excited in the two-loop architecture, it undergoes a random walk along the fast time axis (the time within a single roundtrip) as it propagates from roundtrip to roundtrip (along the slow time axis). This figure is adapted from that in Regensburger et al., 2012.

than the cavity roundtrip period. In other words, our laser gain acts in a nonlocal way with respect to the topological lattice in our laser. This enables skin modes to spontaneously form in our mode-locked laser without us having to selectively pump the different sites in our synthetic temporal lattice.

Comparison with Two-Loop Architecture

In this subsection, we emphasize the architectural differences between the delay line couplings implemented in our topological temporally mode-locked laser and the "two-loop" architecture used to generate photonic mesh lattices in a temporal synthetic dimension. These differences have major implications for the types of physics that we can study in our temporally mode-locked laser.

In Fig. 5.23(a) we present a schematic of the two-loop architecture. This architecture consists of two fiber loops with staggered lengths that are conservatively coupled with a variable beam splitter. If the separation between two pulses in the mesh lattice is T_S, then the roundtrip delay through the larger loop is $(n+1/2)T_S$, while the roundtrip delay through the shorter loop is $(n-1/2)T_S$, for some integer n. As we show in Fig. 5.23(b), the staggered loop lengths create nearest-neighbor coupling between the sites of the mesh lattice. When a single site is excited, it undergoes a random walk, analogous to what occurs when a single waveguide is excited in a one-dimensional waveguide array.

Our delay line architecture, which we present in Fig. 5.24(a) stands in stark contrast to the two-loop architecture. The delay line architecture consists of a single resonant cavity (the "Main Cavity"), which supports N resonant pulses separted by T_R. On

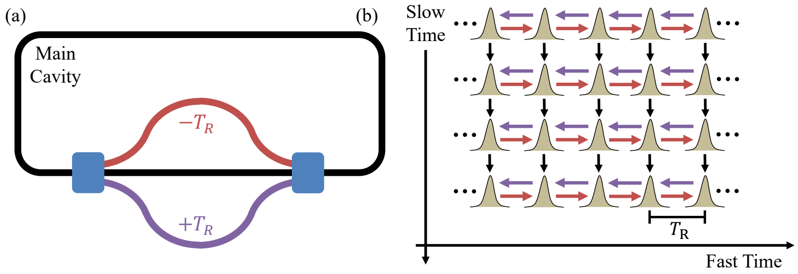

Figure 5.24: Delay Line Architecture for Temporal Synthetic Dimensions

Delay Line Architecture for Temporal Synthetic Dimensions. (a) Our delay line architecture uses optical delay lines to implement dissipative couplings between the sites of a synthetic lattice. The main cavity supports N resonant pulses separated by a repetition period T_R. **(b)** On each roundtrip of the network (the slow time axis), the delay lines couple the sites of the synthetic temporal lattice, which is distributed along the fast time axis (the time within a single roundtrip). The black arrows represent the feedback from the main cavity, which propagates the states in the network from roundtrip to roundtrip.

each roundtrip of the network, a portion of the light in the main cavity is siphoned off and passed through optical delay lines, which are designed to introduce couplings of certain lengths between the pulses in the network. In Fig. 5.24(b), we show how a delay line architecture with two delay lines can implement a one-dimensional synthetic lattice with nearest-neighbor couplings.

For over a decade, this two-loop architecture has enabled many groundbreaking photonic experiments, including photonic demonstrations of parity-time (PT) symmetric lattices Regensburger et al., 2012; Wimmer et al., 2015, topological funneling Weidemann, Kremer, Helbig, et al., 2020, and a topological triple phase transition Weidemann, Kremer, Longhi, et al., 2022. However, there are several reasons why we use the delay line architecture for our topological temporally mode-locked laser rather than the two-loop architecture.

1. *The pulses in the two-loop architecture are not resonant within the individual loops.* In the two-loop architecture, the separation between the pulses in the loops is T_S, but neither loop has a length that is an integer multiple of the pulse-to-pulse separation. This makes the two-loop architecture unsuitable for harmonic mode-locking. In contrast, because the pulses in the delay line architecture are resonant, the main cavity in the delay line architecture may be converted into a harmonically mode-locked laser cavity.

2. *The couplings in the delay line architecture are inherently dissipative and nonreciprocal.* Dissipative couplings are an important feature of our topological temporally mode-locked laser because they enable us to engineer the gain and loss of the different states in our temporal synthetic lattices Leefmans et al., 2022. Nonlocal gain saturation then drives the laser's pulse pattern towards the lowest-loss state defined by the dissipative couplings. For this reason, the dissipative nature of the delay line couplings plays an important role in realizing the dynamics of topological temporal mode-locking.

   The couplings in our delay line architecture are also inherently nonreciprocal because one delay line controls only one direction of the coupling between two pulses. The nonreciprocal nature of the delay line couplings facilitates implementing non-Hermitian topological lattice models, such as the Hatano-Nelson model and the NH-SSH model, in our delay line architecture.

3. *The delay line architecture provides control over the boundary conditions.* Because the main cavity in the delay line architecture is a resonant loop, the "first" pulse sits next to the "last" pulse in our temporal synthetic lattices. This layout facilitates implementing periodic boundary conditions in the delay line architecture, and, by using intensity modulators in the delay lines, we can tune the boundary conditions of our temporal synthetic lattices. In our topological temporally mode-locked laser, this capability enables us to realize a nontrivial point-gap topological winding number in our synthetic Hatano-Nelson lattice and to study the Hatano-Nelson model under different boundary conditions.

   To the best of our knowledge, periodic boundary conditions have not been demonstrated with the two-loop architecture. Therefore, from this perspective, we believe that the delay line architecture may enable access to certain non-Hermitian topological physics that may not be possible to realize with the two-loop architecture.

4. *The delay line architecture is straightforwardly scalable to multiple synthetic dimensions and to lattices with long range couplings.* One major benefit of the delay line architecture studied in this work is its flexibility and scalability Leefmans et al., 2022; Parto, Leefmans, et al., 2023. By including delay lines of different lengths and by carefully engineering the mapping between the pulses in the main cavity and a particular synthetic lattice, the delay line architecture

may be used to implement different lattice types, long-range couplings, and multiple synthetic dimensions.

References

Anderson, P. W. (Mar. 1958). “Absence of Diffusion in Certain Random Lattices”. In: *Phys. Rev.* 109.5. Publisher: American Physical Society, pp. 1492–1505. DOI: `10.1103/PhysRev.109.1492`. URL: `https://link.aps.org/doi/10.1103/PhysRev.109.1492` (visited on 01/04/2022).

Bahari, Babak et al. (Nov. 2017). “Nonreciprocal lasing in topological cavities of arbitrary geometries”. EN. In: *Science*. Publisher: American Association for the Advancement of Science. URL: `https://www.science.org/doi/abs/10.1126/science.aao4551` (visited on 01/05/2022).

Bandres, Miguel A. et al. (Mar. 2018). “Topological insulator laser: Experiments”. EN. In: *Science* 359.6381. Publisher: American Association for the Advancement of Science, eaar4005. DOI: `10.1126/science.aar4005`. URL: `https://www.science.org/doi/abs/10.1126/science.aar4005` (visited on 01/05/2022).

Bergholtz, Emil J., Jan Carl Budich, and Flore K. Kunst (Feb. 2021). “Exceptional topology of non-Hermitian systems”. In: *Rev. Mod. Phys.* 93.1. Publisher: American Physical Society, p. 015005. DOI: `10.1103/RevModPhys.93.015005`. URL: `https://link.aps.org/doi/10.1103/RevModPhys.93.015005` (visited on 01/05/2022).

Black, Eric D. (Jan. 2001). “An introduction to Pound–Drever–Hall laser frequency stabilization”. In: *Am. J. Phys.* 69.1. Publisher: American Association of Physics Teachers, pp. 79–87. ISSN: 0002-9505. DOI: `10.1119/1.1286663`. URL: `https://aapt.scitation.org/doi/10.1119/1.1286663` (visited on 04/08/2022).

Contractor, Rushin et al. (Aug. 2022). “Scalable single-mode surface-emitting laser via open-Dirac singularities”. en. In: *Nature* 608.7924. Number: 7924 Publisher: Nature Publishing Group, pp. 692–698. ISSN: 1476-4687. DOI: `10.1038/s41586-022-05021-4`. URL: `https://www.nature.com/articles/s41586-022-05021-4` (visited on 08/25/2022).

Dikopoltsev, Alex et al. (Sept. 2021). “Topological insulator vertical-cavity laser array”. In: *Science* 373.6562. Publisher: American Association for the Advancement of Science, pp. 1514–1517. DOI: `10.1126/science.abj2232`. URL: `https://www.science.org/doi/10.1126/science.abj2232` (visited on 03/03/2023).

Dutt, Avik et al. (June 2022). “Creating boundaries along a synthetic frequency dimension”. en. In: *Nat Commun* 13.1. Number: 1 Publisher: Nature Publishing Group, p. 3377. ISSN: 2041-1723. DOI: `10.1038/s41467-022-31140-7`. URL: `https://www.nature.com/articles/s41467-022-31140-7` (visited on 08/10/2022).

Englebert, Nicolas et al. (July 2021). “Temporal solitons in a coherently driven active resonator”. en. In: *Nat. Photon.* 15.7. Bandiera_abtest: a Cg_type: Nature Research Journals Number: 7 Primary_atype: Research Publisher: Nature Publishing Group Subject_term: Fibre lasers;Frequency combs;Nonlinear optics;Solitons Subject_term_id: fibre-lasers;frequency-combs;nonlinear-optics;solitons, pp. 536–541. ISSN: 1749-4893. DOI: `10.1038/s41566-021-00807-w`. URL: `https://www.nature.com/articles/s41566-021-00807-w` (visited on 01/06/2022).

Fan, Zhiwei, Danila N. Puzyrev, and Dmitry V. Skryabin (Oct. 2022). “Topological soliton metacrystals”. en. In: *Commun Phys* 5.1. Number: 1 Publisher: Nature Publishing Group, pp. 1–8. ISSN: 2399-3650. DOI: `10.1038/s42005-022-01028-5`. URL: `https://www.nature.com/articles/s42005-022-01028-5` (visited on 10/24/2022).

Gong, Zongping et al. (Sept. 2018). “Topological Phases of Non-Hermitian Systems”. In: *Phys. Rev. X* 8.3. Publisher: American Physical Society, p. 031079. DOI: `10.1103/PhysRevX.8.031079`. URL: `https://link.aps.org/doi/10.1103/PhysRevX.8.031079` (visited on 12/30/2021).

Harvey, G. T. and L. F. Mollenauer (Jan. 1993). “Harmonically mode-locked fiber ring laser with an internal Fabry–Perot stabilizer for soliton transmission”. EN. In: *Opt. Lett.* 18.2. Publisher: Optica Publishing Group, pp. 107–109. ISSN: 1539-4794. DOI: `10.1364/OL.18.000107`. URL: `https://opg.optica.org/ol/abstract.cfm?uri=ol-18-2-107` (visited on 12/19/2022).

Hatano, Naomichi and David R. Nelson (Oct. 1997). “Vortex pinning and non-Hermitian quantum mechanics”. In: *Phys. Rev. B* 56.14. Publisher: American Physical Society, pp. 8651–8673. DOI: `10.1103/PhysRevB.56.8651`. URL: `https://link.aps.org/doi/10.1103/PhysRevB.56.8651` (visited on 04/21/2022).

– (Oct. 1998). “Non-Hermitian delocalization and eigenfunctions”. In: *Phys. Rev. B* 58.13. Publisher: American Physical Society, pp. 8384–8390. DOI: `10.1103/PhysRevB.58.8384`. URL: `https://link.aps.org/doi/10.1103/PhysRevB.58.8384` (visited on 04/21/2022).

Haus, H.A. (Nov. 2000). “Mode-locking of lasers”. In: *IEEE J. Sel. Top. Quantum Electron.* 6.6. Conference Name: IEEE Journal of Selected Topics in Quantum Electronics, pp. 1173–1185. ISSN: 1558-4542. DOI: `10.1109/2944.902165`.

St-Jean, P. et al. (Oct. 2017). “Lasing in topological edge states of a one-dimensional lattice”. en. In: *Nature Photon* 11.10. Bandiera_abtest: a Cg_type: Nature Research Journals Number: 10 Primary_atype: Research Publisher: Nature Publishing Group Subject_term: Polaritons;Semiconductor lasers Subject_term_id: polaritons;semiconductor-lasers, pp. 651–656. ISSN: 1749-4893. DOI: `10.1038/s41566-017-0006-2`. URL: `https://www.nature.com/articles/s41566-017-0006-2` (visited on 01/05/2022).

Jürgensen, Marius, Sebabrata Mukherjee, and Mikael C. Rechtsman (Aug. 2021). "Quantized nonlinear Thouless pumping". en. In: *Nature* 596.7870. Bandiera_abtest: a Cg_type: Nature Research Journals Number: 7870 Primary_atype: Research Publisher: Nature Publishing Group Subject_term: Nonlinear optics;Quantum simulation;Solitons;Topological insulators Subject_term_id: nonlinear-optics;quantum-simulation;solitons;topological-insulators, pp. 63–67. ISSN: 1476-4687. DOI: `10.1038/s41586-021-03688-9`. URL: `https://www.nature.com/articles/s41586-021-03688-9` (visited on 01/05/2022).

Kawabata, Kohei et al. (Oct. 2019). "Symmetry and Topology in Non-Hermitian Physics". In: *Phys. Rev. X* 9.4. Publisher: American Physical Society, p. 041015. DOI: `10.1103/PhysRevX.9.041015`. URL: `https://link.aps.org/doi/10.1103/PhysRevX.9.041015` (visited on 12/30/2021).

Kippenberg, Tobias J. et al. (Aug. 2018). "Dissipative Kerr solitons in optical microresonators". In: *Science* 361.6402. Publisher: American Association for the Advancement of Science, eaan8083. DOI: `10.1126/science.aan8083`. URL: `https://www.science.org/doi/10.1126/science.aan8083` (visited on 10/24/2022).

Le Nguyen Binh and Nam Quoc Ngo (2011). *Ultra-Fast Fiber Lasers: Principles and Applications with MATLAB® Models*. en. 1st ed. CRC Press. URL: `https://www.routledge.com/Ultra-Fast-Fiber-Lasers-Principles-and-Applications-with-MATLAB-Models/Binh-Ngo/p/book/9781138374171` (visited on 01/05/2022).

Leefmans, Christian et al. (Apr. 2022). "Topological dissipation in a time-multiplexed photonic resonator network". en. In: *Nat. Phys.* 18.4. Number: 4 Publisher: Nature Publishing Group, pp. 442–449. ISSN: 1745-2481. DOI: `10.1038/s41567-021-01492-w`. URL: `https://www.nature.com/articles/s41567-021-01492-w` (visited on 04/14/2022).

Li, Guangzhen et al. (Mar. 2023). "Direct extraction of topological Zak phase with the synthetic dimension". en. In: *Light Sci Appl* 12.1. Number: 1 Publisher: Nature Publishing Group, p. 81. ISSN: 2047-7538. DOI: `10.1038/s41377-023-01126-1`. URL: `https://www.nature.com/articles/s41377-023-01126-1` (visited on 04/08/2023).

Lin, Quan et al. (June 2022). "Observation of non-Hermitian topological Anderson insulator in quantum dynamics". en. In: *Nat Commun* 13.1. Number: 1 Publisher: Nature Publishing Group, p. 3229. ISSN: 2041-1723. DOI: `10.1038/s41467-022-30938-9`. URL: `https://www.nature.com/articles/s41467-022-30938-9` (visited on 08/24/2022).

Liu, Yuzhou G. N. et al. (Nov. 2022). "Complex skin modes in non-Hermitian coupled laser arrays". en. In: *Light Sci. Appl.* 11.1. Number: 1 Publisher: Nature Publishing Group, p. 336. ISSN: 2047-7538. DOI: `10.1038/s41377-022-01030-0`. URL: `https://www.nature.com/articles/s41377-022-01030-0` (visited on 12/08/2022).

Longhi, Stefano (Mar. 2019). “Non-Hermitian topological phase transition in *PT*-symmetric mode-locked lasers”. EN. In: *Opt. Lett.* 44.5. Publisher: Optical Society of America, pp. 1190–1193. ISSN: 1539-4794. DOI: `10.1364/OL.44.001190`. URL: `https://www.osapublishing.org/ol/abstract.cfm?uri=ol-44-5-1190` (visited on 12/30/2021).

– (Apr. 2021). “Spectral deformations in non-Hermitian lattices with disorder and skin effect: A solvable model”. In: *Phys. Rev. B* 103.14. Publisher: American Physical Society, p. 144202. DOI: `10.1103/PhysRevB.103.144202`. URL: `https://link.aps.org/doi/10.1103/PhysRevB.103.144202` (visited on 01/05/2022).

Luo, Xunlong, Tomi Ohtsuki, and Ryuichi Shindou (Mar. 2021). “Universality Classes of the Anderson Transitions Driven by Non-Hermitian Disorder”. In: *Phys. Rev. Lett.* 126.9. Publisher: American Physical Society, p. 090402. DOI: `10.1103/PhysRevLett.126.090402`. URL: `https://link.aps.org/doi/10.1103/PhysRevLett.126.090402` (visited on 03/29/2023).

Marandi, Alireza et al. (Dec. 2014). “Network of time-multiplexed optical parametric oscillators as a coherent Ising machine”. en. In: *Nat. Photon.* 8.12. Bandiera_abtest: a Cg_type: Nature Research Journals Number: 12 Primary_atype: Research Publisher: Nature Publishing Group Subject_term: Nonlinear optics;Quantum optics;Ultrafast photonics Subject_term_id: nonlinear-optics;quantum-optics;ultrafast-photonics, pp. 937–942. ISSN: 1749-4893. DOI: `10.1038/nphoton.2014.249`. URL: `https://www.nature.com/articles/nphoton.2014.249` (visited on 01/05/2022).

Mittal, Sunil et al. (Oct. 2021). “Topological frequency combs and nested temporal solitons”. en. In: *Nat. Phys.* 17.10. Number: 10 Publisher: Nature Publishing Group, pp. 1169–1176. ISSN: 1745-2481. DOI: `10.1038/s41567-021-01302-3`. URL: `https://www.nature.com/articles/s41567-021-01302-3` (visited on 04/14/2022).

Parto, Midya, Christian Leefmans, et al. (Mar. 2023). “Non-Abelian effects in dissipative photonic topological lattices”. en. In: *Nat Commun* 14.1. Number: 1 Publisher: Nature Publishing Group, p. 1440. ISSN: 2041-1723. DOI: `10.1038/s41467-023-37065-z`. URL: `https://www.nature.com/articles/s41467-023-37065-z` (visited on 04/08/2023).

Parto, Midya, Steffen Wittek, et al. (Mar. 2018). “Edge-Mode Lasing in 1D Topological Active Arrays”. In: *Phys. Rev. Lett.* 120.11. Publisher: American Physical Society, p. 113901. DOI: `10.1103/PhysRevLett.120.113901`. URL: `https://link.aps.org/doi/10.1103/PhysRevLett.120.113901` (visited on 01/05/2022).

Pottiez, O et al. (Feb. 2002). “Experimental study of supermode noise of harmonically mode-locked erbium-doped fibre lasers with composite cavity”. en. In: *Optics Communications* 202.1-3, pp. 161–167. ISSN: 00304018. DOI: `10.1016/`

S0030-4018(02)01085-4. URL: https://linkinghub.elsevier.com/retrieve/pii/S0030401802010854 (visited on 12/20/2022).

Pottiez, O. et al. (Mar. 2002). “Supermode noise of harmonically mode-locked erbium fiber lasers with composite cavity”. In: *IEEE Journal of Quantum Electronics* 38.3. Conference Name: IEEE Journal of Quantum Electronics, pp. 252–259. ISSN: 1558-1713. DOI: 10.1109/3.985565.

Quinlan, F. et al. (Aug. 2009). “Harmonically mode-locked semiconductor-based lasers as high repetition rate ultralow noise pulse train and optical frequency comb sources”. en. In: *J. Opt. A: Pure Appl. Opt.* 11.10, p. 103001. ISSN: 1464-4258. DOI: 10.1088/1464-4258/11/10/103001. URL: https://dx.doi.org/10.1088/1464-4258/11/10/103001 (visited on 12/16/2022).

Regensburger, Alois et al. (Aug. 2012). “Parity–time synthetic photonic lattices”. en. In: *Nature* 488.7410. Number: 7410 Publisher: Nature Publishing Group, pp. 167–171. ISSN: 1476-4687. DOI: 10.1038/nature11298. URL: https://www.nature.com/articles/nature11298 (visited on 01/05/2023).

Roy, Arkadev, Rajveer Nehra, et al. (Jan. 2022). “Temporal walk-off induced dissipative quadratic solitons”. en. In: *Nat. Photon.* Publisher: Nature Publishing Group, pp. 1–7. ISSN: 1749-4893. DOI: 10.1038/s41566-021-00942-4. URL: https://www.nature.com/articles/s41566-021-00942-4 (visited on 01/31/2022).

Roy, Arkadev, Midya Parto, et al. (Mar. 2022). “Topological optical parametric oscillation”. en. In: *Nanophotonics* 11.8. Publisher: De Gruyter, pp. 1611–1618. ISSN: 2192-8614. DOI: 10.1515/nanoph-2021-0765. URL: https://www.degruyter.com/document/doi/10.1515/nanoph-2021-0765/html (visited on 05/23/2022).

Smirnova, Daria et al. (June 2020). “Nonlinear topological photonics”. In: *Appl. Phys. Rev.* 7.2. Publisher: American Institute of Physics, p. 021306. DOI: 10.1063/1.5142397. URL: https://aip.scitation.org/doi/10.1063/1.5142397 (visited on 01/05/2022).

Song, Yiling et al. (Dec. 2020). “Two-dimensional non-Hermitian Skin Effect in a Synthetic Photonic Lattice”. en. In: *Phys. Rev. Applied* 14.6, p. 064076. ISSN: 2331-7019. DOI: 10.1103/PhysRevApplied.14.064076. URL: https://link.aps.org/doi/10.1103/PhysRevApplied.14.064076 (visited on 07/13/2022).

Srinivasan, Sudharsanan et al. (July 2014). “Harmonically Mode-Locked Hybrid Silicon Laser With Intra-Cavity Filter to Suppress Supermode Noise”. In: *IEEE Journal of Selected Topics in Quantum Electronics* 20.4. Conference Name: IEEE Journal of Selected Topics in Quantum Electronics, pp. 8–15. ISSN: 1558-4542. DOI: 10.1109/JSTQE.2013.2291624.

Su, W. P., J. R. Schrieffer, and A. J. Heeger (June 1979). “Solitons in Polyacetylene”. In: *Phys. Rev. Lett.* 42.25. Publisher: American Physical Society, pp. 1698–1701. DOI: `10.1103/PhysRevLett.42.1698`. URL: `https://link.aps.org/doi/10.1103/PhysRevLett.42.1698` (visited on 01/06/2022).

Tikan, Alexey et al. (Apr. 2022). “Protected generation of dissipative Kerr solitons in supermodes of coupled optical microresonators”. In: *Sci. Adv.* 8.13. Publisher: American Association for the Advancement of Science, eabm6982. DOI: `10.1126/sciadv.abm6982`. URL: `https://www.science.org/doi/full/10.1126/sciadv.abm6982` (visited on 04/12/2022).

Tusnin, A. K., A. M. Tikan, and T. J. Kippenberg (Nov. 2021). “Dissipative Kerr solitons at the edge state of the Su-Schrieffer-Heeger model”. en. In: *J. Phys.: Conf. Ser.* 2015.1, p. 012159. ISSN: 1742-6588, 1742-6596. DOI: `10.1088/1742-6596/2015/1/012159`. URL: `https://iopscience.iop.org/article/10.1088/1742-6596/2015/1/012159` (visited on 02/27/2022).

Tzortzakakis, A. F., K. G. Makris, and E. N. Economou (Jan. 2020). “Non-Hermitian disorder in two-dimensional optical lattices”. en. In: *Phys. Rev. B* 101.1, p. 014202. ISSN: 2469-9950, 2469-9969. DOI: `10.1103/PhysRevB.101.014202`. URL: `https://link.aps.org/doi/10.1103/PhysRevB.101.014202` (visited on 01/04/2022).

Wang, Kai et al. (Mar. 2021). “Generating arbitrary topological windings of a non-Hermitian band”. In: *Science* 371.6535. Publisher: American Association for the Advancement of Science, pp. 1240–1245. DOI: `10.1126/science.abf6568`. URL: `https://www.science.org/doi/10.1126/science.abf6568` (visited on 07/02/2023).

Weidemann, Sebastian, Mark Kremer, Tobias Helbig, et al. (Apr. 2020). “Topological funneling of light”. In: *Science* 368.6488. Publisher: American Association for the Advancement of Science, pp. 311–314. DOI: `10.1126/science.aaz8727`. URL: `https://www.science.org/doi/10.1126/science.aaz8727` (visited on 01/05/2023).

Weidemann, Sebastian, Mark Kremer, Stefano Longhi, et al. (Aug. 2021). “Coexistence of dynamical delocalization and spectral localization through stochastic dissipation”. en. In: *Nat. Photon.* 15.8. Bandiera_abtest: a Cc_license_type: cc_by Cg_type: Nature Research Journals Number: 8 Primary_atype: Research Publisher: Nature Publishing Group Subject_term: Micro-optics;Photonic devices Subject_term_id: micro-optics;photonic-devices, pp. 576–581. ISSN: 1749-4893. DOI: `10.1038/s41566-021-00823-w`. URL: `https://www.nature.com/articles/s41566-021-00823-w` (visited on 01/05/2022).

– (Jan. 2022). “Topological triple phase transition in non-Hermitian Floquet quasicrystals”. en. In: *Nature* 601.7893. Number: 7893 Publisher: Nature Publishing Group, pp. 354–359. ISSN: 1476-4687. DOI: `10.1038/s41586-021-04253-0`. URL: `https://www.nature.com/articles/s41586-021-04253-0` (visited on 06/01/2022).

Wimmer, Martin et al. (July 2015). “Observation of optical solitons in PT-symmetric lattices”. en. In: *Nat Commun* 6.1. Number: 1 Publisher: Nature Publishing Group, p. 7782. ISSN: 2041-1723. DOI: `10.1038/ncomms8782`. URL: `https://www.nature.com/articles/ncomms8782` (visited on 01/05/2023).

Xiao, Lei et al. (July 2020). “Non-Hermitian bulk–boundary correspondence in quantum dynamics”. en. In: *Nat. Phys.* 16.7. Number: 7 Publisher: Nature Publishing Group, pp. 761–766. ISSN: 1745-2481. DOI: `10.1038/s41567-020-0836-6`. URL: `https://www.nature.com/articles/s41567-020-0836-6` (visited on 04/07/2022).

Yang, Zhaoju et al. (Mar. 2020). “Mode-Locked Topological Insulator Laser Utilizing Synthetic Dimensions”. In: *Phys. Rev. X* 10.1. Publisher: American Physical Society, p. 011059. DOI: `10.1103/PhysRevX.10.011059`. URL: `https://link.aps.org/doi/10.1103/PhysRevX.10.011059` (visited on 12/30/2021).

Yao, Shunyu and Zhong Wang (Aug. 2018). “Edge States and Topological Invariants of Non-Hermitian Systems”. In: *Phys. Rev. Lett.* 121.8. Publisher: American Physical Society, p. 086803. DOI: `10.1103/PhysRevLett.121.086803`. URL: `https://link.aps.org/doi/10.1103/PhysRevLett.121.086803` (visited on 01/05/2022).

Yin, Chuanhao et al. (May 2018). “Geometrical meaning of winding number and its characterization of topological phases in one-dimensional chiral non-Hermitian systems”. In: *Phys. Rev. A* 97.5. Publisher: American Physical Society, p. 052115. DOI: `10.1103/PhysRevA.97.052115`. URL: `https://link.aps.org/doi/10.1103/PhysRevA.97.052115` (visited on 01/06/2022).

Zeng, Yongquan et al. (Feb. 2020). “Electrically pumped topological laser with valley edge modes”. en. In: *Nature* 578.7794. Bandiera_abtest: a Cg_type: Nature Research Journals Number: 7794 Primary_atype: Research Publisher: Nature Publishing Group Subject_term: Electrical and electronic engineering;Electronics, photonics and device physics;Optics and photonics Subject_term_id: electrical-and-electronic-engineering;electronics-photonics-and-device-physics;optics-and-photonics, pp. 246–250. ISSN: 1476-4687. DOI: `10.1038/s41586-020-1981-x`. URL: `https://www.nature.com/articles/s41586-020-1981-x` (visited on 01/05/2022).

Zhang, Kai, Zhesen Yang, and Chen Fang (Sept. 2020). “Correspondence between Winding Numbers and Skin Modes in Non-Hermitian Systems”. In: *Phys. Rev. Lett.* 125.12. Publisher: American Physical Society, p. 126402. DOI: `10.1103/PhysRevLett.125.126402`. URL: `https://link.aps.org/doi/10.1103/PhysRevLett.125.126402` (visited on 04/07/2022).

Zhao, Han et al. (Mar. 2018). “Topological hybrid silicon microlasers”. en. In: *Nat Commun* 9.1. Number: 1 Publisher: Nature Publishing Group, p. 981. ISSN: 2041-1723. DOI: `10.1038/s41467-018-03434-2`. URL: `https://www.nature.com/articles/s41467-018-03434-2` (visited on 12/07/2022).

Zykin, A. Y., D. V. Skryabin, and Y. V. Kartashov (May 2021). “Topological solitons in arrays of modelocked lasers”. en. In: *Opt. Lett.* 46.9, p. 2123. ISSN: 0146-9592, 1539-4794. DOI: `10.1364/OL.423666`. URL: `https://opg.optica.org/abstract.cfm?URI=ol-46-9-2123` (visited on 06/06/2022).

Chapter 6

CAVITY SOLITONS ON A LATTICE

6.1 Abstract

Over the past decade, cavity solitons have attracted substantial attention for their rich dynamics and their myriad potential applications. Recently, there has been growing interest in understanding cavity solitons in systems of coupled resonators, where both new physics and applications can emerge. However, despite this interest, cavity solitons have only been experimentally realized in small systems of spatially coupled resonators, and scaling these systems requires overcoming numerous fabrication challenges. Here, we experimentally realize cavity solitons in temporal synthetic lattices. Using the Su-Schrieffer-Heeger (SSH) model as a case study, we find that cavity solitons form preferentially at the boundaries of the lattice when it is in its topologically phase, and we observe the dynamics of coupled cavity solitons that we call soliton pairs. Our work illustrates the rich physics of cavity solitons in synthetic lattices and demonstrates a flexible approach to study cavity solitons in large-scale coupled resonator arrays.

6.2 Introduction

Since their first realization an in optical fiber cavity, cavity solitons have attracted considerable attention for both their rich dynamics and for their potential to enable transformative technologies (e.g., LIDAR, optical clocks, and on-chip spectrometers) (Leo et al., 2010; Kippenberg et al., 2018; Riemensberger et al., 2020; Newman et al., 2019; Bao et al., 2021). While many studies have focused on cavity soliton generation in individual photonic resonators, recently there has been substantial interest in studying cavity solitons in systems of coupled resonators. Preliminary experiments have shown that multi-resonator effects can dramatically influence cavity soliton dynamics, leading to novel phenomena like gear solitons, to practical effects like enhanced conversion efficiencies and tunable frequency combs, and to potential applications like soliton-based memories (Tikan et al., 2021; Komagata et al., 2021; Xue, Zheng, and Zhou, 2019; Helgason et al., 2021; Yuan et al., 2023). However, these experiments, which have utilized spatially coupled ring resonators, have been restricted to small system sizes (fewer than 10 resonators). This has limited the dynamics that they can explore and prevented them from studying the interplay between cavity solitons and lattices of resonators, including those that possess nontrivial topological invariants (Mittal et al., 2021). For this reason, developing an alternative approach to realize cavity solitons in photonic lattices has the potential to both enable and accelerate the general study of cavity solitons in large-scale coupled resonator arrays.

Time-multiplexed resonator networks have emerged as promising platforms for studying large systems of coupled resonators (Leefmans, Dutt, et al., 2022). By leveraging temporal synthetic dimensions (Ozawa and Price, 2019), time-multiplexed networks provide a flexible and scalable architecture for implementing a broad variety of lattices. In the linear regime, these networks have enabled multidimensional dissipative topological lattices (Leefmans, Dutt, et al., 2022), topological invariant measurements (Parto, Leefmans, Williams, Nori, et al., 2023), and non-Hermitian topological sensing (Parto, Leefmans, Williams, and Marandi, 2023). Moreover, time-multiplexed networks have also shown great promise for constructing systems of coupled nonlinear resonators, and they have been adapted to realize both optical Ising machines (Marandi et al., 2014) and a topological temporally mode-locked laser (Leefmans, Parto, et al., 2022). This broad applicability suggests that time-multiplexed networks might also be adapted to study cavity solitons in temporal lattices.

In this work, we use a time-multiplexed resonator network to experimentally study cavity soliton dynamics in temporal lattices. Our experiments focus on the Su-Schrieffer-Heeger (SSH) model (Su, Schrieffer, and Heeger, 1979), which consists of a dimerized, one-dimensional chain with staggered coupling strengths [see Fig. 6.1(a)]. The SSH model is an intriguing system in which to study cavity solitons because it possesses a topologically nontrivial phase. Our study of cavity solitons on SSH lattices reveals two notable phenomena, which we term edge solitons and soliton pairs. Edge solitons form preferentially at the boundaries of our SSH lattice in its topological phase, and they can provide a way distinguish between the topologically trivial and nontrivial phases of the lattice. Meanwhile, soliton pairs arise when solitons form on adjacent sites of our temporal lattice and constructively interfere through our system's dissipative SSH couplings. Our results demonstrate a practical approach to study cavity solitons in large-scale resonator arrays and could enable myriad opportunities to study the interplay between cavity soliton dynamics and lattice physics.

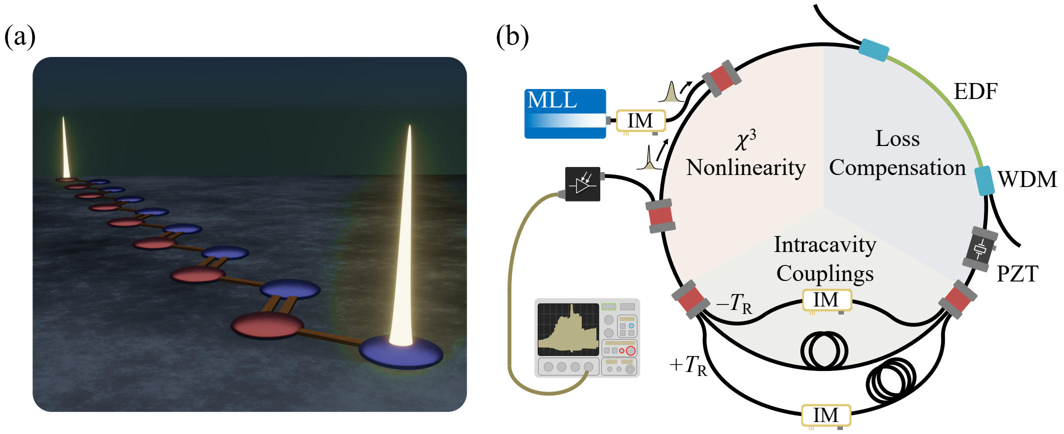

Figure 6.1: Cavity Solitons on a Lattice

Cavity Solitons on a Lattice. (a) Artistic depiction of edge solitons on a Su-Schrieffer-Heeger (SSH) lattice in its topological phase. The SSH lattice consists of a one-dimensional chain with alternating coupling strengths. **(b)** Schematic of the time-multiplexed resonator network used in this work. This network leverages temporal synthetic dimensions to generate lattices capable of supporting cavity solitons.

6.3 Results

To realize cavity solitons on a lattice, we construct the fiber-based time-multiplexed resonator network shown in Fig. 6.1(b). In this network, we use a mode-locked laser to synchronously pump N pulses in a resonant cavity. Each pulse has a width of $\sim$5 ps and a pulse-to-pulse separation of $T_R \approx 8$ ns. During each roundtrip, a portion of each pulse is siphoned off and divided between two delay lines, whose lengths are carefully chosen to produce nearest-neighbor dissipative couplings (Leefmans, Dutt, et al., 2022) between the pulses when the delay lines recombine with the resonant cavity. By letting each pulse in the resonant cavity represent a site in a temporal synthetic lattice, we can map these intracavity couplings to the hopping terms of a tight-binding lattice. Moreover, by using intensity modulators in the delay lines, we can modify these intracavity couplings from pulse-to-pulse, making it is possible to implement couplings that are inhomogeneous, nonreciprocal, and time-varying (Leefmans, Dutt, et al., 2022). In this work, we exploit this flexibility to achieve the staggered couplings of the SSH model.

The intracavity couplings introduced by our network's delay lines enable us to realize synthetic topological lattices, but generating cavity solitons in our network also requires a double balance of gain and loss and of dispersion and self-phase modulation (Kippenberg et al., 2018). While we can use the intrinsic Kerr nonlinearity and

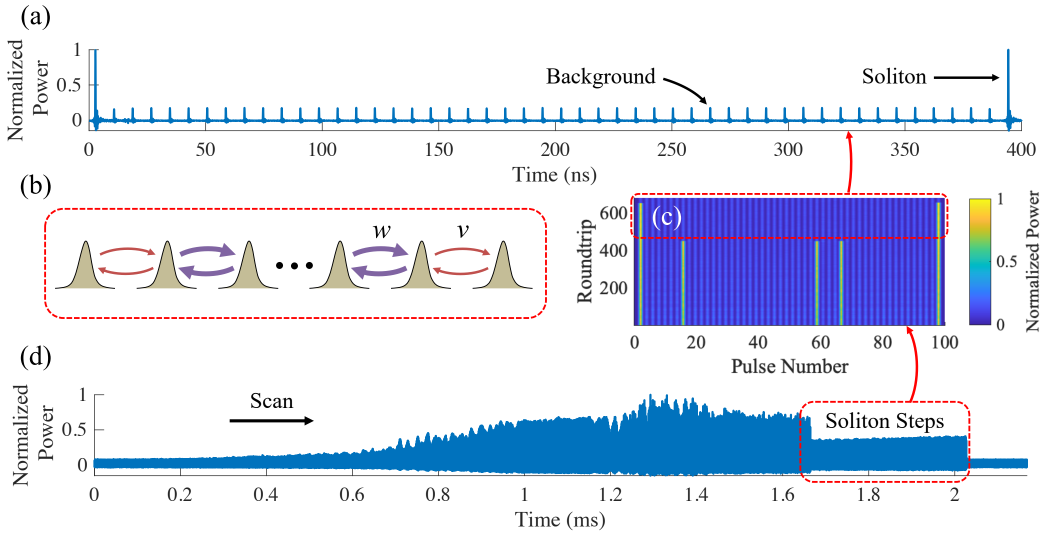

Figure 6.2: Cavity Solitons on an SSH Lattice in the Topological Phase

Cavity Solitons on an SSH Lattice in the Topological Phase. **(a)** A soliton step showing the presence of two edge solitons. This trace is averaged over 150 roundtrips. **(b)** Schematic depiction of an SSH lattice in the topological phase. **(c)** Heat map showing the bulk and edge solitons observed in the resonance under study. Note that the pulses are broadened for visibility. **(d)** The resonance scan corresponding (a) and (c). The inset shows the soliton steps corresponding to the solitons plotted in (c).

group velocity dispersion of our network's fiber to balance the effects of self-phase modulation and the dispersion, the additional losses introduced by the intracavity couplings and various other elements in the network create challenges in terms of balancing the gain and loss. All together, these losses reduce the cavity finesse (without the delay lines) to roughly 1.7. To partially compensate for these losses, we employ an active cavity design (Englebert, Mas Arabí, et al., 2021; Englebert, De Lucia, et al., 2021) by adding a custom section of erbium-doped fiber to our resonant cavity [see Fig. 6.1(b)]. This gain section increases the finesse of our resonant cavity to up to ~ 14.3, which is sufficient to generate cavity solitons in our system. To verify that we observe solitons in our time-multiplexed network, we present spectrum and autocorrelation measurements in Sec. 7.4.

For our experiments, we first program the delay line intensity modulators in our time-multiplexed resonator network to implement a 50-site SSH lattice in the topological phase ($w/v = \sqrt{10} > 1$) [see Fig. 6.2(b)] with open boundary conditions. We drive all 50 sites of the lattice with our mode-locked laser, and we apply a 60 Hz triangular waveform to the cavity's fiber phase shifter [labeled "PZT" in Fig. 6.1(b)] to sweep the cavity length across the optical resonances. Then, using the procedure detailed in Sec. 7.2, we manually tune the length and finesse of our cavity to access an operating regime in which edge solitons appear. An example of these edge solitons is shown in Fig. 6.2(a,c). Here, we clearly see a soliton step in which solitons are present only at the boundaries of the SSH lattice.

We demonstrate the consistency with which these edge solitons form by repeating our measurement procedure multiple times across seven different days. Because our measurement procedure involves tuning the length and finesse of the cavity to find the desired operating regime, the finesse of the main cavity can vary between each measurement. However, we measure a median main cavity finesse of roughly 7.0, a median average driving power[1] in the range of roughly 18.4−18.6 mW, and delay line coupling strength on the order of 15%. For each measurement, we capture resonance scans like that shown in Fig. 6.2(d), and we record whether each resonance in the trace has edge solitons or not. For the topological SSH lattice without additional disorder, we observe 63 resonance scans, 56 of which exhibit solitons on both boundaries, six of which have solitons at only one boundary, and only one which does not have solitons at either boundary[2]. The substantial percentage of resonances that contain solitons on both edges (88.9%) strongly suggests that the dynamics of the system favors edge soliton formation.

Absence of Edge Solitons in a Trivial SSH Lattice

We next modify the couplings of our time-multiplexed resonator network to implement an SSH lattice in the trivial phase ($w/v = 1/\sqrt{10} < 1$), and we observe multiple resonance scans under similar experimental conditions to those used in the topological phase. In the case of the SSH lattice in the trivial phase, we observe 63 resonance scans, and one of these resonance scans is presented in Fig. 6.3(d). Of these scans, no resonances have solitons on both edges, four have a soliton on one edge, 50 have only bulk solitons, and nine exhibit no solitons at all. An example of the bulk solitons captured in the trivial phase is shown in Fig. 6.3(a,c). The low rate of edge soliton formation in the trivial phase (6.2%) suggests that the couplings of the SSH lattice in the topological phase favor edge soliton formation, while the

---

[1] Assuming that the driving pulses are 5 ps Gaussian pulses, the reported average powers correspond to peak powers in the range of 69.3 – 69.6 mW.

[2] Note that all resonance scans reported here with fewer than two edge solitons for both the topological SSH lattices without and with disorder were recorded on the first day of measurements. This suggests that something particular about our measurement procedure on this day led to increased observations of solitons steps with fewer than two edge solitons.

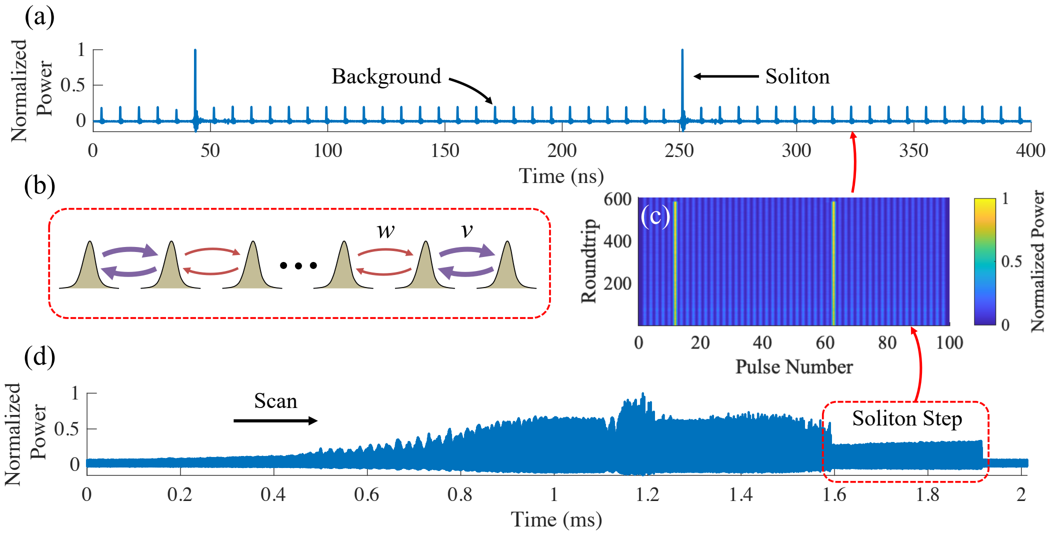

Figure 6.3: Cavity Solitons on an SSH Lattice in the Trivial Phase

Cavity Solitons on an SSH Lattice in the Trivial Phase. **(a)** Trace illustrating the absence of edge solitons in the trivial phase. This trace is averaged over 150 roundtrips. **(b)** Schematic representation of an SSH lattice in the trivial phase. **(c)** Heat map showing the solitons in the trivial phase. The pulses are broadened for visibility. **(d)** Time trace showing the resonance scan corresponding to the solitons presented in (a) and (c). The inset shows the soliton step corresponding to the solitons plotted in (c).

couplings of the SSH lattice in the trivial phase do not.

To gain insight into why edge solitons form preferentially in only the topological phase of the SSH lattice, we record whether the edge solitons or the bulk solitons annihilate at larger detunings in each resonance scan. In 42 of the 63 resonance scans (66.7%) measured in the topological phase of the SSH model, both edge solitons experience a larger existence range than the bulk solitons[3]. In an additional six resonance scans (9.5%), only one edge soliton experiences a larger existence range than the bulk solitons[4]. Furthermore, we find that, when bulk solitons exist at greater detunings than the edge solitons, these bulk solitons tend to occur in pairs that are coupled by the larger of the two SSH couplings (w in the topological phase). Examples of these so-called soliton pairs are visible in Fig. 6.4(a), along with two edge solitons and an isolated bulk soliton. One of the most salient features of Fig. 6.4(a) is that the solitons in each soliton pair have larger intensities than the

---

[3] This includes traces in which bulk solitons are not observed at all.

[4] This does not count two resonance scans for which the existence range of one edge soliton is only slightly greater than that of the bulk solitons. In both instances, there is a bulk soliton directly next to the edge soliton. One of these instances is shown in Fig. 6.5.

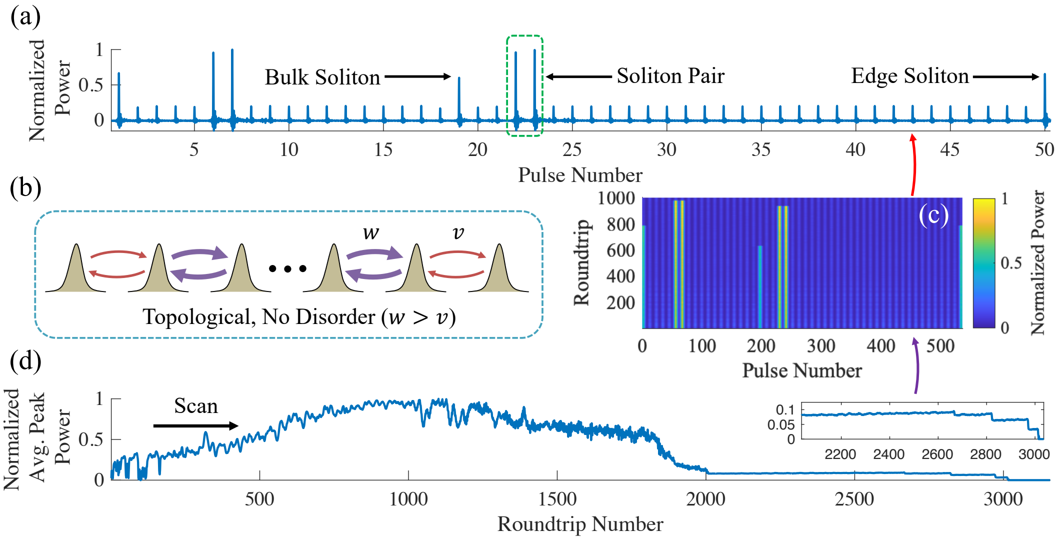

Figure 6.4: Soliton Pairs on an SSH Lattice

Soliton Pairs on an SSH Lattice. **(a)** Time trace showing the solitons that appear in the resonance scan under study. We observe two soliton pairs, which here consist of bulk solitons on neighboring driving pulses that are coupled by the stronger coupling (w) of the SSH lattice. **(b)** Schematic representation of an SSH lattice in the topological phase. **(c)** The soliton pairs exhibit a larger existence region than the isolated solitons in the lattice. **(d)** Time trace showing a resonance scan corresponding to the solitons shown in (a) and (c). The inset shows the soliton steps corresponding to the solitons plotted in (c).

edge solitons, which in turn have larger intensities than the isolated bulk soliton. This difference in intensities offers a possible explanation as to why the different solitons in Fig. 6.4 annihilate at different detunings and why edge solitons form preferentially in the topological phase of the SSH model.

The varying soliton intensities observed in Fig. 6.4(a) suggest that the different existence regions of these solitons are due to phase and amplitude perturbations introduced by the pulse-to-pulse couplings. Ikeda map simulations presented in Sec. 7.5 indicate that the pulse-to-pulse couplings are responsible for producing the intensity differences observed in Fig. 6.4(a). This appears reasonable when we recall that the solitons acquire phase at a different rate than the background driving pulses and that, therefore, coupling between the solitons and the driving pulses is partially destructive. This destructive interference perturbs the solitons, and, if the perturbation is large enough, it can cause the solitons to annihilate.

In our SSH lattice, each isolated bulk soliton is coupled to one driving pulse by the weaker SSH coupling (v in the topological phase) and coupled to one driving pulse by the stronger SSH coupling (w in the topological phase). Therefore, we expect the isolated bulk solitons to experience a stronger coupling perturbation than the edge solitons, which, in the topological phase, are only coupled to one driving pulse by the weaker SSH coupling. This explains why the isolated bulk solitons have lower intensities after the couplings and why they annihilate at smaller detunings. Meanwhile, the larger intensities of the soliton pairs in Fig. 6.4 seems to imply that the solitons within the pairs constructively interfere with one another. It appears that this constructive interference bolsters the solitons against perturbations from the surrounding driving pulses and enables the soliton pairs to exist at greater detunings than the edge solitons.

Similar phase and amplitude perturbations may explain why edge solitons form in the topological phase of the SSH model but not the trivial phase. In the modulation instability regime, the pulses in our synthetic SSH lattice experience varying amplitudes and phases, and they perturb their neighboring pulses through the pulse-to-pulse couplings. As we mentioned above, in the bulk of the SSH lattice, each pulse is coupled to one neighbor by the stronger coupling of the SSH model and to one neighbor by the weaker coupling. At the edges of the SSH lattice, the pulses are coupled to their nearest neighbors by the stronger coupling in the trivial phase and by the weaker coupling in the topological phase. Therefore, both the pulses in the bulk and at the boundary of the trivial lattice appear to experience stronger perturbations relative to the pulses at the boundary of the topological lattice. In the proper operating regime, this appears to create conditions that enable soliton formation at the boundary of the topological lattice while inhibiting soliton formation in the bulk and at the edge of the trivial lattice.

6.4 Outlook

Given that the edge solitons observed in this work exhibit a large degree of overlap with the topological edge states of the SSH model, it is natural to wonder what the relationship is between the edge solitons and the topological edge states. Our experiments show that the edge solitons, like the edge states, occur in the topological phase of the SSH lattice. However, our explanation of the edge solitons in terms of phase and amplitude perturbations suggests that the formation of the edge solitons depends on the perturbations in the immediate vicinity of the boundary and not on the topological phase of the underlying lattice. We confirm that this is the case with Ikeda map simulations in Sec. 7.5, where we simulate soliton formation on a lattice with trivial edge states. With this lattice, we also observe the formation of edge solitons. Therefore, we conclude that, while the observation of edge solitons can distinguish the topological phase of the SSH model from its trivial phase, the presence of nontrivial topology is not necessary to generate edge solitons.

It is also natural to wonder about the relationship between the soliton pairs observed in Fig. 6.4 and the bound solitons previously reported in the literature. In soliton molecules or soliton crystals, soliton binding occurs through the solitons' oscillatory tails (Herink et al., 2017; Cole et al., 2017; Wang et al., 2017). This mechanism can fix the relative positions of the solitons on an otherwise translationally invariant continuous wave background. In stark contrast, the solitons within our soliton pairs constructively interfere with one another through the pulse-to-pulse dissipative couplings of our synthetic lattice. This interference appears to extend the existence range of the solitons within the pair, but any effect on the relative positions of the pulses is not obvious because the soliton positions are already restricted by our use of pulsed driving. In future work, it will be interesting to further study these soliton pairs to uncover what other dynamics, if any, they can exhibit.

In conclusion, we have used time-multiplexed resonator networks to demonstrate a flexible and scalable approach for studying cavity solitons in general systems of coupled resonators, and we used this approach to observe previously unexplored soliton dynamics, which led to the discovery of edge solitons and soliton pairs. From an experimental perspective, the time-multiplexed network utilized in this work presents distinct opportunities to accelerate the study of cavity solitons in coupled resonator arrays, and it may assist in developing practical applications of coupled cavity solitons. Moreover, the ability to controllably add different nonlinearities to time-multiplexed networks opens a door to experimentally realize other types of solitons, such as simultons (Jankowski et al., 2018), in systems of coupled resonators. This capability could contribute to developments in optical gas sensing (Gray et al., 2023). In future work, we will continue to explore how different lattice types can influence soliton dynamics.

6.5 Extended Data

References

Bao, Chengying et al. (Nov. 2021). "Architecture for microcomb-based GHz-mid-infrared dual-comb spectroscopy". en. In: *Nat Commun* 12.1. Number: 1 Publisher: Nature Publishing Group, p. 6573. ISSN: 2041-1723. DOI: `10.1038/s41467-021-26958-6`. URL: `https://www.nature.com/articles/s41467-021-26958-6` (visited on 05/10/2023).

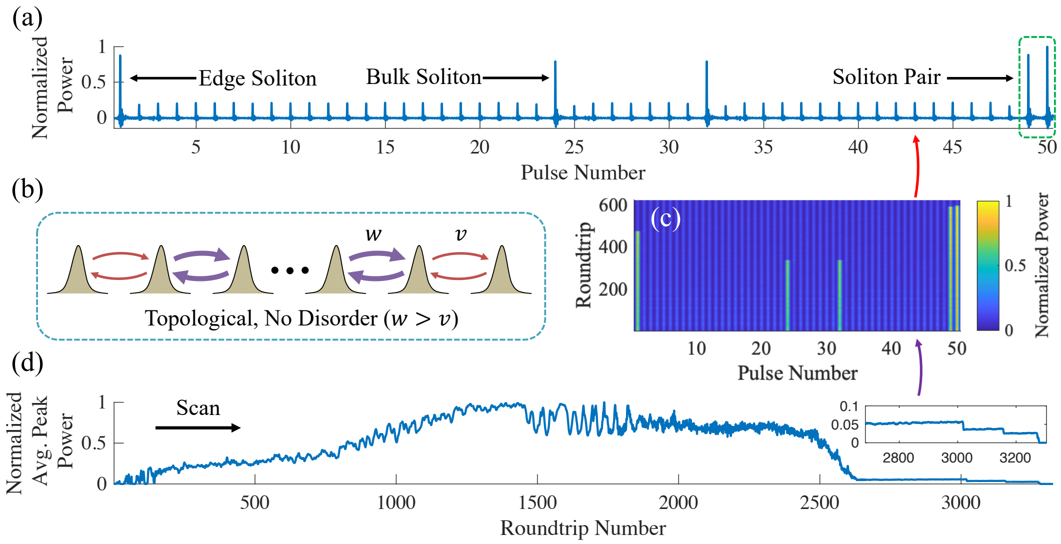

Figure 6.5: Soliton Pair at the Edge of an SSH Lattice

Soliton Pair at the Edge of an SSH Lattice. **(a)** Time trace showing the solitons that appear in the presented resonance scan. We see the emergence of a soliton pair consisting of an edge soliton and its neighboring bulk soliton. Here the solitons are coupled by the weaker coupling of the topological SSH lattice. The solitons appear to interfere constructively because their intensities are larger than those of the isolated solitons in the lattice. **(b)** Schematic representation of an SSH lattice in the topological phase. **(c)** The soliton pairs exhibit a larger existence region than the isolated solitons in the lattice. **(d)** Time trace showing a resonance scan corresponding to the solitons shown in (a) and (c). The inset shows the soliton steps corresponding to the solitons plotted in (c).

Cole, Daniel C. et al. (Oct. 2017). “Soliton crystals in Kerr resonators”. en. In: *Nat. Photon.* 11.10. Bandiera_abtest: a Cg_type: Nature Research Journals Number: 10 Primary_atype: Research Publisher: Nature Publishing Group Subject_term: Frequency combs;Microresonators;Nonlinear optics;Ultrafast lasers Subject_term_id: frequency-combs;microresonators;nonlinear-optics;ultrafast-lasers, pp. 671–676. ISSN: 1749-4893. DOI: `10.1038/s41566-017-0009-z`. URL: `https://www.nature.com/articles/s41566-017-0009-z` (visited on 01/27/2022).

Englebert, Nicolas, Francesco De Lucia, et al. (Nov. 2021). “Parametrically driven Kerr cavity solitons”. en. In: *Nat. Photon.* 15.11. Number: 11 Publisher: Nature Publishing Group, pp. 857–861. ISSN: 1749-4893. DOI: `10.1038/s41566-021-00858-z`. URL: `https://www.nature.com/articles/s41566-021-00858-z` (visited on 03/09/2022).

Englebert, Nicolas, Carlos Mas Arabí, et al. (July 2021). “Temporal solitons in a coherently driven active resonator”. en. In: *Nat. Photon.* 15.7. Bandiera_abtest: a Cg_type: Nature Research Journals Number: 7 Primary_atype: Research Publisher: Nature Publishing Group Subject_term: Fibre lasers;Frequency combs;Nonlinear optics;Solitons Subject_term_id: fibre-lasers;frequency-combs;nonlinear-optics;solitons, pp. 536–541. ISSN: 1749-4893. DOI: `10.1038/s41566-021-00807-w`. URL: `https://www.nature.com/articles/s41566-021-00807-w` (visited on 01/06/2022).

Gray, Robert M. et al. (Jan. 2023). *Cavity-soliton-enhanced mid-IR molecular sensing*. arXiv:2301.07826 [nlin, physics:physics]. DOI: `10.48550/arXiv.2301.07826`. URL: `http://arxiv.org/abs/2301.07826` (visited on 07/21/2023).

Helgason, Óskar B. et al. (Apr. 2021). "Dissipative solitons in photonic molecules". en. In: *Nat. Photonics* 15.4. Number: 4 Publisher: Nature Publishing Group, pp. 305–310. ISSN: 1749-4893. DOI: `10.1038/s41566-020-00757-9`. URL: `https://www.nature.com/articles/s41566-020-00757-9` (visited on 10/21/2022).

Herink, G. et al. (Apr. 2017). "Real-time spectral interferometry probes the internal dynamics of femtosecond soliton molecules". In: *Science* 356.6333. Publisher: American Association for the Advancement of Science, pp. 50–54. DOI: `10.1126/science.aal5326`. URL: `https://www.science.org/doi/full/10.1126/science.aal5326` (visited on 07/13/2022).

Jankowski, Marc et al. (Feb. 2018). "Temporal Simultons in Optical Parametric Oscillators". In: *Phys. Rev. Lett.* 120.5. Publisher: American Physical Society, p. 053904. DOI: `10.1103/PhysRevLett.120.053904`. URL: `https://link.aps.org/doi/10.1103/PhysRevLett.120.053904` (visited on 01/05/2022).

Kippenberg, Tobias J. et al. (Aug. 2018). "Dissipative Kerr solitons in optical microresonators". In: *Science* 361.6402. Publisher: American Association for the Advancement of Science, eaan8083. DOI: `10.1126/science.aan8083`. URL: `https://www.science.org/doi/10.1126/science.aan8083` (visited on 10/24/2022).

Komagata, K. et al. (Dec. 2021). "Dissipative Kerr solitons in a photonic dimer on both sides of exceptional point". en. In: *Commun Phys* 4.1, p. 159. ISSN: 2399-3650. DOI: `10.1038/s42005-021-00661-w`. URL: `http://www.nature.com/articles/s42005-021-00661-w` (visited on 07/17/2022).

Leefmans, Christian, Avik Dutt, et al. (Apr. 2022). "Topological dissipation in a time-multiplexed photonic resonator network". en. In: *Nat. Phys.* 18.4. Number: 4 Publisher: Nature Publishing Group, pp. 442–449. ISSN: 1745-2481. DOI: `10.1038/s41567-021-01492-w`. URL: `https://www.nature.com/articles/s41567-021-01492-w` (visited on 04/14/2022).

Leefmans, Christian, Midya Parto, et al. (Sept. 2022). "Topological Temporally Mode-Locked Laser". In: *arXiv:2209.00762*. arXiv:2209.00762 [cond-mat, physics:physics]. DOI: `10.48550/arXiv.2209.00762`. URL: `http://arxiv.org/abs/2209.00762` (visited on 09/09/2022).

Leo, François et al. (July 2010). "Temporal cavity solitons in one-dimensional Kerr media as bits in an all-optical buffer". en. In: *Nat. Photon.* 4.7. Number: 7 Publisher: Nature Publishing Group, pp. 471–476. ISSN: 1749-4893. DOI: `10.1038/nphoton.2010.120`. URL: `https://www.nature.com/articles/nphoton.2010.120` (visited on 07/01/2022).

Marandi, Alireza et al. (Dec. 2014). "Network of time-multiplexed optical parametric oscillators as a coherent Ising machine". en. In: *Nat. Photon.* 8.12. Bandiera_abtest: a Cg_type: Nature Research Journals Number: 12 Primary_atype: Research Publisher: Nature Publishing Group Subject_term: Nonlinear optics;Quantum optics;Ultrafast photonics Subject_term_id: nonlinear-optics;quantum-optics;ultrafast-photonics, pp. 937–942. ISSN: 1749-4893. DOI: `10.1038/nphoton.2014.249`. URL: `https://www.nature.com/articles/nphoton.2014.249` (visited on 01/05/2022).

Mittal, Sunil et al. (Oct. 2021). "Topological frequency combs and nested temporal solitons". en. In: *Nat. Phys.* 17.10. Number: 10 Publisher: Nature Publishing Group, pp. 1169–1176. ISSN: 1745-2481. DOI: `10.1038/s41567-021-01302-3`. URL: `https://www.nature.com/articles/s41567-021-01302-3` (visited on 04/14/2022).

Newman, Zachary L. et al. (May 2019). "Architecture for the photonic integration of an optical atomic clock". EN. In: *Optica, OPTICA* 6.5. Publisher: Optica Publishing Group, pp. 680–685. ISSN: 2334-2536. DOI: `10.1364/OPTICA.6.000680`. URL: `https://opg.optica.org/optica/abstract.cfm?uri=optica-6-5-680` (visited on 05/10/2023).

Ozawa, Tomoki and Hannah M. Price (May 2019). "Topological quantum matter in synthetic dimensions". en. In: *Nat Rev Phys* 1.5. Bandiera_abtest: a Cg_type: Nature Research Journals Number: 5 Primary_atype: Reviews Publisher: Nature Publishing Group Subject_term: Quantum optics;Topological matter;Ultracold gases Subject_term_id: quantum-optics;topological-matter;ultracold-gases, pp. 349–357. ISSN: 2522-5820. DOI: `10.1038/s42254-019-0045-3`. URL: `https://www.nature.com/articles/s42254-019-0045-3` (visited on 01/05/2022).

Parto, Midya, Christian Leefmans, James Williams, and Alireza Marandi (May 2023). *Enhanced sensitivity via non-Hermitian topology*. arXiv:2305.03282 [physics]. URL: `http://arxiv.org/abs/2305.03282` (visited on 06/21/2023).

Parto, Midya, Christian Leefmans, James Williams, Franco Nori, et al. (Mar. 2023). "Non-Abelian effects in dissipative photonic topological lattices". en. In: *Nat Commun* 14.1. Number: 1 Publisher: Nature Publishing Group, p. 1440. ISSN: 2041-1723. DOI: `10.1038/s41467-023-37065-z`. URL: `https://www.nature.com/articles/s41467-023-37065-z` (visited on 04/08/2023).

Riemensberger, Johann et al. (May 2020). "Massively parallel coherent laser ranging using a soliton microcomb". en. In: *Nature* 581.7807. Number: 7807 Publisher: Nature Publishing Group, pp. 164–170. ISSN: 1476-4687. DOI: `10.1038/s41586-`

020-2239-3. URL: `https://www.nature.com/articles/s41586-020-2239-3` (visited on 05/10/2023).

Su, W. P., J. R. Schrieffer, and A. J. Heeger (June 1979). "Solitons in Polyacetylene". In: *Phys. Rev. Lett.* 42.25. Publisher: American Physical Society, pp. 1698–1701. DOI: `10.1103/PhysRevLett.42.1698`. URL: `https://link.aps.org/doi/10.1103/PhysRevLett.42.1698` (visited on 01/06/2022).

Tikan, A. et al. (May 2021). "Emergent nonlinear phenomena in a driven dissipative photonic dimer". en. In: *Nat. Phys.* 17.5. Number: 5 Publisher: Nature Publishing Group, pp. 604–610. ISSN: 1745-2481. DOI: `10.1038/s41567-020-01159-y`. URL: `https://www.nature.com/articles/s41567-020-01159-y` (visited on 02/27/2022).

Wang, Yadong et al. (Aug. 2017). "Universal mechanism for the binding of temporal cavity solitons". EN. In: *Optica, OPTICA* 4.8. Publisher: Optica Publishing Group, pp. 855–863. ISSN: 2334-2536. DOI: `10.1364/OPTICA.4.000855`. URL: `https://opg.optica.org/optica/abstract.cfm?uri=optica-4-8-855` (visited on 10/24/2022).

Xue, Xiaoxiao, Xiaoping Zheng, and Bingkun Zhou (Sept. 2019). "Super-efficient temporal solitons in mutually coupled optical cavities". en. In: *Nat. Photonics* 13.9. Number: 9 Publisher: Nature Publishing Group, pp. 616–622. ISSN: 1749-4893. DOI: `10.1038/s41566-019-0436-0`. URL: `https://www.nature.com/articles/s41566-019-0436-0` (visited on 10/21/2022).

Yuan, Zhiquan et al. (Jan. 2023). *Soliton pulse pairs at multiple colors in normal dispersion microresonators*. arXiv:2301.10976 [nlin, physics:physics]. URL: `http://arxiv.org/abs/2301.10976` (visited on 05/27/2023).

Chapter 7

SUPPLEMENTARY INFORMATION FOR "CAVITY SOLITONS ON A LATTICE"

7.1 Experimental Setup

In this section we present detailed schematics of the experimental setup used for the soliton step measurements in Ch. 6 and of that used for the spectrum and autocorrelation measurements presented in Sec. 7.4. The primary difference between the two schematics shown in this section is that for the spectrum and autocorrelation measurements we stabilized the system's resonant cavity, while for the soliton step measurements we swept the length of the cavity.

In Fig. 7.1, we show a schematic of the setup used for the soliton step measurements. Here, femtosecond pulses are emitted from a 1550 nm mode-locked laser at a repetition rate of $T_\mathrm{R}/2 \approx 4$ ns. The pulses pass through a 200 GHz filter and are broadened to approximately 5 ps. The pulses then pass through a 90:10 splitter, and 10% of the power is sent to a detector, whose output is filtered and used as a timing reference for our modulator driving electronics. The remaining 90% of the power is amplified with an erbium-doped fiber amplifier (EDFA). After passing through a second 200 GHz filter, which removes amplified spontaneous emission (ASE) noise, the pulses pass through a second 90:10 splitter. Ninety percent of the power from this splitter is sent through our time-multiplexed network in the forward direction. The remaining 10% is sent backward through the network, where it is used to stabilize the delay lines. We will first describe the network's forward propagating path before returning to the backward propagating path.

In the forward propagating direction, light enters the time-multiplexed network through a 99:1 splitter, where 1% of the light is transmitted into the network's main cavity and 99% of the light in the cavity is recirculated. This light passes through a gain section consisting of erbium-doped fiber and then through a 10 nm filter centered at 1550 nm, which is used to shape the gain spectrum in the cavity. The pulses then pass through a fiber phase shifter (FPS), which is used to sweep the length of the cavity; a circulator, which is used to remove light in the backward propagating direction; and a free space delay, which is used to tune the length and finesse of the main cavity. After these elements, the pulses arrive at a 50:50 splitter,

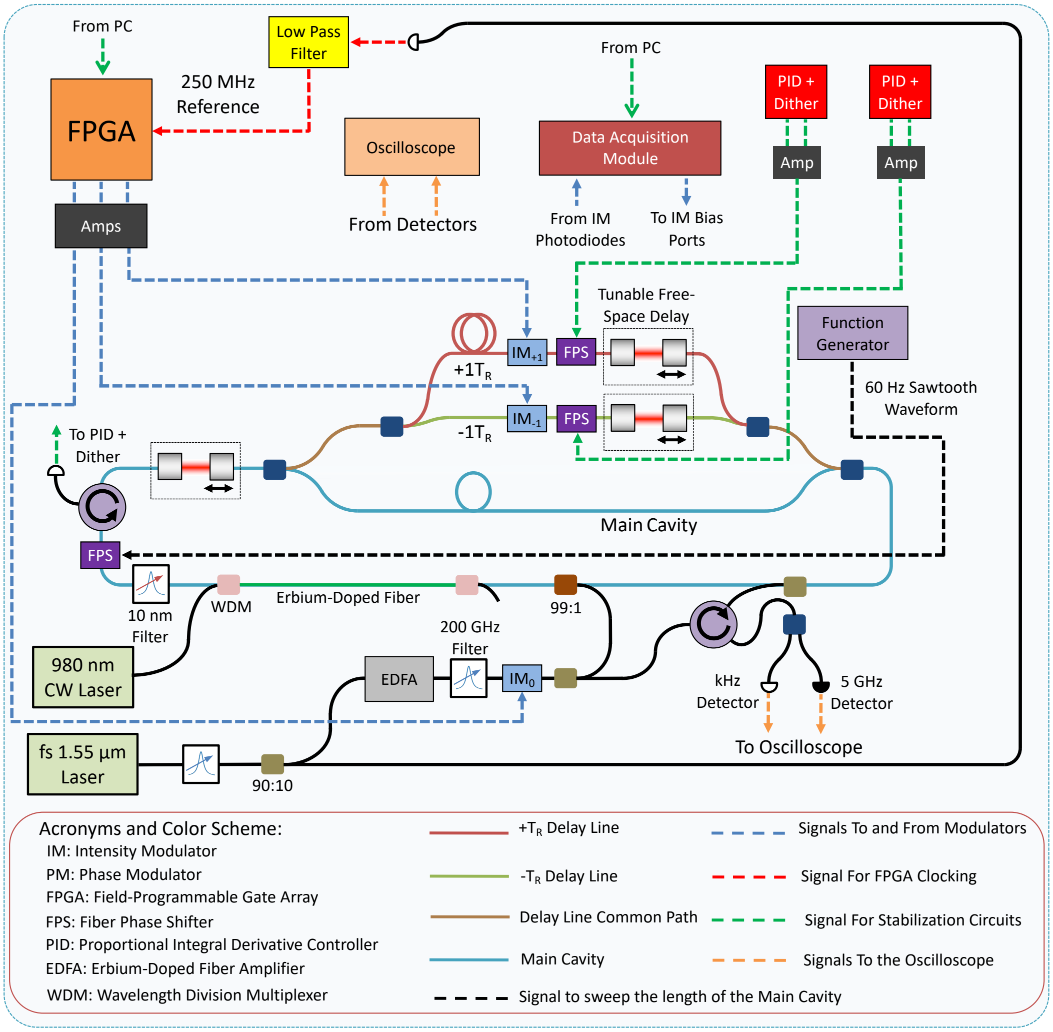

Figure 7.1: Experimental Setup for Soliton Step Measurements

Experimental Setup for Soliton Step Measurements.

which divides the pulses between the main cavity and a common delay line path.

The pulses in the common delay line path are divided between the $\pm 1T_{\mathrm{R}}$ delay lines using another 50:50 splitter. In each delay line, the pulses propagate through an intensity modulator, which is used to control the pulse-to-pulse coupling strength; a fiber phase shifter, which is used to stabilize the coupling phase; and a free space delay, which is used to tune the length of the delay line. After the free space delays, the pulses in the two delay lines are recombined at a 50:50 splitter, and the light from both delay lines is recombined with the main cavity at yet another 50:50 splitter. Finally, 10% of the light in the main cavity is coupled out of the cavity, while 90% is returned to the 99:1 splitter at the input to the cavity. The light coupled out of the cavity passes through a circulator to a 50:50 splitter, where it is divided between a slow (kHz) detector and a fast 5 GHz detector.

The roundtrip time of the main cavity if $T_{\mathrm{RT}} = 68T_{\mathrm{R}} \approx 544$ ns, and therefore our network can support up to a 68 site SSH lattice. During our experiments, we only use 50 of these sites in order to suppress any coupling between the first and final sites of our lattice. This helps to ensure that our synthetic lattice has open boundary conditions.

We now return to the backward propagating path. In the backward direction, the pulses are first sent through the circulator outside the main cavity, and this circulator sends the pulses backwards through the 90:10 splitter at the output of the cavity. This splitter transmits 10% of the backward propagating light into the cavity. These pulses then travel backwards through the main cavity and the delay lines until they reach the circulator in the main cavity. This circulator sends the backwards propagating light to a slow detector, and the signal from this detector for locking both delay lines. We will discuss the stabilization procedure for the delay lines in more depth in Sec. 7.3.

The experimental setup used for our spectrum and autocorrelation measurements is shown in Fig. 7.2. This setup is very similar to that used for the soliton step measurements, but there are several key differences. First, we replace the function generator from Fig. 7.1 with locking electronics. In this configuration, we use the fiber phase shifter in the main cavity to perform a side-of-fringe lock. We will discuss this locking procedure in more depth in Sec. 7.3. Second, we add a tunable filter before the slow detector that monitors the forward-propagating pulses. This filter plays a crucial role in our side-of-fringe locking procedure. Finally, instead of observing the output of our fast detector directly on an oscilloscope, we now send the output to either a spectrum analyzer or an autocorrelator.

7.2 Experimental Procedure

In this section, we describe the procedure that we follow to measure the soliton steps presented in the main text.

As our first step, we check the overlap between the pulses propagating through the delay lines and through the main cavity. To do this, we apply ramp functions to the fiber phase shifters in the delay lines, and we monitor the interference between the backward propagating pulses in the delay lines and the backward propagating pulses in the main cavity. We independently optimize this interference for each delay line.

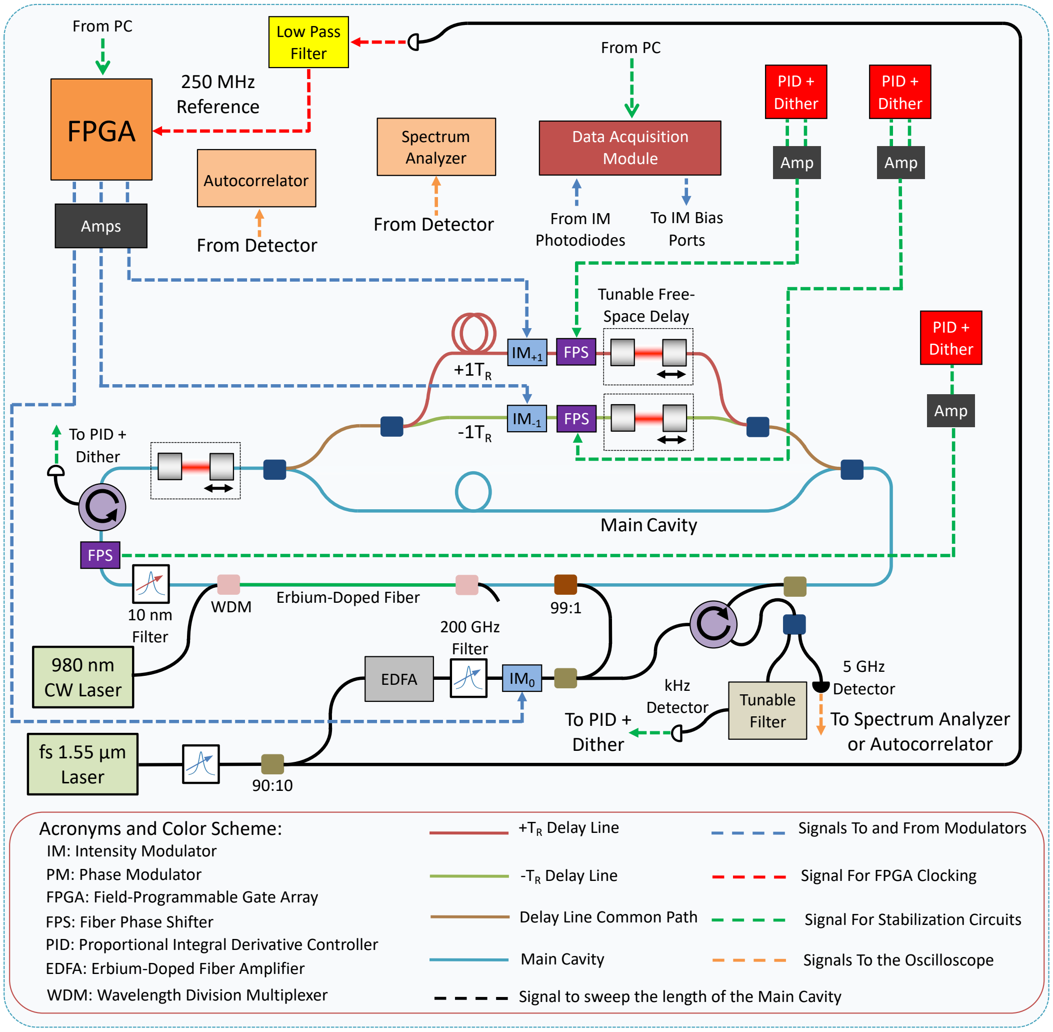

Figure 7.2: Experimental Setup for Spectrum and Auotcorrelation Measurements

Experimental Setup for Spectrum and Auotcorrelation Measurements.

We next proceed to calibrate the delay line intensity modulators.

Our calibration procedure for the delay line intensity modulators (IMs) is complicated by two issues. First, we observe that the optical responses of the delay line modulators exhibits a transient behavior. Therefore, in order to calibrate the responses of the delay line intensity modulators, we need to monitor the delay lines after this transient behavior has completely disappeared. Second, all of the fiber in the main cavity is spliced. In order to accurately calibrate the timing of the delay lines, we must ensure that the path from the mode-locked laser to each intensity modulator is the same as in the experiment. Therefore, during our calibration, we inject light from the mode-locked laser into the main cavity, which then passes into the delay lines. However, because the main cavity is spliced, we cannot open the main cavity to prevent the pulses in the system from resonating. To address these issues, we adopt the two-step procedure described below.

First, we use the fact that the delay line fibers are not spliced to disconnect the common delay line path from where it reconnects with the main cavity. We monitor the output of this path directly with the fast detector in Fig. 7.1. We then perform a preliminary calibration of the delay line modulators in the transitory regime. After blocking the free-space delay of one delay line, we inject a constant train of 100 pulses into the remaining delay line. As these pulses pass through that delay line's intensity modulator, we apply a ramp of voltage pulses to the intensity modulator. We record the optical response of the intensity modulator on our oscilloscope, and we use this information to fit the optical response as a function of the applied voltage. We use this fit to generate a preliminary estimate of the SSH couplings.

For the second step of our procedure, we program the intensity modulator before the input to the main cavity to transmit 50 pulses separated by $T_{\mathrm{R}} \approx 8$ ns on each roundtrip of the network. From our soliton step measurements in the main text, recall that this is equivalent to populating each site of our synthetic SSH lattice equally. Meanwhile, we program the delay line intensity modulators to implement the preliminary SSH couplings derived during the first portion of our calibration procedure. We implement these couplings for several minutes, and we monitor the throughput of one of the delay lines on our oscilloscope. Because the pulses injected into the main cavity are resonant, the amplitudes observed at the output of each delay line fluctuates as the length of the main cavity drifts due to thermal noise. We remedy this by switching our oscilloscope to only trigger when the output of the delay line is approximately at its maximum. We then stop our oscilloscope and measure both the maximum throughput of each delay line as well as the coupling ratio w/v of the SSH couplings. We adjust the maximum couplings of the two delay lines to be roughly the same in both the trivial and topological phases, and we add random noise distributed according to $\mathrm{Unif}(-0.08w, 0.08w)$ in order to study the effect of disorder in our system.

After calibrating our delay line modulators, we reconnect the delay line common path to the main cavity and proceed with our measurement. We program our input intensity modulator to again inject 50 pulses separated by $T_{\mathrm{R}} \approx 8$ ns into the main cavity, and we program the intensity modulators to implement the final SSH couplings from our calibration. We then tune the length and finesse of the main cavity by adjusting the length and coupling of the free-space delay in the main cavity. We tune these parameters until we observe two key features: (1) soliton steps at longer cavity lengths that feature solitons on most or all of the pulses in our 50 site SSH lattice and (2) soliton steps at shorter cavity that also feature solitons on most of the pulses in the SSH lattice. We call such a soliton step at longer cavity lengths a "long cavity reference step," and we refer to a soliton step at shorter cavity lengths as a "short cavity reference step."

We observe that the edge solitons appear at cavity lengths between these two reference steps, and we find this intermediate cavity length as follows. We first decrease the sampling rate on our oscilloscope to 25 MS/s, and we monitor the soliton steps with the output of our slow detector. We tune the cavity length and detuning until we identify a soliton step that resembles the shorter cavity reference steps, and then we tune the cavity towards longer lengths. At some cavity length, the shorter cavity reference steps disappear, and at a slightly longer cavity length, the longer cavity reference steps emerge. After observing the longer cavity reference steps, we can conclude the soliton steps at shorter cavity lengths were indeed the shorter cavity reference steps. At this point, we tune the cavity length to slightly shorter lengths, where the longer cavity reference steps disappear. Here, we often no longer clearly see any soliton step on the output of the slow detector, but we can see hints of solitons present on the undersampled output of the fast detector. We stop tuning the cavity length at this point and increase the sampling rate on the oscilloscope in order to observe the individual pulses on the output of our fast detector. We then detect a single trace on the oscilloscope.

In an effort to methodically represent the differences between the soliton steps that form in the trivial and topological phases of our synthetic SSH lattices, we repeat this tuning procedure before each soliton step measurement. We also use the post-selection procedure described below to discard soliton steps that are not believed to represent the solitons steps between the two reference steps. The three primary reasons that we discard some traces are drift in the main cavity length, drift in the delay line locks, and too few solitons steps being present on a given trace.

We begin our post-selection directly as we adjust the parameters of our oscilloscope to capture a single trace. We visually monitor the locking level on our oscilloscope to ensure that it remains nearly constant while the data is being captured. If the delay line locks are satisfactory, then we inspect the resulting trace on the oscilloscope screen. If we observe a large soliton step that appears to be either one of the reference steps or a precursor to one of the reference steps, we reject the oscilloscope trace. Similarly, we generally reject traces unless there are at least two consecutive soliton steps present in the trace. Our rationale for rejecting these traces is that we can more easily assign a detuning axis to traces that have at least two consecutive soliton steps.

It is important to note that we do not check whether a soliton step has edge solitons or not before rejecting a trace. Our post-selection procedure is performed with the view on the oscilloscope zoomed out to such an extent that we cannot decipher the indvidual pulses on the screen. If we do zoom in on a soliton step to investigate whether the step has edge solitons, then we save that trace.

7.3 Stabilization Procedures

In the first part of this section, we describe our stabilization procedure for the $\pm 1 T_\mathrm{R}$ delay lines. This procedure is implemented both for the soliton step measurements and for the spectrum and autocorrelation measurements presented in Sec. 7.4. In the second part, we discuss our side-of-fringe stabilization procedure for the main cavity. This stabilization procedure is used for the spectrum and autocorrelation measurements but not for the soliton step measurements.

Delay Line Stabilization Procedure

As we mentioned in Sec. 7.1, we stabilize the $\pm 1 T_\mathrm{R}$ delay lines with pulses propagating backwards through our network. During our experiment, the waveform propagating in the backwards direction is the same as that injected into the network in the forward direction: 50 pulses separated by $T_\mathrm{R} \approx 8$ ns. The reason we separate the sites of our synthetic lattice by ~ 8 ns when our laser outputs pules separated by $T_\mathrm{R}/2 \approx 4_\mathrm{ns}$ is so that we can more easily maximize the power that passes through the delay lines in the backwards direction. In particular, while the pulses propagating through the delay lines in the forward direction are modulated to produce the staggered couplings of the SSH model, in the backwards direction, we want all of the pulses to pass through the delay lines with the maximum possible power. We accomplish this by carefully designing our system so that the backward propagating pulses pass through the delay line intensity modulators in different 4 ns windows than the forward propagating pulses. When the backward propagating pulses pass through the intensity modulators, we drive the intensity modulators to produce the maximum throughput. When the forward propagating pulses pass through the intensity modulators, we drive the modulators to produce the couplings of the SSH model.

As we discussed in Sec. 7.1, we remove the backward propagating pulses from the cavity with the circulator in Fig. 7.1. Note that the backward propagating pulses are removed from the cavity before they pass through the section of erbium-doped fiber so that they don't contribute to any gain saturation in the erbium-doped fiber. After leaving the cavity, the pulses are detected with a slow detector. The detector output is both monitored on an oscilloscope (not shown in Fig. 7.1) and sent to the locking electronics depicted in Fig. 7.1.

For our locking electronics, we use a Red Pitaya STEMLabs for each of the delay lines. These modules contain built-in proportional-integral-derivative (PID) controllers that enable us to implement a Pound-Drever-Hall (PDH) locking scheme (Black, 2001). Each Red Pitaya STEMLab produces both the dither and feedback signals for locking a single delay line, and we combine these signals with a custom PCB. We send the combined signal to a piezo driver, where it is amplified, and the amplified signal drives the fiber phase shifter in one of the delay lines.

Main Cavity Stabilization Procedure

To lock the main cavity, we utilize a side-of-fringe locking scheme to stabilize the cavity on a soliton step. To accomplish this, we filter the output from the forward propagating direction of the cavity with a tunable filter. We set the frequency of the filter such that it selects frequencies at an edge of the soliton spectrum. Because the soliton spectrum broadens at greater detunings along the soliton step, the amount of power in the edges of the soliton spectrum increases with greater detunings. Therefore, when we monitor the output of our tunable filter on a slow detector, we observe that the detector signal monotonically increases along the soliton step.

To stabilize the main cavity, we send the output of the slow detector to another Red Pitaya STEMLab. Using the fact that the detector signal monotonically increases along the soliton step, we implement a side-of-fringe locking scheme to stabilize the cavity length in the soliton regime. Once both the main cavity and the delay lines are stabilized, we can measure the average autocorrelation and spectrum of the coupled solitons in the network.

As an aside, we note that we found it easiest to lock the main cavity and delay lines simultaneously when we injected pulses into the network at the repetition period

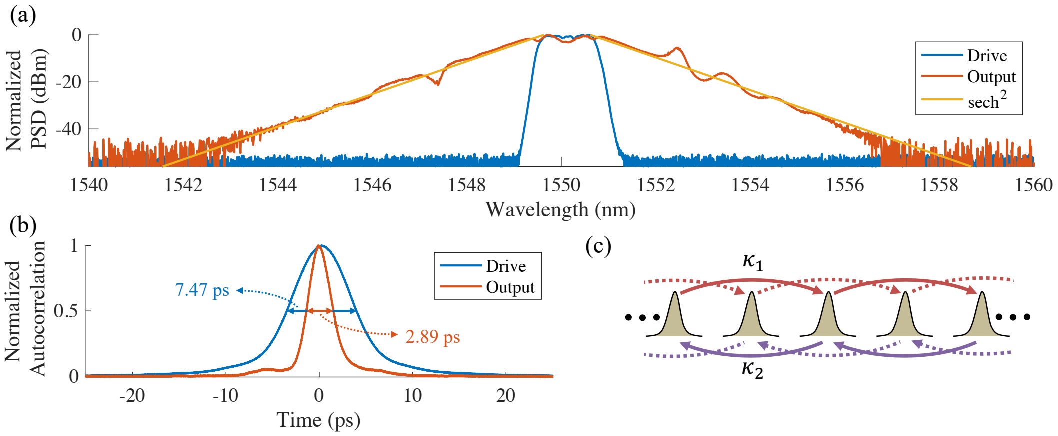

Figure 7.3: Spectrum and Autocorrelation Measurements

Spectrum and Autocorrelation Measurements. (a) Measured spectrum of the cavity output in the presence next-nearest-neighbor intracavity couplings. The spectrum is substantially broadened with respect to that of the coherent drive, and it is well fit by a sech^2 function. **(b)** Measured autocorrelation of the cavity output. **(c)** Schematic illustration of the couplings implemented for the measurements in (a) and (b).

of our laser $T_{\mathrm{R}}/2 \approx 4$ ns. In this operating regime, we implement two interleaved lattices with nearest-neighbor coupling [see Fig. 7.3].

7.4 Spectrum and Autocorrelation Measurements

In this section, we present spectrum and autocorrelation measurements of coupled solitons in our network. It is important to note that these are measurements are averaged over all of the pulses in the network.

As we mentioned in Sec. 7.3, it is easiest to stabilize the main cavity when we reduce the pulse-to-pulse separation to $T_R/2 \approx 4$ ns. Therefore, for our autocorrelation and spectrum measurements, we program the intensity modulator outside of the main cavity to transmit every pulse from our mode-locked laser. We also set the delay line modulators to implement constant couplings for all of the pulses. In this operating regime, our network essentially implements two interleaved lattices with constant nearest-neighbor couplings. Each lattice consists of $N = 68$ pulses, meaning that there are a total of $N = 136$ pulses in the cavity. We schematically depict these interleaved lattices in Fig. 7.3(c).

With the main cavity and the delay lines locked using the procedures outlined in Sec. 7.3, we perform our spectrum and autocorrelation measurements. The results of these measurements are shown in Figs. 7.3(a,b). We find that the measured spectrum is well fit by a sech^2 function, while the full-width-half-maximum of the measured autocorrelation is compressed by a factor of ~ 2.58 relative to that of the driving pulses. Together, these measurements offer compelling evidence that we observe coupled cavity solitons in our system.

7.5 Soliton Simulations

Ikeda Map Simulations

In this section, we consider Ikeda map simulations (Ikeda, 1979; Anderson et al., 2017) of cavity solitons in a time-multiplexed resonator array. These simulations account for the fact that the couplings in our experiment occur discretely on every roundtrip of the network.

On each roundtrip, our Ikeda map simulations implement the following steps. First, we model the injection of equally spaced driving pulses into our cavity with the equation

$$\psi_n = \sqrt{\kappa} E_{\mathrm{IN}} + \sqrt{1-\alpha} e^{-1i\delta} \psi_{n-1}. \tag{7.1}$$

Here ψ_n represents the intracavity field on the n^{th} roundtrip, κ represents the input coupling strength, E_{IN} is the driving field, α models all roundtrip losses, and δ is the detuning. In our simulations, we initialize each point in ψ_0 according to the distribution $1/\sqrt{2}\left[\mathcal{N}(0,10^{-5}) + i\mathcal{N}(0,10^{-5})\right]$, where $\mathcal{N}(\mu,\sigma)$ is the normal distribution with mean μ and standard deviation σ. We also inject noise distributed according to this distribution on each roundtrip. In addition, we let $\kappa = 0.1$ and $\alpha = 0.7$. We let E_{IN} consist of 16 equally spaced, 5 ps Gaussian pulses with peak powers of 75 W, and we sweep the detuning from $\delta = -2$ to $\delta = 5$ in 350 equally spaced steps.

After modeling the injection of the drive into our cavity, we simulate propagation through a 112 m cavity with the nonlinear Schrödinger equation (Anderson et al., 2017),

$$\partial\psi_n \partial z = -\frac{\beta_2}{2}\frac{\partial^2\psi_n}{\partial t^2} + 1i\gamma \left|\psi\right|^2 \psi, \tag{7.2}$$

where z represents the transverse coordinate of the cavity, t is a fast time variable, β_2 is the group velocity dispersion, and γ represents the nonlinear coefficient. For our simulations, we use the parameters $\beta_2 = -2.0 \times 10^{-2}$ ps^{2}m^{-1} and $\gamma = 1.0 \times 10^{-3}$ W^{-1}m^{-1}.

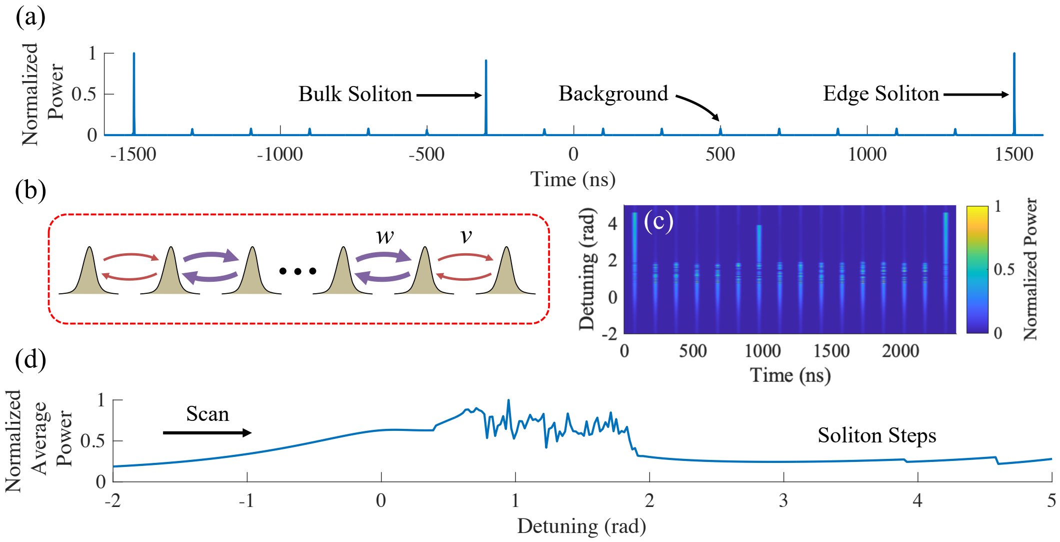

Figure 7.4: Ikeda Map Simulation of an SSH Lattice in the Topological Phase

Ikeda Map Simulation of an SSH Lattice in the Topological Phase.
(a) Roundtrip trace corresponding to the simulated SSH lattice at $\delta = 2.5$.
(b) Schematic illustration of an SSH lattice in the topological phase. **(c)** Heat map showing the evolution of the pulse amplitudes throughout the simulation.
(d) Average power as the cavity is scanned from blue to red detuning.

Finally, to conclude each roundtrip, our Ikeda map simulations implement intracavity couplings between the pulses in ψ. We accomplish this by dividing ψ into 16 equally-spaced time bins and coupling the time bins with SSH model couplings. In our simulations, we implement these couplings with $\max(w, v) = 0.15$ and $\min(w, v) = \max(w, v)/\sqrt{10}$.

In Fig. 7.4 we present an Ikeda map simulation of an SSH lattice in the topological phase [Fig. 7.4(b)]. We find that the system passes through a region of modulation instability before exhibiting solitons [Fig. 7.4(c,d)]. For the seed selected for this simulation, we observe edge solitons as well as a single bulk soliton [Fig. 7.4(a,c)]. This soliton annihilates before the edge solitons, leaving a region where our synthetic SSH lattices possesses only edge solitons [Fig. 7.4(c)].

We contrast the simulation in Fig. 7.4 with that of a trivial SSH lattice, which is shown in Fig. 7.5. For the seed chosen for this simulation, we observe two bulk solitons and no edge solitons [Fig. 7.5(a,c)]. For numerous other seeds, we also observed no edge solitons when simulating the trivial phase of the SSH lattice. Therefore, our simulations appear to confirm our conclusion that the appearance of edge solitons can distinguish the topological phase of the SSH model from the

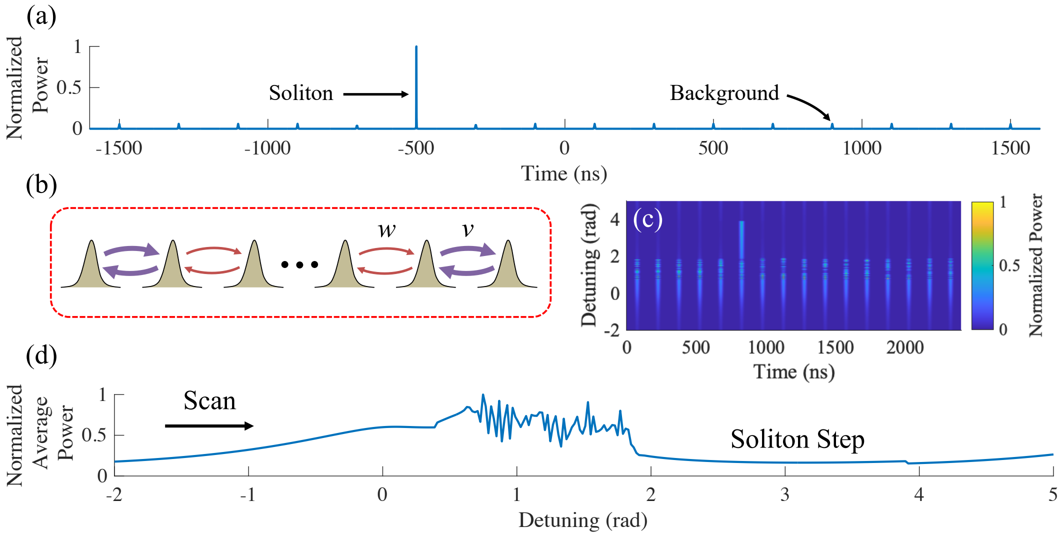

Figure 7.5: Ikeda Map Simulation of an SSH Lattice in the Trivial Phase

Ikeda Map Simulation of an SSH Lattice in the Trivial Phase. **(a)** Roundtrip trace corresponding to the simulated trivial SSH lattice at $\delta = 2.5$. **(b)** Schematic illustration of an SSH lattice in the trivial phase. **(c)** Heat map showing the evolution of the pulse amplitudes throughout the simulation. **(d)** Average power as the cavity is scanned from blue to red detuning.

trivial phase.

In the trace shown in Fig. 7.4(a), the bulk soliton possesses a smaller peak intensity than the edge solitons. These solitons are plotted directly after the couplings, and we can evaluate the effect of the couplings on the soliton intensities by plotting the peak powers of the sites that exhibit solitons before and after the couplings. We plot the intensities prior to the couplings in Fig. 7.6(a) and the intensities after the couplings in Fig. 7.6(b).

Before the onset of modulation instability, the bulk and edge pulses exhibit very similar pre-coupling peak intensities, but the bulk pulse exhibits a larger post-coupling peak intensity. In the soliton regime, we find that the edge and bulk solitons exhibit relatively similar peak intensities prior to the couplings. However, just before the bulk soliton annihilates, we observe that its pre-coupling peak intensity becomes increasingly larger than that of the edge solitons. After the couplings, we find that the peak intensities of the edge solitons are consistently larger than that of the bulk soliton, although the peak intensity of the bulk soliton approaches those of the edge solitons at greater detunings.

In the main text, we argued that the edge solitons form in the topological phase of

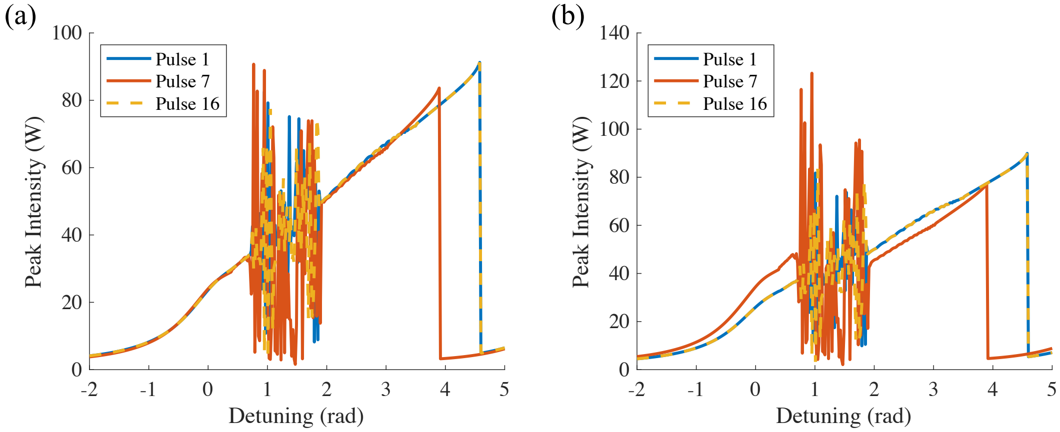

Figure 7.6: Peak Intensities in the Simulation of an SSH Lattice in the Topological Phase

Peak Intensities in the Simulation of an SSH Lattice in the Topological Phase. **(a)** Pre-coupling peak intensities of the sites that exhibit solitons in the simulation of the SSH lattice in the topological phase. **(b)** Post-coupling peak intensities of the sites that exhibit solitons in the simulation of the SSH lattice in the topological phase.

the SSH model because the edge sites see fewer amplitude and phase perturbations than the bulk sites or the edge sites of the SSH model in its trivial phase. Because these perturbations are local, it appears that it might also be possible to generate edge solitons in a lattice without nontrivial topology. We verify that this is the case by simulating soliton formation in a model with a trivial edge state. This model is shown in Fig. 7.7. The edge sites are coupled to the bulk with a weaker coupling v and the remaining sites are coupled by a stronger coupling w. For our simulation we use $w = 0.15$ and $w/v = \sqrt{10}$.

The results of our simulation are shown in Fig. 7.7. To simultaneously generate edge solitons, it appears necessary to use larger detuning steps, and we sweep the detuning from $\delta = -2$ to $\delta = 5$ in 150 equally spaced steps. For smaller detuning steps, and even for other initial seeds with detuning steps of the same size, an edge soliton only forms on one of the edges. Nonetheless, the fact that we can observe edge solitons with this trivial model suggests that local perturbations are indeed responsible for the formation of edge solitons.

Comments on Simulations

While we observe the formation of edge modes in our Ikeda map simulations, we note that there are some differences between our simulations and our experiments.

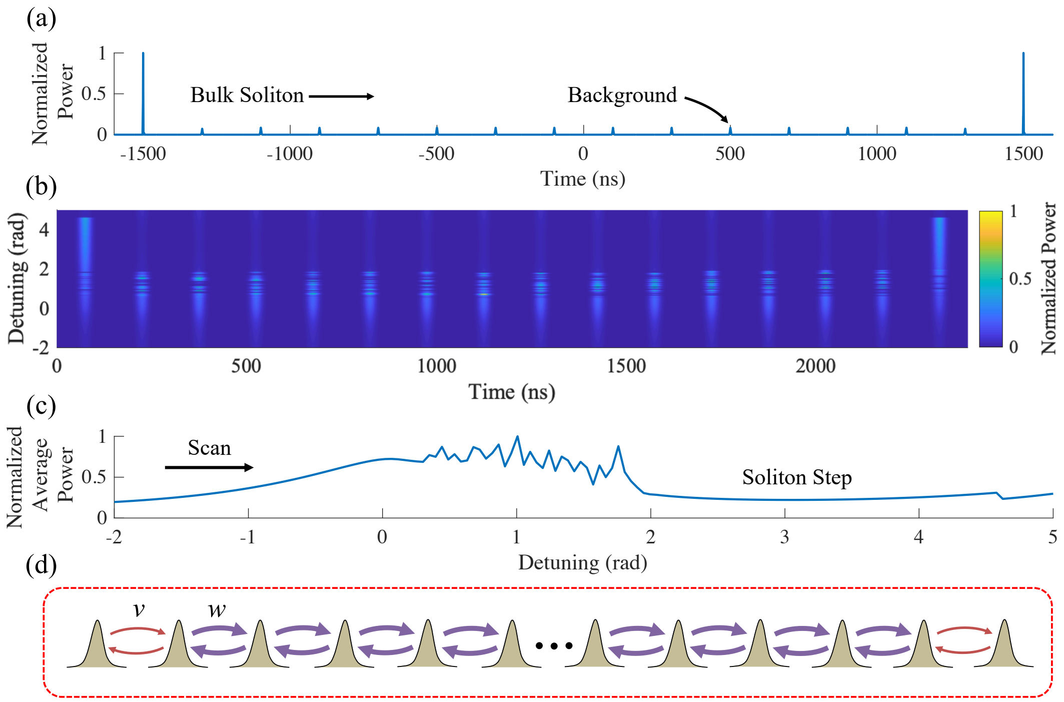

Figure 7.7: Ikeda Map Simulation of a Lattice Possessing a Trivial Edge State

Ikeda Map Simulation of a Lattice Possessing a Trivial Edge State. **(a)** Roundtrip trace corresponding to the simulated trivial SSH lattice at $\delta = 2.5$. **(b)** Heat map showing the evolution of the pulse amplitudes throughout the simulation. **(c)** Average power as the cavity is scanned from blue to red detuning. **(d)** Schematic representation of the simulated lattice, which possesses a trivial edge state.

Most notably, in our experiments we use active gain to compensate for the system's roundtrip losses, while the cavities in our simulations are passive. While ideally, the active gain in our experiments would operate as a linear amplifier, in reality, we observe that the amplifier exhibits some nonlinearity at the power levels used in our experiments. Moreover, the filter added after our erbium doped fiber enables us to shape the gain spectrum in our cavity, but it might also limit the width of our soliton spectrum. Evidently, neither the filter nor the gain saturation prevent the formation of edge solitons.

Another major difference between our simulations and our experiments is that we use a 99:1 splitter to inject the driving pulses in our experiment, while we simulate a 90:10 splitter. We observe that the larger input coupling is necessary to generate solitons with the levels of loss considered in our simulations. In our experiments, we hypothesize that the active gain allows us to achieve the high power levels necessary to generate solitons. The reason we believe this is that most of the loss in our system is concentrated right before the driving pulses are injected into the cavity, while the gain section lies directly after the cavity input. Therefore, the amplified pulses traverse the majority of the cavity at a higher power while experiencing relatively little loss.

Two final differences between our simulations and experiment are the driving powers and the roundtrip losses. In the Ikeda map simulations, we consider a peak power of 75 W. For our experiments, we estimate an input peak power closer to 69.5 W. Similarly, for our experiments, our median roundrip loss measurement is roughly 59.7%, while for our simulations we use a roundtrip loss of 70%. Interestingly, we find that our simulations do not appear to exhibit solitons for a peak power of 69.5 W and 59.7% roundtrip loss. While the roundtrip loss in our experiment is likely greater because of gain saturation, some differences between our simulations and experiment still persist if we consider a peak driving power of 69.5 W and 70% roundtrip loss. Specifically, we typically observe a number of bulk solitons next to the edge solitons when simulating the SSH lattice in the topological phase.

As a concluding remark, our simulations also suggest that pulsed driving is key to generating the edge solitons studied in our experiments. The reason for this appears to be that, with continuous-wave driving, the location of soliton formation is random. On the other hand, pulsed driving forces solitons to form at specific locations, which enables the conditions suitable for edge soliton formation. In the future, it would be interesting to see whether continuous-wave driving can be combined with techniques like phase modulation (Jang et al., 2015) or dichromatic pumping (Lu et al., 2021) to enable edge soliton formation in the continuous-wave driving regime.

References

Anderson, Miles et al. (Aug. 2017). “Coexistence of Multiple Nonlinear States in a Tristable Passive Kerr Resonator”. In: *Phys. Rev. X* 7.3. Publisher: American Physical Society, p. 031031. DOI: `10.1103/PhysRevX.7.031031`. URL: `https://link.aps.org/doi/10.1103/PhysRevX.7.031031` (visited on 05/27/2022).

Black, Eric D. (Jan. 2001). “An introduction to Pound–Drever–Hall laser frequency stabilization”. In: *Am. J. Phys.* 69.1. Publisher: American Association of Physics Teachers, pp. 79–87. ISSN: 0002-9505. DOI: `10.1119/1.1286663`. URL: `https://aapt.scitation.org/doi/10.1119/1.1286663` (visited on 04/08/2022).

Ikeda, Kensuke (Aug. 1979). “Multiple-valued stationary state and its instability of the transmitted light by a ring cavity system”. en. In: *Optics Communications* 30.2, pp. 257–261. ISSN: 0030-4018. DOI: `10.1016/0030-4018(79)90090-7`. URL: `https://www.sciencedirect.com/science/article/pii/0030401879900907` (visited on 07/01/2022).

Jang, Jae K. et al. (June 2015). “Temporal tweezing of light through the trapping and manipulation of temporal cavity solitons”. en. In: *Nat Commun* 6.1. Number: 1 Publisher: Nature Publishing Group, p. 7370. ISSN: 2041-1723. DOI: `10.1038/ncomms8370`. URL: `https://www.nature.com/articles/ncomms8370` (visited on 10/24/2022).

Lu, Zhizhou et al. (May 2021). “Synthesized soliton crystals”. en. In: *Nat Commun.* 12.1. Number: 1 Publisher: Nature Publishing Group, p. 3179. ISSN: 2041-1723. DOI: `10.1038/s41467-021-23172-2`. URL: `https://www.nature.com/articles/s41467-021-23172-2` (visited on 04/14/2022).